

# The Quest for Better Stellar Models

*A Tale in Three Dimensions*

Jakob Lysgaard Rørsted

PhD Thesis

Aarhus University

Jakob Lysgaard Rørsted (Mosumgaard)

*The Quest for Better Stellar Models — A Tale in Three Dimensions*

PhD thesis submitted to the Graduate School of Science and Technology,  
Aarhus University.

December 2019

PhD project supervised by Víctor Silva Aguirre.

Co-supervised by Jørgen Christensen-Dalsgaard and Achim Weiss.

Typeset by the author using LuaL<sup>A</sup>T<sub>E</sub>X and the memoir document class.

The main typeface is Arno Pro at 12.0/14.5pt.

The captions, headings, headers, and folio are set in Scala Sans.

Electronic version

# Abstract

Understanding stellar structure and evolution is one of the key ingredients in astrophysics. It is a fundamental requirement for the studies of our Milky Way galaxy, of high-energy astrophysical phenomena, and of exoplanets. The success of present and future space missions rely critically on an accurate description of the properties of stars.

Perhaps the primary tool for obtaining knowledge about stars is to perform calculations of stellar structure and how it changes in time using a so-called *stellar evolution code*. These are one-dimensional numerical models, which have been developed and tested through decades; as a result they are highly optimised and very efficient. However, in several aspects they are also severely simplified and can be improved. The deficiencies relevant for this research are confined on the outer stellar layers as revealed by the study of oscillations in stars, *asteroseismology*.

A promising way of attacking the inadequacies in the stellar models is to use the results from realistic and highly detailed three-dimensional (3D) hydrodynamics simulations of stellar atmospheres. These simulations are able to accurately reproduce the convection in stars from only fundamental physical principles. The main focus of my PhD research is trying to improve the present-day stellar models by combining them with the sophisticated 3D atmospheres.

In this thesis, three approaches of applying the 3D convection simulations in stellar models are developed and carefully verified with asteroseismology. The first technique revolves around the extraction of condensed information from the simulations that is easy to use for stellar evolution. The second method does not alter the evolution, but instead directly substitutes the outer layers of a model with the structure from a 3D simulation. The third and most important approach seeks to combine the best of the other two by introducing a novel method that robustly incorporated averaged 3D atmospheres in stellar evolution on the fly has been developed and verified. This constitutes a major step forward in the research field of stellar evolution theory.



# Resumé (Dansk)

En af de vigtigste ingredienser i astrofysik er forståelsen af stjerners struktur og udvikling. Det er en uundværlig brik i studier af vores galakse Mælkevejen, af astrofysiske højenergifænomener og af exoplaneter. Nuværende og fremtidige rummissioners succes er i høj grad afhængig af en præcis beskrivelse af stjerners egenskaber.

Det måske vigtigste værktøj til at opnå en forståelse af stjerner er at lave beregninger af stjernestruktur, og hvordan den ændres som tiden går ved at bruge en såkaldt *stjerneudviklingskode*. Disse er én-dimensionelle numeriske modeller, som er udviklet og kontrolleret gennem årtier, og derfor er hyperoptimerede og meget effektive. Adskillige aspekter af dem er dog kraftigt forsimplede og kan forbedres. Studiet af svingninger i stjerner benævnes *asteroseismologi*, og ved brug af dette kan det påvises, at de mangler, der er relevante for denne forskning, er begrænset til de ydre stjernelag.

En lovende metode til at forbedre disse utilstrækkeligheder i en stjernemodel er at anvende resultater fra realistiske og yderst detaljerede tredimensionelle (3D) simuleringer af hydrodynamikken i stjerneatmosfærer. Disse simuleringer er i stand til at reproducere konvektionen i stjerner kun ved brug af basale fysiske principper. Hovedfokus i min PhD-forskning er at forsøge på at forbedre vores nuværende stjernemodeller ved at kombinere dem med de avancerede 3D-atmosfærer.

I denne afhandling vil tre forskellige metoder til at anvende konvektive 3D-simuleringer i stjernemodeller blive udviklet samt efterprøvet med asteroseismologi. Den første teknik drejer sig om at udtrække komprimeret information fra simuleringerne, som er nem at anvende til stjerneudvikling. Den anden procedure ændrer ikke ved udviklingen, men udskifter i stedet de ydre lag i en model med strukturen fra en 3D-simulering. Den tredje og vigtigste metode ønsker at kombinere det bedste fra to første ved at introducere en nyskabende metode, der på sikker vis kan inkludere 3D-atmosfærer i stjerneudvikling på farten. Dette udgør et stort skridt fremad for forskningen i stjerneudviklingsteori.



# Contents

<b>Abstract</b>	<b>iii</b>
<b>Resumé (Dansk)</b>	<b>v</b>
<b>Contents</b>	<b>vii</b>
<b>Preface</b>	<b>xi</b>
<b>List of Publications</b>	<b>xiii</b>
<b>Abbreviations and Acronyms</b>	<b>xix</b>
<b>Introduction</b>	<b>1</b>

## **I Scientific Background**

<b>1 The Making of Stars</b>	<b>7</b>
1.1 A Brief History of Timescales . . . . .	7
1.2 The Fundamental Equations . . . . .	9
1.3 The Life of a Star . . . . .	13
1.4 Generation and Transport of Energy . . . . .	15
1.5 Stellar Convection . . . . .	19
1.6 Models of Stellar Structure and Evolution . . . . .	24

<b>2</b>	<b>Asteroseismology</b>	<b>31</b>
2.1	Basic Theory of Stellar Oscillations . . . . .	32
2.2	Observing Solar-like Oscillations . . . . .	36
2.3	Oscillation Frequencies of Stellar Models . . . . .	40
2.4	The Asteroseismic Surface Effect . . . . .	43
<b>3</b>	<b>Determination of Stellar Properties</b>	<b>47</b>
3.1	Observations of Stars . . . . .	47
3.2	Chemical Composition . . . . .	50
3.3	Asteroseismic Inference . . . . .	52
3.4	Grid-based Modelling . . . . .	56
<b>4</b>	<b>Modelling of Stellar Atmospheres</b>	<b>61</b>
4.1	Numerical Simulations of Surface Convection . . . . .	62
4.2	The Link to Stellar Models I . . . . .	64
4.3	The Link to Stellar Models II . . . . .	65
4.4	The Link to Stellar Models III . . . . .	67

## II Research Results

<b>5</b>	<b>Condensed 3D in 1D</b>	<b>71</b>
5.1	Introduction . . . . .	72
5.2	3D Simulations of Stellar Atmospheres . . . . .	74
5.3	Implementation . . . . .	76
5.4	Stellar Evolution with 3D Results . . . . .	79
5.5	Comparison to Earlier Works . . . . .	88
5.6	Conclusions . . . . .	90
5.A	Models with SC15 Settings . . . . .	91
5.B	Correction of the Gradients . . . . .	91
<b>6</b>	<b>Patching with Interpolated 3D Atmospheres</b>	<b>93</b>
6.1	Introduction . . . . .	95
6.2	Constructing Patched Models . . . . .	95
6.3	The Solar Case . . . . .	105
6.4	Selecting Atmosphere Parameters . . . . .	110
6.5	Stars in the <i>Kepler</i> field . . . . .	113
6.6	Conclusions . . . . .	124

<b>7</b>	<b>On The Fly I</b>	<b>127</b>
7.1	Introduction . . . . .	129
7.2	Implementation . . . . .	129
7.3	A Solar Calibration . . . . .	132
7.4	Conclusions . . . . .	138
<b>8</b>	<b>On The Fly II</b>	<b>139</b>
8.1	Introduction . . . . .	140
8.2	Method . . . . .	141
8.3	Solar Models . . . . .	144
8.4	Stellar Evolution . . . . .	153
8.5	Asteroseismic Application . . . . .	158
8.6	Red-Giant Branch Models . . . . .	163
8.7	Conclusions . . . . .	168
8.A	Grid Morphology . . . . .	171
<b>9</b>	<b>Conclusions and Outlook</b>	<b>173</b>
	<b>Glossary</b>	<b>177</b>
	<b>List of Figures</b>	<b>183</b>
	<b>List of Tables</b>	<b>185</b>
	<b>Bibliography</b>	<b>187</b>
	<b>Appendices</b>	
<b>A</b>	<b>The Dynamic Approach in MESA</b>	<b>211</b>
A.1	Modification of radiative gradient . . . . .	212
A.2	Boundary conditions . . . . .	212



# Preface

This thesis comprises the scientific research work that I have conducted during my PhD studies from February 2015 to December 2019 under the supervision of Víctor Silva Aguirre, with co-supervision of Jørgen Christensen-Dalsgaard and Achim Weiss.

As is standard procedure, I was admitted to the PhD program without having obtained a Master's degree – in fact, I started almost just after having obtained my Bachelor's degree, which permitted a duration of almost five years. The work has mainly been carried out at the Stellar Astrophysics Centre (SAC) at the Department of Physics and Astronomy, Aarhus University; and during a highly productive stay at the Max-Planck-Institut für Astrophysik in Garching, Germany. Note that I changed my surname from 'Mosumgaard' to 'Rørsted' in 2018, however all of my publications are associated with 'Mosumgaard'.



In accordance with the rules of GSST (the Graduate School of Science and Technology, Aarhus University), it has to be noted that parts of this thesis were also used in the progress report for the qualifying examination.



First of all, I want to sincerely thank my supervisor, Víctor. You have in all aspects been the best advisor I could have wished for – all the way from when I was a young student that entered your office, sent by Hans (who suddenly needed to travel) to do stellar models. Thank you for always taking an interest and for never lowering the bar. Without you, I would not be the scientist I am today.

My co-supervisors also deserves a special mention. Achim, thank you for letting me work on your wonderful stellar evolution code. But more importantly, I really appreciate my time at MPA, which was very productive and central to my PhD research. You are never short of valuable advice and have inspired me to become a better researcher. And Jørgen, thank you for never failing to answer a question, and for always taking the time to properly address the bi-annual bureaucratic PhD-planning.

Hans, you also deserve a special mention. Thank you for “handing me over” to Víctor during by Bachelor’s project: that opened my eyes to the wonders of theoretical stellar modelling and asteroseismology. Also thanks for our time together on the teaching committee.

Thank you to everyone at the Stellar Astrophysics Centre. You have been excellent colleagues through the years and I cannot imagine a better place to conduct a PhD. Especially thanks to all current and former members of *The Christmas Office* for brightening the many hours of Danish winter. Also Louise and Brigitte, you have been excellent in helping with any administrative issues. Thanks to Tim Bedding and Jørgen for letting me use your plots.

All of my family and friends, thank you for the support and the good memories. Especially the people at TÅGEKAMMERET: you have been a major part of my time at Aarhus University. Without you, the years would have been significantly harder and not nearly as entertaining. FUHI (Mathias), thank you for contributing to my preamble; and for our many discussions about L<sup>A</sup>T<sub>E</sub>X, typography, and design. A special heartfelt thanks is directed at my dear friends and faithful proofreaders: Amalie and Mathias. Amalie, you are the best office mate ever to exist. Mathias, I could never have wished for a better best-man than you.

Tak til min familie, for altid at tro på mig og tilskynde mig at følge mine drømme. Far, tak for at introducere mig til god typografi i en ung alder og for aldrig at have ladet mig aflevere en grim stil. Og Mor, tak for at lære mig om glæderne ved naturvidenskab, for at lade mig sprænge ting i luften i garagen og for altid at holde sammen på os alle.

Finally, Mette, my wonderful wife. You have been my strongest support through my studies – and even more so during this thesis writing process. Without you I would never have finished! But I want to stress: performing french Can Can in the living room is *not* something to be frowned upon!

# List of Publications

A full list of publications and their details are also available from my library at ADS (The SAO/NASA Astrophysics Data System):

[ui.adsabs.harvard.edu/user/libraries/jj\\_CoZbtSS0ELK43DmYt9w](http://ui.adsabs.harvard.edu/user/libraries/jj_CoZbtSS0ELK43DmYt9w).

## First Author Peer-reviewed Publications

The following two publications are included in this thesis.

- ✎ *Coupling 1D stellar evolution with 3D-hydrodynamical simulations on-the-fly II: Stellar Evolution and Asteroseismic Applications.*  
**Mosumgaard, J. R;** Jørgensen, A. C. S.; Weiss, A; Silva Aguirre, V; and Christensen-Dalsgaard, J.  
— Monthly Notices of the Royal Astronomical Society, 2585, October 2019.
  
- ✎ *Stellar models with calibrated convection and temperature stratification from 3D hydrodynamics simulations.*  
**Mosumgaard, J. R;** Ball, W. H; Silva Aguirre, V; Weiss, A. and Christensen-Dalsgaard, J.  
— Monthly Notices of the Royal Astronomical Society, 478, 5650, August 2018.

## Co-author Peer-reviewed Publications, part I

The following two publications are included in this thesis in a (partially) re-written form.

- ✎ *Coupling 1D stellar evolution with 3D-hydrodynamical simulations on the fly - I. A new standard solar model.*  
 Jørgensen, A. C. S; **Mosumgaard, J. R.**; Weiss, A; Silva Aguirre, V. and Christensen-Dalsgaard, J.  
 — Monthly Notices of the Royal Astronomical Society, 481, L35, November 2018.
  
- ✎ *Theoretical oscillation frequencies for solar-type dwarfs from stellar models with 3D-atmospheres.*  
 Jørgensen, A. C. S; Weiss, A; **Mosumgaard, J. R.**; Silva Aguirre, V. and Sahlholdt, C. L.  
 — Monthly Notices of the Royal Astronomical Society, 472, 3264, December 2017.

## Co-author Peer-reviewed Publications, part II

- ✎ *The subgiant HR 7322 as an asteroseismic benchmark star*  
 Stockholm, A; Nissen, P. E; Silva Aguirre, V; White, T. R; Lund, M. N; **Mosumgaard, J. R.**; Huber, D. and Jessen-Hansen, J.  
 — Monthly Notices of the Royal Astronomical Society, 489, 928, October 2019.
  
- ✎ *A Hot Saturn Orbiting an Oscillating Late Subgiant Discovered by TESS.*  
 Huber, D; Chaplin, W. J; Chontos, A; Kjeldsen, H; Christensen-Dalsgaard, J; Bedding, T. R; Ball, W; Brahm, R; Espinoza, N; Henning, T; Jordán, A; Sarkis, P; Knudstrup, E; Albrecht, S; Grundahl, F; Fredslund Andersen, M; Pallé, P. L; Crossfield, I; Fulton, B; Howard, A. W; Isaacson, H. T; Weiss, L. M; Handberg, R; Lund, M. N; Serenelli, A. M; **Mosumgaard, J. R.**; Stockholm, A; Bieryla, A; Buchhave, L. A; Latham, D. W; Quinn, S. N; Gaidos, E; Hirano, T; Ricker, G. R; Vanderspek, R. K; Seager, S; Jenkins,

J. M; Winn, J. N; Antia, H. M; Appourchaux, T; Basu, S; Bell, K. J; Benomar, O; Bonanno, A; Buzasi, D. L; Campante, T. L; Çelik Orhan, Z; Corsaro, E; Cunha, M. S; Davies, G. R; Deheuvels, S; Grunblatt, S. K; Hasanzadeh, A; Di Mauro, M. P; García, R. A; Gaulme, P; Girardi, L; Guzik, J. A; Hon, M; Jiang, C; Kallinger, T; Kawaler, S. D; Kuszlewicz, J. S; Lebreton, Y; Li, T; Lucas, M; Lundkvist, M. S; Mann, A. W; Mathis, S; Mathur, S; Mazumdar, A; Metcalfe, T. S; Miglio, A; Monteiro, M. J. P. F. G; Mosser, B; Noll, A; Nsamba, B; Ong, J. M. J; Örtel, S; Pereira, F; Ranadive, P; Régulo, C; Rodrigues, T. S; Roxburgh, I. W; Silva Aguirre, V; Smalley, B; Schofield, M; Sousa, S. G; Stassun, K. G; Stello, D; Tayar, J; White, T. R; Verma, K; Vrad, M; Yıldız, M; Baker, D; Bazot, M; Beichmann, C; Bergmann, C; Bugnet, L; Cale, B; Carlino, R; Cartwright, S. M; Christiansen, J. L; Ciardi, D. R; Creevey, O; Dittmann, J. A; Do Nascimento, J.-D; Van Eylen, V; Fürész, G; Gagné, J; Gao, P; Gazeas, K; Giddens, F; Hall, O. J; Hekker, S; Ireland, M. J; Latouf, N; LeBrun, D; Levine, A. M; Matzko, W; Natinsky, E; Page, E; Plavchan, P; Mansouri-Samani, M; McCauliff, S; Mullally, S. E; Orenstein, B; Garcia Soto, A; Paegert, M; van Saders, J. L; Schnaible, C; Soderblom, D. R; Szabó, R; Tanner, A; Tinney, C. G; Teske, J; Thomas, A; Trampedach, R; Wright, D; Yuan, T. T. and Zohrabi, F.  
— *Astronomical Journal*, 157, 245, June 2019.

☞ *Helium abundance in a sample of cool stars: measurements from asteroseismology.*

Verma, K; Raodeo, K; Basu, S; Silva Aguirre, V; Mazumdar, A; **Mosumgaard, J. R**; Lund, M. N. and Ranadive, P.  
— *Monthly Notices of the Royal Astronomical Society*, 483, 4678, March 2019.

☞ *Testing asteroseismic radii of dwarfs and subgiants with Kepler and Gaia.*  
Sahlholdt, C. L; Silva Aguirre, V; Casagrande, L; **Mosumgaard, J. R.** and Bojsen-Hansen, M.

— *Monthly Notices of the Royal Astronomical Society*, 476, 1931, May 2018.

- ☞ *Confirming chemical clocks: asteroseismic age dissection of the Milky Way disc(s).*  
 Silva Aguirre, V; Bojsen-Hansen, M; Slumstrup, D; Casagrande, L; Kawata, D; Ciuca, I; Handberg, R; Lund, M. N; **Mosumgaard, J. R.**; Huber, D; Johnson, J. A; Pinsonneault, M. H; Serenelli, A. M; Stello, D; Tayar, J; Bird, J. C; Cassisi, S; Hon, M; Martig, M; Nissen, P. E; Rix, H. W; Schönrich, R; Sahlholdt, C; Trick, W. H. and Yu, J.  
 — Monthly Notices of the Royal Astronomical Society, 475, 5487, April 2018.
- ☞ *Convective-core Overshoot and Suppression of Oscillations: Constraints from Red Giants in NGC 6811.*  
 Arentoft, T; Brogaard, K; Jessen-Hansen, J; Silva Aguirre, V; Kjeldsen, H; **Mosumgaard, J. R.** and Sandquist, E. L.  
 — Astrophysical Journal, 838, 115, April 2017.
- ☞ *Standing on the Shoulders of Dwarfs: the Kepler Asteroseismic LEGACY Sample. II. Radii, Masses, and Ages.*  
 Silva Aguirre, V; Lund, M. N; Antia, H. M; Ball, W. H; Basu, S; Christensen-Dalsgaard, J; Lebreton, Y; Reese, D. R; Verma, K; Casagrande, L; Justesen, A. B; **Mosumgaard, J. R.**; Chaplin, W. J; Bedding, T. R; Davies, G. R; Handberg, R; Houdek, G; Huber, D; Kjeldsen, H; Latham, D. W; White, T. R; Coelho, H. R; Miglio, A. and Rendle, B.  
 — Astrophysical Journal, 835, 173, 2017.
- ☞ *Standing on the Shoulders of Dwarfs: the Kepler Asteroseismic LEGACY Sample. I. Oscillation Mode Parameters.* Lund, M. N; Silva Aguirre, V; Davies, G. R; Chaplin, W. J; Christensen-Dalsgaard, J; Houdek, G; White, T. R; Bedding, T. R; Ball, W. H; Huber, D; Antia, H. M; Lebreton, Y; Latham, D. W; Handberg, R; Verma, K; Basu, S; Casagrande, L; Justesen, A. B; Kjeldsen, H. and **Mosumgaard, J. R.**  
 — Astrophysical Journal, 835, 172, 2017.

## Selected Publications in Preparation

☞ *The Aarhus Red Giants Challenge I: Stellar structures in the red giant branch phase.*

Silva Aguirre, V; Christensen-Dalsgaard, J; Cassisi, S; Miller Bertolami, M; Serenelli, A. M; Stello, D; Weiss, A; Angelou, G; Jiang, C; Lebreton, Y; Spada, F; Bellinger, E. P; Deheuvels, S; Ouazzani, R. M; Pietrinferni, A; **Mosumgaard, J. R**; Townsend, R. H. D; Battich, T; Bossini, D; Constantino, T; Eggenberger, P; Hekker, S; Mazumdar, A; Miglio, A; Nielsen, K. B. and Salaris, M.

— Accepted for publication in *Astronomy and Astrophysics*,  
arXiv:1912.04909.

## Publications without Peer-review

☞ *Improving 1D Stellar Models with 3D Atmospheres.*

**Mosumgaard, J. R**; Silva Aguirre, V; Weiss, A; Christensen-Dalsgaard, J. and Trampedach, R.

— *European Physical Journal Web of Conferences*, 160, 03009,  
October 2017.



# Abbreviations and Acronyms

- 2MASS** Two Micron All Sky Survey; 48, 181
- ADIPLS** Aarhus adiabatic pulsation code; 42, 59, 86, 105, 113, 114, 134, 144, 159, 165, 177
- ASTECC** Aarhus stellar evolution code; 44, 96, 177
- BASTA** BAYesian STellar Algorithm; 58, 59, 93, 115, 116, 122, 159–161, 164, 170, 177
- BASTI** Bag of Stellar Tracks and Isochrones; 59, 88, 177
- BFM** best-fitting model; 115–117, 122, 160, 162–164, 170, 178
- BISON** Birmingham Solar-Oscillations Network; 37, 38, 40, 41, 43, 44, 86, 87, 105, 107, 135, 137, 145–147, 178
- CHE** core-hydrogen exhaustion; 14, 15, 83, 90, 178
- COROT** CONvection ROTation and planetary Transits; 50, 164, 178
- EOS** equation of state; 11, 12, 44, 81, 106, 107, 113, 122, 131, 132, 134, 142, 144, 145, 155, 158, 162, 163, 169, 178
- FST** full-spectrum theory; 24, 107, 178
- GARSTEC** Garching stellar evolution code; 27, 28, 44, 59, 67, 71, 75–82, 84, 86, 88–92, 97, 104, 106, 113, 114, 128–130, 134, 141, 144, 145, 151, 154, 157, 159, 162, 163, 173, 175, 178

- HRD** Hertzsprung-Russel diagram; 13, 15, 74, 111, 114, 124, 139, 140, 168, 179
- IRFM** InfraRed Flux Method; 48, 117, 179
- MESA** Modules for Experiments in Stellar Astrophysics; 71–74, 76, 77, 79–81, 83, 84, 86–92, 173, 180, 211–213
- MLT** mixing-length theory; 22–24, 27, 61, 63–66, 73, 79, 80, 88, 107, 133, 140, 144, 180, 211
- MS** main sequence; 14–16, 22, 32, 35, 36, 50, 55, 82, 89, 99, 103, 124, 149, 154–156, 158, 160, 169, 170, 174, 179
- PDF** probability density function; 58, 59, 115, 180
- PLATO** PLAnetary Transits and Oscillation of stars; 50, 175, 180
- PMS** pre-main sequence; 14, 28, 72, 75, 82–84, 90, 131, 132, 169, 180
- PM** patched model; 63–65, 74, 87, 88, 90, 94–97, 99, 105, 106, 108–113, 115–124, 129, 135, 137, 138, 162, 163, 168, 170, 174, 180
- RGB** red-giant branch; 14, 15, 32, 36, 72, 73, 82–84, 90, 140, 147–149, 151–153, 155, 163, 165, 167–170, 181
- RG** red giant; 15, 42, 50, 56, 73, 99, 139–141, 155, 158, 163, 164, 168, 170, 174, 180
- RHD** radiation-coupled hydrodynamics; 61–66, 73, 77, 89, 90, 95, 96, 99, 105, 124, 125, 127, 129, 140, 141, 150, 155, 158, 167, 170, 173, 175, 180
- SSM** standard solar model; 28, 35, 43, 44, 51, 64, 66, 72, 81, 84, 89, 90, 95, 96, 105, 122–124, 129, 132, 133, 137, 138, 140, 144–146, 149–151, 154, 156, 169, 181
- TESS** Transiting Exoplanet Survey Satellite; 50, 181
- UPM** un-patched model; 94–97, 105–107, 109–124, 182
- ZAMS** zero-age main sequence; 14, 36, 114, 155, 182

# Introduction

Looking up at the clear sky at night, you see them: the sparkly dots. But what are they? In Disney's *The Lion King*, they are suggested to be either "fireflies that, uh... got stuck up on that big bluish-black thing" or "balls of gas burning billions of miles away". Science favours the latter explanation. More specifically, almost all of the dots are *stars*. A star is a sphere of very hot gas held together by its own gravity. For most of a star's life, the gravitational forces are delicately balanced by interior forces directed outwards: this is called *hydrostatic equilibrium*. In the centre of a star, nuclear processes generate energy that is transported to the surface and radiated away into space. But why do we care about those sparkly dots so far, far away from us?

## Why study stars?

Stars are the building blocks of astrophysics. Through their lives and when they die, different nuclear processes will produce most known chemical elements. In fact, stars are the main source of chemical evolution in the Universe.

By analysing the combined light of all stars contained in a distant galaxy, it is possible to gain an understanding of galactic properties. When the stars can be *resolved by observations* (that is, seen as individual objects), the light emitted from each of them can be collected and analysed, and used to infer their individual properties. This is the case for the stars in our own Milky Way galaxy, where the field of *galactic archaeology* uses stars as "fossils" that contain an imprint of their birth environment. To understand the structure and evolution of our Galaxy this way, it is of utmost importance to accurately determine the *ages* of stars.

In the past decade, it has been a very prominent research field to study of planets orbiting stars other than the Sun: the so-called *exoplanets*. The various methods to infer their properties depend critically on knowing the properties of the host star: its *mass*, *radius*, and *age*. A popular saying is “*know thy star, know thy planet*”: to analyse populations of exoplanets, the host stars must first be characterised accurately.

Last but not least, stars are interesting in themselves. In order to understand all intricate details, many different branches of physics must be utilised – from atomic and nuclear physics, through statistical mechanics and hydrodynamics, to quantum mechanics and electrodynamics. Fundamental physics can be tested by relying on the extreme conditions in the stellar interior or in the even-more extreme environment when a star explodes in an exotic incident such as a supernova or gamma-ray burst. Moreover, as stars are the progenitors of these high-energy phenomena, the theory of stars must be well understood to properly characterise the actual event.

### What is inside stars?

A star is observed by the light emitted from its surface. However, if we really want to understand the details of stellar physics (or determine how old a star is), we cannot limit ourselves to studying the outside: knowledge about the deep interior is required. This is easier said than done, because stellar surface layers are opaque.

It turns out that many stars pulsate or oscillate: like giant musical instruments or bells ringing into space. In the same way as earthquakes can be used to study the deep hidden layers of our Earth with *seismology*, these starquakes can be used to probe the interior of a star through the imprint they leave in the emitted light. The study of stellar oscillations are known as *asteroseismology* and it is a central pillar in modern stellar physics research.

As not all things we want to know about stars can be directly measured, we need to infer the characteristics of stars based on our current best theoretical understanding of them. Therefore, when determining the fundamental properties of stars, an important tool is a *stellar model*: a numerical computer simulation of stellar structure and evolution. Stellar models are necessary for all of the applications listed above and are as such invaluable. Calculations of stellar evolution are performed with codes that have been highly optimised and improved through several decades.

One question stands: how do we know if our models are correct? An ideal tool to use in the search for the answer to this question is *asteroseismology* – or *helioseismology* in the case of the Sun. Given a stellar model, it is possible to predict how the star in theory should pulsate. This prediction from stellar models can then be put to the test by comparing it to what is actually observed. Performing this test leads to an uncomfortable truth: our models, however refined they might be, do not match our observations perfectly. In other words, the theory of stellar structure and evolution cannot be said to be a solved problem.

### What is wrong?

From detailed helioseismic analyses it turns out that stellar models are incorrect in how they describe the outermost layers near the stellar surface. This is a result of a combination of physical inadequacies in stellar models giving rise to what is collectively known as the *surface effect*.

At the root of the problem is the phenomenon known as *convection*: the stochastic motion of gasses in the outer regions of stars like the Sun. The characteristic timescale for these motions is very short compared to the timescale governing the nuclear reactions in the stellar centre and hence its total lifetime. In order to be able to follow the larger parts of stellar evolution, stellar models cannot simultaneously resolve the convection timescale and must therefore rely on a simplified parametric theory. Moreover, all of the models so far can be considered as one-dimensional (1D) as they assume perfect spherical symmetry. However, dynamical phenomena like convection are inherently multi-dimensional and in principle too complex for such simplified descriptions.

Another completely different approach to convection is to instead focus on the short timescales and perform three-dimensional (3D) numerical computations of the outer stellar layers. These highly sophisticated ‘3D simulations’ can reproduce the solar convection from first principles and are very physically accurate. However, they cannot be used to investigate stellar evolution: they are extremely computationally expensive and therefore they do not simulate the entire star, but only a tiny region with convection near the surface. Furthermore, due to the timescales of the overall problem, it is not feasible to simulate just a tiny fraction of a star’s evolution.

## What can be done?

The key motivational point of my research is now reached: how can we get the “*best of both worlds*” by combining 3D simulations with stellar evolution models? That is the research question behind my PhD studies and this thesis work.

The thesis is structured in two main parts. In the first, the theoretical background required to understand the research are given, as well as a review of the current status of the field. The fundamental principles of stellar structure and evolution are given in chapter 1, followed by a concise review of asteroseismology in chapter 2. In chapter 3, the techniques and tools to determine stellar properties are introduced. Finally, chapter 4 will present an overview of the different possible methods for combining the 3D simulations and stellar models, thus introducing the next part of the thesis.

In the second part, my research results are presented. Each chapter corresponds to a published, peer-reviewed scientific paper. One option to include information from 3D simulations is presented in chapter 5, where the basic idea is to extract quantities that are easy to use for stellar evolution from the 3D simulations. An alternative method that is built on patching the full structure of the two model types together is described in chapter 6; the impact on the models is large but does not affect the evolution. Each of the two schemes has their drawbacks, which motivated the work leading to the main research result presented in a pair of papers and reproduced in chapters 7 and 8. Here the best of the two methods is combined to effectively yield the use of 3D simulations on-the-fly for stellar evolution. Finally, in chapter 9 I will briefly summarise the key results and put them into context.

— Now, let us have a closer look at those sparkly dots.

Part I



*Scientific Background*



# The Making of Stars

The understanding of stellar structure and evolution is a key topic in astrophysics, and near the very core of this thesis. As the research goal is to improve the computed models of stars, a basic knowledge foundation is required. Hence, this chapter provides a condensed description of the tools required to understand the evolution of stars and their interior structure.

The topic is concisely introduced by Silva Aguirre (2018), presenting a condensed overview from a “stellar modelling” point-of-view. A more comprehensive account focusing on the basic physical principles can be found in Christensen-Dalsgaard (2008c), or in the very complete reference work by Kippenhahn, Weigert, and Weiss (2012). These are the main references for this chapter.

The chapter is organised as follows. Just below, the important timescales governing stars are reviewed, and in section 1.2 the central equations and constitutive relations are introduced. The evolution of stars similar to the Sun are sketched in section 1.3. Energy production and transport are treated in section 1.4, and section 1.5 is dedicated to convection and the theory to describe it. Finally, how to combine the ingredients and produce stellar evolution models are discussed in section 1.6, with emphasis on technical aspects relevant for later chapters.

## 1.1 A Brief History of Timescales

Changes in a star takes place on a range of different timescales. The variations are a result of the interplay between the energy sources in a star acting

simultaneously – the gravitational contraction and the thermonuclear reactions. However, generally the forces acting on a star are very nearly balanced; a situation known as *hydrostatic equilibrium*, which is one of the central pillars in stellar structure theory (see section 1.2).

The shortest relevant timescale is the so-called *free-fall* or *dynamical* timescale  $t_{\text{dyn}}$ . This timescale describes the characteristic time for motions in a gravitational field on stellar scales, or the time required by the star to recover its equilibrium if disturbed by a dynamical process. It is given by

$$t_{\text{dyn}} \simeq \left( \frac{R^3}{GM} \right)^{1/2} \simeq \left( \frac{1}{G \langle \rho \rangle} \right)^{1/2}, \quad (1.1)$$

where  $G$  is the gravitational constant, while  $R$ ,  $M$  and  $\langle \rho \rangle$  are the radius, mass and mean density of the star, respectively. For the Sun, the dynamical timescale is in the order of 20-30 minutes.

If the star has no internal sources of energy – or if the nuclear reactions are not efficient – the star will contract and therefore radiate energy. The relevant timescale of this process is the *Kelvin-Helmholtz* timescale  $t_{\text{KH}}$ , which is also known as the *thermal* timescale. It can be estimated as

$$t_{\text{KH}} \simeq \frac{GM^2}{RL}, \quad (1.2)$$

where  $L$  is the surface luminosity of the star, i.e., the amount of energy it radiates per unit time. It is an estimate of the time the star can continue to shine at its current luminosity through this process – or the time it would take to radiate away all of its thermal energy. Moreover,  $t_{\text{KH}}$  can be considered as the timescale of thermal adjustment of a star; the time it takes for a thermal fluctuation to travel from the centre to the surface. For the Sun it is around 30 million years.

The final and longest relevant timescale to be mentioned is the *nuclear* timescale  $t_{\text{nuc}}$ . It is a description of how long a star can shine at its current luminosity with nuclear fusion as the only energy source. Assuming a constant luminosity, it is defined as

$$t_{\text{nuc}} = \frac{E_{\text{n}}}{L}, \quad (1.3)$$

where  $E_{\text{n}}$  is the total amount of nuclear energy that can be released. The most important case is the fusion of hydrogen into helium, in which around

0.7 percent of the mass is lost in the reaction. Using Einstein's mass-energy equivalence, this equates to roughly 10 billion years for our Sun, assuming the conversion of the inner 10 percent of the total mass. Since the vast majority of a star's life is spent in the hydrogen burning phases (section 1.3)  $t_{\text{nuc}}$  also provides an estimate of the total lifetime of a star.

As is evident from the numbers quoted above, large differences exist between the mentioned timescales, which are ordered as

$$t_{\text{dyn}} \ll t_{\text{KH}} \ll t_{\text{nuc}} . \quad (1.4)$$

The extreme contrast in magnitude between them imply, that it is numerically not possible to track the details of dynamic phenomena over the entire lifetime of a star. As the goal of stellar evolution theory is to follow a larger part of the evolution of a star, the shortest timescales must be properly treated over long periods of time. This is done using simplifying assumptions and parametrisations, which are described in the remainder of this chapter.

## 1.2 The Fundamental Equations

For a spherically symmetric star near equilibrium, the structural changes are described by a system of four basic differential equations which will be introduced in the following. In the equations,  $r$  is the distance from the centre of the star and  $m$  is the contained mass within that distance; ranging from  $r = 0$  and  $m = 0$ , to  $r = R$  and  $m = M$  at the surface. As it is custom to (almost) always consider the evolution of a star with a given mass – and because  $R$  varies strongly as a function of time while  $M$  is almost constant – it is convenient to use the contained mass  $m = m(r)$  as the coordinate. In the following, the thermodynamic variables are always defined at the corresponding point  $r$  or  $m$  in the star.

The first two of the four equations provide the mechanical component of the problem. It is the equation of *mass conservation*

$$\frac{\partial r}{\partial m} = \frac{1}{4\pi r^2 \rho} , \quad (1.5)$$

and of *hydrostatic equilibrium*

$$\frac{\partial P}{\partial m} = -\frac{Gm}{4\pi r^4} , \quad (1.6)$$

where  $\rho = \rho(m)$  is the density and  $P = P(m)$  is the pressure. The assumption of hydrostatic equilibrium translates is one of the cornerstones of stellar structure theory and implies that the external forces are balanced by the pressure gradient. These mechanical equations are coupled to the next part only through the density  $\rho$ , which depends on the temperature  $T$ .

The final two equations of the system constitute the thermo-energetic part of the problem. The *energy conservation equation* is the first of these and can be written as

$$\frac{\partial L}{\partial m} = \varepsilon_n - \varepsilon_\nu + \varepsilon_g , \quad (1.7)$$

where  $L = L(m)$  is the luminosity at the given position in the star;  $\varepsilon_n$  is the rate of energy generated by nuclear reactions per unit mass,  $\varepsilon_\nu$  is the energy loss from neutrinos, and  $\varepsilon_g$  is the work resulting from expansion or contraction of the star contains time derivatives of thermodynamic quantities. The fourth and final equation is

$$\frac{\partial T}{\partial m} = -\frac{GmT}{4\pi r^4 P} \nabla , \quad \text{where} \quad \nabla := \frac{d \ln T}{d \ln P} \quad (1.8)$$

is the temperature gradient and  $T = T(m)$  is the temperature at the given point. This is the equation of *energy transport*, where the value of the crucial temperature gradient  $\nabla$  must be determined from the thermodynamical properties of the stellar matter. Specifically, it will depend on the exact type of energy transport taking place (elaborated in section 1.4).

The eqs. (1.5)–(1.8) are commonly referred to as the stellar structure equations – they describe the constitution of a star at a *specific time* and *composition*. Thus, to complete the picture, the chemical evolution must be taken into account. Specifically, the system must be augmented with the following set of equations

$$\frac{\partial X_i}{\partial t} = r_{X_i} , \quad i = 1, \dots, I , \quad (1.9)$$

where  $t$  is time, which simply defines the time evolution of the nuclei  $i$  with the rate of change  $r_{X_i}$  for all of the  $I$  species. Here,  $X_i$  denotes the fraction of a unit mass consisting of element  $i$ , hence requiring

$$\sum_i X_i = 1 . \quad (1.10)$$

For many purposes, it is sufficient to specify the mass fractions of hydrogen (H), helium (He) and “the rest”. Hence, it is customary to introduce the specific notation

$$X := X_{\text{H}} \quad , \quad Y := X_{\text{He}} \quad , \quad Z := 1 - X - Y \quad , \quad (1.11)$$

which will be used throughout this thesis.

If only nuclear reactions create or destroy a given species  $i$  of mass  $m_i$ , the rate of change from eq. (1.9) can be rewritten in terms of the (nuclear) reaction rates as

$$r_{X_i} = \frac{m_i}{\rho} \left( \sum_j r_{ji} - \sum_k r_{ik} \right) \quad , \quad (1.12)$$

where  $r_{ji}$  is the rate with which the element is created and  $r_{ik}$  is the destruction rate.

Rather than being stationary, the solutions to these stellar equations evolve with time as a result of e.g. nuclear reactions and gravitational contraction. It is useful to recall that under normal conditions, the nuclear timescale is much larger than the other relevant timescales, cf. eq. (1.4). Thus, in most cases the chemical parts (1.9) can be decoupled from the spatial parts in eqs. (1.5)–(1.8).

### 1.2.1 Constitutive Relations

In order to solve the stellar equations, a description of the properties of stellar matter is required. Specifically, we must be able to express the right-hand sides in terms of the dependent variables via relations between these and the remaining physical quantities. These are known as *constitutive relations* or *equations* and are derived from atomic physics, nuclear physics, and thermodynamics. In the following, a few of the central ones are listed.

Perhaps the most fundamental of such a relation is the *equation of state* (EOS), which provides one of the thermodynamic quantities in terms of the others (and the chemical composition); a simple example is the ideal gas law. Generally, it can be written as

$$\rho = \rho(P, T, \mu) \quad , \quad (1.13)$$

where  $\mu$  is just an indicator of the chemical composition – sometimes this is denoted by  $X_i$  instead. When computing models of stars (see section 1.6), the **EOS** is obtained from a compilation relevant for the stellar conditions. Several of such compilations exist; the most commonly used is the one by **OPAL** group (Rogers, Swenson, and Iglesias, 1996; Rogers and Nayfonov, 2002). Another one is the **Mihalas-Hummer-Däppen EOS** (or just **MHD-EOS**) (Däppen et al., 1988; Hummer and Mihalas, 1988; Mihalas, Däppen, and Hummer, 1988; Mihalas et al., 1990), which is especially relevant in the low-temperature regime. A detailed comparison of the two is presented by Trampedach, Däppen, and Baturin (2006). A final alternative to mention is the *Free-EOS*<sup>1</sup> (Cassisi, Salaris, and Irwin, 2003), which is publicly available.

Another essential property regards the absorption of photons: How impenetrable the stellar matter is to radiation. This is known as the opacity  $\kappa$ , which is inversely related to the photon mean free path. A known relation of similar form as above is assumed as

$$\kappa = \kappa(P, T, \mu) . \quad (1.14)$$

As was the case for the **EOS**, the opacity of stellar material is obtained from large compilations. What is actually employed is a specific average introduced in eq. (1.24) below. The two main collections of radiative opacities are from the **OPAL** group (Rogers and Iglesias, 1992; Iglesias and Rogers, 1996) and the **Opacity Project** (**OP**, Badnell et al., 2005). These are typically complemented by dedicated low-temperature radiative opacities, where the most widely used are from Alexander and Ferguson (1994) and Ferguson et al. (2005). A set of alternative low-temperature opacities are provided by Trampedach et al. (2014a), which will be used in chapter 5. Finally, to properly deal with degenerate matter, the radiative opacities must be supplemented by conductive opacities, which are supplied by Cassisi et al. (2007) or the older calculations by Itoh et al. (1983).

The final case to be mentioned is related to the energy production (see also section 1.4.1). It is the energy generation rate  $\varepsilon$ , again written as

$$\varepsilon = \varepsilon(P, T, \mu) . \quad (1.15)$$

1: The code is available from <http://freeeos.sourceforge.net/>

This could equally well be written in terms of the individual rate  $\epsilon_{jk}$ , which is product of the reaction rate  $r_{jk}$  transforming nuclei  $j$  to  $k$  and the energy released by that reaction. The reaction rates are determined from the so-called nuclear cross sections that describe the probability of a reaction occurring. As was the cases above, these must be obtained from extensive libraries: most frequently used are the large compilations of cross sections by the NACRE collaboration (Angulo et al., 1999) and the Solar Fusion team (Adelberger et al., 1998; Adelberger et al., 2011). Typically, the important rates are updated to match the latest results, when these are published.

### 1.3 The Life of a Star

Before moving on to the details of stellar structure it is instructive to consider the overall evolution of a star not too different from our Sun. The main quantity governing the life of a star – how evolution proceeds, its lifetime, and its final fate – is the total stellar mass, with the chemical evolution also playing a role.

Insight into the structure and evolution of a star mainly comes from a so-called stellar evolution code, which will be introduced in section 1.6.2. In short, such a code solves the equations listed above, while taking care of the intricate physics to be introduced in the remainder of the chapter.

It is customary to follow stellar evolution by visualising the output of a stellar evolution code in terms of surface- or global parameters. Traditionally, the effective temperature  $T_{\text{eff}}$  is shown against the total photospheric luminosity  $L$  in the well-known *Hertzsprung-Russel diagram* (HRD) – for historical reasons (to match with the original colour definitions) the  $T_{\text{eff}}$  axis is inverted. An alternative is the “spectroscopic HRD”, where instead of  $L$  the logarithm of the surface gravity

$$\log g = \log \left( \frac{GM}{R^2} \right) , \quad (1.16)$$

in cgs-units is used. This is also known as a *Kiel diagram* and is the preferred option in this thesis; to keep the link to the HRD the  $\log g$  axis is inverted. Note that in the present work “log” always implies “ $\log_{10}$ ”, whereas the natural logarithm is “ln” and rarely used. The evolution of a  $1 M_{\odot}$  star calculated with a stellar evolution code in such a diagram is shown in fig. 1.1, with annotations of various evolutionary phases to be explained below.

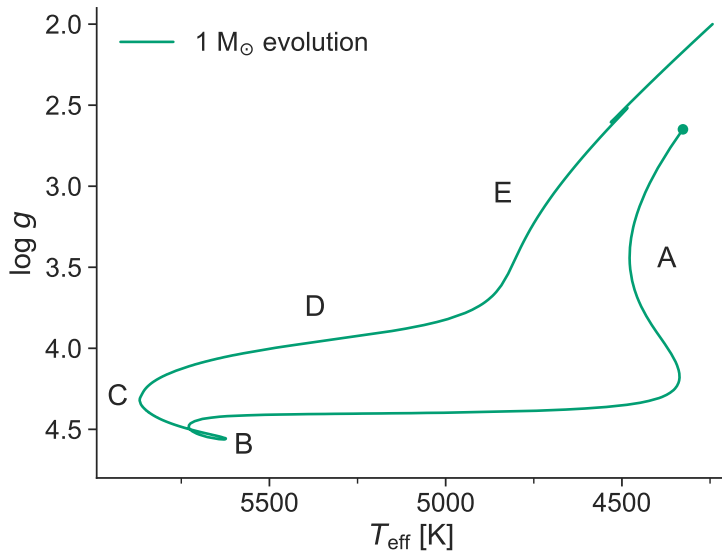


**Figure 1.1 | Evolution of a 1 solar mass star in a Kiel diagram.** Calculated at current solar composition starting from the dot. Important evolutionary stages/points are marked (details in text). **A)** *Pre-main sequence (PMS)*, **B)** *Zero-age main sequence (ZAMS)*, **C)** *Core-hydrogen exhaustion (CHE)*, **D)** *Sub-giant phase*, **E)** *Red-giant branch (RGB)*.

A star is born from a fragment of a cloud of interstellar matter contracting under its own gravity. This contraction releases gravitational potential energy, heating up the matter. At some point, hydrostatic equilibrium is reached and the fully convective star will descend along the so-called *Hayashi track* – marked by ‘A’ in the plot. This initial evolutionary phase with no nuclear fusion is generally known as the *pre-main sequence (PMS)*.

Eventually the temperature in the centre is sufficiently high for nuclear reactions to take place: this is the onset of hydrogen fusion (energy production will be treated in section 1.4.1). This stops the contraction and the rate of energy generated balances the radiation from the surface. A star in this *core-hydrogen burning* phase of evolution is said to be on the *main sequence (MS)*, and the beginning of this stage is known as the *zero-age main sequence (ZAMS)* – annotated as ‘B’ in fig. 1.1.

At this point, the solar-mass star consists of a core with ongoing fusion, an intermediate radiation zone, and an outer envelope with convection – the

mechanisms of energy transport will be reviewed in sections 1.4.2 and 1.4.3. As already mentioned, a star will spend the majority of its lifetime on the **MS**. At some point (marked with ‘C’ in the **Kiel diagram**) the supply of hydrogen is exhausted in the core and the star leaves the **MS**: this is either known as the *turn-off* point or the point of *core-hydrogen exhaustion (CHE)*.

Now the interior of the star is an inert helium core with a hydrogen-burning shell around and an outer envelope. Stars in this evolutionary state are called *subgiant* stars (point ‘D’), and the evolution is roughly governed by  $t_{\text{KH}}$ . The core contracts and slowly heats up, while the outer parts expand rapidly and the temperature drops; the luminosity is approximately constant, and the star moves across the **HRD** or **Kiel diagram**.

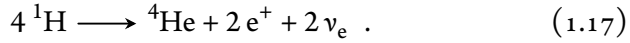
When the luminosity starts to increase, the star is said to move up the *red-giant branch (RGB)* marked by ‘E’. A *red giant (RG)* star has a very deep convective envelope (in radius-coordinates), hydrogen fusion in a shell, and a very dense helium core. It will continue moving upwards until the core is eventually hot enough to ignite helium fusion (not pictured in the evolution sketch). For stars with masses below  $\sim 2.5 M_{\odot}$  their cores are degenerate and the onset of helium core fusion will happen in a violent event known as the *helium flash*. Afterwards, the star settles on the “helium-burning **MS**”, also known as the “horizontal branch”, and the star is now called a *red-clump* star. This evolutionary phase is not of any importance to the present project and will not be elaborated, and neither will the stages beyond.

## 1.4 Generation and Transport of Energy

The theory of energy transport in stars is in itself a complex and very comprehensive topic, and a central pillar in stellar structure theory. Energy is produced in the centre of the star by thermonuclear reactions and steadily flows to the surface, where it is radiated away. Ignoring for the moment degenerate matter (in which conductive transfer becomes highly efficient), the transport mechanisms of energy fall into two main categories: *radiative transfer* and *convective motions*. Both of these mechanisms are described below, but before that, the production of energy in the central part of stars is briefly treated.

### 1.4.1 Energy Generation

Thermonuclear fusion reactions take place in the very centre of a star – commonly referred to as the stellar core. A star spends most of its overall lifetime on the **MS** fusing hydrogen into helium. The overall net reaction is



The reaction does not follow the written reaction verbatim due to the completely negligible probability that four protons collide. Rather, the fusion is accomplished through two fundamentally different ways; the first is the *proton-proton chain(s)* – in short *p-p chain(s)* – which is a sequence of reactions strictly involving lighter elements, where the first reaction is between two protons. The second possible reaction series is the *CNO cycle*, which (as the name suggests) uses *carbon*, *nitrogen*, and *oxygen* as a form of catalysts. A list of the different sub-chains and reactions for the two channels are not given here, but provided in all of the three references given in the beginning of the chapter.

The p-p chain and CNO cycle are competing and usually take place simultaneously with efficiencies depending on the conditions in the stellar interior (and hence total stellar mass). Specifically, the temperature sensitivity of the nuclear energy generation rates for the two channels differ significantly. The dependence of the average rates are

$$\epsilon_{\text{pp}} \sim T^4 \quad , \quad \epsilon_{\text{CNO}} \sim T^{20} \quad \text{at} \quad T \simeq 1.5 \times 10^7 \text{ K} \quad (1.18)$$

Since the exact values of the exponents are based on estimates, they will vary slightly depending of the used reference and they also depends on the chosen evaluation temperature. In the Sun the central temperature is just around  $1.5 \times 10^7 \text{ K}$  and more than 90 % of the energy is produced by the p-p chain.

The different temperature dependencies have a direct impact on  $\epsilon(m)$ , i.e., how confined the energy production is. If hydrogen burning is dominated by the CNO cycle, it will be concentrated in the very centre of the star. Consequently, such a star will typically harbor a convective core as a result of the increased energy flux (see section 1.5), which will affect its structure and evolution of the star.

At the later stages of a star's life, the temperature in the core might increase to the much higher values required to fuse helium into carbon.

Stars in this phase are not treated further in this thesis, but mentioned for completeness. Helium burning is happening through the *triple-alpha* ( $3\alpha$ ) reaction with the overall signature



In practice, it is not a true three-body collision of  $\alpha$ -particles, but is instead happening through the unstable  $^8\text{Be}$ . The  $3\alpha$  process has an even stronger temperature sensitivity than the CNO cycle with  $\varepsilon_{3\alpha} \sim T^{40}$  at  $T \simeq 10^8$  K. For the most massive stars, different fusion processes and exotic burning stages will continue all the way to iron, but they will not be discussed here.

### 1.4.2 Energy Transport by Radiation

The energy needs to be transported from the production site in the stellar core to the stellar surface, where it is radiated away. One of the two main mechanisms is transport by photons or *radiation*. A complete treatment of radiative energy transport and especially the complex interaction between matter and radiation is required when studying stellar atmospheres (elaborated in chapter 4). Radiative transfer is a full research field in its own right, and the present section will only barely scratch the surface.

In the interior of stars, it is sufficient with a simplified description, where the transport can be treated as a diffusive process. This is derived from the limit where the mean free path of the photons is very short and much smaller than the stellar radius, which is therefore also known as the *diffusion approximation*. This breaks down near the surface, where the density decreases and the photons instead flow freely away.

The regime where the diffusion approximation holds is also known as *optically thick*, because the radiation is effectively trapped. In this case, it can be derived that the radiative flux  $F_{\text{rad}}$  is given by

$$F_{\text{rad}} = -\frac{4ac}{3} \frac{T^3}{\kappa\rho} \frac{\partial T}{\partial r} , \quad (1.20)$$

where  $c$  is the speed of light and  $a$  is the radiation density constant (related to the Stefan-Boltzmann constant  $\sigma_{\text{SB}}$  by  $\sigma_{\text{SB}} = ac/4$ ). The flux can be replaced using the total amount of energy transported through a sphere, i.e, the local

luminosity  $L = L(r) = 4\pi r^2 F_{\text{rad}}$ . Solving for the gradient and transforming to  $m$  as the independent variable yields

$$\frac{\partial T}{\partial m} = -\frac{3}{64\pi ac} \frac{\kappa L}{r^4 T^3} , \quad (1.21)$$

which is the desired energy transport equation. However, it is useful to cast this expression into the form of eq. (1.8). Hence, to describe the temperature variation with depth if only caused by radiation, it is convenient to introduce the so-called *radiative gradient*

$$\nabla_{\text{rad}} := \left( \frac{d \ln T}{d \ln P} \right)_{\text{rad}} = \frac{3}{16\pi ac G} \frac{\kappa L P}{m T^4} , \quad (1.22)$$

where the subscript “rad” denotes that this would be the gradient required to transport all energy by radiation. From this, eq. (1.21) can be re-written in the desired form as

$$\frac{\partial T}{\partial m} = -\frac{GmT}{4\pi r^4 P} \nabla_{\text{rad}} , \quad (1.23)$$

which can be recognised as eq. (1.8) with  $\nabla = \nabla_{\text{rad}}$ . This is the energy transport equation in the case where essentially all of the energy is transported by radiation.

In the treatment above, the natural wavelength dependency of opacities has been neglected. The assumption is that they can be replaced by some sort of mean opacity, which is averaged over all wavelengths to make the problem wavelength independent. In stellar physics, the most common way to perform this averaging is using the so-called *Rosseland mean* opacities. These are calculated as an integral over all wavelengths  $\nu$  of the Planck function  $B(\nu, T)$ , which is the intensity distribution as a function of wavelength of radiation from a blackbody with a given temperature. It is formally defined as

$$\frac{1}{\kappa} = \frac{\pi}{acT^3} \int_0^\infty \frac{1}{\kappa_\nu} \frac{\partial B}{\partial T} d\nu , \quad (1.24)$$

where  $B = B(\nu, T)$  is the Planck function introduced above, and  $\kappa_\nu$  is the wavelength dependent opacity. The opacity compilations listed in section 1.2.1 consist of such Rosseland mean opacities.

### 1.4.3 Energy Transport by Convection

The other main mechanism for transporting the energy is mass motions or *convection*. Convection is a collective term for the complex hydrodynamical phenomena when energy cannot be transported by radiation alone, and an accurate description is still a key challenge in astrophysics. As was the case for radiative transfer, only a brief introduction of the important concepts is presented – and with the the present context of models of energy transport in the stellar interior in mind.

No definitive method for calculating neither the motion nor the resulting energy transport exists. The most sophisticated approach is to use state-of-the-art numerical simulations of hydrodynamics in three dimensions to carefully model the intricate details of stellar atmospheres. Such simulations are treated in chapter 4. However, as will be discussed there, such simulations cannot be directly used in the context of stellar evolution.

Luckily, a far less complete description is required for computing stellar models, where the overall properties of stars are in focus. What is necessary is a relation for the temperature gradient required to transport the luminosity by convection. Specifically, an expression to substitute  $\nabla$  in eq. (1.8) is desired. However, convection being such a central topic of this thesis, some further details are required before answering the question. This will be the focus of the next section.

## 1.5 Stellar Convection

When the temperature gradient is too steep for radiation to efficiently carry all of the energy outwards, the so-called *convective instabilities* set in. The first task is to determine when this is the case, i.e., to establish a criterion of (in)stability. Such a criterion must be able to decide if the small perturbations always present in a medium stay small or grow larger to affect the structure. Phrasing the problem in terms of buoyancy: When will a gas bubble that is accidentally displaced upwards or downwards, continue to move in that direction as opposed to returning to its initial state.

A bubble of gas rising (or falling) in a background medium is the typical physical picture used to consider the instabilities. The main assumption is that the timescale of the movement is too short for any appreciable exchange of heat between the bubble and the surroundings, i.e., that the process is

*adiabatic*. Moreover, it is assumed that the motion is sufficiently slow for the bubble to stay in pressure balance with the background.

When describing adiabatic processes, it is often useful to define the so-called *adiabatic exponents*  $\Gamma_i$  (sometimes the term “index” is used instead of “exponent”). These are given as

$$\Gamma_1 := \left( \frac{\partial \ln P}{\partial \ln \rho} \right)_s, \quad \Gamma_2 := \left( \frac{\partial \ln P}{\partial \ln T} \right)_s, \quad \Gamma_3 - 1 := \left( \frac{\partial \ln T}{\partial \ln \rho} \right)_s, \quad (1.25)$$

where the subscript “s” denotes derivatives at a constant specific entropy. From these, it is convenient to also introduce the *adiabatic (temperature) gradient*

$$\nabla_{\text{ad}} := \left( \frac{\partial \ln T}{\partial \ln P} \right)_{\text{ad}} = \left( \frac{\partial \ln T}{\partial \ln P} \right)_s = \frac{\Gamma_2 - 1}{\Gamma_2}, \quad (1.26)$$

where the subscript “ad” highlights that it is valid for adiabatic changes. For a fully ionised perfect ideal gas  $\nabla_{\text{ad}} = 2/5$ . It is changed from this value e.g. in the ionisation zones where it decreases.

It can be shown that, under the assumption of chemical homogeneity, the condition for convective stability is

$$\nabla < \nabla_{\text{ad}}, \quad (1.27)$$

with  $\nabla$  defined the usual way as in eq. (1.8). Some authors define instead the condition for *instability*, in which the inequality is naturally reversed.

When the temperature decreases too rapidly out through the star, instabilities will set in as eq. (1.27) is *not* fulfilled. Commonly, to determine the circumstances where convection is expected to occur, a model where energy is transported through radiation is considered. Here  $\nabla = \nabla_{\text{rad}}$ ; thus, a radiative layer will remain stable against convection as long as

$$\nabla_{\text{rad}} < \nabla_{\text{ad}}. \quad (1.28)$$

This is known as the *Schwarzschild* criterion, which is by far the most common stability criterion used in stellar modelling. If desired, the assumption of homogeneous composition can be lifted to also take the chemical gradient  $\nabla_\mu$  into account. Then, a more general expression for testing the stability of a radiative layer can be obtained in the form of the *Ledoux* criterion

$$\nabla_{\text{rad}} < \nabla_{\text{ad}} + \frac{\varphi}{\delta} \nabla_\mu, \quad (1.29)$$

where the thermodynamic derivatives are defined as

$$\delta := - \left( \frac{\partial \ln \rho}{\partial \ln T} \right)_{P, \mu}, \quad \varphi := \left( \frac{\partial \ln \rho}{\partial \ln \mu} \right)_{P, T}, \quad (1.30)$$

in which  $\mu$  is the mean molecular weight and the subscripts denote quantities kept constant in the derivatives.

Based on eqs. (1.22) and (1.28) it is possible to make some qualitative predictions about where to expect convection in stars. The first case is when there is a high average energy generation rate per unit mass, i.e. when  $L/M$  is large. Typically this is true in the core of a (relatively) massive star where the energy is generated by the CNO cycle. Secondly, several conditions predict the existence of convection zones in the outer parts of relatively cool stars – meaning either low-mass stars burning hydrogen or red giants (see section 1.3). These occur when  $\kappa$  is large; when  $\rho/T^3$  is large; or when  $\nabla_{\text{ad}}$  is small. Such zones are usually dubbed *convective envelopes* and are at the heart of the research presented in this thesis.

No introduction to stellar convection would be complete without the iconic drawing by Prof. Jørgen Christensen-Dalsgaard from his equally iconic lecture notes on stellar structure and evolution known as the “red notes” (Christensen-Dalsgaard, 2008c). This representation of stellar convection zones as a function of mass is provided in fig. 1.2 on the following page and summarises the cases mentioned above. As it is customary, the symbol  $\odot$  is used to represent the Sun. Finally, it must be noted that the mass motions naturally lead to mixing of the material in convective regions, affecting the composition – the mixing is typically sufficiently fast for such regions to be chemically homogeneous.

### 1.5.1 Mixing-Length Theory

Now that it is established when convective instabilities are expected to set in, we can return to the original question: How to obtain the  $\nabla$  to use in eq. (1.8) when the energy is transported by convection. To do this, a theoretical framework is needed. As a calculation governing the long-term evolution of a star cannot directly resolve the short timescales of dynamic phenomena, an approximative description suitable for such a calculation is required.



**Figure 1.2 | Drawing of the typical occurrences of stellar convection zones.** The shaded areas represent convective regions, while the empty regions mark radiation zones. This schematic overview is valid for the stars on the **MS** and the mass bins are very approximate. The transition mass for convective cores are closer to  $1.2\text{--}1.3 M_{\odot}$ . Reproduced from Christensen-Dalsgaard (2008c, Figure 6.2) with permission.

One of the most successful parametric approaches from an astrophysical point of view is the *mixing-length theory (MLT)*. As described e.g. in the excellent review by Gough and Weiss (1976), the mixing-length approach to convection was developed from hydrodynamics in the early 20th century by several independent authors (e.g. Ludwig Prandtl). The **MLT** was introduced in an astronomical context by Biermann (1932), and transferred in a generalised form to stellar modelling by Erika Böhm-Vitense (Vitense, 1953; Böhm-Vitense, 1958), whose formalism has since been the most common one. An alternative formulation of the theory is from Cox and Giuli (1968) – such different implementations are usually referred to as **MLT-flavors**. A detailed account of the theory (in the Böhm-Vitense flavor) is also given by Kippenhahn, Weigert, and Weiss (2012) and will be outlined below.

The basic idea of **MLT** is similar to what was used to consider instabilities; namely to treat convection as rising and falling elements called *eddies*, *bubbles*, *blobs* or just *convective elements*. These blobs move adiabatically in a background medium, where pressure equilibrium is assumed as well as symmetry between the up- and downflows; the background is the mean stratification. To characterise the conditions of the medium it is useful to

introduce the (local) *pressure scale height*  $H_p$  defined as

$$H_p := -\frac{dr}{d \ln P} = \frac{P}{\rho g} , \quad (1.31)$$

where the last equality is valid under the assumption of hydrostatic equilibrium and  $g$  is the (local) gravitational acceleration. A blob moves a certain distance  $\Lambda$  (also often denoted  $l$  or  $\ell$ ) before dissolving/mixing instantaneously into the ambient medium – this distance is therefore called the *mixing length*. The mixing length  $\Lambda$  is assumed to be proportional to the local pressure scale height  $H_p$  as

$$\Lambda = a H_p , \quad (1.32)$$

where  $a$  is called the mixing-length parameter and is typically denoted as  $a_{\text{MLT}}$ . This is the main free parameter in the theory, and determines the efficiency of the convection (see eq. (1.33) below). Perhaps the main weakness of **MLT** is that the value of  $a_{\text{MLT}}$  cannot be derived from first principles. Instead, the usual approach is to calibrate it against the Sun (see section 1.6.3) and assume it constant for all stars. A more physically motivated treatment is to let it vary with stellar parameters as described by e.g. Ludwig, Freytag, and Steffen (1999) and Trampedach et al. (2014b), which will be investigated in detail in chapter 5.

With a variety of assumptions, it is possible to derive the following expression for the average convective flux

$$F_{\text{conv}} = \rho c_p T \sqrt{g \delta} \frac{\Lambda^2}{4\sqrt{2}} H_p^{-3/2} (\nabla - \nabla_e)^{3/2} . \quad (1.33)$$

Here  $c_p$  is the specific heat at constant pressure,  $\delta$  is the thermodynamic derivative from eq. (1.30), and  $\nabla_e$  is the temperature variation of an element during its motion. This equation must be complemented by four other equations. These five equations constituting the problem can then be transformed into the so-called *cubic equation of MLT* (see Kippenhahn, Weigert, and Weiss, 2012, eq. 7.18). This central dimensionless equation is solved numerically to obtain  $\nabla$ , i.e., the average temperature gradient to which the given convective layer settles.

It turns out that except near the surface, stellar convection is essentially almost adiabatic and the temperature gradient will mimic the adiabatic value

$\nabla \simeq \nabla_{\text{ad}}$ . The quantity  $\nabla - \nabla_{\text{ad}}$  is sometimes known as the *super-adiabaticity* or *super-adiabatic gradient*. This increases dramatically just below the surface (or photosphere, see section 1.6.1) in the so-called super-adiabatic peak, near which the modelling deficiencies treated in this thesis arise. And just to repeat, if the energy is transported by radiation, then  $\nabla = \nabla_{\text{rad}}$ .

For completeness, it should be mentioned that even though **MLT** is by far the most commonly used, alternative theories exist. The most noticeable of these are the works by Canuto and Mazzitelli (1991, 1992) and Canuto, Goldman, and Mazzitelli (1996), which rely on the “full spectrum of turbulent eddies” and is sometimes dubbed *full-spectrum theory (FST)*. Another class is the non-local and/or time-dependent theories (see e.g. Gough and Weiss, 1976; Gough, 1977a,b). Neither of these will be discussed further in the present work.

## 1.6 Models of Stellar Structure and Evolution

Now all of the essential ingredients have been introduced and they can be combined to form a stellar model. The full problem faced is the set of partial differential equations defined by eqs. (1.5)–(1.9), with the mass coordinate  $m$  and time  $t$  as the independent variables. It is customary to define the evolution as starting at a given time  $t = t_0$ , and assume the total mass  $M$  to not vary with time. A solution  $\{r(m), P(m), T(m), L(m), X_i(m)\}$  in the interval  $[0, M]$  for a given time  $t$  is dubbed a *stellar model*. Obtaining this solution naturally requires a specification of the initial values (e.g.  $X_i(m, t_0)$ ) as well as suitable boundary conditions; the latter is an important aspect of the research presented in this thesis and will be discussed below (as well as in the chapters 4–8).

Given the complexity of the problem, the models are computed numerically using a so-called *stellar evolution code*. The basic principles across stellar evolution codes are very similar, however the different implementations and decisions will impact the results even for identical input (cf. the work conducted in the *Aarhus Red Giants*: Silva Aguirre et al., accepted). For transparency, the following sections follows the details in Kippenhahn, Weigert, and Weiss (2012).

Calculating a model of the stellar interior is a *boundary value problem*, where the four boundary conditions are split: Some are given at the surface

and some naturally defined in the centre. Those in the centre ( $m = 0$ ) are straightforward, because a singularity is not allowed. Hence, both the density and energy sources must remain finite and thus

$$r(0) = 0 \quad \text{and} \quad L(0) = 0 \quad , \quad (1.34)$$

which are the central boundary conditions. Unfortunately, the central temperature and pressure are not known in advance and must instead be given at the outer limit with  $m = M$  and hence  $r = R$ . This requires a bit more thought.

### 1.6.1 Outer Boundary Conditions

In general, correct outer boundary conditions will ensure that the interior solution fits smoothly to the solution from a stellar atmosphere. By far the most common approach is to use a simplified analytic approach as outlined below.

The first step is to determine where to actually establish the outer boundary. In other words, it is required to define a point which can reasonably be called the “stellar surface” with  $r = R$  and  $m = M$ . Typically, this is taken to be the *photosphere*, i.e., where the bulk of radiation is emitted from. This can conveniently be defined in terms of the optical depth

$$\tau(r) := \int_r^\infty \kappa \rho \, dr \quad , \quad (1.35)$$

which at the photosphere is denoted  $\tau_{\text{phot}} = \tau(R)$ , with a numerical value depending on the adopted atmosphere model. The *effective temperature*  $T_{\text{eff}}$  of a star is defined from the total luminosity  $L_{\text{tot}}$  by the Stefan–Boltzmann law as

$$L_{\text{tot}} = 4\pi R^2 \sigma_{\text{SB}} T_{\text{eff}}^4 \quad , \quad (1.36)$$

and is equivalent to the temperature at the photosphere  $T(R) = T_{\text{eff}}$ . Some authors simply define the photospheric radius as the point where  $T = T_{\text{eff}}$ . For these reasons, the optical depth at the photosphere will also be denoted  $\tau_{\text{eff}} = \tau_{\text{phot}}$  in the later chapters.

It will be necessary to know the temperature structure in the atmosphere, which is dubbed the  $T(\tau)$  relation. It can be generally defined through the so-called *Hopf function* denoted  $q(\tau)$  as

$$\frac{4}{3} \left( \frac{T}{T_{\text{eff}}} \right)^4 = q(\tau) + \tau . \quad (1.37)$$

The most common choice in stellar modelling is the *Eddington approximation* or *Eddington grey atmosphere* with a constant  $q(\tau) = 2/3$  and  $\tau_{\text{phot}} = 2/3$  – which clearly results in  $T = T_{\text{eff}}$  for  $\tau = 2/3$ . Alternative choices found in the literature are the works by Krishna Swamy (1966) or Vernazza, Avrett, and Loeser (1981). A newer approach can be found in Trampedach et al. (2014a), which will be explored in detail in chapter 5. The  $T(\tau)$  relation employed in the model has a non-negligible impact on the structure and evolution (see e.g. Salaris and Weiss, 2002; Tanner, Basu, and Demarque, 2014).

To obtain the pressure at the photosphere, eq. (1.35) can be transformed into a differential equation of  $dr/d\tau$ . Imposing hydrostatic equilibrium yields the atmospheric equation

$$\frac{dP}{d\tau} = \frac{Gm}{r^2\kappa} , \quad (1.38)$$

where  $\kappa$  is the Rosseland mean opacity. This equation must be integrated from  $\tau = 0$  to  $\tau = \tau_{\text{phot}}$  using a  $T(\tau)$  relation, whereby the pressure at the photosphere  $P_{\text{phot}} = P(R)$  can be obtained.

All in all, the photospheric conditions are given by eqs. (1.36) and (1.38). They provide the outer boundary for the transport equation, which relies on the diffusion approximation where a small mean free path of photons is assumed. However, this central assumption is not strictly valid at this point in the star, since the bulk of the radiation escapes from the photosphere. This apparent paradox is the main defect of the outer boundary conditions and the correct solution would be to use a full stellar atmosphere model. Mending this problem is one of the central topics of this work.

## 1.6.2 Stellar Evolution Codes

As introduced earlier, to calculate the interior structure of stars and its time evolution, with all of the many details and facettes, stellar evolution codes

are used. The research in this thesis (also including the track in fig. 1.1) is performed using the *Garching stellar evolution code* (**GARSTEC**) described by Weiss and Schlattl (2008) – which is a descendent of the original stellar structure code by Rudolf Kippenhahn. Details of the implementations used in the code – e.g. the **MLT** equations and numerical scheme – are also included in the textbook (Kippenhahn, Weigert, and Weiss, 2012).

Based on the general structure of the system of equations (see also earlier discussions on timescales), it is suggestive to split the problem into two sub-systems, which are treated alternately. Firstly, the *structure* eqs. (1.5)–(1.8) are solved for a given  $X_i(m)$  to obtain a stellar model. Subsequently, the *chemical* eq. (1.9) is applied for a small time step  $\Delta t$ , and then the structure equations are solved again for the new  $X_i(m)$ , followed by another application of the chemical equation; this is then repeated to construct an evolutionary sequence of stellar models.

To obtain the numerical solution, the codes employ a numerical technique known as *relaxation*, which is an iterative procedure for solving a system of equations. In stellar evolution codes it is typical to use a specific method known as the *Henyey-method* or *-scheme* (Henyey, Forbes, and Gould, 1964; Henyey, Vardya, and Bodenheimer, 1965) – which is tailored to the problem of the four stellar structure equations. The basic idea is to improve on a trial solution by performing several iterations in which corrections are applied to the variables until the convergence criterion is met. In the current research context, it is important to note that in each (Henyey) iteration, the outer boundary conditions are calculated from eqs. (1.36) and (1.38).

Generally, a stellar model is defined from centre ( $r = 0, m = 0$ ) to photosphere ( $r = R, m = M$ ) and the stellar structure equations are solved in this region. However, as has been mentioned several times, an analytic atmosphere is integrated as a function of optical depth to obtain the photospheric conditions. This (massless) post-photospheric region – dubbed the *atmospheric part* in this work – can be stored with the model by **GARSTEC**. Note that here  $r > R$ . It will turn out to be useful to introduce the label “*interior model*” for the actual structure model below the atmosphere.

Many numerical (and some physical) details have been left out of the present discussion, as they are not directly relevant for the research in this thesis. However, one to be mentioned is the so-called (*microscopic*) *diffusion*, which is the differential movement of chemical species between layers in

a star (and not just in convective regions). This is comprised of several physical processes, but dominated by an effect of the pressure gradient known as “sedimentation” or “gravitational settling” – heavier elements diffuse towards regions of higher pressure. In **GARSTEC**, the formulation from Thoul, Bahcall, and Loeb (1994) is included to treat this.

### 1.6.3 Solar Calibration

Perhaps the most fundamental computation with a stellar evolution code is to construct a model of the Sun. Specifically, the task which is either known as performing a *solar calibration* or producing a *standard solar model (SSM)*. A very extensive amount of literature is dedicated to solar modelling; to mention one, a very clear presentation of the topic is given by Serenelli (2016); alternatively the procedure is treated in Kippenhahn, Weigert, and Weiss (2012, chap. 29).

A *SSM* is the result of the computation of a  $1 M_{\odot}$  model from the *PMS* to the solar age  $t_{\odot} = 4.57$  Gyr. The evolution always includes microscopic diffusion (e.g. Christensen-Dalsgaard, Proffitt, and Thompson, 1993). Otherwise, different choices of microphysics – e.g. which compilation of opacities to use – can be made (section 1.2.1). Additionally, the chosen atmospheric  $T(\tau)$  relation (section 1.6.1) plays an important role; as does the convection description and/or implementation.

For the model to be an *SSM*, at  $t_{\odot}$  it must match the solar radius  $R_{\odot}$ , the solar luminosity  $L_{\odot}$ , and the photospheric composition in the form of metal-to-hydrogen mass fraction  $(Z/X)_{\odot}$ . To fit the three observational constraints, three quantities in the initial model are adjusted: The initial mass fractions  $Y_{\text{ini}}$  and  $Z_{\text{ini}}$ , and the mixing-length parameter  $\alpha_{\text{MLT}}$ . Evolutionary sequences with varying initial parameters are computed in an optimisation scheme until the desired accuracy of typically  $10^{-5}$  is reached.

Depending on the stellar evolution code the values of the solar values to match can vary slightly (as can other physical constants, with  $G$  being the most noteworthy). For reference, in **GARSTEC**  $1 M_{\odot} = 1.9891 \times 10^{33}$  g and the solar values to match are defined as

$$\begin{aligned} R_{\odot} &= 6.95508 \times 10^{10} \text{ cm} \\ L_{\odot} &= 3.846 \times 10^{33} \text{ erg s}^{-1} . \end{aligned}$$

With  $(Z/X)_{\odot}$  the situation is a bit less straightforward and the value will depend on the chosen solar composition. The reason for the additional complications is the so-called *solar abundance problem*: There is tension between *helioseismology* and the most recent determinations of the chemical composition of the Sun (see section 3.2).

Now, the suite of numerical tools to describe the structure and evolution of a star has been reviewed, and they can be employed to gain knowledge of how different stars behave through their lifespan.



# 2

## Asteroseismology

The previous chapter was devoted to models of stellar structure. Now the question remains: How well do these models represent real stars? An answer to that question naturally requires information about stellar interiors, which unfortunately is not straightforward to obtain.

Gaining knowledge of stars hinges on a most crucial fact: Only the light emitted from the stellar photosphere can be directly observed. It was put very clear in the first paragraph of the iconic work *The Internal Constitution of the Stars* by Sir Arthur Stanley Eddington:

*At first sight it would seem that the deep interior of the Sun and stars is less accessible to scientific investigation than any other region of the universe. Our telescopes may probe farther and farther into the depths of space; but how can we ever obtain certain knowledge of that which is hidden behind substantial barriers? What appliance can pierce through the outer layers of a star and test the conditions within? (Eddington, 1926)*

In other words, it was deemed impossible to obtain detailed knowledge about the internal structure of stars – and thereby to properly address the accuracy of stellar models.

However, the situation changed drastically when oscillations were detected in the Sun in the 1960-70s. The field devoted to the study of these oscillations is known as **helioseismology** and in the general case as **asteroseismology**. Through the constant advancements from both theoretical and observational sides, **asteroseismology** has truly revolutionised our understanding of stellar physics by enabling high-precision measurements of

stellar interiors – a detailed background is given the textbook by Aerts, Christensen-Dalsgaard, and Kurtz (2010).

Different mechanisms are responsible for generating the waves in the stellar interior: in the Sun the waves are stochastically driven by acoustic excitation via turbulent motions in the outer convection zone. Oscillations driven this way are called *solar-like* and are found in stars on the lower **MS**, as well as in cool **subgiants** and on the **RGB** – a schematic overview is given in e.g. Aerts, Christensen-Dalsgaard, and Kurtz (2010, fig. 1.12). Such oscillations are relevant for the present research and hence the focus of this chapter.

The chapter is structured as follows. In the section just below, selected parts of the fundamental theory of solar-like oscillations relevant for the project are reviewed, including a brief introduction to asymptotic theory. In section 2.2, useful tools as well as the basic ideas behind observing such oscillations are presented. The principles for obtaining predicted frequencies from stellar models are briefly presented in section 2.3, and finally the key topic of comparing those model frequencies to observations is given treated in section 2.4.

The main source for this chapter is the already mentioned monumental reference work by Aerts, Christensen-Dalsgaard, and Kurtz (2010), which is supplemented by a few great reviews: Christensen-Dalsgaard (2002) focusing on **helioseismology**, Chaplin and Miglio (2013) putting more effort into determination of stellar parameters, and the excellent introduction to observational **asteroseismology** by Bedding (2014).

## 2.1 Basic Theory of Stellar Oscillations

Stellar oscillations are essentially waves in a fluid. Like any other such waves, the properties of these are governed by equations that can be derived from fundamental hydrodynamics. Below, a brief overview of selected results and key assumptions are sketched, and a full treatment can be found in e.g. Aerts, Christensen-Dalsgaard, and Kurtz (2010, chap. 3) including all derivations, but is not important for this thesis work.

Given a stationary equilibrium the oscillations are treated as small perturbations. Waves in stars propagate in three dimensions and due to the spherical geometry of stars, the expressions are typically written in spherical

coordinates: the distance to the centre  $r$ , the longitude  $\phi$ , and the co-latitude  $\theta$  measured from the pole.

One of the central pillars is the *adiabatic approximation*. The motion is essentially adiabatic, because the timescale for energy exchange is much longer than the relevant pulsation periods – note that this breaks down near the surface of the star. Another key assumption is that the equilibrium state is spherically symmetric and time-independent, which allows the solution to be separated in time  $t$  and the angular coordinates. Time dependence can be expressed as a harmonic function characterised by a frequency; either the typical *cyclic* oscillation frequency  $\nu$  or the *angular* frequency  $\omega = 2\pi\nu$ .

The expressions presented below are written in complex form for convenience, but oscillation frequencies are strictly real in the adiabatic approximation. Under the listed assumptions, the solutions to the equations of motion can be expressed by the displacements (in the notation of Aerts, Christensen-Dalsgaard, and Kurtz, 2010, chap. 1)

$$\xi_r(r, \theta, \phi, t) = a(r) Y_l^m(\theta, \phi) \exp(-i\omega t) \quad (2.1)$$

$$\xi_\theta(r, \theta, \phi, t) = b(r) \frac{\partial Y_l^m(\theta, \phi)}{\partial \theta} \exp(-i\omega t) \quad (2.2)$$

$$\xi_\phi(r, \theta, \phi, t) = \frac{b(r)}{\sin \theta} \frac{\partial Y_l^m(\theta, \phi)}{\partial \phi} \exp(-i\omega t) , \quad (2.3)$$

where  $a(r)$  and  $b(r)$  are amplitudes, and  $l$  and  $m$  are characteristic integers explained below. Here  $Y_l^m$  are the spherical harmonics defined as

$$Y_l^m(\theta, \phi) = (-1)^m c_{lm} P_l^m(\cos \theta) \exp(im\phi) , \quad (2.4)$$

in which  $c_{lm}$  is a normalisation constant defined to make the integral over the unit sphere of  $|Y_l^m|^2$  equal to unity, and  $P_l^m$  are Legendre functions given by

$$P_l^m(\cos \theta) = \frac{1}{2^l l!} (1 - \cos^2 \theta)^{m/2} \frac{d^{l+m}}{d \cos^{l+m} \theta} (\cos^2 \theta - 1)^l . \quad (2.5)$$

Hence, it is useful to visualise stellar oscillations as discrete spherical harmonics specified by a set of “quantum numbers”. The number of surface nodes is given by  $l$  (sometimes stylised as  $\ell$ ), which is known as the *degree*. Moreover,  $l$  is the foundation of a commonly used nomenclature: The

simplest oscillation mode – a swelling and contraction of the star – is characterised by  $l = 0$  and known as a *radial* mode. Modes with  $l \geq 1$  are called *non-radial* modes.

The number of nodal shells in the radial direction, or just the number of radial nodes, is referred to as the *order* (or sometimes *overtone*) of the mode and is given by  $n$ . Finally,  $m$  is the *azimuthal order* and  $|m|$  is how many of the surface nodes which are lines of longitude. In this thesis stars will always be assumed to be non-rotating, in which case the azimuthal order is  $m = 0$ , and the expressions above are simplified significantly.



Two main types of solutions of the oscillation equations exist: the so-called *p-modes* and *g-modes*. The restoring force of *p-mode* (or pressure-modes) is indeed arising from the pressure gradient; these are acoustic waves and the gas motion is primarily vertical. For *g-mode* (or gravity-modes) buoyancy is the restoring force, and results in primarily horizontal gas motion.

To investigate the behaviour of the modes, it is useful to introduce the characteristic frequencies for adiabatic oscillations: The *Brunt-Väisälä frequency*  $N$ , the *Lamb frequency*  $S_l$  and the *acoustical cut-off frequency*  $\omega_{ac}$  for an isothermal atmosphere. In that order, they are given as

$$N^2 = g \left( \frac{1}{\Gamma_1 P} \frac{\partial P}{\partial r} - \frac{1}{\rho} \frac{\partial \rho}{\partial r} \right) , \quad (2.6)$$

$$S_l^2 = \frac{l(l+1)c_s^2}{r^2} , \quad (2.7)$$

$$\omega_{ac}^2 = \frac{c_s^2}{4H_P^2} , \quad (2.8)$$

in which  $g$  is the gravitational acceleration,  $\Gamma_1$  is the adiabatic exponent defined in eq. (1.25),  $P$  is pressure,  $\rho$  is density,  $H_P$  is the pressure scale height, and  $c_s$  is the *adiabatic* sound speed given as

$$c_s^2 = \frac{\Gamma_1 p}{\rho} . \quad (2.9)$$

Generally, these quantities all depend on the properties of the stellar material and will change throughout the star – a so-called propagation diagram with

the characteristic frequencies for a solar model can be seen in Christensen-Dalsgaard (2002, Fig. 5).

The propagation of **g-modes** is governed by the **Brunt–Väisälä frequency**, because only in regions where  $N$  is positive, buoyancy can act as a restoring force and drive the oscillations. This is true in layers stable against convection as it will become negative in unstable regions. The **g-modes** have angular frequencies  $\omega < N$ ; thus, they are trapped in the radiative interior and will decay exponentially in the convection zone.

On the other hand, a **p-mode** is confined in the outer regions of the star and essentially controlled by the sound speed  $c_s$ , which depends on the thermodynamic properties of the medium. The inner turning point is located where the angular frequency reaches  $\omega = S_l$ , and the outer turning point is defined by  $\omega_{ac}$ . The latter is located near the surface, while the former is placed deeper in the interior; the lower the degree, the nearer the core (note that  $l = 0$  penetrates the centre). As the main focus of the research presented in this thesis is related to the convective outer parts of stars, the focus will be on **p-modes**.



As the observable **p-modes** in **MS** stars have high radial orders  $n$ , it is a fair approximation that  $l/n \rightarrow 0$ , and it is therefore possible to apply asymptotic theory to characterise the oscillations. Various procedures and simplifications exist, but perhaps the most complete is based on the full oscillation equations utilising the *Cowling approximation*, in which the perturbation to the gravitational potential is neglected. Full works are dedicated to this approach, which can provide valuable insight into the properties of oscillations – and also on how to interpret the numerical solutions (see next section). The turning-point arguments presented above are typically given in an asymptotic context. It is also possible to derive a different and more general expression for the **acoustical cut-off frequency** (e.g. Christensen-Dalsgaard, 2002, eq. 42).

No full treatment is presented here; but the resulting expression to describe the frequency of acoustic **p-modes** is quite useful. For low degree modes, the cyclic oscillation frequency  $\nu_{nl}$  can to first order be written as

$$\nu_{nl} \simeq \Delta v \left( n + \frac{l}{2} + \varepsilon \right), \quad (2.10)$$

where

$$\Delta\nu = \left(2 \int_0^R c_s^{-1} dr\right)^{-1} \quad (2.11)$$

is the inverse of the acoustic diameter (i.e., twice the sound travel time from surface to centre); and  $\varepsilon$  is a coefficient that depends on the boundary conditions close to the surface. Hence, a uniform spacing  $\Delta\nu$  in  $n$  for low-degree modes is predicted, i.e., a regular frequency pattern in stars exhibiting solar-like oscillations is expected to be observed. This spacing  $\Delta\nu$  between modes of consecutive order with the same degree is known as the *large frequency separation*.

The *large frequency separation*  $\Delta\nu$  is one of the key quantities and diagnostics in *asteroseismology*. The *p-mode* is controlled by the adiabatic sound speed, which explicitly depends on the density. Assuming an ideal gas,  $\Delta\nu$  can be shown to scale with the mean density  $\langle\rho\rangle$  of the star (Ulrich, 1986; Kjeldsen and Bedding, 1995)

$$\Delta\nu \propto \langle\rho\rangle^{1/2} \propto \left(\frac{M}{R^3}\right)^{1/2}. \quad (2.12)$$

Recalling section 1.3, the radius of a star with a given mass will continuously increase as evolution proceeds from the *ZAMS* through the *MS* and *RGB* phases. Thus, for a fixed mass,  $\Delta\nu$  is an important indicator of evolution.

## 2.2 Observing Solar-like Oscillations

The search for oscillating stars are bound by the same fundamental restriction as was highlighted in the beginning of this chapter: Only the emitted light from stars is accessible to us. However, the displacements caused by the acoustic oscillations slightly disturb the stellar surface thereby changing the brightness as a function of time. Thus, even though the sound waves cannot be directly captured, they leave a tiny imprint in the emitted light. Note also that oscillating stars (not counting the Sun) are essentially point sources. As only their integrated light can be observed, cancellation effects between the oscillations will become significant and only modes with low  $l$  can be observed.

In order to study the oscillations a given star must be observed for an extended period of time (with a very sensitive instrument to resolve the tiny

features). The tiny variations in the signal are a result of a superposition of the multitude of the different modes excited in the star. Determining the underlying frequencies composing the signal is the quintessential task for observational **asteroseismology**.

The typical signal data in **asteroseismology** is brightness as a function of time and dubbed a *time series*. Extracting information from such data is known as *time-series analysis* and much research effort is put into this topic. Perhaps the most central procedure is decomposing the signal by utilising Fourier techniques; specifically the data is (Fourier) transformed from time domain to frequency domain by computing the so-called *frequency spectrum* (or *power spectrum*). Such a spectrum displays the power contained in the different oscillation frequencies, i.e., it contains information on the strength of the various modes present in the star.

An example of a power spectrum computed using observations from *Birmingham Solar-Oscillations Network (BISON)* (see e.g. Chaplin et al., 1996) by Bedding (2014) is shown in fig. 2.1 on the next page. From **BISON** it is possible to obtain observations of the “Sun as-a-star”, i.e., simulating a point source through unresolved/disk-integrated sunlight. This enables the study of the global oscillations in the form of low-degree **p-mode** frequencies, which is similar to what is observed in other stars. A compilation of such frequencies for the Sun has been published by Broomhall et al. (2009) and Davies et al. (2014) and will be used throughout this research as reference. Generally, if the data is of high enough quality, the individual oscillation frequencies can be extracted from the power spectrum – a task commonly referred to as *peak-bagging*, which is not necessarily straightforward and much effort has been put into optimising these procedures (see references in the beginning of the chapter, especially Chaplin and Miglio, 2013).

Returning to the “Sun as-a-star” power spectrum in fig. 2.1, it can be seen from the top panel that the oscillations form a comb-like pattern (in agreement with the asymptotic prediction) and that the peak heights trace a gaussian envelope. The centroid of this envelope is known as the *frequency of maximum power* and denoted as  $\nu_{\max}$ , which is another of the central asteroseismic quantities. For the Sun, its value is approximately  $\nu_{\max} \simeq 3100 \mu\text{Hz}$ . Unlike  $\Delta\nu$  above,  $\nu_{\max}$  cannot be directly translated into fundamental properties using strict theory. However, it was assumed by Brown et al. (1991) to depend on the near-surface layers due to its connection with excitation and dampening of modes. The relevant characteristic frequency in this region

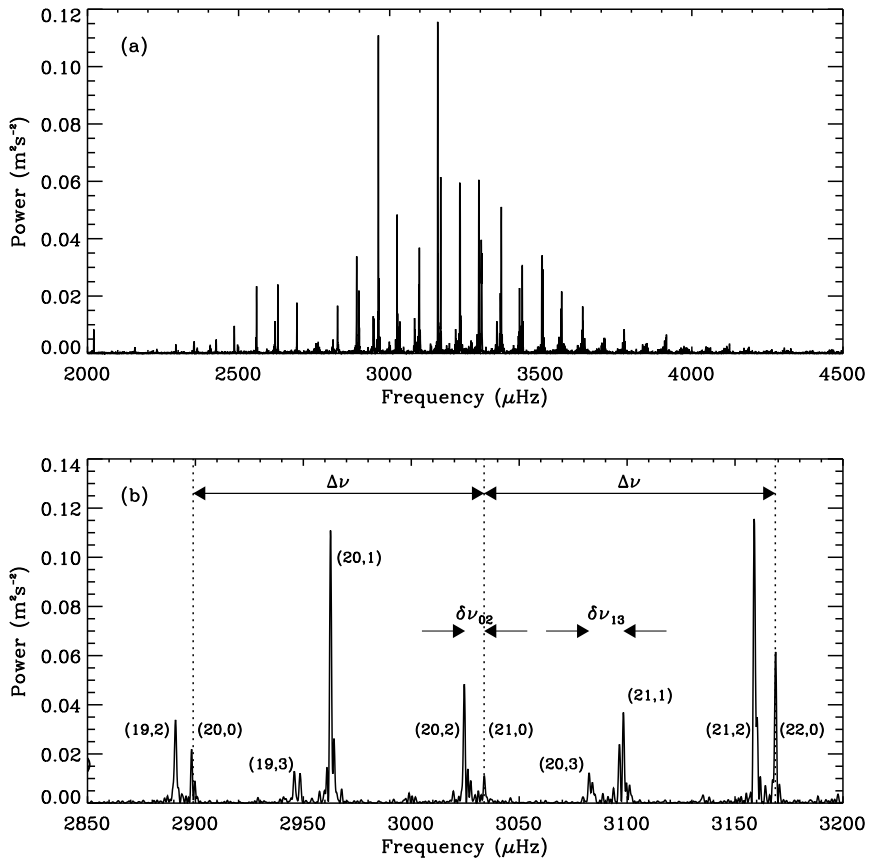


**Figure 2.1 | Frequency spectrum of the Sun as-a-star.** Produced using 10 days of observations from **BISON** (details in the text). **a)** Frequency versus oscillation power in arbitrary units. **b)** Zoom-in with labelling of the modes with  $(n, l)$ , and radial modes highlighted with dotted lines. The large and small frequency separations are indicated as well (details in text). Figure reproduced from Bedding (2014) with permission.

is the **acoustical cut-off frequency**  $\nu_{\text{ac}} = \omega_{\text{ac}}/(2\pi)$ , and hence Brown et al. (1991) conjectured a proportionality between the two. Assuming an ideal gas and isothermal atmosphere, Kjeldsen and Bedding (1995) formulated the scaling as

$$\nu_{\text{max}} \propto \nu_{\text{ac}} \propto \frac{c_s}{H_p} \propto \frac{g}{T_{\text{eff}}^{1/2}} , \quad (2.13)$$

in which the first proportionality is the disputed one.

If the attention is turned towards the lower panel of fig. 2.1, a close-up of the central part of the spectrum with additional annotations is revealed. The peaks are denoted by their order  $n$  and degree  $l$ ; the radial modes with  $l = 0$  are marked with dotted lines and the spacing between these constitute  $\Delta\nu$ . Strictly speaking, it would have been more correct to label it as the *average large frequency separation*  $\langle \Delta\nu_{nl} \rangle$ , which is what can be determined from observations. However, this is actually a good estimate of the “true” quantity in eq. (2.11), and it will generally be written as  $\Delta\nu$  even though it refers to the observations. For the Sun, the value is around  $\Delta\nu \simeq 135 \mu\text{Hz}$ . Generally, it is relatively easy to obtain  $\Delta\nu$  and  $\nu_{\text{max}}$  from stars exhibiting solar-like oscillations, even from data of sub-optimal quality.

In fig. 2.1, the remaining annotations are two of the so-called *small frequency separations*. The quantity  $\delta\nu_{02}$  is the spacing between adjacent modes (where  $n$  differs by one) with  $l = 0$  and  $l = 2$ ; likewise  $\delta\nu_{13}$  is between a pair with  $l = 1$  and  $l = 3$ . Because the  $l = 1$  modes does not fall exactly between pairs of  $l = 0$  modes, it is customary to also define the separation  $\delta\nu_{01}$  as the offset from the midpoint of the  $l = 1$  mode. From the frequencies  $\nu_{n,l}$  the small separations can be written as (in the notation of Bedding, 2014)

$$\delta\nu_{02} = \nu_{n,0} - \nu_{n-1,2} , \quad (2.14a)$$

$$\delta\nu_{13} = \nu_{n,1} - \nu_{n-1,3} , \quad (2.14b)$$

$$\delta\nu_{01} = \frac{\nu_{n,0} + \nu_{n+1,0}}{2} - \nu_{n,1} . \quad (2.14c)$$

The small frequency separation contribute to the second-order term not written in eq. (2.10), and depends on the sound-speed gradient near the core, which in turn depends critically on evolution. These separations can be combined into a powerful asteroseismic diagnostic, which is discussed in section 3.3.



The final observational tool to be introduced is the so-called échelle diagram, which is a very convenient way of displaying oscillation frequencies. To produce such a diagram, the basic idea is to divide the spectrum into equal segments, each of length  $\Delta\nu$ . Those segments are stacked on top of each other, which will align modes of the same degree vertically in separate ridges. In practice, this is often done from the extracted individual oscillation frequencies, which are plotted against their value modulo the **large frequency separation**. Note that for stars other than the Sun, it is not typical to be able to measure  $l \geq 3$  (and often not even  $l = 3$ ) due to the cancellation effects mentioned earlier.

An example from Bedding (2014) of the Sun using **BISON** frequencies is shown in fig. 2.2. The échelle diagram is very sensitive to the adopted value of  $\Delta\nu$ . Using a too large/small value will shift the ridges and tilt them sideways, as is evident from the example in the figure. Remembering the earlier discussion, this can be very useful for tracing the evolutionary state of a star. Moreover, the curvature is sensitive to any departures from regularity – in particular this includes variations as a function of frequency in the frequency separations. From this it is clear that the asymptotic relation is not exact.

### 2.3 Oscillation Frequencies of Stellar Models

In order to fully utilise the ever-growing pool of high-quality asteroseismic observations the asymptotic description is not adequate: precise determination of stellar parameter requires the ability to compare the observations to models (see chapter 3). The common tool to make this link is a *stellar pulsation code*, which is one of the main ingredients in this thesis work. Such codes operate under the basic principle: Given a stellar structure model, the (adiabatic) oscillations it will exhibit are predicted. A full review of the theory is given by Aerts, Christensen-Dalsgaard, and Kurtz (2010) as introduced in the beginning of the chapter.

In other words, a numerical solution of the stellar oscillation equations are sought, which translates to a determination of the eigenvalues. Typically, the equations are cast into a form that makes them easier to solve numerically, and the input equilibrium model is re-defined in terms of carefully

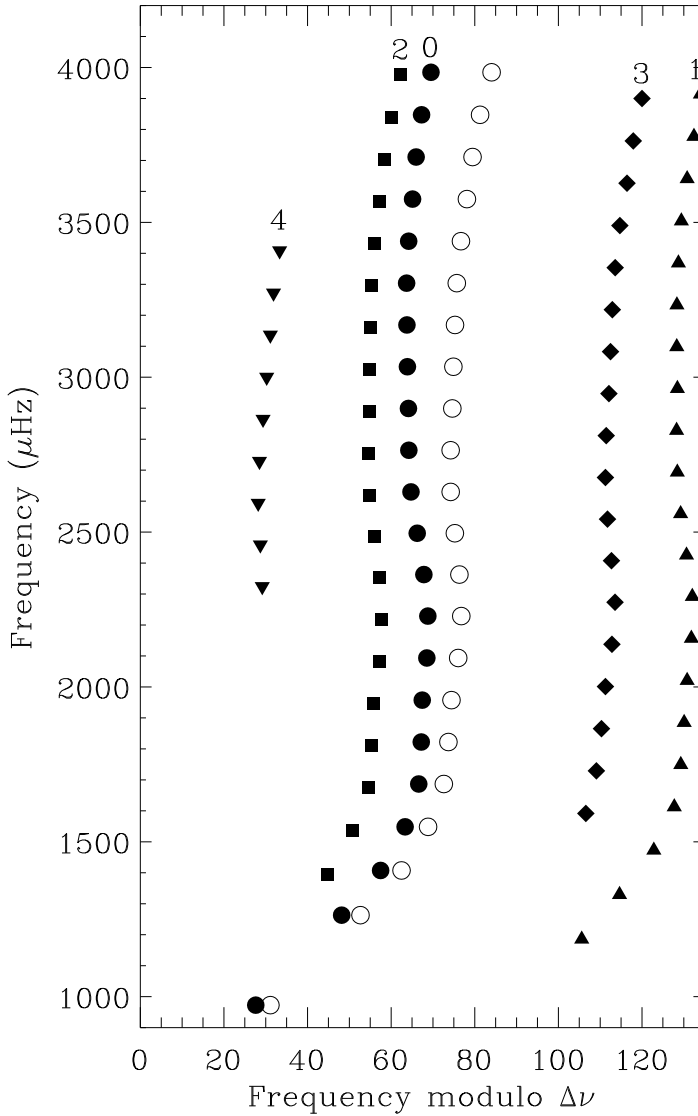


**Figure 2.2 | Échelle diagram of the observed low-degree frequencies in the Sun.** Produced using the **BISON** frequencies from Broomhall et al. (2009). Filled symbols depict the frequencies of modes with different  $l$  (listed above the symbols) using a **large frequency separation** of  $\Delta\nu = 135.0 \mu\text{Hz}$ . The open symbols show the effect on the radial modes of using instead  $\Delta\nu = 134.5 \mu\text{Hz}$ . Figure reproduced from Bedding (2014) with permission.

selected (dimensionless) variables (see e.g. Christensen-Dalsgaard, 2008a; Townsend and Teitler, 2013). Moreover, as the resolution requirements are typically higher than for stellar evolution, another common procedure is to change the mesh of the input model: adding more mesh points, but also performing a redistribution of them to increase the mesh density in rapidly changing parts of the star. The redistribution can also help reduce numerical effects, such as spikes in the derivatives.

As is always the case, boundary conditions are required to solve the equations. For pulsation calculations, the outer boundary is located above the photosphere, i.e., in the atmosphere of the model. Common choices include the simple choice of a vanishing pressure perturbation at the given point; or an isothermal atmosphere, which means that the interior solution is continuously matched to the solution in an isothermal atmosphere extending from the outer-most model point. In this research, the isothermal atmosphere is always applied.

The pulsation code used for this thesis work is the *Aarhus adiabatic pulsation code* (**ADIPLS**) – sometimes also known as the *Aarhus adiabatic oscillation package* – by Christensen-Dalsgaard (2008a), which is a very efficient tool for calculating adiabatic oscillation frequencies. It is especially suited for non-rotating solar-like oscillators and has served as a reference tool for *helioseismology*. Full technical details are given in Christensen-Dalsgaard (2008a) as well as in the documentation shipped with the package<sup>1</sup>. The development is on-going and has over the last years improved the computation of frequencies of **RG**-stars and very lately *subgiants*.

Several alternatives for calculating stellar oscillations exists, which are specialised for various requirements – in particular for a specific type of stars. One to mention in the present context is the open-source code **GYRE** (Townsend and Teitler, 2013; Townsend, Goldstein, and Zweibel, 2018), which is becoming more and more popular in the field, but has not been used in the present research. Townsend and Teitler (2013) also presents a brief overview of various codes with different approaches. For the remainder of this work, whenever adiabatic oscillations are computed from models, the computation is performed with **ADIPLS**.

1: Available from: [http://astro.phys.au.dk/jcd/adipack.v0\\_3/](http://astro.phys.au.dk/jcd/adipack.v0_3/). Note that this thesis work relies on the un-published currently un-published development version of the code, which is not publicly available.

## 2.4 The Asteroseismic Surface Effect

When comparing the predicted oscillation frequencies from a **SSM** to the observations, a systematic offset is found. Above a certain point, the model frequencies are too, and the deviation increases with frequency. This tendency was observed in the Sun and confirmed by **helioseismology** to stem from near-surface deficiencies in the stellar models (Brown, 1984; Christensen-Dalsgaard and Gough, 1984; Christensen-Dalsgaard, Dappen, and Lebreton, 1988). The phenomenon thus became known as the *surface term* or more generally as the (*asteroseismic*) *surface effect*.

Commonly, the physical model deficiencies constituting the **surface effect** are divided into two main components: the *structural* part and the *modal* part (see e.g. Trampedach et al., 2017). The latter is related to the dynamics of the individual pulsation modes: the breakdown of the adiabatic approximation, and interaction between pulsations and convection. The modal part will not be investigated in this thesis. On the other hand, the *structural* part stems directly from inaccurate descriptions of the stellar structure in the models. In particular, it is related to superadiabatic convection and an expansion of the atmosphere – see also chapter 4 for modelling attempts using realistic simulations of stellar convection. Mending these structural inadequacies is one of the main driving mechanisms behind this thesis.

The typical way of presenting the **surface effect** is to display the difference between oscillation frequencies predicted by the model and the corresponding observations. This is shown for the Sun in fig. 2.3 on the following page using the “Sun as-a-star” **BISON** frequencies from Broomhall et al. (2009) and Davies et al. (2014). To keep the plot simple, the comparison is only shown for  $l = 0$  modes (from  $n = 7$  to  $n = 28$ ). It is clear that above 2300 – 2500  $\mu\text{Hz}$  a significant and increasing deviation from the observations is found. The effect is also present in the Sun across large ranges of mode orders and degrees as can be seen in e.g. Aerts, Christensen-Dalsgaard, and Kurtz (2010, fig. 7.24). An alternative visualisation can be produced with an échelle diagram, which will be used in some of the later chapters.

Looking at the figure, it is also obvious that the effect is not completely independent on the chosen **SSM**. Two different cases are shown: The first model is the famous *Model S* from Christensen-Dalsgaard et al. (1996),

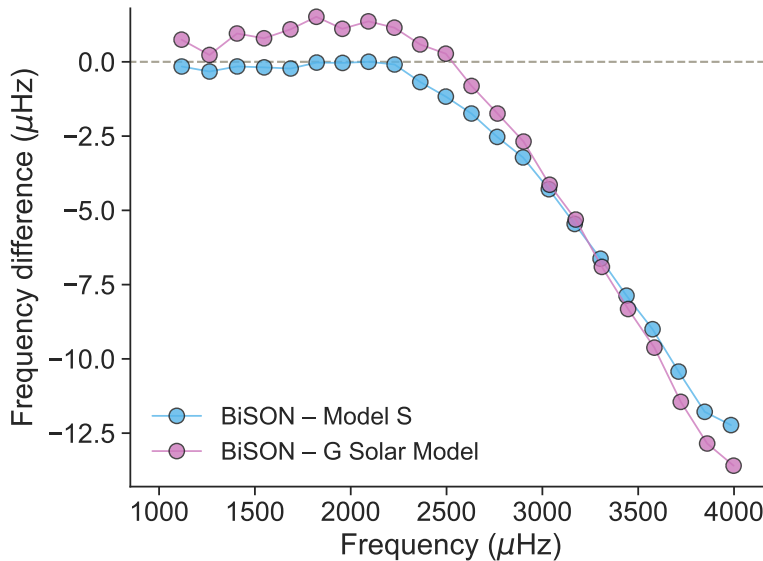


**Figure 2.3 | Asteroseismic surface effect in the Sun.** Frequency difference between observations from **BiSON** (only radial modes with orders between 7 and 28) and predictions based on a stellar evolution model of the Sun. *Model S* is the well-known helioseismic reference and *G Solar Model* is the result of a standard solar calibration performed with **GARSTEC** (details on both are given in the text).

which has been used extensively for **helioseismology** and is often taken as *the* reference solar model. To compute the model, an earlier version of the *Aarhus stellar evolution code (ASTEC)* by Christensen-Dalsgaard (2008b) was utilised, using **EOS** and opacities from the **OPAL** group (see section 1.2.1). The second case in fig. 2.3 is the result of a standard solar calibration with **GARSTEC**, which is not specifically tuned to match the solar frequencies. This models also relies on the **OPAL** group for opacities and **EOS**, but the newer version of the tables – and augmented in the low temperature regime by the **MHD-EOS**. Moreover, the solar composition Asplund et al. (2009) is assumed for this model, whereas *Model S* was based on the older determinations from Grevesse and Noels (1993).



As demonstrated, the **surface effect** will systematically shift a comparison between model and observation, which must be counteracted to avoid biased

results. In the context of helioseismic inversions, the surface term is typically suppressed by introducing a constraint based on a series of polynomials (e.g. Christensen-Dalsgaard, 2002, and references therein). For applications in **asteroseismology**, an empirically-derived function known as a *surface correction* is commonly used.

What used to be the most widely applied surface correction is the power law by Kjeldsen, Bedding, and Christensen-Dalsgaard (2008), which is inspired by the Sun and constructed from a fit to the frequencies. Along the same lines is the work by Christensen-Dalsgaard (2012) more directly using the shape from the solar frequencies, but scaled to the star in question. A fundamentally different one is the work by Sonoi et al. (2015), which used 3D convective simulations (see chapter 4) to derive what they describe as a “modified Lorentzian”.

The final parametrisation to be mentioned is the preferred option in this research, namely the one from Ball and Gizon (2014). It is inspired by theoretical arguments from Gough (1990) and has quickly risen in popularity for its efficiency also for different types of solar-like oscillators. The frequency correction  $\delta\nu$  (not to be confused with the small frequency separation) from Ball and Gizon (2014) is given as

$$\delta\nu = \frac{a_{-1}}{\mathcal{I}} \left( \frac{\nu}{\nu_{\text{ac}}} \right)^{-1} + \frac{a_3}{\mathcal{I}} \left( \frac{\nu}{\nu_{\text{ac}}} \right)^3, \quad (2.15)$$

where  $a_{-1}$  and  $a_3$  must be determined from a fit to the model in question,  $\mathcal{I}$  is the normalised mode inertia (e.g. Aerts, Christensen-Dalsgaard, and Kurtz, 2010, eq. 3.140), and  $\nu_{\text{ac}}$  is the **acoustical cut-off frequency** used to normalise the frequencies. In the procedure by Ball and Gizon (2014), the latter is to be determined from the scaling relation

$$\frac{\nu_{\text{ac}}}{\nu_{\text{ac},\odot}} \simeq \frac{g}{g_{\odot}} \left( \frac{T_{\text{eff}}}{T_{\text{eff},\odot}} \right)^{11/2}, \quad (2.16)$$

with  $\nu_{\text{ac},\odot} = 5000 \mu\text{Hz}$ . Note that this is identical to the last part of eq. (2.13).

Even though this surface correction is based on physical arguments and performs well, it would be preferable to not rely on an empirical derivation. Thus, alternative procedures to avoid a surface correction is central to this thesis research and is explored in the chapters 5–8.



# 3

## Determination of Stellar Properties

A star is characterised by a set of fundamental parameters of which the most important are mass, chemical composition and age. Knowing these is necessary to describe the star by a stellar model and to make inferences about e.g. stellar populations.

The determination of fundamental stellar properties is a key task in stellar studies. In its standard form, it requires observational data of a given star and a model framework to make predictions based on the observables. In recent year, a new class of methods has emerged: the *data-driven* approaches that make inferences of the fundamental parameters only based on the observations (e.g. *The Cannon*, Ness et al., 2015). This thesis will however be restricted to the more traditional approach which is reviewed below.

This chapter is structured as follows. In section 3.1 some basic observational techniques are briefly mentioned with special emphasis on space-based photometry. A brief detour is taken in section 3.2 to give some details on the controversy of the chemical composition of the Sun. The different main categories of parameter estimation using *asteroseismology* are presented in section 3.3. That topic is continued in the context of grid-based modelling in section 3.4, where the inference code used for the research in this thesis is also introduced.

### 3.1 Observations of Stars

Observing stars means gathering light. How the light is dealt with is what sets apart the main types of stellar observations: *photometry* and *spectroscopy*. In

the former, the light is directly collected from the telescope onto an imaging device, while in the latter it is passed through a spectrograph splitting it according to wavelength.

The observational method of photometry relies on counting photons within a given time window to determine the brightness of a given target. Measurements can be repeated at different times, whereby stellar brightness as a function of times can be determined – a special case of this is space-based photometry (see section 3.1.1). The clear advantage of photometry is the ability to easily characterise large numbers of stars.

Using a set of filters, it is possible to measure the colour of stellar light, which can be used to determine atmospheric parameters. One particular example is the Strömgren system (Strömgren, 1966), which has been successfully applied for all-sky surveys (Nordström et al., 2004; Casagrande et al., 2014). From the colours and indices, it is straightforward to obtain  $T_{\text{eff}}$ ; and (bulk) metallicity can also be determined using a suitable calibration (Schuster and Nissen, 1988, 1989).

An alternative method to obtain precise effective temperatures is the *InfraRed Flux Method (IRFM)* described by e.g. Casagrande et al. (2010) relying on infrared photometry from *Two Micron All Sky Survey (2MASS)* (Skrutskie et al., 2006). This has been successfully applied by Casagrande et al. (2011) to re-analyse the survey data from Nordström et al. (2004), is the foundation of Casagrande et al. (2014), and was utilised by Sahlholdt et al. (2018). In the two latter works it was to *asteroseismology*.



Unlike photometry where all stars in a frame can in principle be extracted, spectroscopic observations are generally of a single star at a time. In spectroscopy, the observed light is fed from the telescope into a spectrograph to produce a spectrum of the light from a given star. Spectroscopy is the analysis of the absorption lines produced in the stellar atmosphere present in the stellar spectrum. A good description of spectroscopic methods and applications are given by e.g. da Silva et al. (2006) and Bergemann et al. (2014). As only parameters supplied by external sources are used in this research, the details of such analyses will not be further elaborated upon.

The procedures generally yield stellar parameters of high precision and provide the standard auxiliary inputs to the various inference methods reviewed in section 3.4 – especially important are  $T_{\text{eff}}$  and metallicity (in

the form of  $[\text{Fe}/\text{H}]$  which will be defined in section 3.2). Classically, the surface gravity can also be determined from spectroscopy, however from **asteroseismology** much higher precision on that can be obtained (see section 3.3). In contrast to photometry, spectroscopy will not only provide an estimate of the bulk metallicity, but yield detailed individual abundances. Several large spectroscopic surveys are mapping huge portions of the sky. One to be mentioned is APOGEE (The Apache Point Observatory Galactic Evolution Experiment, Majewski et al., 2017), which has also been combined with **asteroseismology** from *Kepler* (Pinsonneault et al., 2014; Serenelli et al., 2017).



For completeness, a few other methods must be named. The first one is *interferometry*, in which the light from several telescopes is combined and inferences made from the interference patterns. It can provide independent constraints on stellar effective temperature and radius, and be combined with **asteroseismology** for powerful results (e.g. Creevey et al., 2007; White et al., 2013; Stokholm et al., 2019).

A final class to mention is *astrometry*: the measurements of celestial positions, parallaxes and proper motions. This kind of information is vital for studies of our Milky Way galaxy and solar neighbourhood. Currently, the data from the on-going *Gaia* mission (Gaia Collaboration et al., 2016, 2018) is revolutionising the stellar population studies. However, for the research presented here it has not been applied and will not be described in further detail.

### 3.1.1 Space-based Photometry

Another main class of observables – which is especially relevant in the current context – belongs to **asteroseismology**. An overview of the observational efforts (also in a historical context) to measure solar-like oscillations in other stars than the Sun are presented clearly by Bedding (2014).

The central concept in observational **asteroseismology** is the ability to observe tiny variation as a function of time and then conduct time series analysis to extract characteristic frequencies of the mode oscillations. For optimal performance the ideal data are uninterrupted and regularly sampled in order to minimize transformation artefacts in the power spectrum. The

longer the time series, the better signal-to-noise ratio. One way of extracting the power spectrum is using photometry and as the number of gaps in the data should be minimized, space photometers are ideal as there will be no day-night gaps or bad-weather gaps in the time series. This allows for higher precision for relatively smaller telescopes compared to earth-based telescopes.

A regular revolution in the field came with the space-telescope missions *CO*nvection *RO*tation and *planetary Transits* (*COROT*) (Baglin et al., 2006; Michel et al., 2008) and *Kepler* (Borucki et al., 2010; Gilliland et al., 2010; Koch et al., 2010). They have provided high-quality data for thousands of *MS* and *RG* stars exhibiting solar-like oscillations. The field is continually pushed forward by new missions: the (now terminated) renaissance mission of *Kepler*, *K2* (Chaplin et al., 2015; Lund et al., 2016a,b), the on-going *Transiting Exoplanet Survey Satellite* (*TESS*) (Ricker et al., 2014), and the future *PLANetary Transits and Oscillation of stars* (*PLATO*) (officially *PLATO 2.0*, Rauer et al., 2014).

With four years of continuous observations, *Kepler* has provided data of unprecedented quality that have driven revelations in stellar physics. Even among the great *Kepler* data on solar-like oscillators some stars stand out, and two collections of such deserve to be mentioned. A sample of the 66 *MS* stars with highest data quality was compiled and uniformly analysed by Lund et al. (2017) and Silva Aguirre et al. (2017), and is known as the *Kepler asteroseismic LEGACY sample*. This collection serves as a benchmark reference and will be referred to in the later chapters. Another compilation to mention is that of Silva Aguirre et al. (2015) and Davies et al. (2016) consisting of 33 (or 35 if counting the two excluded from the modelling paper) planet-candidate host stars from *Kepler* showing solar-like oscillations of very high data quality – this is sometimes named the *KAGES* sample (though the term is not used in the original references). All of the asteroseismic data in this thesis work are from the *Kepler* mission and one of the two listed samples.

## 3.2 Chemical Composition

For some parameters there is a difference between what is observed and what is required for stellar models. Perhaps the most noteworthy example is the chemical composition, which deserves a mention.

For stellar models, the overall composition is given in terms of the mass fractions  $X$ ,  $Y$ , and  $Z$  as introduced in eq. (1.11). From observations, the composition is typically given relative to the Sun in terms of logarithmic abundance ratios using the *bracket* notation. For the elements “B” and “C” this is defined in terms of the number of atoms  $N$  as

$$[B/C] := \log\left(\frac{N_B}{N_C}\right) - \log\left(\frac{N_B}{N_C}\right)_\odot . \quad (3.1)$$

Sometimes it is instead given in terms of the abundance  $A$  relative to number of hydrogen atoms  $A_B = N_B/N_H$ . Typically what is provided by observations is an estimate of the bulk stellar metallicity in the shape of the iron abundance  $[\text{Fe}/\text{H}]$ . In order to convert it into mass fractions, it is customary to assume

$$[\text{Fe}/\text{H}] \simeq \log\left(\frac{Z}{X}\right) - \log\left(\frac{Z}{X}\right)_\odot . \quad (3.2)$$

In this fundamental assumption, the solar reference value  $\log(Z/X)_\odot$  plays an important role (also recall section 1.6.3). This quantity is determined from the distribution of heavy elements in the Sun – the so-called *solar mixture* or *solar abundances*.

As described in the detailed review by Asplund et al. (2009), the determination of element abundances in the Sun is a somewhat controversial topic and the obtained values have changed over the last decades. Mainly, there is a quite large discrepancy between the “classical” determinations from Anders and Grevesse (1989), Grevesse and Noels (1993), and Grevesse and Sauval (1998), and the newer works based on more sophisticated 3D atmosphere models (see also chapter 4) by Asplund, Grevesse, and Sauval (2005), Asplund et al. (2009), and Caffau et al. (2011).

However, the new and improved values significantly worsen the agreement between a *SSM* and helioseismic inferences (especially the sound speed profile) – for this reason, some parts of the astrophysics community are reluctant to adopt the new values. This is known as the *solar abundance problem* and is very well-described in the short review Serenelli (2016), or specifically from a stellar-modelling point-of-view by e.g. Serenelli et al. (2009) and Serenelli (2010). The full (asteroseismic) implications of the still unresolved problem are reviewed by e.g. Bahcall et al. (2005) and Basu and Antia (2008).

### 3.3 Asteroseismic Inference

A key concept of observational (stellar) astrophysics is the ability to estimate properties of stars based on observables. Traditionally, this has been particularly successful for stars with additional constraints: e.g. in clusters (e.g. Salaris and Weiss, 2002; VandenBerg et al., 2013) or eclipsing binaries (e.g. Torres, Andersen, and Giménez, 2010) to name a few. However, **asteroseismology** has proved to be a very powerful tool as it can provide very precise parameters of (oscillating) field stars. How to determine fundamental stellar properties of solar-like oscillators is nicely reviewed by Chaplin and Miglio (2013), upon which this section is loosely based. Depending on quality of data and requirements, different approaches and observables can be utilised as discussed in the following. It should also be noted that complementary, non-seismic inputs are required to reach the full potential of **asteroseismology**.

#### 3.3.1 Global Asteroseismic Parameters

When the data quality is insufficient to reliably determine the individual oscillation frequencies, it is still possible to use the global asteroseismic quantities, the **large frequency separation**  $\Delta\nu$  and the **frequency of maximum power**, which can be extracted at lower signal-to-noise ratio. Thus, this class of inference is very important for stellar population studies (e.g. Miglio et al., 2013, 2017; Serenelli et al., 2017). Serenelli et al. (2017) also provides a nice review of several different pipelines and methods to extract the average seismic quantities from data.

Recall the scaling relations from eqs. (2.12) and (2.13):  $\Delta\nu$  scales with the mean density, and  $\nu_{\max}$  with surface gravity and effective temperature. Thus, combined with an independent determination of  $T_{\text{eff}}$ , an estimate of  $\langle\rho\rangle$  and  $\log g$  – and hence stellar mass  $M$  and radius  $R$  – can be obtained. This is sometimes referred to as the “direct method” (Chaplin and Miglio, 2013). It is customary to assume that scaling the quantities to the well-determined

solar values denoted by  $\odot$  is safe; hence, the relations can be re-written as

$$\frac{R}{R_{\odot}} \simeq \frac{\nu_{\max}}{\nu_{\max,\odot}} \left( \frac{\Delta\nu}{\Delta\nu_{\odot}} \right)^{-2} \left( \frac{T_{\text{eff}}}{T_{\text{eff},\odot}} \right)^{0.5} \quad (3.3)$$

$$\frac{M}{M_{\odot}} \simeq \left( \frac{\nu_{\max}}{\nu_{\max,\odot}} \right)^3 \left( \frac{\Delta\nu}{\Delta\nu_{\odot}} \right)^{-4} \left( \frac{T_{\text{eff}}}{T_{\text{eff},\odot}} \right)^{1.5}, \quad (3.4)$$

which are often seen in literature.

An alternative procedure is to use  $\Delta\nu$  and  $\nu_{\max}$  as inputs for *grid-based modelling*, where the basic principle is to search for a best match to the observations in a large ensemble of stellar models. One of the advantages is that prior information is implicitly included from stellar evolution theory – e.g. the narrow range of  $T_{\text{eff}}$  allowed for a given  $M$  and  $R$  – which typically lowers the uncertainties. Calculating the quantities from the stellar models, it is instructive to re-arrange the solar-scaled expressions and applying the Stefan-Boltzmann law from eq. (1.36) to obtain

$$\frac{\Delta\nu}{\Delta\nu_{\odot}} \simeq \left( \frac{M}{M_{\odot}} \right)^{0.5} \left( \frac{R}{R_{\odot}} \right)^3 \left( \frac{L}{L_{\odot}} \right)^{0.75} \quad (3.5)$$

$$\frac{\nu_{\max}}{\nu_{\max,\odot}} \simeq \frac{M}{M_{\odot}} \left( \frac{R}{R_{\odot}} \right)^{3.5} \left( \frac{L}{L_{\odot}} \right)^{-1}, \quad (3.6)$$

in which  $L$  is the total (photospheric) luminosity. Some authors prefer to keep  $T_{\text{eff}}$  instead of transforming to  $L$ .

The grid-based method can be further improved by not relying on the scaling relation above to estimate  $\Delta\nu$ . Specifically, if adiabatic pulsations are computed (see section 2.3) for the models in the grid, it is possible to determine  $\Delta\nu$  from the predicted individual frequencies. It was shown by White et al. (2011) that the average quantity can be robustly estimated from a fit to the  $l = 0$  modes weighted around  $\nu_{\max}$ . Moreover, the authors also suggested how to improve the applicability across different evolutionary stages.

Recently, some effort has been invested into validating the scaling relations, especially in the light of the high-quality data from *Gaia* (e.g. Sahlholdt et al., 2018; Sahlholdt and Silva Aguirre, 2018). These works also proposed

corrections to the scaling relations to account for trends across different stellar parameters. Finally, it should be noted that the validity of  $\nu_{\max}$  scaling with the **acoustical cut-off frequency** is also still disputed; e.g. Viani et al. (2017) suggested to add an extra term taking the molecular weight into account.

### 3.3.2 Individual Oscillation Frequencies

The use of individual frequencies instead of global quantities naturally increases the amount of information provided by the asteroseismic input; and thus, significantly more precise inferred parameters – including the all-important stellar age – are obtained (e.g. Chaplin and Miglio, 2013). As was briefly mentioned in section 2.2, the extraction of these oscillation frequencies (known as “peak-bagging”) requires high signal-to-noise data. Moreover, to obtain robust values and especially reliable uncertainties, advanced statistical and computational methods are typically applied – a comprehensive discussion on Bayesian Markov chain Monte Carlo methods are presented by e.g. Handberg and Campante (2011) and Lund et al. (2017).

To estimate stellar parameters, the basic principle is to minimise the deviation between observations and models. In this case, all of the individual oscillation frequencies are included as observables and the procedure is commonly referred to as ‘fitting’ (*individual*) frequencies. As before, this is often performed in a grid-based framework and of course requires calculation of adiabatic pulsations.

An important thing to keep in mind is that the asteroseismic **surface effect** must be taken into account when fitting frequencies, as was described in section 2.4. Note that all of the empirical corrections effectively assume the lowest  $l = 0$  mode to be virtually unaffected, and that the star in question shows deviations with a shape not too different from that of the Sun.



Another possibility is to entirely circumvent the problems of the surface term by using instead the so-called frequency separation ratios, which can be computed from the individual frequencies. They are typically employed in the form defined by Roxburgh and Vorontsov (2003) and relies on the small frequency separations introduced in eq. (2.14). However, instead of

using  $\delta v_{01}$  based on three points, Roxburgh and Vorontsov (2003) found it superior to instead take the smoother five-point small frequency separations  $d_{01}$  defined as

$$d_{01}(n) = \frac{v_{n-1,0} - 4v_{n-1,1} + 6v_{n,0} - 4v_{n,1} + v_{n+1,0}}{8} , \quad (3.7a)$$

$$d_{10}(n) = -\frac{v_{n-1,1} - 4v_{n,0} + 6v_{n,1} - 4v_{n+1,0} + v_{n+1,1}}{8} , \quad (3.7b)$$

in which  $v_{n,l}$  are the given oscillation frequencies as usual. Denoting the large separation as  $\Delta v_l(n) = v_{n,l} - v_{n-1,l}$  the ratios are defined as

$$r_{02}(n) = \frac{d_{02}(n)}{\Delta v_1(n)} , \quad (3.8a)$$

$$r_{01}(n) = \frac{d_{01}(n)}{\Delta v_1(n)} , \quad r_{10}(n) = \frac{d_{10}(n)}{\Delta v_0(n+1)} , \quad (3.8b)$$

where  $d_{02}(n) = \delta v_{02} = v_{n,0} - v_{n-1,2}$  is the small frequency separation defined in eq. (2.14) – the renaming is just to keep the notation constant (and to hopefully avoid any ambiguity with the  $\delta v$  denoting frequency deviation in regards to the surface term). Typically the ratios are combined into one unique set of observables, e.g.

$$r_{010} = \{ r_{01}(n), r_{10}(n), r_{01}(n+1), r_{10}(n+1), \dots \} , \quad (3.9)$$

which can then be combined with the  $r_{02}$ 's if desired. Note that use of the  $r_{010}$  in combination with  $r_{02}$  was disputed by Roxburgh (2018), due to the risk of overfitting the data, and instead suggested using the single series  $r_{102}$  (or  $r_{012}$ ).

The frequency separation ratios has been shown to be almost insensitive to the surface layers and primarily probe the deep stellar layers (e.g. Roxburgh and Vorontsov, 2003; Oti Floranes, Christensen-Dalsgaard, and Thompson, 2005; Roxburgh, 2005; Silva Aguirre et al., 2011). They have proved very useful for asteroseismic inferences of solar-like oscillators on the MS as demonstrated by e.g. Silva Aguirre et al. (2015, 2017), but they do not work for more evolved stars.

For completeness, it should be added that a large group of asteroseismic observables – relevant for stars in the later evolutionary stages – have so far been ignored and will only just be very briefly mentioned here as they are not relevant for the research presented later in this thesis.

Firstly, the phenomenon of *mixed modes*: these have **g-mode** character in the core and **p-mode** character in the envelope (e.g. Chaplin and Miglio, 2013; Bedding, 2014). They occur in **subgiants** and **RG** stars, where the star is effectively divided into two coupled cavities by the large density gradient outside the core. The **g-mode** frequencies are increased sufficiently by the high gravitational acceleration near the core to interact with the **p-modes** of same angular degree. This results in *mode bumping* or *avoided crossings*, where the frequencies depart from their otherwise regular spacing. Including such mixed modes in the analysis can add significant information for asteroseismic inferences of **subgiants** (e.g. the recent works by Huber et al., 2019; Stokholm et al., 2019). As soon as mixed modes stars appear, the otherwise powerful frequency separation ratios are rendered useless.

Secondly, it is possible to utilise that the **g-modes** asymptotically spaced in period (like **p-modes** are in frequency). Taking advantage of this *period spacing* providing invaluable insight into the cores of **RG** stars (e.g. to determine if helium burning has ignited, Bedding et al., 2011).

### 3.4 Grid-based Modelling

The general principle in all stellar modelling and fitting efforts is to answer the question: Which model provides the best fit to the observations? Or a natural extension of that query: Estimate the fundamental parameters with uncertainties of the observed star. An extensive overview of seven different asteroseismic modelling pipelines is given by Silva Aguirre et al. (2017).

Before moving on to grid-based modelling, an important class of procedures deserves a mention: the *forward-modelling* methods. Instead of searching in a grid, such schemes compute stellar models and adiabatic oscillation frequencies as a part of an optimization routine to match the observables. A solar calibration (see section 1.6.3) can be thought of as a special case of forward modelling. The resulting best model typically fits very well, and therefore such procedures are also very suitable as the basis of

inversion methods (e.g. Buldgen et al., 2015). However, forward modelling can be very time consuming for determining parameters of ensembles of stars as each star is treated individually.



A grid-based modelling approach tries to provide an answer to the query listed above given a set of observables, a pool of stellar models, and suitable statistical methods. Essentially, it is the well-known procedure of matching observations to stellar evolutionary tracks or the special case of *isochrone fitting* (e.g. Jørgensen and Lindegren, 2005, and references therein). Typically, the label *grid-based modelling* is applied when the schemes are upgraded with the powerful diagnostic information from **asteroseismology**.

The underlying idea is to move as much as the computation time as possible to the preparation phase such that parameter determination can be done quickly for a large number of stars. Another main strength is the ability to easily obtain uncertainties on the estimated parameters, because a range of models is considered and not just the best one (see section 3.4.1 below).

No grid-based method is better than the grid of models it relies on. Such a grid typically consists of a large number of evolutionary tracks computed with a set of input physics (see section 1.6); and along the tracks the individual structure models are stored and their adiabatic oscillations calculated. This leads to perhaps the main disadvantage: the physics in a grid of models is “locked”. Moreover, the grids are generally very time-consuming to compute; hence, it is not necessarily a straightforward task to test how different choices of microphysics affect the solution for a given star (unlike forward modelling).

How to invoke a grid-based method with asteroseismic observables was discussed in the previous sections above. The main principles are naturally very similar across different modelling tools, however the realisation and details can differ a lot. Also note that additional information are required – often in the form of  $T_{\text{eff}}$  and  $[\text{Fe}/\text{H}]$  from spectroscopy. As mentioned above, a great overview of a range of different (mostly grid-based) pipelines is provided by Silva Aguirre et al. (2017). Instead of discussing the different options, the focus will be put on just one of the mentioned tools.

### 3.4.1 The Bayesian Stellar Algorithm

The *BAyesian STellar Algorithm (BASTA)* code was originally described by Silva Aguirre et al. (2015) roughly based on the methods presented Serenelli et al. (2013). The toolkit has evolved much since and its current capabilities will be described in an upcoming paper (Silva Aguirre et al., in prep.) – a few of the main characteristics will be reviewed in the following.

At the foundation of *BASTA* is the framework of *Bayesian statistics*, in which the probability is related to the degree of belief in a given event. A thorough introduction of its application in astronomy is presented by Pont and Eyer (2004) or in the excellent work by Jørgensen and Lindegren (2005) transparently using isochrone fitting as an example. The latter clearly highlights one of the main selling points of Bayesian inference: the ability to take prior information into account, e.g. the evolutionary speed of stars in different phases. It must be noted that this can also be considered the main drawback as a Bayesian estimate can never be fully independent of these priors.

In a Bayesian framework, the objective is to determine the probability distributions for the desired stellar parameters (e.g. mass, age and composition), which are introduced as random variables. Following the notation of Silva Aguirre et al. (2015): if  $\mathbf{v}$  is a set of stellar model parameters and  $O$  is the data from observations, then Bayes' theorem yields the probability  $\mathcal{P}$  of  $\mathbf{v}$  given  $O$  as

$$\mathcal{P}(\mathbf{v} | O) \propto \mathcal{P}(\mathbf{v}) \mathcal{L}(O | \mathbf{v}) , \quad (3.10)$$

which is sometimes called the *probability density function (PDF)*. Here  $\mathcal{L}(O | \mathbf{v})$  is the likelihood of  $O$  given  $\mathbf{v}$  and  $\mathcal{P}(\mathbf{v})$  is the prior knowledge of the parameters. Suitable choices of priors are discussed by Serenelli et al. (2013) and Silva Aguirre et al. (2015), and typically include an initial mass function complemented by flat priors on most parameters.

If the errors are assumed to be Gaussian distributed, the likelihood of each model can be calculated as

$$\mathcal{L}(O | \mathbf{v}) = \frac{1}{(2\pi)^{1/2} |\mathbf{C}|^{1/2}} \exp\left(-\frac{\chi^2}{2}\right) , \quad (3.11)$$

with

$$\chi^2 = (\mathbf{o}_{\text{obs}} - \mathbf{o}_{\text{model}})^T \mathbf{C}^{-1} (\mathbf{o}_{\text{obs}} - \mathbf{o}_{\text{model}}) , \quad (3.12)$$

in which  $\mathbf{C}$  is the covariance matrix of the observed values  $\mathbf{o}_{\text{obs}}$ , and  $\mathbf{o}_{\text{model}}$  is the same quantities determined from the model. After the full **PDF** has been computed, the *marginalised posterior* of any stellar quantity can be computed by integration over all models/tracks properly accounting for the volume of the parameter space by applying suitable weights (to handle non-uniform sampling). The value reported for each quantity is the median of the posterior with the 16 and 84 percentiles, i.e., the 68 % bayesian credibility intervals. Note that more information is contained in the complete posteriors, which are typically plotted as a part of the output.

The **BASTA** code is very flexible and can fit classical observables – like  $T_{\text{eff}}$ ,  $\log g$ ,  $[\text{Fe}/\text{H}]$ – as well as asteroseismic data. For **asteroseismology**, it is possible to fit global asteroseismic parameters or utilise the full diagnostic potential by fitting individual frequencies or frequency separation ratios. The latter is one of the main strengths of **BASTA**. Another key feature is the ability to quickly process multiple targets by fitting many stars to the same grid of models.

As input, model grids are constructed from stellar models calculated with **GARSTEC** and adiabatic pulsations computed with **ADIPLS**. In **BASTA** it is also possible to use other libraries as input models. Currently, full support for the extensive compilation of isochrones from *Bag of Stellar Tracks and Isochrones* (**BASTI**) (Pietrinferni et al., 2004; Hidalgo et al., 2018) is implemented and they have been used in several projects (e.g. Silva Aguirre et al., 2018). However, for the research presented in this thesis, grids calculated with **GARSTEC** to fit the specific purposes are used.



# 4

## Modelling of Stellar Atmospheres

An essential part of stellar structure is the description of convection: the hydrodynamical phenomenon when energy cannot be transported by radiation alone. As described in chapter 1, it is customary to use an approximative, parametric description of convection in stellar structure models, and the most common is the **MLT** (section 1.5.1). However, as it has also been highlighted in the previous chapters, this simplified description of convection leads to physical inadequacies in the outer-most parts of the models.

A fundamentally different approach to stellar (surface) convection is to make a full three-dimensional (3D) simulation of the hydrodynamics in the outer layers coupled with radiative transfer. Such numerical simulations employ what is known as *magneto-hydrodynamics*; however as magnetic fields are ignored in the present context, it is commonly dubbed *radiation-coupled hydrodynamics* (**RHD**). The hydrodynamical simulations do not require a parametric description of convection and are inherently more realistic. To improve the modelling of the outer convective regions in stellar evolution codes, an option is to utilise this kind of simulations – and this is the focus of this chapter.

The basic principle of such stellar atmosphere simulations will be briefly reviewed in the next section below. In the remainder of the chapter (sections 4.2–4.4) different approaches of including 3D models in stellar evolution codes will be introduced. These methods will subsequently be elaborated upon in the next part of the thesis.

## 4.1 Numerical Simulations of Surface Convection

The idea behind 3D RHD simulations is to solve the fluid equations – conservation of mass, momentum, and energy – with a full treatment of radiative transfer. The exact equations are not relevant for the current discussion and will not be presented here; they can be found in the excellent reviews by Nordlund, Stein, and Asplund (2009) and Kupka and Muthsam (2017) with an extensive theoretical background and a great amount of details.

A range of programs to solve the equations exists; one such example (originally anelastic and later fully compressible) is described by Nordlund (1982), Nordlund and Dravins (1990), Nordlund and Stein (1990), and Stein and Nordlund (1998). The references include details on e.g. the radiative transfer scheme, the boundary conditions, and the numerical diffusion required to stabilise the solutions. The code has undergone continuous development and improvement, and different forks exist; it is now known as the STAGGER code, and various versions of it have been used to produce the models utilised in this thesis work.

Different types of hydrodynamical simulations of other phenomena exist – e.g. convective cores or late-stage shell sources – but this discussion is restricted to 3D RHD simulations of surface convection. These simulations cover both the radiative outer atmosphere as well as the superadiabatic convective sub-photospheric layers, reaching the quasi-adiabatic deeper convective layers. No parametric theory is needed to generate the convection; only fundamental physics. As discussed by e.g. Magic et al. (2013b), the choice of methods for obtaining the temporal and spatial averages of the simulations can play an important role, and the selection will depend on the desired application.

The 3D simulations have produced impressive results by e.g. being able to reproduce the observed solar granulation from first principles (Stein and Nordlund, 1998, 2000). Generally, they have altered our understanding of stellar convection and how it is driven (Stein and Nordlund, 1989; Nordlund, Stein, and Asplund, 2009). Using the simulations, it is possible to produce spectral line profiles in very good agreement with observations (Asplund et al., 2009). Moreover, exactly these atmosphere models are the foundation of the new determinations of the chemical abundances of the Sun (section 3.2); and this is the key point of the solar abundance problem. The 3D RHD simulations are very trustworthy, but seemingly not fully compatible with the also very trustworthy helioseismology.

A major drawback of this kind of simulations is that they are computationally very expensive. Therefore it is customary to pre-compute a range of atmosphere models to form a grid in  $(T_{\text{eff}}, \log g)$ , which can then be used for a variety of analyses. One such example is the grid by Trampedach et al. (2013), which will be referred to as the *Trampedach grid*. It has been computed with a custom version of a precursor of the STAGGER code and consists of 37 simulations at solar metallicity – the parameters of the atmospheres will be displayed in fig. 5.1 on page 75. This grid has been used for different studies, including a recent analysis of the contribution to the *surface effect* from atmospheric expansion Trampedach et al. (2017). Moreover, the simulations have been calibrated against 1D MLT models and distilled to extract information to be used in stellar evolution codes (Trampedach et al., 2014a,b) which is the focus of section 4.3.

Another example is the STAGGER grid by Magic et al. (2013a) consisting of around 200 simulations of varying chemical composition. Of those, 29 have solar metallicity and their surface parameters will be shown in fig. 6.3 on page 101. The grid has been employed for several different applications, including calibration of convective efficiency in MLT (Magic, Weiss, and Asplund, 2015) and computation of limb-darkening coefficients (Magic et al., 2015). It has also been applied in the context of *patched models* (see next section), and is the main grid utilised for the results in the next part.

As was written earlier, it has been suggested to use 3D RHD simulations to improve on the inadequacies in the outer regions of stellar structure models – especially with the asteroseismic *surface effect* (section 2.4) in mind. In the context of stellar evolution, it is important to note the different characteristic timescales involved. The simulations are designed to study the stellar granulation, which operates on very short timescales compared to nuclear processes in the star as discussed in section 1.1 (also cf. Stein and Nordlund, 1998). Thus, these simulations cannot be directly utilised to calculate stellar evolution models as they are not able to follow the timescales required. Finally, they are not directly compatible with the usual 1D models in terms of physics, e.g. related to turbulent pressure and kinetic energy flux. Thus, in order to harness their power, they must be processed carefully as described by the following sections.

How to include information from **RHD** simulations in stellar evolution models can be tackled in two fundamentally different ways. In the following they are dubbed the *static* and the *dynamic approach*. The following section just below deals with the former, while the latter is treated in section 4.3.

## 4.2 The Link to Stellar Models I: *Static*

What is here dubbed the *static approach* is typically referred to as *patching* or *patched models* in the community. Basically, the idea is to substitute the outer layers of a stellar structure model – often referred to as a **1D** model – by the mean stratification of **3D RHD** simulations. The end-product is called a patched model and requires a high degree of physical consistency between the two model parts. It is also necessary to perform a careful fit of the **1D** model to the **3D** counterpart to ensure that the fundamental stellar surface parameters of the two match. A patching procedure consists of two steps: firstly a standard calculation with a stellar evolution code (using a traditional  $T(\tau)$  relation and **MLT** convection), and secondly the replacement of the outer layers. Hence, the **3D** atmosphere model is not used for the evolution, but applied afterwards – thus, the descriptive term “static”.

Naturally, the first attempts to apply stellar atmosphere simulations to investigate model deficiencies and the **surface effect** was centered around the Sun. Schlattl, Weiss, and Ludwig (1997) produced an improved **SSM** by combining the structure model with **1D** and **2D** model atmospheres and a calibrated mixing-length parameter  $a_{\text{MLT}}$  to stitch them together. One could argue whether this work belongs in this static section or in the next. Another early effort was the leading work by Rosenthal et al. (1999). They used **3D** simulations and envelope models to study the difference between observed and theoretical oscillation frequencies in the Sun.

More recently, Piau et al. (2014) patched averaged **3D** convection simulations onto a solar model and investigated the frequency impact – as for the earlier solar attempts, the **surface effect** was significantly reduced. A similar analysis with the same conclusion was performed by Magic and Weiss (2016) based on the solar model from the above-mentioned **STAGGER grid**. Moving away from the Sun, Sonoi et al. (2015) and Ball et al. (2016) produced patched models for respectively 10 and four simulations, both comparing against standard parametric descriptions of the surface

term (recall section 2.4). The two works used different base models and different codes to perform the 3D simulations, but reached similar conclusions about the morphology of the frequency deviation – however, they disagree on which one is the most suitable surface correction to capture this shape. Finally, the already mentioned work by Trampedach et al. (2017) derived frequency shifts caused by convective expansion from carefully matched 1D envelope models and 3D atmospheres.

As already highlighted, these methods are based on pre-calculated 3D atmospheres/envelopes due to the high computational cost of RHD simulations. A major limitation of these patching procedures is that they have limited applicability: They can only be used to analyse a star with parameters exactly matching those of a computed simulation. In order to circumvent this, Jørgensen et al. (2017) established a new method to interpolate between 3D simulations in atmospheric parameters ( $\log g$  and  $T_{\text{eff}}$ ). The scheme is able to reliably reproduce the mean structure of 3D envelopes from the two existing sets of simulations mentioned above: the **STAGGER grid** and the **Trampedach grid**. We also constructed patched models for stars not matching any existing simulation point – including several stars observed by *Kepler*. This work is presented in full length in chapter 6 and provides the background of the main work in chapters 7 and 8.

### 4.3 The Link to Stellar Models II: *Dynamic*

An inherent drawback of the patching methods is that they do not take information from 3D simulations into account *during* the entire evolution. Only at the final model the outer layers are substituted; the evolution prior to this point is calculated using a stellar evolution code using a standard MLT-prescription and analytical boundary condition. As was argued earlier, the 3D atmospheres cannot be directly used in a stellar evolution code for several reasons (however, see section 4.4 below). Hence, the *dynamic approach* tries instead to extract information from the RHD simulations, which can then be applied in stellar evolutionary calculations.

An important part of these methods is the modification of the convective efficiency in the MLT prescription. The principle is to invoke an MLT-based 1D model and to calibrate mixing-length parameter  $a_{\text{MLT}}$  to match the convection in a corresponding RHD atmosphere simulation. Note that such a

calibration will only be valid for models using the exact same flavor of **MLT** (section 1.5.1).

Such calibrations were performed in the early work by Ludwig, Freytag, and Steffen (1999) using 2D hydrodynamical simulations to construct a solar model and validated against quantities inferred from **helioseismology**. Moreover, they performed the calibration for a range of solar-type simulations and derived a fitting formula of the effective  $a_{\text{MLT}}(T_{\text{eff}}, \log g)$  to be included in stellar models.

In the work by Trampedach et al. (2014b), a similar calibration of  $a_{\text{MLT}}$  using the 3D **RHD** simulations from the **Trampedach grid** was performed. Here a fitting formula was not provided, but instead the values of  $a_{\text{MLT}}(T_{\text{eff}}, \log g)$  for all simulations and the possibility to interpolate between them for arbitrary values of the surface parameters. They found similar trends of the mixing length as Ludwig, Freytag, and Steffen (1999) did for the 2D simulations.

Moreover, in order to fully overcome the shortcomings listed above and improve the stellar models, Trampedach et al. (2014a) took another path of including 3D information in stellar evolution. They distilled each simulation into a  $T(\tau)$  relation capable of reproducing the 3D photospheric transition, which can be used as a boundary condition in a stellar model. These derived stratifications can also be interpolated and must be used alongside the calibrated  $a_{\text{MLT}}$  for consistency. Thus, stellar evolutionary sequences can be computed with extracted information from 3D **RHD** atmospheres throughout the track (with surface parameters inside the simulation grid), hence the label “dynamic”. It is also referred to as using “*condensed* 3D simulations” because the information is distilled into carefully selected quantities – this terminology is applied in chapter 5.

How stellar evolution is affected by employing the parametrised results from Trampedach et al. (2014a,b) was initially investigated by Salaris and Cassisi (2015). They used the 3D  $T(\tau)$  relation and  $a_{\text{MLT}}$  separately and found the former to have a larger influence on the resulting tracks. A comparison with other  $T(\tau)$  relations (section 1.6.1) was also presented and good agreement with the semi-empirical relation from Vernazza, Avrett, and Loeser (1981) was found. However, as will be argued in section 5.5, the implementation by Salaris and Cassisi (2015) might not be fully consistent and they did not scale  $a_{\text{MLT}}$  to the Sun as suggested by Ludwig, Freytag, and Steffen (1999) and Trampedach et al. (2014b). Moreover, only the impact on the evolutionary tracks was considered.

Recently, a work I led published details on how to consistently implement the results in a stellar evolution code (Mosumgaard et al., 2018). We also presented an in-depth analysis of the structural and asteroseismic impact. The work is presented in full length in chapter 5. In that chapter, a detailed comparison to the results from Salaris and Cassisi (2015) is also presented.

## 4.4 The Link to Stellar Models III: 3D *On the Fly*

As was described above and shall be seen in the next chapters, the *static* and *dynamic* approaches both have their strengths and weaknesses. The static approach has a large effect on the model stratification, but does not contribute to stellar evolution. On the other hand, the dynamic approach affects the evolutionary tracks, but only has a small structural and asteroseismic impact. In other words, the optimal solution would have the *best of both worlds*.

That was the inspiration to a project jointly lead by Andreas C.S. Jørgensen and myself. Based on our earlier work from Jørgensen et al. (2017), we implemented in **GARSTEC** the use of interpolated 3D atmospheres from the **STAGGER grid**. The project resulted in a pair of papers presenting our novel method to include averaged 3D envelopes on the fly in stellar evolution (Jørgensen et al., 2018; Mosumgaard et al., 2019). The papers are reproduced in full length in chapters 7 and 8 and therefore not elaborated any further here.



## Part II



## *Research Results*



## Condensed 3D Atmospheres in 1D Stellar Models

In the previous chapters, the deficiencies in the outer parts of stellar models and how to mend them have been discussed. In this chapter, the use of *condensed 3D simulations* in 1D stellar evolution models is presented – following what was dubbed the *dynamic approach* in the previous chapter. The work reproduced in this chapter was **originally published in:**

J. R. Mosumgaard, W. H. Ball, V. Silva Aguirre, A. Weiss, and J. Christensen-Dalsgaard (2018). “Stellar models with calibrated convection and temperature stratification from 3D hydrodynamics simulations”. *Monthly Notices of the Royal Astronomical Society* 478, pp. 5650–5659

A preliminary version of the **GARSTEC** implementation was earlier presented in Mosumgaard et al. (2017), but is superseded by this work.

I led the project, made the implementation in **GARSTEC**, performed all of the analyses, and wrote the paper. We also implemented the procedures from Trampedach et al. (2014a,b) into *Modules for Experiments in Stellar Astrophysics (MESA)*, which is an open-source stellar evolution code by Paxton et al. (2011, 2013, 2015, 2018, 2019) – that part of the project was carried out by Warrick Ball.

The presented text has been re-formatted from the journal version to match the format and layout of the thesis, but is otherwise rather close to its original form. However, some minor language corrections have been applied, and the content has been altered (mostly reduced) to include references to material introduced earlier in this thesis, hence removing a lot

of references. The introduction is significantly shortened to avoid overlap with previous chapters, and by the same token most of section 5.2.1 has been removed. A lot of references related to microphysics have been deleted as they are presented in section 1.2.1. Finally, to not break the flow, the original *Appendix A* from the paper moved has been moved to appendix A on page 211, as it only contains technical details on our implementation in MESA. The two remaining appendices from the paper are reproduced in the end of the chapter as section 5.A and section 5.B.

## Summary of the Chapter

Stellar evolution codes play a major role in present-day astrophysics, yet they share common simplifications related to the outer layers of stars. We seek to improve on this by the use of results from realistic and highly detailed 3D hydrodynamics simulations of stellar convection. We implement a temperature stratification extracted directly from the 3D simulations into two stellar evolution codes to replace the simplified atmosphere normally used. Our implementation also contains a non-constant mixing-length parameter, which varies as a function of the stellar surface gravity and temperature – also derived from the 3D simulations. We give a detailed account of our fully consistent implementation and compare to earlier works, and also provide a freely available MESA-module. The evolution of low-mass stars with different masses is investigated, and we present for the first time an asteroseismic analysis of a SSM utilising calibrated convection and temperature stratification from 3D simulations. We show that the inclusion of 3D results has an almost insignificant impact on the evolution and structure of stellar models – the largest effect are changes in effective temperature of order 30 K seen in the PMS and on the RGB. However, this work provides the first step for producing self-consistent evolutionary calculations using fully incorporated 3D atmospheres from interpolation in grids of simulations on the fly.

## 5.1 Introduction

Understanding stellar structure and evolution is one of the key ingredients in astrophysics. One of the primary tools for doing so is comparing numerical calculations of stellar structure with observations and analysing changes in

time using a stellar evolution code. These are 1D numerical models, which have been tested and developed through the years; as a result they are very efficient and highly optimised. However, in several aspects they are also simplified and can be improved.

The first problem addressed is related to the outer boundary conditions of the models, which are required to solve the stellar equations. Traditionally they are established by integration of a simplified  $T(\tau)$  relation, which combined with hydrostatic equilibrium provides the pressure for the outermost point in the model (see section 1.6.1). Secondly we address one of the most fundamental problems in stellar physics: the treatment of stellar convection. The most adopted method for parametrising this process in stellar evolution calculations is the **MLT** formalism (see section 1.5.1) with its main free parameter  $a_{\text{MLT}}$ .

Usually the value of  $a_{\text{MLT}}$  is constrained by the Sun. However, in several recent studies on the detailed modelling of **RG**-stars,  $a_{\text{MLT}}$  has been highlighted as a focus point. For instance Li et al. (2018) reported the need of modifying  $a_{\text{MLT}}$  in the **RGB** by using eclipsing binaries from *Kepler* as calibrators. Tayar et al. (2017) found similar problems based on several thousand **RG**-stars – although this claim has been disputed in the very recent work by Salaris et al. (2018). Hjørringgaard et al. (2017) have reported on discrepancies between constraints from different independent methods when determining the parameters of the very well-studied **RG**-star HD 185351. Moreover, the problem of an unconstrained  $a_{\text{MLT}}$  is not unique to **RG**-stars: White et al. (2017) showed that their parameter determinations using **MESA** changed significantly when  $a_{\text{MLT}}$  was free to vary compared to a fixed solar value.

Another very different approach to superadiabatic convection in the outer layers of stars is to make a full 3D **RHD** simulation. As was argued in section 4.1, these simulations cannot be directly utilised to calculate stellar evolution models but must be carefully processed.

In this work, we seek to remedy some of the issues in stellar evolution models by the use of results from the realistic and highly detailed 3D **RHD** simulations of stellar convection. The ultimate goal is to employ full structures from the 3D simulations on the fly in stellar evolutionary calculations, thus producing the next generation of stellar models.

The chapter is organised as follows. In the next section, a description of the 3D simulations and the data used is given. We present our implementation in some detail in section 5.3 and the impact of using it in evolutionary

and asteroseismic calculations in section 5.4. In section 5.5 we present a discussion, where we also compare our implementation with the previous work by Salaris and Cassisi (2015) and finally a conclusion in section 5.6. In appendix A on page 211 we review the technical details of our MESA-module, which we make freely available.

## 5.2 3D Simulations of Stellar Atmospheres

We have used data from the grid of 37 atmospheric 3D simulations of stellar convection by Trampedach et al. (2013, 2014a,b) – earlier introduces as the **Trampedach grid**. All of the simulations are computed with solar metallicity and the coverage in a **Kiel diagram** is shown in fig. 5.1. It should be noted that the simulations were calculated using a non-standard solar composition based on Anders and Grevesse (1989, AG89); the exact composition is given in Trampedach et al. (2013, table 1) and is actually very close to Grevesse and Noels (1993, GN93).

### 5.2.1 Patched Models

The most common synergy between 3D convection simulations and typical stellar evolution models are the so-called *patched models*, in which the surface layers are peeled of a stellar structure model and replaced with data from a 3D simulation averaged over time and the horizontal directions. These were described in section 4.2, and here it was also argued that it is not possible to do time evolution with the patched models as they are purely static, and only sample discrete points in the **HRD**. Stellar evolution is the main focus of the dynamic implementation we present in the following, which is based on the principles developed by Trampedach et al. (2014a,b), as described in section 4.3.

### 5.2.2 Condensed Simulations

Firstly, 1D envelope models were used to calibrate the mixing-length parameter,  $a_{\text{MLT}}$ , for each simulation. The basic principle behind the calibration is similar to the patching procedure, but using envelope models instead of full structure models – and of course varying  $a_{\text{MLT}}$  as a part of the process. The

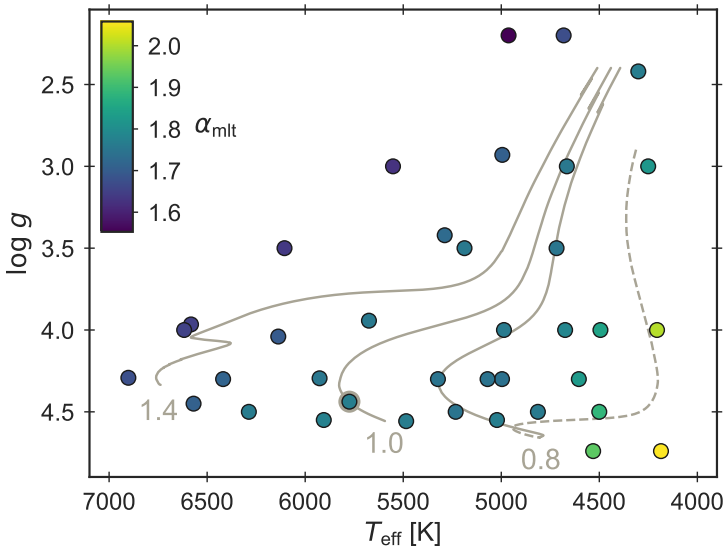


**Figure 5.1** | A Kiel diagram showing the **Trampedach grid** of 3D simulations. Simulation points coloured to show the corresponding value of the calibrated mixing-length parameter  $\alpha_{\text{MLT}}$  from Trampedach et al. (2014b). Evolutionary tracks from **GARSTEC** for stars of different masses (in units of the mass of the Sun) are shown for reference – the **PMS** of one of the tracks is shown with dashes.

authors went to great length to ensure compatible (micro)physics between their 1D and 3D models. The exact procedure is described by Trampedach et al. (2014b) and the resulting values are visualised in fig. 5.1. Stellar evolution tracks of different masses are also shown in the figure to display the coverage of the grid. A similar work was done using 2D simulations by Ludwig, Freytag, and Steffen (1999), who found similar trends with stellar parameters.

Secondly, the authors devised a way of distilling the averaged temperature stratification from the full 3D simulations. They have taken great care in the treatment of convective effects and enforcing radiative equilibrium; a detailed description is given by Trampedach et al. (2014a). The output is given as a function of the Rosseland mean optical depth  $\tau$  in the form of a *generalised* Hopf function  $q(\tau)$ , as defined in eq. (1.37) on page 26. It is important to note that these extracted  $T(\tau)$  relations were also used

in Trampedach et al. (2014b) to perform the  $a_{\text{MLT}}$ -calibration mentioned above in order to ensure maximum consistency.

The  $q(\tau)$  and calibrated  $a_{\text{MLT}}$  provided by Trampedach et al. (2014a,b) are stored for all simulations as a function of  $T_{\text{eff}}$  and  $\log g$ . The main advantage of the described approach is that the extracted quantities behave smoothly with varying  $T_{\text{eff}}$  and  $\log g$ , making it feasible to directly interpolate between the simulations. Thus, it is possible to include the 3D effects during the evolution of stars within the full range of the grid of simulations.

### 5.3 Implementation

We have consistently implemented the use of information from 3D atmospheric simulations from Trampedach et al. (2014a,b) into **GARSTEC** and **MESA**. The basic principle of our implementation is that in each iteration of the stellar evolution code, the current  $T_{\text{eff}}$  and  $\log g$  of the model are used to obtain corresponding information from the 3D simulations. More specifically, as a function of  $T_{\text{eff}}$  and  $\log g$ , we extract from a table the  $a_{\text{MLT}}$  and corresponding  $q(\tau)$ , which can be transformed to a  $T(\tau)$  relation. To interpolate in the irregular grid of simulations, we use the routine supplied by Trampedach et al. (2014a,b), which is based on linear interpolation between the nodes in a Thiessen triangulation (Cline and Renka, 1984).

#### 5.3.1 The Mixing-Length Parameter

The first change to the stellar structure model involves the mixing-length parameter, which is vital for the treatment of convection. Instead of a constant value we use the variable 3D-calibrated  $a_{\text{MLT}}(T_{\text{eff}}, \log g)$  throughout the model.

We are not taking the value directly as provided by the interpolation in the table, but introduce a scaling factor as recommended by Ludwig, Freytag, and Steffen (1999) and Trampedach et al. (2014b). The actual  $a_{\text{MLT}}$  used in the code is given by

$$a_{\text{MLT}}(T_{\text{eff}}, \log g) = K_{\text{MLT}} \cdot a_{\text{MLT, grid}}(T_{\text{eff}}, \log g) , \quad (5.1)$$

where  $K_{\text{MLT}}$  is the scaling factor and  $a_{\text{MLT, grid}}$  is the value returned from the interpolation routine.

The scaling factor must be determined from a solar calibration with the 3D  $T(\tau)$  relation and variable mixing-length parameter activated. This scaling ensures that the solar model is calibrated to the correct radius with the variable  $\alpha_{\text{MLT}}$ .

### 5.3.2 The $T(\tau)$ Relation

The other aspect of our implementation is related to the use of a realistic  $T(\tau)$  relation derived from the 3D RHD simulations. As mentioned above, the interpolation routine supplies as a function of optical depth the current stratification in the form of the generalised Hopf function,  $q(\tau)$ , which is updated in each iteration.

The changes made in **GARSTEC** and **MESA** are nearly identical. We provide a detailed account of the **GARSTEC** implementation and at the end highlight how the modifications in the two codes differ. We will split the description in two, one for each part of a **GARSTEC** structure model: atmosphere and interior.



The *atmospheric part* of the model is used to provide the outer boundary conditions for the equations of stellar structure and evolution (see section 1.6.1). In the standard setting, the code uses an Eddington grey atmosphere, which is anchored to the interior model at an optical depth of  $\tau = 2/3$ .

In our implementations, we have altered the atmospheric module to obtain the temperature stratification from the generalised Hopf function  $q(\tau)$  extracted from the 3D simulations. The new temperature structure at a given optical depth can be obtained from eq. (1.37) on page 26 as

$$T_{\text{hopf}} := T(\tau) = \left(\frac{3}{4}\right)^{1/4} (q(\tau) + \tau)^{1/4} T_{\text{eff}} , \quad (5.2)$$

under the assumption of radiative equilibrium (the  $T_{\text{hopf}}$  notation is for consistency with fig. 5.2).

In **GARSTEC**, the stratification is integrated inwards from  $\tau_{\text{surf}} = 10^{-4}$  to obtain the pressure at the bottom of the atmosphere. This point is the fitting point or transition point to the interior model, which is defined to have the temperature  $T = T_{\text{eff}}$  and commonly referred to as the photosphere. As opposed to the Eddington grey case, the 3D  $T(\tau)$  relation from the generalised

Hopf function is not anchored at  $\tau_{\text{fit}} = 2/3$ , or any other constant value of  $\tau$ . Instead, we require that the temperature of the outermost point in the interior model matches that of the bottom point in the atmosphere. Thus the fitting point  $\tau_{\text{fit}} = \tau_{\text{eff}}$  is defined at the value of  $\tau$  where  $T = T_{\text{eff}}$ , or

$$q(\tau_{\text{eff}}) + \tau_{\text{eff}} = 4/3 . \quad (5.3)$$

This value is not constant, which means that in each iteration of the code before the actual integration, the point  $\tau_{\text{eff}}$  is determined from the current 3D  $T(\tau)$  relation with interpolation. Usually  $\tau_{\text{eff}} \simeq 0.5$  is obtained.

It is very important to choose the correct optical depth of the photosphere of the stellar structure model, otherwise  $T_{\text{eff}}$  and  $\log g$  of the model will not actually correspond to the output from the 3D interpolation. In other words, selecting a constant optical depth (e.g.  $\tau = 2/3$ ) for the photosphere of the model – hence defining  $T_{\text{eff}}$  at this point – will clearly lead to small inconsistencies if used with a  $T(\tau)$  relation where  $T_{\text{eff}}$  corresponds to a different optical depth.



Besides the above-mentioned change to a variable mixing-length parameter, our implementation directly modifies the *interior part* of the model as well.

As explained,  $q(\tau)$  is extracted from the 3D simulations under the assumption of radiative equilibrium, which is also assumed when applying eq. (5.2) to obtain the temperature stratification. Nonetheless, we want to properly take convection into account below  $\tau_{\text{eff}}$  to recover the correct stratification from the 3D simulations. According to Trampedach et al. (2014a, eq. 35) the radiative temperature gradient therefore needs to be altered. The corrected gradient is calculated as

$$\nabla_{\text{rad}} = \tilde{\nabla}_{\text{rad}} \cdot [1 + q'(\tau)] , \quad (5.4)$$

where  $\tilde{\nabla}_{\text{rad}}$  is the usual expression for the radiative gradient based on the diffusion approximation (eq. (1.22) on page 18) and  $q'(\tau)$  is the derivative of the Hopf function with respect to  $\tau$ . In **GARSTEC**, this is determined directly from an Akima spline interpolation (Akima, 1970, 1991) of  $q(\tau)$  on a fine mesh – we use this method because the derivative  $q'(\tau)$  is changing rapidly in the region around  $\tau = \tau_{\text{eff}} \simeq 0.5$  (as can be seen in the appendix fig. 5.9 on page 92).

The radiative gradient is corrected before performing the actual **MLT** calculation. Hence, the modified  $\nabla_{\text{rad}}$  is used as input instead of the usual  $\tilde{\nabla}_{\text{rad}}$ , such that the resulting temperature gradient  $\nabla$  is properly corrected for 3D effects and does not need to be modified further.

The altered radiative gradient is used until an optical depth of  $\tau = 10$  is reached, since the correction factor goes to 0;  $q'(\tau)$  is always below  $10^{-4}$  and usually below  $10^{-5}$  from this point inwards. Our implementation is fully flexible with respect to this lower point and the effect of changing it to a higher value (the table extends down to  $\tau = 100$ ) is completely negligible as the corrections in this region are minute.

A full schematic overview and summary of how our implementation changes a stellar model (both atmospheric and interior part) can be seen in fig. 5.2.



The **MESA** implementation incorporates the stellar atmosphere as part of the interior model by placing the outermost meshpoint at an optical depth  $\tau_{\text{surf}} = 2 \times 10^{-4} \tau_{\text{eff}} \simeq 10^{-4}$ . However, all photospheric quantities are determined at  $\tau_{\text{eff}}$  by interpolation. The correct temperature stratification for the 3D  $T(\tau)$  relation is obtained by the same method that **GARSTEC** uses in the interior below the photosphere. The only distinction is the interpolation in  $\tau$ , which is performed using the one-dimensional monotone cubic piecewise interpolation routines distributed with **MESA** (Huynh, 1993; Suresh and Huynh, 1997). The radiative gradient is modified using the so-called “porosity factor” (see appendix A on page 211).

The new outermost meshpoint requires a new boundary conditions, which we choose to be equivalent to an Eddington grey atmosphere evaluated at the optical depth of the point (details given in the appendix). In effect, these are the same as the boundary conditions **MESA** uses when integrating an atmosphere down to the photosphere.

## 5.4 Stellar Evolution with 3D Results

We have taken much care to adopt as similar as possible microphysics in the stellar evolution code as in the 3D simulations in order to produce a consistent model. The envelope models utilised by Trampedach et al. (2014b) to perform the 3D  $a_{\text{MLT}}$ -calibration were calculated with the **MLT**-treatment

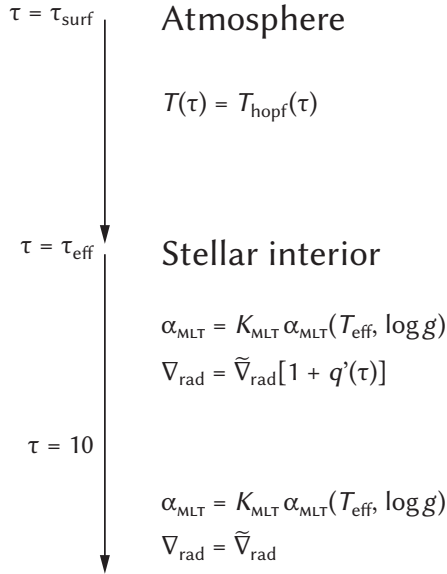


**Figure 5.2 | The implemented changes to a stellar structure model.** Shown for the **GARSTEC** implementation. In the radiative atmosphere, a different temperature stratification given by eq. (5.2) is used and the transition point is altered. In the outer convective parts of the interior model, the radiative gradient is modified according to eq. (5.4). Everywhere in the interior of the star, the calibrated mixing length from eq. (5.1) is used. In **MESA**, the *stellar interior* extends all the way to  $\tau_{\text{surf}}$ , but the photospheric quantities are correctly determined at  $\tau = \tau_{\text{eff}}$ .

from Böhm-Vitense (1958). To include the calibrated  $\alpha_{\text{MLT}}$  values, we also use a standard of convection in our stellar evolution calculations. Strictly speaking, the  $\alpha_{\text{MLT}}$  calibration is only valid for precisely the same **MLT**-implementation. But it is important to note, that even different **MLT**-flavors will yield the same temperature evolution, if  $\alpha_{\text{MLT}}$  is properly calibrated to the Sun (Gough and Weiss, 1976; Pedersen, Vandenberg, and Irwin, 1990; Salaris and Cassisi, 2008). In **MESA** the formulation from Cox and Giuli (1968) is employed, while **GARSTEC** relies on the prescription from Kippenhahn, Weigert, and Weiss (2012).

As mentioned earlier, the 3D simulations use a non-standard solar mixture. This mixture will be used in **GARSTEC**, while we for the **MESA** models settle for the almost identical **GN93**. The atmospheric simulations use the

MHD-EOS, which we have readily available in **GARSTEC**, but not in **MESA**. To span the temperature range necessary for a full structure model, we complement the MHD-EOS with the OPAL EOS in **GARSTEC**. In **MESA** we only use OPAL.

Trampedach et al. (2014a) calculated their own low-temperature opacities for the 3D simulations. In the envelope model used for the  $\alpha_{\text{MLT}}$ -calibration, these were merged with interior opacities from OP. We have used the available OP data to calculate opacity tables for the quite specific mixture used in the 3D simulations and merged them with the atmospheric opacities from Trampedach et al. (2014a) provided by R. Trampedach (private communication). These custom opacities are used in **GARSTEC**. In **MESA**, we instead combine the low-temperature Trampedach-opacities with tables from the OPAL group.

#### 5.4.1 Solar Calibration

The first step is to calculate a **SSM** using our new implementation. This is done by performing a solar calibration, which determines the initial chemical composition and the  $\alpha_{\text{MLT}}$  scaling factor from eq. (5.1). Microscopic diffusion is included in all of our models, as it is required to perform the procedure.

A solar calibration with the 3D results activated yields a scaling factor of  $K_{\text{MLT}} = 1.024$  for **GARSTEC** and  $K_{\text{MLT}} = 1.034$  for **MESA**. The value of  $\alpha_{\text{MLT}}$  for the solar simulation in the grid of 3D simulations is  $\alpha_{\text{MLT, grid}, \odot} = 1.764$ ; thus, the corresponding values are  $\alpha_{\text{MLT}, \odot} = 1.807$  for **GARSTEC** and  $\alpha_{\text{MLT}, \odot} = 1.828$  for **MESA**.

In the following we will compare the models with our new 3D implementation to *standard reference* models, i.e., evolution with a constant solar-calibrated  $\alpha_{\text{MLT}}$  and Eddington grey atmosphere, but otherwise using the same microphysics. When performing these standard Eddington solar calibrations we obtain virtually the same initial abundances as with our 3D implementations. For reference, we get  $\alpha_{\text{MLT}, \odot} = 1.702$  for **GARSTEC** and  $\alpha_{\text{MLT}, \odot} = 1.672$  for **MESA**, which is already a clear indication that the outermost structure has changed compared to the 3D case.

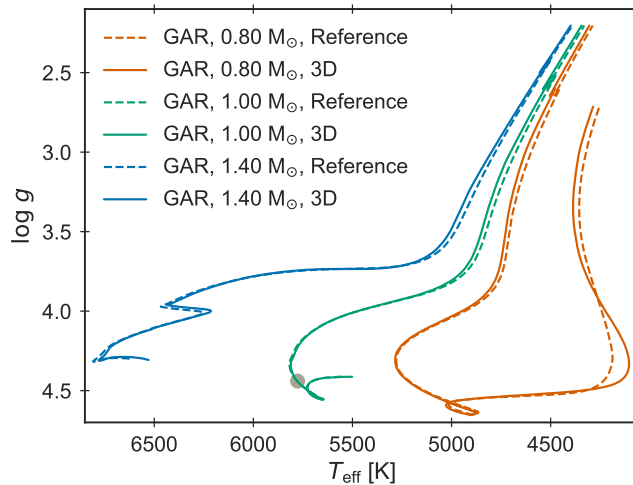


**Figure 5.3 | Stellar evolutionary tracks from GARSTEC.** The *reference*-tracks are computed using a constant solar calibrated  $\alpha_{\text{MLT}}$  and an Eddington atmosphere. The *3D*-tracks use our implementation of variable  $\alpha_{\text{MLT}}$  and a  $T(\tau)$  relation from 3D simulations. To not clutter the plot, the full **PMS** phase is only shown for the  $0.80 M_{\odot}$  track. The present-day Sun is marked in grey.

#### 5.4.2 Evolution

After the solar calibration, the first natural test of our new implementation is to calculate evolutionary tracks and compare to reference tracks. This is shown in figs. 5.3 and 5.4.

From the plots it is clear that the **MS** of the  $1.00 M_{\odot}$  evolution is nearly identical for the two tracks. This is just as expected, as the solar calibration ensures that both of them go through the same point at the Sun’s age (highlighted in grey in the figure). The **turn-off** is almost identical as well, with a temperature difference of less than 7 K. The same is the case for the **turn-off** of the  $0.80 M_{\odot}$  track, where the tracks differ by 5 K. For the  $1.40 M_{\odot}$  evolution, the tracks are separated by 35 K at the leftmost point in the hook.

The two sets of tracks are more clearly distinguished from each other on the **PMS** and on the **RGB**, where the superadiabatic convection is more extended. For the **GARSTEC** tracks, the temperature difference in the **RGB** at  $\log g = 3.2$  between *3D* and *reference* is 25 K for the  $0.80 M_{\odot}$  track, 28 K

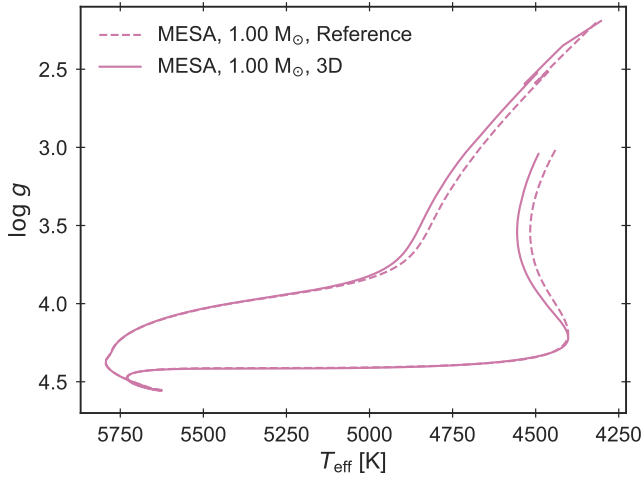


**Figure 5.4 | Stellar evolutionary tracks from MESA.** As fig. 5.3, but showing only the  $1.00 M_{\odot}$  track including the PMS phase. The extrapolation on the RGB is treated differently (details in the text).

for  $1.00 M_{\odot}$ , and 29 K for  $1.40 M_{\odot}$ . At the RGB-bump, the difference is unchanged in the case of  $0.80 M_{\odot}$ , roughly halved for  $1.00 M_{\odot}$ , and reduced to 11 K for the  $1.40 M_{\odot}$  track. The RGB-bump for the  $1.00 M_{\odot}$  MESA tracks differs by 32 K.

As expected, the evolutionary pace of the models is also almost unchanged by our new implementation. At the exhaustion of hydrogen in the core (CHE, defined as a central hydrogen content of less than  $10^{-5}$ ), the age difference between the two sets of tracks is less than 0.1 % for all of the masses. The maximum age difference for the  $1.00 M_{\odot}$  evolution is obtained if we instead define the turn-off in a more observational sense – where  $T_{\text{eff}}$  reaches its highest value – which yields a change in age of around 2 percent (or 150 Myr).

From the work by Salaris and Cassisi (2015), the  $T(\tau)$  relation is expected to play the largest role in the temperature change (see also section 5.5). We find that the variable  $\alpha_{\text{MLT}}$  plays an important role as well, especially on the RGB. A fixed  $\alpha_{\text{MLT}}$  makes the two tracks move up the RGB in parallel, i.e., with a constant separation. However, with the 3D implementation, the variations in  $\alpha_{\text{MLT}}$  as the star evolves will give rise to changes in the

slope of the ascent. This is visible from the varying temperature differences along the **RGB** evolution.

One clear *limitation of the method* is the coverage of the grid, and therefore the treatment of the borders is important. If the 3D-implementation is fully switched off when the star leaves the valid grid range, the track will suddenly experience a jump in  $\alpha_{\text{MLT}}$  as well as a different outer boundary condition, and immediately changes temperature accordingly. To avoid this, we rely on extrapolation just outside the boundaries of the grid, which is especially important in the fully convective **PMS** phase where the lower mass tracks will leave the grid very briefly. We have tested this near the boundaries at high  $\log g$  for both the hot and cold edge using stars with higher/lower mass than the 0.80-1.40  $M_{\odot}$  range, and the transition is confirmed to occur smoothly.

On the **RGB**, extrapolation is required to continue the evolution towards lower  $\log g$  and the situation is a bit more complicated. From the top right corner of fig. 5.4 it can be seen that the 3D-track suddenly cools and crosses the reference track. What is happening is that the track leaves the grid resulting in a fast drop in the value of  $\alpha_{\text{MLT}}$ , which effectively makes the track change to a different adiabat and continue its ascent. Clearly, simple extrapolation from the triangulation does not work properly in this region. What is done instead in **GARSTEC** is to use the last valid values from the grid, i.e. keeping  $\alpha_{\text{MLT}}$  and the  $T(\tau)$  relation fixed during **RGB** evolution. This produces a smooth evolution as can be seen from fig. 5.3, but is not to be trusted going high up the **RGB**.

### 5.4.3 Model Structure

We now compare the structure of the calibrated solar models with the 3D  $\alpha_{\text{MLT}}$  and  $T(\tau)$  relation, to the reference **SSMS** with an Eddington  $T(\tau)$  relation and constant solar calibrated  $\alpha_{\text{MLT}}$ . As the implementation only affects the layers above and just below the photosphere, this is where we mainly expect to see changes in the models.

In fig. 5.5, the temperature structure in the form of  $T(\tau)$  is displayed for the solar models with 3D effects activated from both **MESA** and **GARSTEC**. They are compared to the  $T(\tau)$  relation from the solar entry in the table from Trampedach et al. (2014a,b). The transition point at  $\log \tau \simeq -0.3$  (corresponding to  $\tau \simeq 0.5$ ) is marked for clarity. For reference, also displayed on

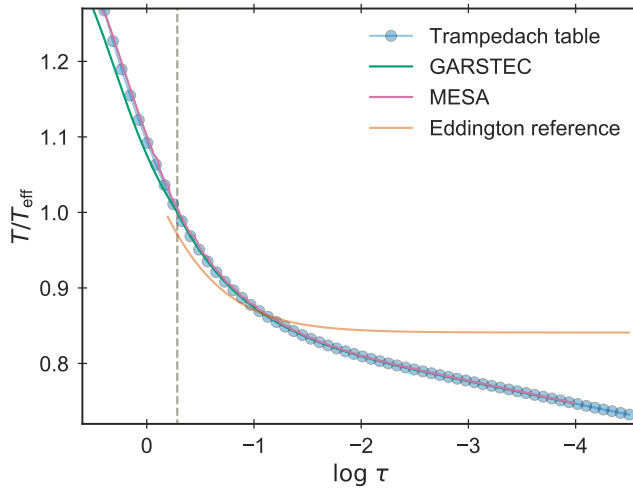


**Figure 5.5 | Temperature as a function of optical depth in the outermost parts of the solar models.** The grey dashed line marks the photosphere of the stellar structure models to which the temperature is normalised. The curve *Trampedach table* shows the 3D  $T(\tau)$  relation of the solar simulation from the table. The result using an Eddington grey  $T(\tau)$  relation is added for reference.

the figure is the Eddington grey  $T(\tau)$  relation, which is anchored at  $\tau = 2/3$  and therefore differs at the marked photosphere. The figure clearly shows that both models trace the 3D  $T(\tau)$  relation used in the calculation closely in the atmosphere.

We show the temperature stratification as  $T(r)$  for the same solar models in fig. 5.6. In this figure, they are compared to the actual structure extracted directly from the 3D simulation of the Sun (provided by R. Trampedach, private communication). Note, that this implies that the reference curves in fig. 5.5 and fig. 5.6 are different: The former is from the table of extracted results, the latter directly from the averaged 3D simulation. This also explains the different sampling of the reference curves in the two figures. It is evident that the models very accurately reproduce the underlying  $\langle 3D \rangle$  simulation. Thus, the stellar models are able to recover the actual temperature stratification from the atmosphere simulation. Below the photosphere the models naturally deviate as convection starts to influence the structure, which is also the case in fig. 5.5.

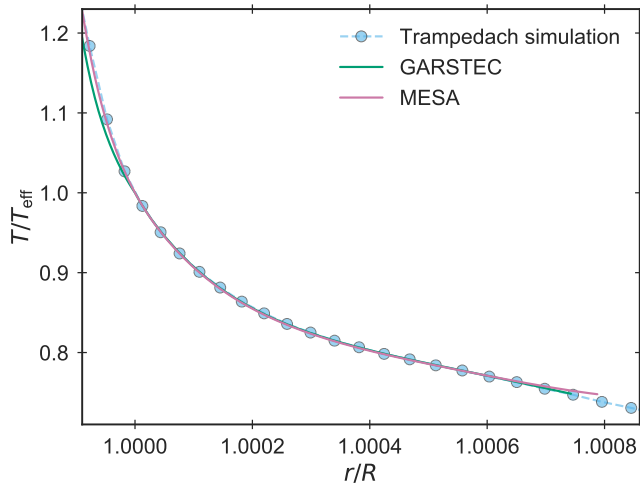


**Figure 5.6 | Temperature as a function of radius.** As fig. 5.5, but normalised radius (and slightly different scale). The *Trampedach simulation* is the temperature stratification from the averaged 3D simulation of the Sun.

Turning to the *interior of the stellar models*, we see that the implementation of the 3D results has an insignificant impact on the structure. In general the models are indistinguishable – e.g. with respect to the hydrogen profile. Specifically, the depth of the outer convection zone is left virtually unchanged; the relative difference between 3D and reference is below 0.01 % for both **MESA** and **GARSTEC**.

**Asteroseismology** and **helioseismology** are excellent tools for probing the interior of stars by observing the imprint of the stellar oscillations in the emitted light (see chapter 2).

In the present case, we can compare the structure of the calibrated solar models with the observed frequencies from the Sun. We have calculated theoretical oscillation frequencies for our solar models using **ADIPLS**, and as observations we use solar data from **BISON**. The comparison is shown in fig. 5.7 as a difference between the two set of oscillation frequencies for the **MESA** solar models.

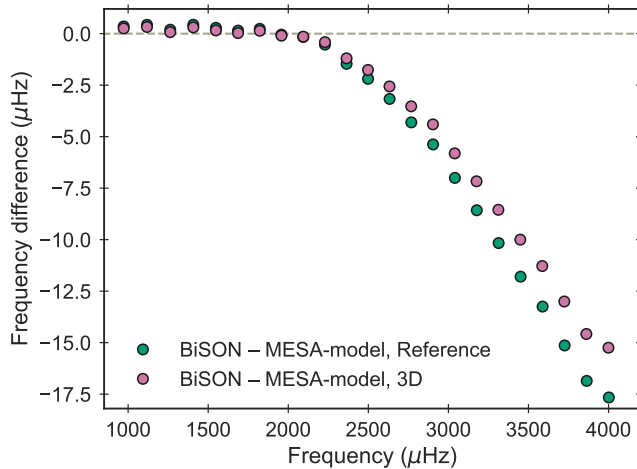


**Figure 5.7 | Difference between observed and calculated oscillation frequencies of the Sun.** The observations are from **BiSON** and the model frequencies are from the **MESA** solar models with and without our modifications.

The general deviation, which increases for higher frequencies, is well-known and expected: it is the asteroseismic **surface effect** (section 2.4), consequence of the near-surface deficiencies in stellar models. Oscillations of higher and higher frequency probe regions closer and closer to the surface; thus, it is evident from the figure that the two models differ in the surface layers. This is just as anticipated, as the implementation changes the outer boundary condition and the correction from eq. (5.4) is only significant just below the photosphere. Hence, the inclusion of the 3D effects shifts the oscillation frequencies, which is a known effect of changing the atmospheric structure (e.g. Morel et al., 1994). The frequencies are decreased, thus seemingly bringing the model closer to the observations, but the impact is rather modest.

The **surface effect** can be further improved on by fully replacing the outer layers of the model with an averaged 3D simulation in a so-called patched model (see section 4.2). However, this is (currently) only performed as a final step after the stellar evolution calculation; it is *currently* not possible to perform the procedure along the way during the evolution (but see chapters 7 and 8). Furthermore, a full treatment of the **surface effect** would additionally involve the inclusion of the *modal* effects, i.e. the

effects of nonadiabaticity and the full interaction between convection and pulsations (e.g. Houdek et al., 2017). This as is also evident from the results of patched models shown in chapter 6 and by e.g. Rosenthal et al. (1999), Sonoi et al. (2015), and Ball et al. (2016).

## 5.5 Comparison to Earlier Works

As was mentioned in section 4.3, an analysis similar to the one we present in this paper was carried out by Salaris and Cassisi (2015, hereafter SC15) using the **BASTI** stellar evolution code. They implemented the same 3D results, namely the calibrated  $a_{\text{MLT}}$  and  $T(\tau)$  relations from Trampedach et al. (2014a,b). However, the description of their implementation is brief and differs from ours in a few ways.

One central topic is the transition point between atmosphere and stellar interior, and the location of the photosphere in the model. SC15 used a constant  $\tau_{\text{fit}} = 2/3$  as transition point (and mention that they have tested various other values down to  $\tau_{\text{fit}} = 100$ ). The crucial matter is not the exact value, but whether this transition point has been used as the photosphere in the stellar model or not. The optical depth  $\tau_{\text{eff}}$  in the 3D  $T(\tau)$  relation at which  $T = T_{\text{eff}}$  varies, but is always close to  $\tau_{\text{eff}} \simeq 0.5$ . As argued earlier in section 5.3.2, it will produce a slightly inconsistent model, if the global *photospheric quantities* like  $T_{\text{eff}}$  and  $\log g$ , are still determined at the usual  $\tau_{\text{fit}} = 2/3$  or another  $\tau_{\text{fit}} \neq \tau_{\text{eff}}$ ; especially if these quantities are passed to the 3D interpolation routine. We have taken great care in this respect, either by making sure the transition happens at the correct  $\tau_{\text{fit}} = \tau_{\text{eff}}$  each time (**GARSTEC**) or by properly determining the global quantities at this point (**MESA**).

SC15 mention the use of Trampedach et al. (2014a, eqs. (35) and (36)) to correct the temperature gradients. First of all, as explained earlier, it is only necessary to apply a correction to the radiative temperature gradient  $\nabla_{\text{rad}}$  (by using eq. 35 from Trampedach et al., 2014a)); the **MLT** calculation with this modified gradient as input will ensure a properly corrected  $\nabla$  without further modifications (R. Trampedach, private communication). Secondly, SC15 find the corrections to be minuscule, as they state a difference between the two sets of temperature gradients of “much less than 1 %”. We agree for higher values of  $\tau$ , but just below the photosphere the correction term in

eq. (5.4) is significant – e.g. for the solar models, the temperature gradient is changed by around 20 % at  $\tau \simeq 1$ . A plot of the correction is shown in section 5.B.

As argued earlier – and also by Ludwig, Freytag, and Steffen (1999) and Trampedach et al. (2014b) – it is appropriate to introduce a calibrated scaling factor instead of using  $\alpha_{\text{MLT}}$  directly as supplied from the grid. SC15 mention such a scaling as required to produce a SSM, but did not employ this  $\alpha_{\text{MLT}}$  scaling factor in their stellar evolution calculations.

### 5.5.1 Results

A general difference between our work and SC15 is the focus of the investigation. SC15 did calculate models utilising both the 3D  $\alpha_{\text{MLT}}$  and  $T(\tau)$  relation, but also analysed them separately in order to isolate the impact of the 3D  $\alpha_{\text{MLT}}$  and  $T(\tau)$  relation, respectively. We choose to follow the advice of the original work by Trampedach et al. (2014b), who stress the importance of *always* employing the extracted results together (as well as using them alongside the corresponding atmospheric opacities).

For their comparison tracks (with different  $T(\tau)$  relations), SC15 used the  $\alpha_{\text{MLT},\odot}$  from the 3D RHD solar simulation directly, instead of a traditional solar calibrated value. We have chosen to make solar calibrations for both the 3D and reference Eddington case separately, in order to show the difference between using the 3D results and what “modellers usually do”. Thus, a direct comparison of our results to SC15 is not possible. For example, in SC15 the Eddington tracks are generally hotter than the 3D ones while we see the opposite behaviour. Looking at figure 3 in SC15, this is an effect of the choice to not individually calibrate the reference tracks to the Sun in SC15; the MS evolution of the  $1.00 M_{\odot}$  Eddington track is significantly hotter than the 3D counterpart, where our tracks basically coincide. If we perform evolutionary calculations with similar assumptions – i.e. disable scaling of  $\alpha_{\text{MLT}}$  for the 3D case, and for the reference case directly use the  $\alpha_{\text{MLT},\odot}$  from the grid instead of a solar-calibrated value – we obtain results which are very similar to SC15 (see section 5.A).

SC15 briefly analyse the impact on the SSM and state that they “find it necessary to rescale the RHD  $\alpha_{\text{MLT}}$  calibration by a factor of just 1.034 to reproduce the solar radius”. This is exactly the same we find for the MESA 3D solar calibration and very close to our GARSTEC value. However, this

scaling factor was not used to calculate their evolutionary tracks. They do not dig deeper into the interior structure of the **SSM**, so we are unable to compare our asteroseismic analysis to their work.

## 5.6 Conclusions

We have consistently implemented results extracted from 3D **RHD** simulations of stellar convection in the stellar evolution codes **GARSTEC** and **MESA**. The new implementation consists of a temperature stratification in the form of  $T(\tau)$  relations and corresponding corrected temperature gradients, and a calibrated, variable mixing-length parameter  $a_{\text{MLT}}(T_{\text{eff}}, \log g)$ . We have presented a very detailed account of our implementations, and compared to the earlier implementation of the same 3D results in a stellar evolution code by Salaris and Cassisi (2015). Moreover we make our **MESA** implementation freely available (see appendix A on page 211).

We calculate the evolution of different low-mass stars after a solar calibration. We compare to a set of reference models which uses an Eddington grey atmosphere and constant solar-calibrated  $a_{\text{MLT}}$ . In the **PMS** and in the **RGB** we see the largest effect of the 3D implementation on the temperature evolution. Regarding the evolutionary speed, we see no significant change in the age of the models at **CHE**.

Furthermore, we compare the model structures of the calibrated solar models and see no significant changes. For the first time we present an helioseismic analysis of a **SSM** with a  $T(\tau)$  relation and variable  $a_{\text{MLT}}$  extracted from 3D simulations. The use of the 3D effects makes a small, positive impact on the asteroseismic **surface effect**.

We note that the method is limited by the coverage in parameter space of the grid of 3D simulations. To make this method widely applicable, an extended coverage in terms of  $\log g$  and  $T_{\text{eff}}$  is required, but more importantly: simulations of varying metallicity. One option in this respect would be to extract similar information from the **STAGGER grid**.

The future aim is to exploit the concept of patched models – which provide a more realistic structure but is static – with the current dynamic approach, to allow for the evolution of more realistic models. Our implementation is one step further along that path and another is the work by

Jørgensen et al. (2017) (see chapter 6). The ultimate goal is to facilitate on-the-fly patching of 3D simulations as outer boundary conditions for stellar evolution calculations (see chapters 7 and 8).

## 5.A Models with SC15 Settings

Here we present models calculated with **GARSTEC** utilising similar settings as those used by SC15 (i.e., Salaris and Cassisi, 2015). The 3D case is calculated without scaling of  $\alpha_{\text{MLT}}$  by adopting the values directly from the grid. The reference Eddington tracks do not rely on a solar calibrated  $\alpha_{\text{MLT}}$ , but rather the value  $\alpha_{\text{MLT},\odot}$  directly from the solar 3D simulation. Moreover, the tracks are calculated with the GN93 composition and without diffusion. The resulting tracks for the  $1 M_{\odot}$  star can be seen in fig. 5.8 on the following page, which is very similar to the corresponding track in figure 3 of SC15. The figure can also be compared to our tracks shown in fig. 5.3 and especially fig. 5.4 on page 83.

## 5.B Correction of the Gradients

In this appendix we highlight the impact of the correction factor in eq. (5.4) on page 78 on the temperature gradients. The result from the **MESA** solar model as well as  $1 + q'(\tau)$  derived directly from the Trampedach data table is shown in fig. 5.9 in the region near the photosphere. It is clear that the changes are significant around the photosphere and quickly decrease going into the star – and that the model accurately reproduce the table.

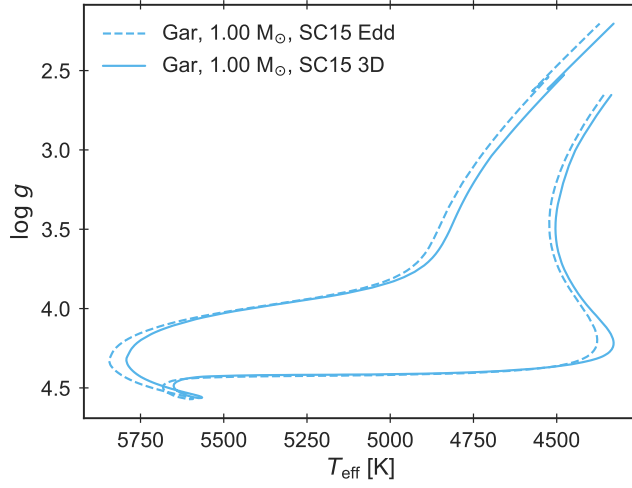


**Figure 5.8 | Stellar evolution with sc15 settings.** Reproduction of the tracks using GARSTEC with identical settings (see text for details).

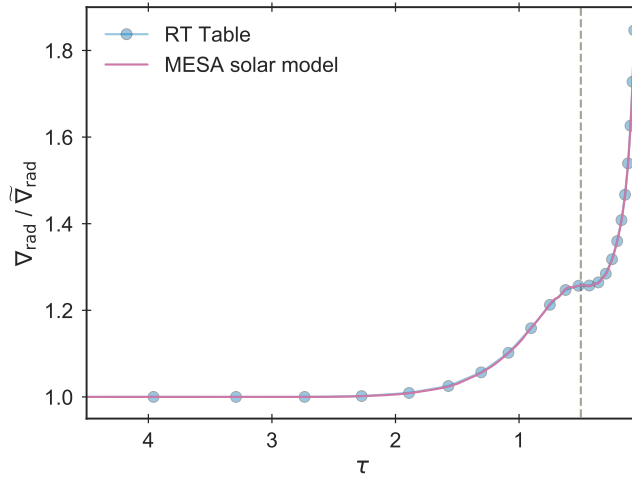


**Figure 5.9 | Magnitude of the gradient correction term.** The term from eq. (5-4) is extracted from the MESA solar model and derived directly from the table of 3D results. The grey dashed line marks the photosphere at  $\tau_{\text{eff}} \approx 0.5$ .

# 6

## Patching with Interpolated 3D Atmospheres

In this chapter, the *static approach* of improving the outer convective parts of stellar models is presented. This work makes use of patched models and a new scheme is implemented to interpolate in a grid of 3D simulations. Contrary to earlier works, this allows a star with any atmospheric parameters (inside the grid) to be modelled this way. Moreover, the principles behind the interpolation procedure are the foundation of the work presented in chapters 7 and 8. The work reproduced in this chapter was **originally published in:**

A. C. S. Jørgensen, A. Weiss, J. R. Mosumgaard, V. Silva Aguirre, and C. L. Sahlholdt (2017). “Theoretical oscillation frequencies for solar-type dwarfs from stellar models with <3D>-atmospheres”. *Monthly Notices of the Royal Astronomical Society* 472.3, pp. 3264–3276

Andreas C.S. Jørgensen developed the original idea and method and wrote the code for the patching and interpolation routines. I participated in detailed discussions as well as in performing and devising tests. I also provided the models for section 6.5 and performed all of the fitting with **BASTA**. Andreas C.S. Jørgensen wrote the paper, but the current version is a product of many iterations, where I was closely involved.

As opposed to the previous chapter (and the next chapters as well), the text presented here is quite heavily modified from its original form. All of the figures (but not captions) and results are left unaltered, but the text itself

has undergone an extensive revision. Many parts have been rewritten to improve readability and to match the presentation style of the rest of the thesis. Moreover, some sections have been restructured and others almost or completely removed.

Finally, just a remark on notation. The following abbreviations will be used: *patched model* (PM) and *un-patched model* (UPM). Especially the former might cause confusion, as it would be PMs in plural, which is hard to distinguish from PMS meaning *pre-main sequence*. To avoid this potential mix-up, *patched models* will instead be denoted as PM's – and likewise UPM's for consistency.

## Summary of the Chapter

We present a new method for replacing the outermost layers of stellar models with interpolated atmospheres based on results from 3D simulations in order to correct for structural inadequacies of these layers. This replacement is known as patching. Tests are performed based on 3D atmospheres from three different codes and interior models with different input physics. Using solar models, we investigate how different patching criteria affect the eigenfrequencies. These criteria include the depth at which the replacement is performed, the quantity on which the replacement is based, and the mismatch in  $T_{\text{eff}}$  and  $\log g$  between the UPM and patched 3D atmosphere. We find the eigenfrequencies to be unaltered by the patching depth, while changing the patching quantity or the employed atmosphere grid leads to frequency shifts that may exceed  $1 \mu\text{Hz}$ . Likewise, the eigenfrequencies are sensitive to mismatches in  $T_{\text{eff}}$  or  $\log g$ . Furthermore, a thorough investigation of the accuracy of the new scheme for interpolating mean 3D stratifications within the atmosphere grids is performed. Throughout large parts of the 3D grids our interpolation scheme yields sufficiently accurate results for the purpose of *asteroseismology*. We apply our procedure in asteroseismic analyses of four *Kepler* stars and draw the same conclusions as in the solar case: correcting for structural deficiencies lowers the eigenfrequencies. This correction is slightly sensitive to the patching criteria, and the remaining frequency discrepancy between models and observations is less frequency-dependent. Our work shows the applicability and relevance of patching in *asteroseismology*.

## 6.1 Introduction

To avoid the necessity of empirical relations to correct for the **surface effect**, different authors have employed **PM's** (section 4.2) utilising the mean stratification of 3D **RHD** simulations, to which we will refer as (3D)-atmospheres. While the patching procedure has been used to calibrate relations for surface corrections, it has only been applied directly in a very limited set of cases including the Sun. The aim of this paper is to present a new and more robust patching method, including an alternative interpolation scheme. Moreover, we aim to shed light on the impact of stellar patching on asteroseismic analyses, based on solar models and data from *Kepler* on other solar-like oscillators.

The obtained theoretical oscillation frequencies are not expected to perfectly match observations, as the patching procedure only corrects for structural effects. More specifically, analyses based on **PM's** are expected to slightly underestimate the observed frequencies, and modal effects must be taken into account in order to correct for the remaining frequency difference. Modal effects include non-adiabatic energetics and contributions from the turbulent pressure to the oscillation equations. According to Houdek et al. (2017), modal effects counteract structural effects reducing the purely structural frequency correction yielding results that are in very good agreement with observations. However, including modal effects is beyond the scope of this paper.

The general features of our patching procedure are described in section 6.2, with section 6.2.3 dedicated to interpolation between 3D simulations. Having established these procedures, we present a selection of patched solar models in sections 6.3 and 6.4 investigate how different assumptions and choices affect the asteroseismic results. Finally, we present an asteroseismic analysis based on **PM's** of four stars observed with *Kepler* in section 6.5.

## 6.2 Constructing Patched Models

We construct a patched stellar model (**PM's**) by replacing the outermost stratification of a regular stellar model – referred to as the un-patched model (**UPM**) – by the mean stratification of 3D stellar atmospheres. In accordance with other authors, we perform the replacement at a given evolutionary

point and we therefore refer to our procedure as post-evolutionary patching. The previous evolution up to this point is therefore computed without replacing the outermost layers.

The employed 3D RHD simulations are all of the *box-in-a-star* type covering a representative volume of the surface layers. We had access to two grids of such stellar convection simulations: The **Trampedach grid** and the **STAGGER grid** introduced in section 4.1. The mean stratifications ( $\langle 3D \rangle$ ) are both spatial averages over horizontal layers and temporal averages.

Several possibilities exist for performing the spatial average. As shown by Magic and Weiss (2016), many of the common averaging choices – such as one taken over Rosseland optical depth – violate hydrostatic equilibrium and consequently affect the asteroseismic results. Therefore we choose to use a spatial average taken over layers of constant geometrical depth, which will preserve hydrostatic equilibrium. Moreover, according to Magic and Weiss (2016), the mean stratifications are not affected by whether the temporal average is taken over layers of constant depth or over horizontally averaged layers of constant column density.

### 6.2.1 The Interior Models

When constructing post-evolutionary **PM's**, it is assumed that the inadequate treatment of the outermost layers by the 1D stellar evolution code has a negligible effect on the evolution prior to the patching, but it is unclear to which extent it holds true. A more rigorous approach would thus be to patch  $\langle 3D \rangle$ -atmospheres throughout the stellar evolution taking the results consistently into account along the evolutionary path – this is beyond the scope of this work, but see chapters 7 and 8.

When analysing patched solar models in section 6.3 we will be using a reference **SSM** as the **UPM** to facilitate an easy comparison with the results published by other authors, in particular Ball et al. (2016). Specifically, we will use “*Model S*” from Christensen-Dalsgaard et al. (1996), which was computed with **ASTEC** and introduced in section 2.4.

It is important for the **UPM** and  $\langle 3D \rangle$ -envelope to be as compatible as possible. Hence, in order to construct **UPM's** with input physics closely matching the assumptions made in the 3D simulations, we will use the  $T(\tau)$  relation and calibrated  $\alpha_{\text{MLT}}$  from Trampedach et al. (2014a,b) based on the **Trampedach grid** of 3D-atmospheres. As described in chapter 5, this was

implemented in **GARSTEC** by Mosumgaard et al. (2018). These **GARSTEC** models will be employed when dealing with the *Kepler* stars in section 6.5.

### 6.2.2 The Patching Procedure

When constructing a **PM**, we discard all mesh points in the **UPM** beyond a certain interior patching point (“*i.p.*”). Likewise, we discard all mesh points below the so-called atmosphere patching point (“*a.p.*”), in the  $\langle 3D \rangle$ -atmosphere. We then replace the stellar structure of the **UPM** beyond the interior patching point with the remaining mesh points from the  $\langle 3D \rangle$ -atmosphere. Figure 6.1 on the next page illustrates the corresponding change in the stellar structure and the nomenclature introduced in this section.

There are different viable approaches one may take when selecting the patching points. We will follow several of those in order to facilitate an easy comparison with Ball et al. (2016), and to evaluate the influence of different patching criteria. We will generally use  $\beta$  to denote an arbitrary patching quantity; suitable choices include the temperature  $T$ , the total pressure  $P$ , the density  $\rho$ , and the first adiabatic index  $\Gamma_1$ . These choices will be investigated further in section 6.3.

One option for determining where to patch is to simply pre-select the *atmosphere* patching point at a given pressure or depth. The patching is then performed at the distance  $r(\beta_{a.p.})$  from the stellar centre of the **UPM**, at which a given  $\beta$  takes the same value in the **UPM** as at the *a.p.* in the  $\langle 3D \rangle$ -envelope. Since a mesh point exactly matching the value of  $\beta$  at the *a.p.* may not exist in the **UPM**, this approach requires interpolation between the mesh points in the **UPM**. Instead of pre-selecting the atmosphere patching point, another option is to instead pre-select the *interior* patching point.

It is also possible to define patching criteria based on more than one patching quantity. Involving additional quantities requires selecting a set of patching points that overall gives the best match between the *a.p.* and the interior model for all of the quantities. For instance, one may perform the patch at that point in the  $(P, \rho)$ -plane, at which  $\rho(P)$  predicted by the  $\langle 3D \rangle$ -atmosphere lies closest to  $\rho(P)$  predicted by the **UPM**.

When involving several patching quantities, the values of those at the *a.p.* are most probably not all matched by the **UPM** simultaneously. In other words, each patching quantity assigns a different distance from the stellar centre to the *a.p.*, and a suitable compromise of these distances must be

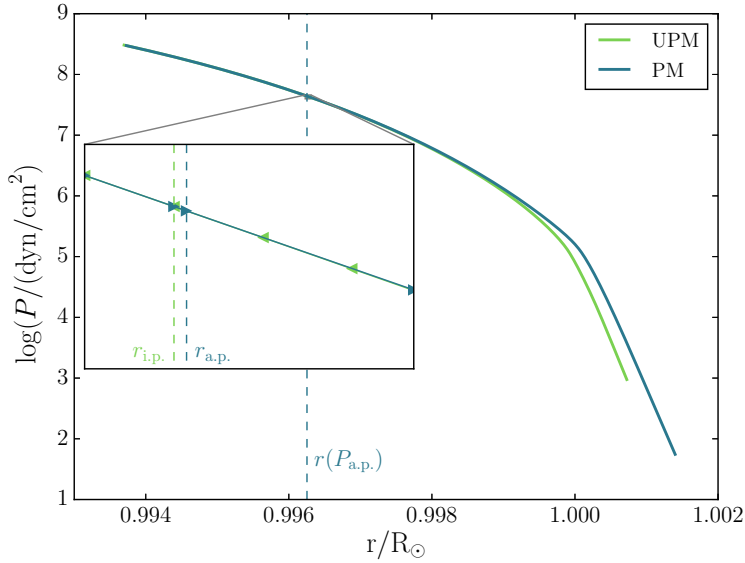


**Figure 6.1 | Pressure stratification of a PM and an UPM.** The patching foundation is *Model S* and the 3D solar simulation from the **STAGGER** grid. The total pressure  $P$  is the patching quantity, entering the selection of the patching points and corresponding radii. The zoom-in includes the interior patching point (i.p.), i.e. the outermost mesh point of the interior model; and the atmosphere patching point (a.p.), i.e. the innermost mesh point of the patched atmosphere. Also marked are the associated radii:  $r_{i.p.}$  and  $r_{a.p.} = r(P_{a.p.})$ .

defined. As an example, when finding the best match in the  $(P, \rho)$ -plane we use the respective discrepancies in  $P$  and  $\rho$  between the *i.p.* and *a.p.* to weight  $r(\rho_{a.p.})$  and  $r(P_{a.p.})$ .

~

None of the listed patching methods explicitly ensures the conservation of hydrostatic equilibrium at the patching points. Therefore we introduce yet another way of selecting the patching point, where we construct models by determining  $r_{a.p.}$  as

$$r_{a.p.} = r_{i.p.} - \frac{2(P_{a.p.} - P_{i.p.})r_{i.p.}^2}{G \cdot m(r_{i.p.})(\rho_{a.p.} + \rho_{i.p.})}, \quad (6.1)$$

to ensure hydrostatic equilibrium to first order.

We finally note that 3D RHD simulations are computed in the plane-parallel approximation assuming constant surface gravity  $g$ . Hence, a possibility is to adjust  $g$  or  $\log g$  at the *a.p.* based on the interior model to correct for sphericity when constructing PM's. If applied, this is done iteratively: The difference between the assumed constant  $g$  of the (3D)-atmospheres and the actual  $g$  at the associated distance from the stellar centre of the PM's starting at the lowermost mesh point. This difference in  $g$  is then used to correct the distance between the considered mesh point and its next neighbour in the patched atmosphere based on hydrostatic equilibrium. However, for the shallow atmospheres of solar-like MS stars, we find this correction to have little impact.

### 6.2.3 The Interpolation Scheme

Constructing meaningful PM's for any given model or star based on discrete atmosphere grids often requires interpolation. To motivate our suggested interpolation scheme, we start out by noting that  $\log \rho$  as a function of  $\log P$  looks similar across the models in a grid and also between grids. Specifically,  $\log \rho(\log P)$  behaves linearly at high and low pressure with similar inclinations and intercept, while a characteristic feature occurs near the stellar surface corresponding to a local minimum in  $\partial \log \rho / \partial \log P$ . We will refer to this minimum as the *density jump*.

Shifting  $\log \rho(\log P)$  by the position of the density jump results in nearly coinciding stratifications as can be seen from fig. 6.2. This is a key observation, as the position of the density jump in the  $(\log \rho, \log P)$ -plane behaves rather linearly as a function of both  $\log T_{\text{eff}}$  and  $\log g$  as can be seen from fig. 6.3 on page 101. Thus, the position of the density jump can reliably be computed by interpolation, which is central to our new scheme.

It is worth noting that while  $\log \rho(\log P)$  is thus suitable for interpolation across the mapped  $(T_{\text{eff}}, \log g)$ -plane,  $\log P(\log \rho)$  is not. This is due to the density inversion that can take place in the envelopes of evolved RG-stars, a phenomenon found by Schwarzschild (1975).

To compute interpolated atmosphere models we select a suitable subset of 3D atmospheres having the same metallicity as the atmosphere that we attempt to construct. Firstly, we shift the stratification of each of those by the position of their respective density jumps as described above. Now, the

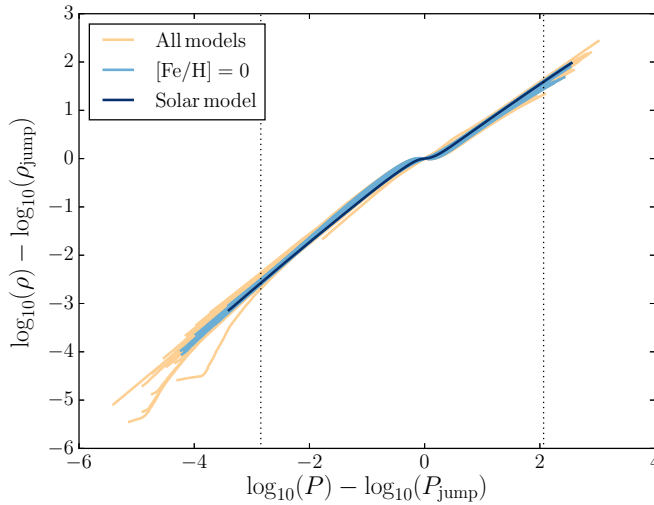


**Figure 6.2 | Shifting the stratification by the position of the density jump.** Density as a function of pressure on logarithmic scale of all models in the **STAGGER grid**. The models at solar metallicity and the solar simulation have been highlighted. The dotted lines show the interpolation range for solar metallicity.

simulation points are triangulated in the  $(\log T_{\text{eff}}, \log g)$ -plane to compute  $\log \rho$  for fixed values of  $\log P$ . Given  $T_{\text{eff}}$  and  $\log g$  of the desired atmosphere, the triangulated interpolation yields a complete  $\log \rho(\log P)$  stratification. Then, the corresponding density jump is likewise obtained by interpolation in the  $(\log T_{\text{eff}}, \log g)$ -plane, and finally applied to shift back the obtained interpolated stratification.

Regarding the last step, the key quantity – which is also a fundamental part of our scheme – is the pressure at the density jump  $P_{\text{jump}}$ , which is shown in fig. 6.3 for all models in the **STAGGER grid** at solar metallicity. As can be seen from the figure,  $P_{\text{jump}}$  evolves rather linearly as a function of both  $\log T_{\text{eff}}$  and  $\log g$ . The same holds true for the corresponding density, and also at different metallicities. We also investigated this for the **Trapedach grid** atmosphere, where the same nice behaviour is found.

Having obtained  $\rho(P)$  the depth  $z$  below a given point can now easily be established based on the requirement of hydrostatic equilibrium. Furthermore, our interpolation scheme computes both  $\log T$  and  $\Gamma_1$  as a function of

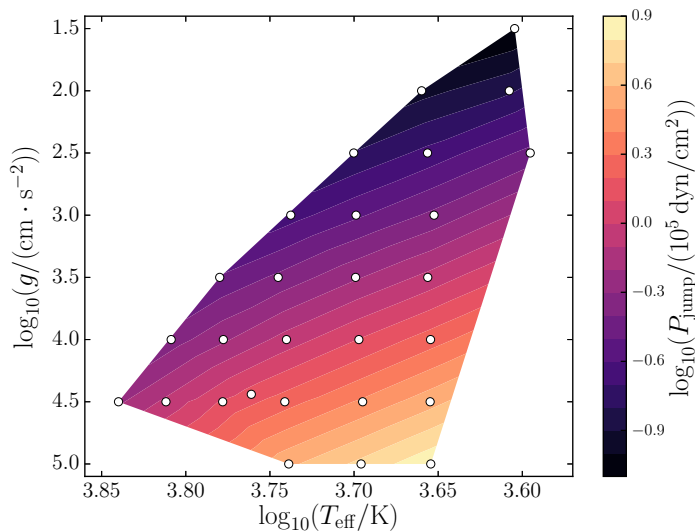


**Figure 6.3 | Behaviour of the pressure at the density jump.** The logarithm of the pressure at the density jump  $P_{\text{jump}}$ . The density jump is defined in the text. The quantity is derived from the **STAGGER** grid at solar metallicity marked with white dots.

$\log P$  based on the interpolation in the  $(\log T_{\text{eff}}, \log g)$ -plane. Also for these quantities it is important to perform the scaling by the density jump.

Based on the established stratifications, the derivatives needed for frequency calculations are determined using an Akima spline interpolation (Akima, 1970). A similar procedure was also used to determine the derivative of the Hopf function in chapter 5. While cubic splines may show ripples in the neighbourhood of discontinuities, this piece-wise sub-spline method yields a smooth transition even when encountering abrupt changes in the derivatives. This feature is important near the patching points.



To evaluate how accurately our interpolation scheme reproduces the correct structure across the  $(\log T_{\text{eff}}, \log g)$ -plane, we have excluded models from the grids and subsequently reconstructed the excluded models based only on their  $T_{\text{eff}}$  and  $\log g$ .

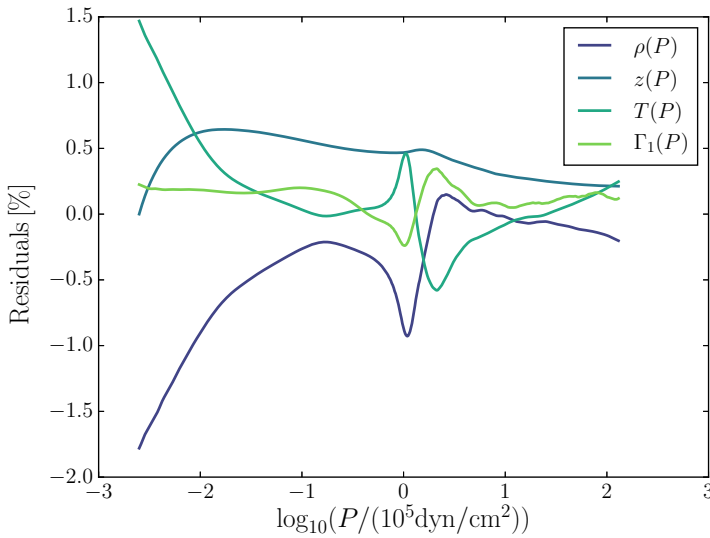


**Figure 6.4 | Reproduction of the solar simulation using interpolation.** Comparison between an interpolated solar model based on the **STAGGER grid**, and the correct structure excluded from the grid prior to the interpolation. The figure shows the relative residuals as a function of pressure.

An example of such a reconstruction is given in fig. 6.4, showing the relative residuals between the solar simulation from the **STAGGER grid** (with  $T_{\text{eff}} = 5769 \text{ K}$  and  $\log g = 4.44$ ) and the corresponding interpolated atmosphere. As can be seen from the figure, all interpolated quantities are reproduced within 2 % of the expected values at all pressure values (spanning more than five orders of magnitude).

Moving beyond the Sun, we reconstructed all of the models in the **STAGGER grid** except for those at the grid borders. As can be seen from fig. 6.5, the relative errors introduced in  $\rho(P)$  by interpolation are generally of the order of a few percent; and for all but one high-temperature model they lie below 10 %. The residuals are determined at a pressure  $10^{1.9}$  times higher than  $P_{\text{jump}}$ , as this value lies close to the highest pressure available for all atmospheres in the grids. The computed residuals constitute an upper bound of the expected error.

Magic and Weiss (2016) presents an alternative interpolation scheme for the **STAGGER grid** based instead on a generic form of the normalized en-

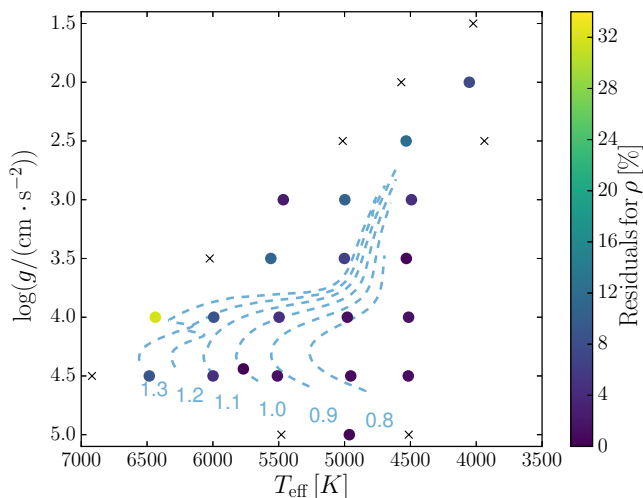


**Figure 6.5 | Residuals from interpolation when excluding simulations.** Residuals of  $\rho(P)$  between interpolated models and the corresponding excluded atmospheres in the **STAGGER** grid at solar metallicity (boundaries excluded), measured at a pressure  $1 \times 10^{1-9}$  higher than at the density jump. To guide the eye, evolutionary tracks corresponding to different solar masses are shown.

tropy stratification. Comparing our results qualitatively with the published test cases (Magic and Weiss, 2016, fig. 6), we conclude that our simple interpolation scheme is able to reconstruct the correct stratifications with similar or even higher accuracy throughout the  $(T_{\text{eff}}, \log g)$ -plane.



Having established that our interpolation scheme yields reasonably accurate results in the case of the regular **STAGGER** grid, we now take a closer look at the irregular **Trapedach** grid (the grid morphology is shown in fig. 5.1 on page 75). Here we find the accuracy to be strongly affected by the sampling. In regions with a dense sampling, we are able to reconstruct the stratifications within 1 % and acceptable accuracy is obtained for most **MS** stars. However, in regions with a sparse sampling, the errors may reach 20 % – the highest error is again reached for **MS** stars at high temperatures. Figure 6.6 shows the error in  $\rho(P)$  across the  $(T_{\text{eff}}, \log g)$ -plane and should be compared to fig. 6.5.

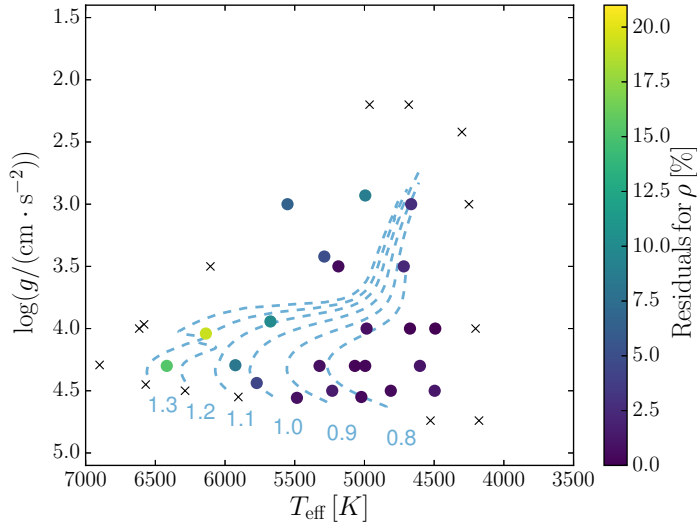


**Figure 6.6** | Residuals from interpolation when excluding simulations. As fig. 6.5 but for the **Trampedach grid**.

As regards the solar atmosphere in the **Trampedach grid** we are able to reproduce  $\rho(P)$  only within 5 %, although the sampling is higher in the vicinity of the solar atmosphere than in the corresponding region of the **STAGGER grid**. We will explore the implications of this in section 6.3.2.

Note that the increased errors may partially reflect that we are relying on a standard method for interpolating in a two-dimensional plane, which might perform better for a regular mesh like the **STAGGER grid**. For the interpolation in chapter 5 a triangulation specifically designed for an irregular mesh (Cline and Renka, 1984) was utilised. These routines will also be applied for the implementation of the interpolation in **GARSTEC** in chapters 7 and 8.

Finally, it should be mentioned that the stratification of some quantities in the **Trampedach grid** show ripples. In order to remove such ripples, we smooth the interpolated atmospheres before patching when dealing with the **Trampedach grid**, although we found that these ripples have a negligible effect on the model frequencies.

## 6.3 The Solar Case

Having summarized the main aspects of (interpolated) post-evolutionary patching above, we turn our attention towards the Sun and an investigation of how the helioseismic predictions are affected by the implementation of our procedure. In order to perform this analysis, we computed adiabatic frequencies of stellar **p-mode** oscillations of the patched stellar models using **ADIPLS**. When presenting frequency shifts  $\delta\nu_{nl}$  we only include radial modes ( $l = 0$ ).

### 6.3.1 Patched Solar Models

As mentioned earlier, we will use the reference **SSM Model S** as our **UPM**. We will construct **PM**'s using both the **STAGGER grid** and **Trampedach grid**. Moreover, for a direct comparison with Ball et al. (2016), we will also employ the solar 3D simulation from Beeck et al. (2013) calculated with the **RHD**-code called “**MURAM**” by Vögler and Schüssler (2003) and Vögler et al. (2005), and averaged over surfaces of constant geometric depth and time. As observational reference we use the radial mode frequencies from **BISON**.

In accordance with Ball et al. (2016), we use a weighted combination of  $P$  and  $\rho$  as patching quantities. Figure 6.7 shows the frequency difference between **BISON** data and the model frequencies of the **PM** with **MURAM**. The resulting oscillation frequencies are in good agreement with the results published by Ball et al. (2016), and we were able to reduce the frequency difference between model frequencies and observations from roughly 12  $\mu\text{Hz}$  to 4  $\mu\text{Hz}$ .

As also stressed by Ball et al. (2016) this is generally consistent with the findings of other authors – including Piau et al. (2014), who present patched solar models in which they adopted the average profile of the temperature gradient,  $P$ ,  $\rho$ ,  $\Gamma_1$ , and the **Brunt–Väisälä frequency** from 3D **RHD** simulations. Piau et al. (2014) decreased the radius of their **UPM** in order to correct for the fact that the **PM** is slightly larger than the **UPM**, as a result of the (3D)-atmospheres being more extended than their 1D counterparts (due to e.g. turbulent pressure). Like Ball et al. (2016) and Magic and Weiss (2016), we do not take this effect into account, as we keep the interior structure of the **UPM** constant. Thus, the radius of our patched solar models are roughly 100 km larger than the constraints on the radius from Model S.

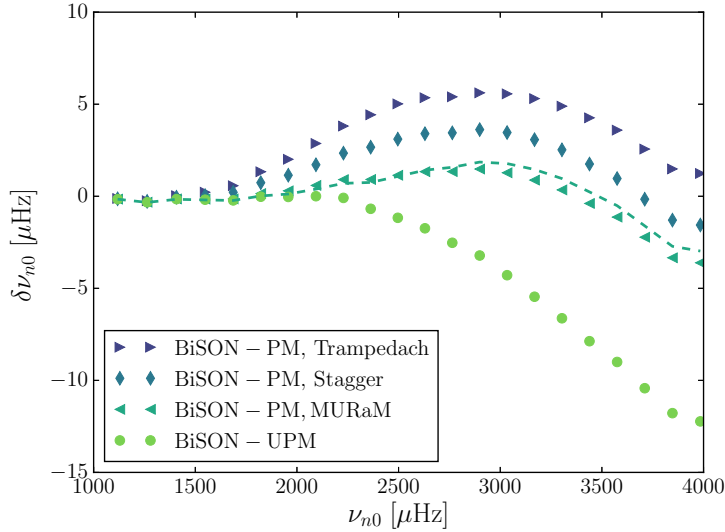


**Figure 6.7 | Comparing different patched solar models.** Frequency difference of radial modes between observations and solar models. The reference **UPM** is *Model S* and the **PM**'s use the specific solar simulation from one of the grids. For all models, a weighted combination of  $P$  and  $\rho$  serve as the patching quantity; and the patching points are chosen within the adiabatic regions at the depth where the closest match between the interior and atmosphere in the  $(P, \rho)$ -plane is found. The markers are larger than the observational errorbars. The dashed line shows the results presented by Ball et al. (2016) with MURaM for comparison.

We also constructed **PM**'s based on *Model S* and our standard 3D solar atmospheres from the **STAGGER** grid and the **Trapedach** grid. The resulting model frequencies are also shown in fig. 6.7. Compared to the **MURaM PM** they are lower by  $2 \mu\text{Hz}$  and  $5 \mu\text{Hz}$ , respectively. We note that these frequency deviations are comparable to the discrepancy between model predictions and observations. As expected, the helioseismic results are very sensitive to the exact input physics of the atmosphere.

The same statement holds true for the interior model, as can be seen from fig. 6.8 summarising results obtained with two different **GARSTEC** models. Both models use the mixture from Asplund et al. (2009), the **OPAL-EOS**

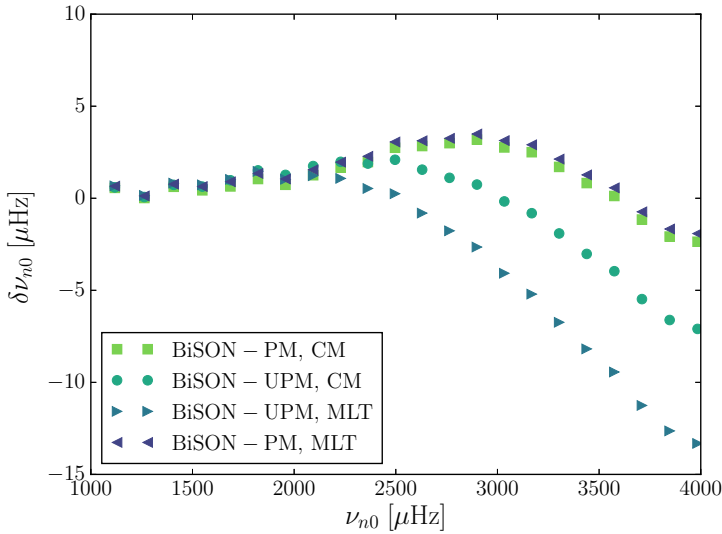


**Figure 6.8 | Comparison of convection theories using patched models.** Frequency difference of radial modes between observations and solar models constructed using the solar simulation from the **STAGGER grid**. The patching quantities are  $P$  and  $\rho$ , and the resulting patching point is located 2.7 Mm below the surface.

augmented by the **MHD-EOS** in the low temperature regime and the **OPAL** opacities with standard low-temperature opacities (see section 1.2.1). They differ only in their treatment of convection: one uses standard **MLT**, while the other employs the **FST** (section 1.5.1) – both calibrated to the Sun. Although the **FST** convection leads to model frequencies that are in better agreement with observations (“**UPM, CM**” in fig. 6.8), patching the solar simulation from the **STAGGER grid** to either of the two yields almost identical results. This implies that the patch is performed at a depth below which the two **UPM**’s are nearly indistinguishable. Note, that for the remainder of the chapter we will restrict ourselves to models with **MLT** convection.

As can be seen from figs. 6.7 and 6.8, none of the presented patched solar models actually reproduces the observed **BISON** frequencies, as we only take structural effects into account. As mentioned earlier, modal effects are expected to counteract the structural effects (e.g. Houdek et al., 2017).

The adiabatic frequencies obtained after solely including structural effects depend on the treatment of turbulent pressure in the frequency calculations (cf. Sonoi et al., 2017). In accordance with Ball et al. (2016), we assume that the relative Lagrangian perturbation of the turbulent and thermal pressure are equal – this is equivalent to the *gas  $\Gamma_1$  approximation* in the nomenclature of Rosenthal et al. (1999).



We now take a closer look at the details of the patching procedure. We begin by discussing possible choices of the patching quantity, as this determines the patching points and the distance of the *a.p.* from the stellar centre  $r_{\text{a.p.}}(\beta)$ . The implication is twofold: Firstly, this determines the size of the acoustic cavity affecting the oscillation frequencies. Secondly, the stratification of the chosen quantity is smooth by construction, while discontinuities may occur for the remaining quantities. Since the frequency computation relies on  $P(r)$ ,  $\rho(r)$ , and  $\Gamma_1(r)$ , each of these constitutes a suitable selection. An obvious alternative is the temperature – also because some of our stellar models in the upcoming sections rely on a  $T(\tau)$  relation extracted from 3D simulations. Hence, the question arises as to which degree the asteroseismic results are affected by the choice of patching quantity.

As can be seen from fig. 6.9, **PM's** based on different patching quantities yield the same oscillation frequencies within 1 – 2  $\mu\text{Hz}$  in the case of the solar **STAGGER grid** atmosphere. Repeating the analysis for the **MURAM** solar simulation and the solar atmosphere from the **Trampedach grid**, we find the choice of patching quantities to affect the model frequencies by up to 3  $\mu\text{Hz}$ . This is of the same order as the frequency differences presented in fig. 6.7 and small compared to the **surface effect** itself.

As mentioned in section 6.2, another patching option is to determine  $r_{\text{a.p.}}(\beta)$  by eq. (6.1) to ensure hydrostatic equilibrium to first order. We also tested the construction of **PM's** with this procedure, and the resulting model frequencies are consistent with the frequencies obtained when using  $P$  as the patching quantity.

Another experiment we performed was to vary the patching depth using different patching quantities:  $T$ ,  $P$ ,  $\rho$ , and  $\Gamma_1$ . For these, we find the model frequencies to be relatively insensitive to the patching depth if situated sufficiently deep within the adiabatic region – this result is independent of the used solar atmosphere.

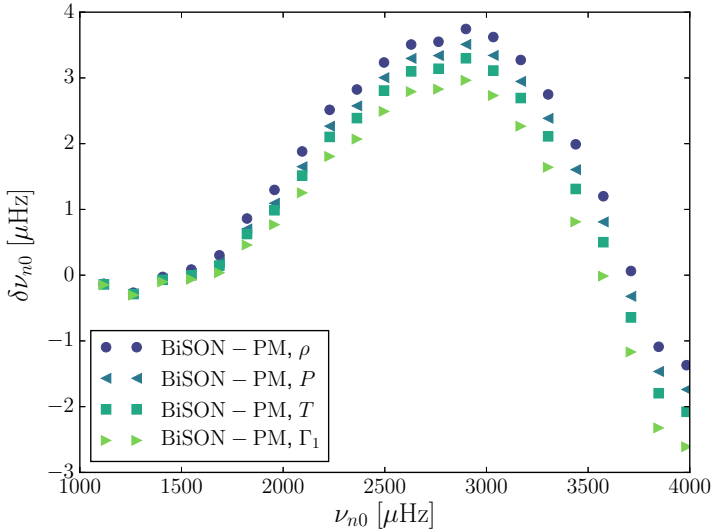


**Figure 6.9 | Comparison of different patching quantities.** Radial mode frequency difference between observations and **PM**'s constructed using Model S and the solar atmosphere from the **STAGGER** grid. Different quantities have been utilised for the selection of the interior patching point and  $r_{\text{a.p.}}(\beta)$ . All models are patched 2.7 Mm below the surface.

Another patching quantity not treated so far is the optical depth used by Piau et al. (2014) to construct their **PM**'s. If we apply this patching quantity in our approach, it leads to prominent discontinuities in the remaining quantities and yields model frequencies which are rather sensitive to the patching depth. These discontinuities become more prominent with increasing patching depth, which most probably reflects the accumulation of discrepancies that stem from the integration over the opacity. These results reflect the inconsistent physical assumptions that enter the **UPM** and the **<3D>**-atmosphere.

Finally, we note that in order to facilitate an easy comparison with Ball et al. (2016) all models presented in figs. 6.7–6.9 have been computed without correcting for sphericity or discrepancies in  $\log g$ . In the case of the shallow solar atmosphere, these corrections have little effect on the overall structure and hence on the oscillation frequencies. However, for some of

the models to be presented in section 6.4, these corrections strongly alter the frequencies, due to a sufficiently large mismatch between  $g$  of the **UPM** and  $g$  of the patched atmosphere.

### 6.3.2 Helioseismic Tests of the Interpolation Scheme

Earlier, we tested our interpolation scheme by excluding the solar atmosphere from the grid of 3D simulations and then reconstructed it based on its  $T_{\text{eff}}$  and  $\log g$ . The structural residuals were investigated using both the **STAGGER grid** and **Trampedach grid**, and in the case of the **STAGGER grid** the atmospheric structure can be reliably reproduced within 2% or better (fig. 6.4 on page 102).

Now, we want to use the reconstructed solar atmosphere to assess if the accuracy of our interpolation scheme is sufficiently high for the purpose of asteroseismic analysis. Therefore, we constructed **PM's** based on these *interpolated* solar atmospheres and compared the helioseismic results with the model frequencies obtained from a **PM** built with with the *original* solar  $\langle 3D \rangle$ -atmospheres.

The interpolated solar atmosphere yields the expected model frequencies within 1  $\mu\text{Hz}$  for all frequencies between 1000  $\mu\text{Hz}$  and 4000  $\mu\text{Hz}$  independently of the chosen patching quantity. Thus, the errors introduced by the interpolation scheme are of the order as the uncertainty associated with the averaging of the 3D simulations (Ball et al., 2016; Magic and Weiss, 2016).

However, in the case of the **Trampedach grid** a more complex picture emerges. As briefly mentioned in section 6.2.3, here the interpolation scheme strongly underestimates  $\rho(P)$  affecting the selection of the patching points and the computation of  $r_{\text{a.p.}}(\beta)$ . Hence, when utilising the stratification-matching in the  $(P, \rho)$ -plane to perform the patch, the errors in the model frequencies reach 6  $\mu\text{Hz}$  – this can be compared to fig. 6.7 on page 106, where the same patching choice was made. Better agreement is found when using  $T$  as the patching quantity.

## 6.4 Selecting Atmosphere Parameters

As pointed out by Magic et al. (2013a), the temperature stratification of  $\langle 3D \rangle$ -atmospheres may severely deviate from their 1D counterparts. Thus,

the naive patch between an interior model and an atmosphere with the *same*  $T_{\text{eff}}$  will not necessarily yield a good fit in  $T(r)$  when using other quantities to determine the patch, and vice versa. Therefore, we introduce another method of selecting the atmosphere to use in the patching: *minimization of the discontinuities* near the bottom.

The principle is to construct a large pool of interpolated atmospheres with different values of  $T_{\text{eff}}$  and  $\log g$  in the vicinity of the **UPM** – in the case of ‘real’ stars, the restriction is three standard deviations of the observational value. From the pool, the interpolated atmosphere minimizing the sum of squared relative differences in  $T$ ,  $\rho$ , and  $\Gamma_1$  near the bottom of the interpolated atmosphere is found. The selection is weighted by

$$w_{\text{patch}} = 1 + (100 \cdot \Delta \log g)^2, \quad (6.2)$$

where  $\Delta \log g$  is the difference in  $\log g$  at the surface. By imposing this restriction, we prefer atmospheres where  $\log g$  matches the value of the **UPM**, as any mismatch in  $g$  has to be subsequently corrected for in order to obtain physically meaningful **PM’s**. The interpolation takes place at a pressure  $10^{1.9}$  times higher than at the density jump, as this value lies close to the highest pressure that is common for all models in the grids, such that no extrapolation is required.



When constructing **PM’s** with fixed interior structures for stars across the **HRD**, two different approaches for selecting a suitable atmosphere can be followed: The first is to patch an interpolated atmospheres with exactly the same  $\log g$  and  $T_{\text{eff}}$  as the **UPM’s**. The second is to select the global parameters of the atmospheres based on the requirement to minimize the discontinuities near the bottom of the atmospheres as introduced above. Both approaches are rather simplistic and have their drawbacks: While the former approach will lead to un-physical discontinuities, the latter may simply disguise inadequacies of the **UPM** or the  $\langle 3D \rangle$ -atmospheres without ensuring a physically correct representation of the stellar structure. When constructing **PM’s** for the *Kepler* stars in section 6.5 we will follow both of the approaches and compare them.

To test the impact of a mismatch in  $T_{\text{eff}}$  and  $\log g$  between the **UPM** and the patched atmosphere on helioseismic results, we constructed several **PM’s** based on *Model S* and interpolated atmospheres with different global

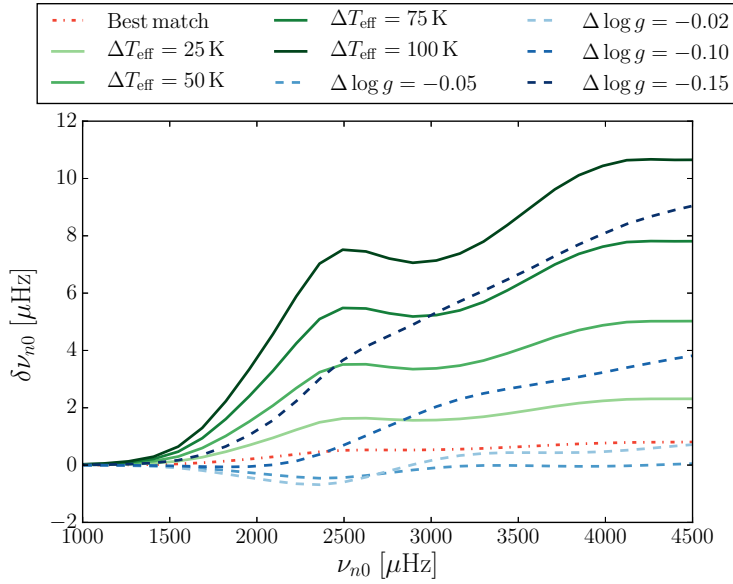


**Figure 6.10 | The effect of deviation in atmospheric parameters.** Frequency differences between **PM**'s utilising interpolated atmospheres with different global parameters, and the solar simulation from the **STAGGER** grid. All **PM**'s are constructed from *Model S* using  $P$  and  $\rho$  as patching quantities. We have adjusted  $\log g$  to fit the interior model at the atmosphere patching point and corrected for sphericity. When varying the effective temperature,  $\log g$  has been kept fixed and vice versa.

parameters. The results are presented in fig. 6.10, from which it can be seen that a mismatch in  $T_{\text{eff}}$  of 100 K leads to frequency shifts of around 10  $\mu\text{Hz}$ . This exceeds by far the error expected to arise from the interpolation scheme alone based on the analysis presented earlier.

Figure 6.10 also contains a **PM** model with the atmosphere minimizing the discontinuities at the bottom of the atmosphere and yields the optimal match to the **UPM**. In the case of the **STAGGER** grid, the best match is found at  $T_{\text{eff}} = 5778$  K, which is close to the  $T_{\text{eff}}$  of the solar **UPM**. In contrast, in the case of the **Trapedach** grid, we find  $T_{\text{eff}}$  of the best matching atmosphere to deviate significantly from that of the **UPM**. Thus, different selection criteria for the global parameters of the patched atmosphere can severely affect the asteroseismic results. Moreover, fig. 6.10 emphasizes the

importance of our interpolation scheme presented: Simply selecting the nearest atmospheres in the grid will severely distort the results and is hence unsuitable for correcting the structural **surface effect**.

## 6.5 Stars in the *Kepler* Field

In the following, we present an asteroseismic analysis using **PM's** of several stars observed with *Kepler*. We only consider solar-type dwarfs in a limited mass range guided by the established accuracy of the interpolation scheme in different regions of the  $(T_{\text{eff}}, \log g)$ -plane. Due to the restrictions imposed by the **Trampedach grid**, we only select objects with metallicities consistent with being solar within one standard deviation of their spectroscopic value.

The stars we investigate are a part of either the **KAGES** sample (Silva Aguirre et al., 2015; Davies et al., 2016) or the **LEGACY** sample (Lund et al., 2017; Silva Aguirre et al., 2017) – or sometimes both, as the two samples overlap. The observed oscillation frequencies are in both cases obtained from a Bayesian Markov chain Monte Carlo “peak-bagging” approach (see section 3.3.2). The additional observational constraints are given in the listed reference.

### 6.5.1 Selecting the **UPM's** and Atmospheres

For the analysis, we utilise two different grids of stellar evolution models computed with **GARSTEC**. The first serves as a reference, and consists of tracks calculated with a standard grey Eddington atmosphere and constant solar-calibrated  $\alpha_{\text{MLT}} = 1.79$ . The opacities and **EOS** are from **OPAL**, and the composition is **GS98** (Grevesse and Sauval, 1998). This grid includes stars with masses between  $0.70 M_{\odot}$  and  $1.30 M_{\odot}$  in steps of  $0.01 M_{\odot}$ , for which the **large frequency separation** lies between  $\Delta\nu = 13 \mu\text{Hz}$  and  $\Delta\nu = 180 \mu\text{Hz}$ . The metallicity  $[\text{Fe}/\text{H}]$  is treated as a free parameter and varied between  $-0.50$  dex and  $0.50$  dex in steps of  $0.05$  dex. The theoretical oscillation frequencies are computed of all models with **ADIPLS**. We refer to this set of models as “*standard input models*”.

The second is our main grid, where we want to ensure consistency between the interior model and the patched  $\langle 3\text{D} \rangle$ -atmosphere. Therefore we construct **UPM's** employing the composition imposed by Trampedach

et al. (2013), and the  $T(\tau)$  relation and calibrated  $\alpha_{\text{MLT}}$  from Trampedach et al. (2014a,b) implemented in **GARSTEC** by Mosumgaard et al. (2018) (see chapter 5). The remaining input physics are listed in chapter 5, where details on the implementation are also provided. Using this condensed 3D information, we constructed a grid of stellar models with masses between  $0.70 M_{\odot}$  and  $1.20 M_{\odot}$  in steps of  $0.01 M_{\odot}$ , covering the parameter range of the 3D simulations in the **Trampedach grid**. All models with  $\Delta\nu$  between  $60 \mu\text{Hz}$  and  $170 \mu\text{Hz}$  are stored – which for a  $1 M_{\odot}$  star roughly covers the evolution from **ZAMS** to some point during the **subgiant** phase – and their oscillation frequencies computed with **ADIPLS**. We refer to this grid as “*3D-calibrated models*”.

Above the photosphere, the structure of the 3D-calibrated **UPM’s** are dictated by the  $T(\tau)$  relation derived from the 3D simulations. Below the photosphere, the 3D simulations are taken into account via the variable  $\alpha_{\text{MLT}}$  and adjustments to the radiative gradient. For further details, we refer to chapter 5. Nevertheless, the 3D-calibrated **UPM’s** do not perfectly reproduce the  $\langle 3\text{D} \rangle$ -atmospheres. Also, they have been computed neglecting e.g. turbulent pressure and convective back-warming (see e.g. Trampedach et al., 2017); especially the turbulent pressure can be important, as it significantly contributes to the total pressure throughout large parts of the  $\langle 3\text{D} \rangle$  atmospheres. Moreover, the employed mixing length that takes a constant value within the model – i.e., does not vary with depth – cannot encapsulate the detailed structure of 3D-simulations. Consequently, discontinuities also occur for these models when patching below the photosphere, which we will discuss in section 6.5.3.

While the outermost layers of the 3D-calibrated models do not perfectly mimic the underlying 3D simulations, the implementation of the associated  $T(\tau)$  relation leads to more physically accurate boundary conditions than the Eddington atmosphere, providing a better description of the transition between optically thin and optically thick regions. Furthermore, the calibrated  $\alpha_{\text{MLT}}$  that is employed by the 3D-calibrated models varies with  $T_{\text{eff}}$  and  $\log g$  and gives a more realistic description of convection throughout the **HRD** than a constant mixing length does. Finally, while the structure of the outermost layers of the 3D-calibrated models does not perfectly match the corresponding  $\langle 3\text{D} \rangle$ -atmospheres, the implementation by Mosumgaard et al. (2018) guarantees a high level of consistency between the input physics of these models and the input physics of the 3D simulations.

Having established the two grids of 1D UPM's, they must be compared to the observations. To perform this task we use **BASTA**, which is introduced in section 3.4.1. We either use the individual frequencies after applying the surface correction by Ball and Gizon (2014), or the surface-insensitive frequency separation ratios:  $r_{01}$ ,  $r_{10}$ , and  $r_{02}$  (see section 3.3.2). From **BASTA** we both obtain an estimate of the stellar parameters from their respective PDF, as well as the UPM with the highest assigned likelihood: the *best-fitting model* (**BFM**). The inferred parameters is reported as the median of the PDF and the 68.3 percentiles.

The modelling efforts with the two different grids of the four *Kepler* stars are summarised in table 6.1 on the following page, where the stars are identified by their KIC-number. The table provides the observational constraints (subscript 'con'). It also lists the stellar parameters and uncertainties determined from the **BASTA** probabilities (subscript 'P'), as well as the specific parameters of the best-fitting UPM's (subscript 'U'). Note that the **BFM** does not generally correspond to the inferred median parameters. Finally, the global parameters of the interpolated <3D>-atmospheres minimizing the bottom-discontinuities as described above are given (subscript 'S' for the **STAGGER** grid and 'T' for the **Trampedach** grid).

As can be seen from table 6.1, the metallicities of the best-fitting standard input UPM's are in agreement with the assumption of solar metallicity, and the inferred values of  $\log g$  are in good agreement with the previous works by Silva Aguirre et al. (2015, 2017). Moreover, the masses of the standard input UPM's are in very good agreement with the masses of the 3D-calibrated UPM's – and with the findings of Silva Aguirre et al. (2017). For all four stars,  $T_{\text{eff}}$  of the standard input UPM's are lower and in better agreement with the spectroscopic constraints than their 3D-calibrated counterparts.

### 6.5.2 Asteroseismic Analyses of Patched Models

Based on the detailed investigation of our patching procedure in the solar case, we decided to make a range of different PM's in the following analyses. For all eight cases listed in table 6.1, we constructed a total of six PM's (three with the **STAGGER** grid and three with the **Trampedach** grid). The first four are built using an atmosphere where  $T_{\text{eff}}$  and  $\log g$  match the exact values of the best-fitting UPM: two employing  $T$  as the patching quantity (one for

**Table 6.1 | Parameters of the analysed Kepler stars.** The subscript ‘con’ indicates input constraints. The index ‘p’ refers to the probability output from a **BASTA** fit with 68.3 % credibility intervals. By ‘U’ is denoted the best-fitting **UPM**; and the corresponding **PM** is marked by ‘S’ if constructed from the **STACGER grid** or ‘T’ if from the **Trampedach grid**. The asterisk denotes *standard input models*, while the remaining are *3D-calibrated models*.

KIC	$T_{\text{eff,con}}$ (K)	$\log g_{\text{con}}$ (cgs)	$M_p$ ( $M_{\odot}$ )	[Fe/H] <sub>p</sub> (dex)	$T_{\text{eff,p}}$ (K)	$\log g_p$ (cgs)	$T_{\text{eff,U}}$ (K)	$\log g_U$ (cgs)	$T_{\text{eff,S}}$ (K)	$T_{\text{eff,T}}$ (K)
9025370*	5270 ± 180	4.423 <sup>+0.004</sup> <sub>-0.007</sub>	1.016 <sup>+0.007</sup> <sub>-0.007</sub>	0.06 <sup>+0.09</sup> <sub>-0.07</sub>	5758 <sup>+71</sup> <sub>-61</sub>	4.430 <sup>+0.003</sup> <sub>-0.003</sub>	5771	4.430	5773	5729
9025370	5270 ± 180	4.423 <sup>+0.004</sup> <sub>-0.007</sub>	0.988 <sup>+0.019</sup> <sub>-0.008</sub>	0	5905 <sup>+38</sup> <sub>-19</sub>	4.428 <sup>+0.003</sup> <sub>-0.003</sub>	5908	4.427	5761	5764
9955598*	5457 ± 77	4.497 <sup>+0.005</sup> <sub>-0.007</sub>	0.900 <sup>+0.010</sup> <sub>-0.010</sub>	0.07 <sup>+0.07</sup> <sub>-0.08</sub>	5370 <sup>+61</sup> <sub>-61</sub>	4.497 <sup>+0.002</sup> <sub>-0.002</sub>	5396	4.497	5506	5417
9955598	5460 ± 75	4.495 <sup>+0.002</sup> <sub>-0.002</sub>	0.884 <sup>+0.003</sup> <sub>-0.005</sub>	0	5599 <sup>+19</sup> <sub>-26</sub>	4.496 <sup>+0.002</sup> <sub>-0.001</sub>	5596	4.496	5506	5445
11133306*	5982 ± 82	4.314 <sup>+0.004</sup> <sub>-0.007</sub>	1.050 <sup>+0.040</sup> <sub>-0.040</sub>	0.00 <sup>+0.10</sup> <sub>-0.10</sub>	5956 <sup>+68</sup> <sub>-78</sub>	4.313 <sup>+0.007</sup> <sub>-0.007</sub>	5960	4.313	5991	5904
11133306	5982 ± 82	4.314 <sup>+0.004</sup> <sub>-0.007</sub>	1.010 <sup>+0.030</sup> <sub>-0.020</sub>	0	6010 <sup>+70</sup> <sub>-70</sub>	4.307 <sup>+0.006</sup> <sub>-0.008</sub>	5998	4.306	5989	5870
11772920*	5180 ± 180	4.500 <sup>+0.008</sup> <sub>-0.005</sub>	0.840 <sup>+0.010</sup> <sub>-0.020</sub>	-0.11 <sup>+0.08</sup> <sub>-0.06</sub>	5345 <sup>+70</sup> <sub>-60</sub>	4.503 <sup>+0.003</sup> <sub>-0.003</sub>	5354	4.502	5506	5330
11772920	5180 ± 180	4.500 <sup>+0.008</sup> <sub>-0.005</sub>	0.854 <sup>+0.003</sup> <sub>-0.004</sub>	0	5476 <sup>+28</sup> <sub>-21</sub>	4.506 <sup>+0.002</sup> <sub>-0.002</sub>	5479	4.505	5506	5313

each 3D grid); and two using a combination of  $P$  and  $\rho$  as patching quantities (again one for each 3D grid). The final two **PM's** are constructed utilising the approach to minimize the discontinuities between the interior model and the  $\langle 3D \rangle$ -atmosphere near the bottom of the atmosphere (yet again one for each 3D grid). These latter two are those corresponding to  $T_{\text{eff}, S}$  and  $T_{\text{eff}, T}$  in table 6.1 and in the following plots.

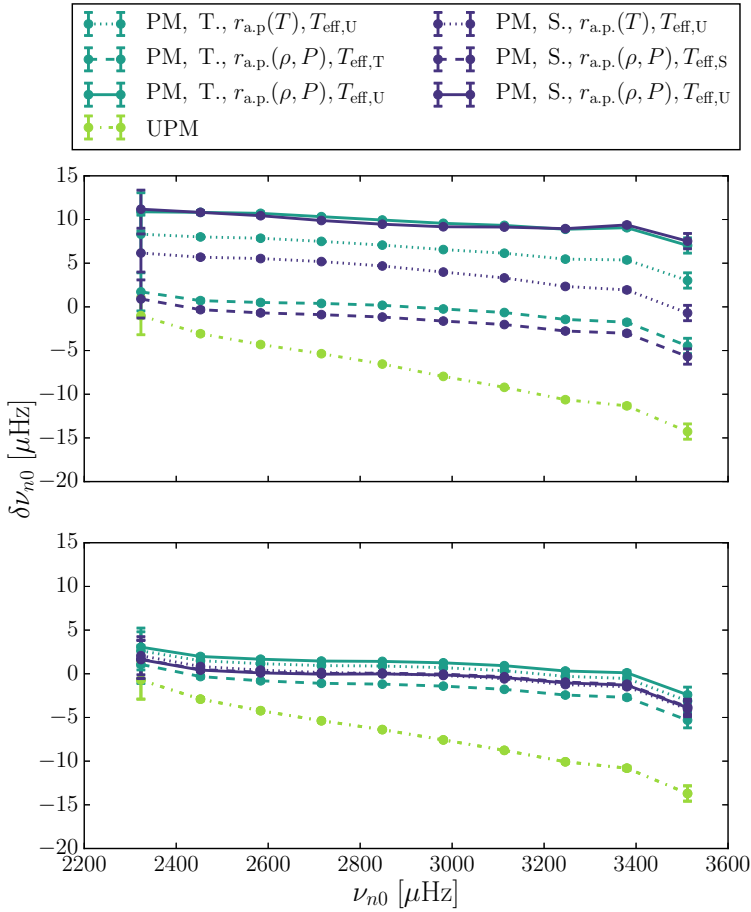


Starting with *KIC 9025370*, fig. 6.11 shows a comparison between observations and model frequencies for the **UPM's** and the associated **PM's**. Each of two panels corresponds to one of the two grids of 1D stellar models. The observed frequencies are from the **LEGACY** sample. We selected the shown **UPM's** based on the individual frequencies, but found that an analysis relying on the frequency separation ratios will lead to similar results. From table 6.1 we note that  $T_{\text{eff}}$  of the 3D-calibrated **UPM** does not lie within three standard deviations of the spectroscopic value and that the  $T_{\text{eff}}$  of the standard input model likewise lies above the spectroscopic value. This may suggest that the spectroscopic constraints underestimate the effective temperature in the case of *KIC 9025370* – this is also supported by Sahlholdt et al. (2018) using the **IRFM**.

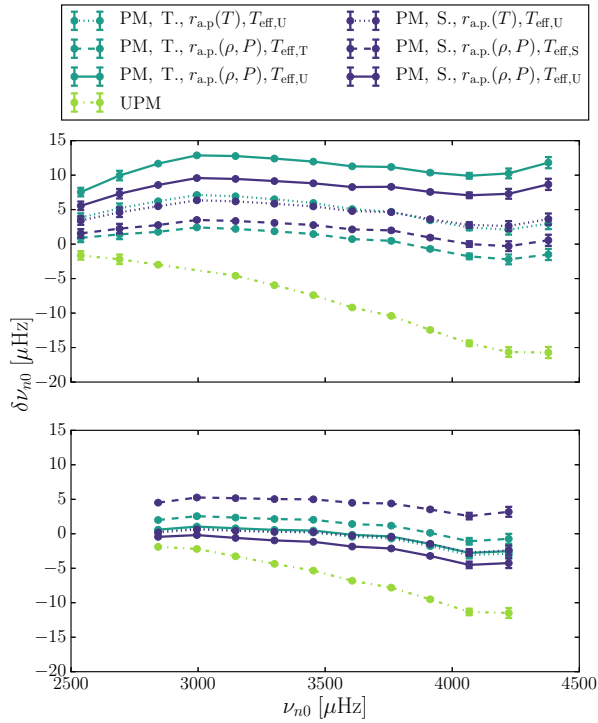
Figure 6.12 on page 119 displays the computed model frequencies for *KIC 9955598* that appears in both samples. For the sake of comparison, we exploited that the star is in both the **KAGES** the **LEGACY** sample, and used the two different sets of frequencies to select the 3D-calibrated and standard input **UPM's**, respectively. Similar best-fitting **UPM's** are found, when fitting frequency ratios and individual frequencies from either sample.

Figure 6.13 on page 120 visualises the asteroseismic results obtained for the star *KIC 11133306*. When constructing **PM's** of *KIC 11133306* based on the **STAGGER** grid and either **UPM**, the discontinuity-minimization did not lead to a unique solution within the spectroscopic and asteroseismic constraints. On the contrary, two distinct local minima are found in the investigated region of the  $(T_{\text{eff}}, \log g)$ -plane. We chose the atmosphere with  $T_{\text{eff}}$  closest to that of the **UPM**. This example underlines the necessity of establishing a rigid scheme for selecting the  $\langle 3D \rangle$ -atmosphere when constructing **PM's**.

Figure 6.14 on page 121 summarizes the obtained results for our final case, *KIC 11772920*. As was the case with *KIC 11133306*, the suggested



**Figure 6.11 | Patched model analysis of KIC 9025370.** Frequency differences between observations and 2 **UPM** as well as 12 **PM**'s. The latter are produced from interpolated atmospheres from either the **Trampedach grid** (T.) or the **STAGGER grid** (S.). The patches are constructed with either the same  $T_{\text{eff}}$  as the **UPM** ( $T_{\text{eff,U}}$ ); or with  $T_{\text{eff,S}}$  or  $T_{\text{eff,T}}$  (cf. table 6.1). Different patching quantities are used: either a combination of  $P$  and  $\rho$ , or  $T$ . In all cases, the patching points are chosen at the depth, at which the closest match in the  $(P,\rho)$ - or  $(P,T)$ -plane between the interior and the atmosphere is found. **Upper panel)** 3D-calibrated **UPM**. **Lower panel)** Standard input **UPM**.



**Figure 6.12 | Patched model analysis of KIC 9955598.** As fig. 6.11. The associated effective temperatures are listed in table 6.1. **Upper panel)** 3D-calibrated **UPM**, using KAGES frequencies. **Lower panel)** Standard input **UPM**, using LEGACY frequencies.

minimization of discontinuities did not lead to a unique solution in the case of the **STAGGER** grid. Here we found local minima at 5043 K and 5506 K. However, when constructing **PM**'s from the colder atmosphere, we obtained models smaller than the corresponding **UPM**, which is inconsistent with our other patched models. Consequently, we discard this solution and settle for the warmer minimum.

### 6.5.3 Discussion

Generally, the use of 3D **PM**'s reduce the model frequencies resulting in an improvement of the **surface effect**. Using different atmosphere grids,

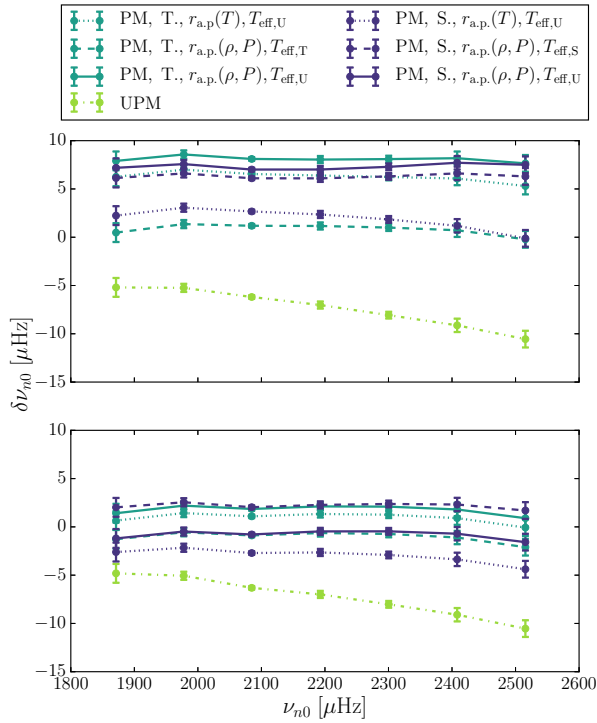


Figure 6.13 | Patched model analysis of KIC 11133306. As fig. 6.11.

interior stellar models, or patching quantities affect the frequency difference by up to a few microhertz. These impacts are small compared to the **surface effect** itself, but substantial compared to the residual discrepancy between model frequencies and observations. While the **surface effect** increases with frequency for the **UPM's**, the discrepancies between observations and the model frequencies for all 48 **PM's** are not strongly frequency dependent.

We emphasize again that the **PM's** are not expected to completely reproduce the observations as the modal effects are not accounted for. According to Houdek et al. (2017), disregarding modal effects is expected to result in **PM's** which underestimate (and hence *over-correct*) the eigenfrequencies – so this is what we expect to obtain from our **PM's**. Hence, **PM's** already *under-correcting* the frequencies are not expected to correctly reproduce the actual structure if the modal effects are added on top. While most of the *3D-calibrated* **PM's** does indeed *over-correct* the model frequencies as

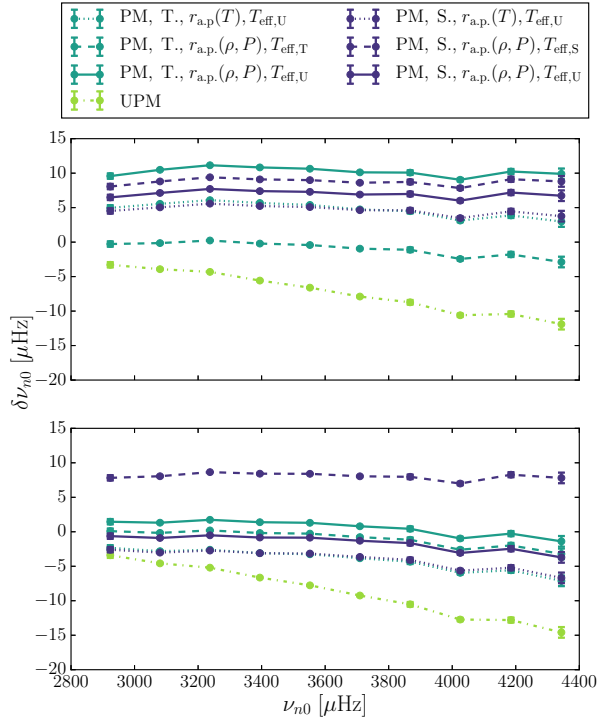


Figure 6.14 | Patched model analysis of KIC 11772920. As fig. 6.11.

expected, roughly half of *standard input PM's* do not. Thus, the 3D-calibrated models perform much better than their standard input counterparts in this respect.

The discrepancy in  $T_{\text{eff}}$  between the **UPM** and the atmosphere minimizing the discontinuities are generally found to be larger for the 3D-calibrated models (cf. table 6.1). Just as in the solar case, such high discrepancies in  $T_{\text{eff}}$  strongly affect the evaluated surface correction. Consequently, the frequency differences between the different 3D-calibrated **PM's** are larger than in the case of the standard input models. This seemingly reflects the rather simplistic approaches of selecting the global parameters of the patched atmospheres.

Each of the four 3D-calibrated **UPM** has a  $T_{\text{eff}}$  larger than the respective standard input models. A part of this effect probably stem from the fact that we kept the metallicity fixed when fitting the 3D-calibrated models

with **BASTA**, while it is a free variable for the fit to the standard input models. Moreover, in contrast to the standard input models, the 3D-calibrated models have been computed neglecting atomic diffusion due to the restrictions imposed by the **Trapedach grid**. According to e.g. Silva Aguirre et al. (2015), the neglect of diffusion affects the global parameters of the best-fitting **UPM**'s for stars in this mass regime.

The **p-mode** oscillation frequencies of the 3D-calibrated models are more sensitive to the choice of the patching quantity than the standard input models are. A larger sensitivity to the choice of the patching quantity generally implies larger discontinuities between the patched atmosphere and the interior **UPM** at the patching point.

The frequency shifts between the different choices of patching quantities are in the order of a few microhertz and several factors may contribute to this behaviour. First of all we note that a direct comparison between the panels of figs. 6.11–6.14 is actually misleading: The global parameters of the 3D-calibrated models and their standard input counterparts are not identical; neither are the input physics (**EOS**, opacities, mixtures) in the two sets. Secondly, it will partially reflect the accuracy of the interpolation scheme as concluded from the analysis of the solar **PM**'s.

Thirdly, the outermost layers of the 3D-calibrated models do not perfectly mimic the underlying 3D simulations, which contributes to the sensitivity to the choice of the patching quantity. In order to assess how well the implementation of the 3D  $T(\tau)$  relation and the calibrated  $\alpha_{\text{MLT}}$  actually reproduces the structure of the **Trapedach grid** atmospheres, we constructed **PM**'s with the calibrated **SSM** from the 3D-calibrated grid as the **UPM**. The 3D-calibrated solar **UPM** has the same  $T_{\text{eff}}$  as the solar atmosphere in the **Trapedach grid**, and consequently no interpolation is required. The resulting frequencies are shown in fig. 6.15.

As can be seen from the figure, we find the choice of the patching quantity to affect the eigenfrequencies by up to 4  $\mu\text{Hz}$ , i.e. by roughly the same amount as we found for *Model S* when patching the same solar atmosphere (see section 6.3.1). This frequency difference reflects the structural change arising from a shift in the distance of the patching point from the solar centre: Because the temperature of the atmosphere is roughly 1 % higher at the base than the temperature of the **UPM** at the same pressure,  $r_{\text{a.p.}}(T)$  is roughly

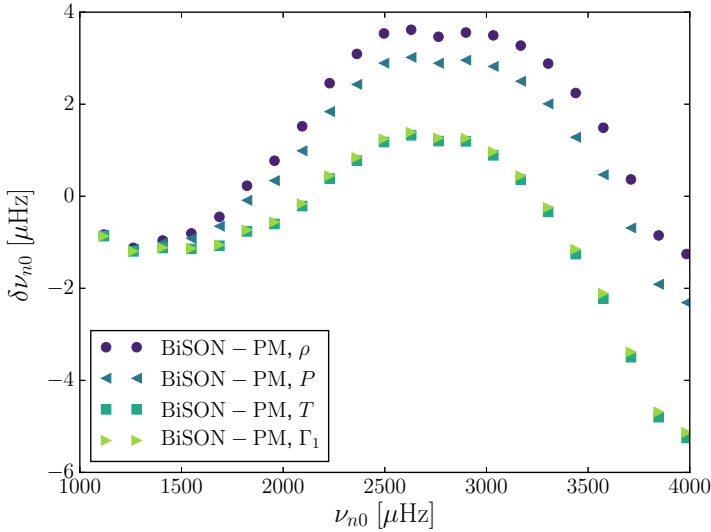


**Figure 6.15 | Comparison of patching quantities in a solar model.** Frequency differences as in fig. 6.9 on page 109, but for a 3D-calibrated solar model and the solar atmosphere in the **Trampedach grid**. All models are patched 2.5 Mm below the surface.

40 km less than  $r_{\text{a.p.}}(P)$ . Thus, we find the frequencies to be very sensitive to changes in the structure of the **PM** in accordance with our study of *Model S*.

For comparison, we performed yet another solar calibration. We used the same input physics as the 3D-calibrated **SSM** in fig. 6.15, but employed a traditional Eddington atmosphere and constant  $a_{\text{MLT}}$ —i.e., a calibration equivalent to the standard *Eddington reference* in chapter 5. When constructing **PM**'s from this solar model, they show the same sensitivity to the patching criteria as the 3D-calibrated **UPM** in fig. 6.15. Changing the boundary conditions and  $a_{\text{MLT}}$  merely increases the model frequencies by less than 1  $\mu\text{Hz}$  for all patching quantities. This finding is also in good agreement with the results presented in fig. 6.8 on page 107, showing that the boundary layers have little influence on the interior structure sufficiently deep within the star.

A final note: To facilitate an easy comparison between fig. 6.15 and figs. 6.7–6.9, we have not corrected for sphericity or adjusted  $\log g$  to fit the

interior model at the *a.p.* in the displayed **PM's**. Applying such corrections will increase the model frequencies of the presented solar model by up to 1  $\mu\text{Hz}$ .

## 6.6 Conclusions

In this work, we presented an analysis of patched stellar models (**PM's**) built using a new scheme to improve on the near-surface deficiencies of stellar models leading to the asteroseismic **surface effect**. We have developed a new method to interpolate in the mean structure of 3D **RHD** simulations enabling the constructing of **PM's** with arbitrary  $T_{\text{eff}}$  and  $\log g$ . This is a significant improvement over earlier efforts, which have been restricted to constructing **PM's** exactly matching an underlying 3D atmosphere.

We tested our interpolation scheme by reconstructing existing atmospheres and found a correct representation in the case of cold **MS** stars. In other regions of the **HRD**, a denser sampling of the underlying 3D grids is required to reach the precision required for the purpose of **asteroseismology**.

Having established a robust interpolation scheme, we investigated how a mismatch in  $T_{\text{eff}}$  and  $\log g$  between the base un-patched model (**UPM**) and the patched  $\langle 3\text{D} \rangle$ -envelope affects the asteroseismic results. In order to overcome the non-negligible effects from even small mismatches, we present a new method of minimizing the discontinuities at the bottom of the atmosphere when patching. This new scheme yields different model frequencies compared to the traditional approach with matching  $T_{\text{eff}}$  and  $\log g$ , and thus illustrate the important of establishing a rigid matching scheme.

We also investigated how different patching criteria affect the helioseismic results based on patched solar models. While the model frequencies are mostly unaffected by the patching depth (if the patch is performed sufficiently deep within the adiabatic region, the choice of patching quantity may shift the model frequencies by a few microhertz. These shifts are small compared to the **surface effect** itself but comparable to the residual discrepancy between model frequencies and observations.

Our **PM's** were applied on the Sun and on four stars observed with *Kepler*. We find the resulting model to have frequencies in much better agreement with observations and have thus decimated the structural **surface effect**. Comparing to earlier works, the results are consistent considering

that modal effects have not been taken into account. Based on the presented results, we are able to identify several steps in the post-evolutionary patching procedure, for which different choices (all of which are seemingly equally valid) affect the outcome of asteroseismic analyses.

All in all, the present chapter clearly underlines the potential of post-evolutionary patching, showing how the implementation of information from 3D RHD simulations can be used to improve 1D stellar models. A significant improvement of the method would be to include an equally robust implementation of the 3D results from 3D simulations throughout the stellar evolution. The implementation from chapter 5 as a step along the way, but must be combined with the results presented in this work to have a large impact on the structure. We will continue this endeavour in the following chapters.



## Stellar Evolution with 3D Simulations On the Fly I

In the previous chapters, two different approaches of improving stellar evolution models using 3D RHD hydrodynamics simulations of stellar surface convection have been presented. Neither of them proved fully satisfactory: the *dynamic/condensed* technique from chapter 5 only had a small structural impact, and the *static/patching* method from chapter 6 left the evolution unaltered.

This was the motivation for our project aiming at creating a novel procedure for using averaged 3D envelopes for stellar evolution on the fly– the goal was to have the “best of both worlds”. The ⟨3D⟩-envelopes are obtained from an interpolation procedure based on the work presented in chapter 6; and are used as boundary conditions to determine the interior structure, as well as appended in each iteration of the calculation. This project led to a pair of companion papers, and the first part of the work was *originally published in*:

A. C. S. Jørgensen, J. R. Mosumgaard, A. Weiss, V. Silva Aguirre, and J. Christensen-Dalsgaard (2018). “Coupling 1D stellar evolution with 3D-hydrodynamical simulations on the fly - I. A new standard solar model”. *Monthly Notices of the Royal Astronomical Society* 481, pp. L35–L39

and is reproduced in this chapter. The second paper has recently been published, and can be found in chapter 8 on page 139. The project was jointly

lead by Andreas C.S. Jørgensen and myself. We developed the method, conducted the tests, and performed the analyses in close collaboration. Based on a rough implementation by him I wrote the final code in **GARSTEC**. Our implementation relies on the same interpolation and triangulation routines (Akima, 1970; Cline and Renka, 1984; Akima, 1991) I had already implemented in **GARSTEC** for the work presented in chapter 5. The first draft of the paper was written by A. Jørgensen, but we reworked it together.

The content has been reformatted, but the presented text is not far from its original form. But once again, alterations have been performed to increase readability, minimise text overlap, and to include references to earlier chapters. The introduction has been significantly reduced, and so has the conclusion. Finally, in the original paper we referred to the Jørgensen et al. (2017) as “J17”, however that has been replaced by a reference to chapter 6.

## Summary of the Chapter

Standard 1D stellar evolution models do not correctly reproduce the structure of the outermost layers of stars with convective envelopes as known from **helioseismology**. This has been a long-standing problem in stellar modelling affecting both the predicted evolutionary paths and the attributed oscillation frequencies, and indirectly biasing numerous quantities derived from stellar evolution calculations. We present a novel method that mostly eliminates these structural defects by appending mean 3D simulations of stellar envelopes. In contrast to previous attempts we impose the complete structure derived from 3D simulations at each time step during the entire evolution. For this purpose, we interpolate in grids of pre-computed 3D simulations and use the resulting structure as boundary conditions in order to solve the stellar structure equations for the 1D interior at each time step. Our method provides a continuous transition in many quantities from the interior to the imposed interpolated 3D surface layers. We present a solar calibration model and show that the obtained structure of the surface layers reliably mimics that of the underlying 3D simulations for the present Sun. Moreover, we perform a helioseismic analysis, showing that our method mostly eliminates the structural contribution to the discrepancy between model frequencies and observed **p-mode** frequencies.

## 7.1 Introduction

As described in chapter 4, an approach to avoid empirical corrections of the asteroseismic **surface effect** is to use patched models (**PM's**), where the outer layers are substituted by a  $\langle 3D \rangle$  envelope from **RHD** simulations. The fact that patching is performed after a traditional 1D evolutionary calculation has been performed, can lead to inconsistencies and discontinuities in the **PM's** (see also chapter 6). Nevertheless, as shown by Houdek et al. (2017), this kind of approach does mend the structural inadequacies of stellar models and results in model frequencies that are in good agreement with observations once so-called modal effects including non-adiabatic energetics have been taken into account.

In order to instead include information from 3D simulations during the entire evolution, Mosumgaard et al. (2018) – see chapter 5 – implemented the  $T(\tau)$  relation and calibrated  $\alpha_{MLT}$  from 3D **RHD** simulations. However, as shown earlier, this does not significantly reduce the structural **surface effect**.

In this chapter a new **SSM** is presented: throughout the entire evolution the outermost layers are substituted with a mean 3D structure, adjusting the interior model accordingly in each iteration at every time step. This solar model has been obtained using a traditional solar calibration procedure (cf. section 1.6.3). We compare the obtained structure with the employed 3D simulations and present **p-mode** frequencies.

## 7.2 Implementation

We compute stellar structure models with **GARSTEC**. In each iteration, at every time step, the pressure and temperature stratifications of the outermost layers have been adopted from interpolated mean 3D **RHD** simulations of stellar atmospheres – denoted  $\langle 3D \rangle$ -envelopes hereafter. For this purpose, we have used the **STAGGER grid** and the interpolation method presented by chapter 6. We have only included models with solar metallicity: For the sake of consistency between the interior model and the **STAGGER grid**, we use the composition published by Asplund et al. (2009, AGSS09). Of the corresponding 29 3D simulations in the **STAGGER grid** we have excluded one that is not fully relaxed.

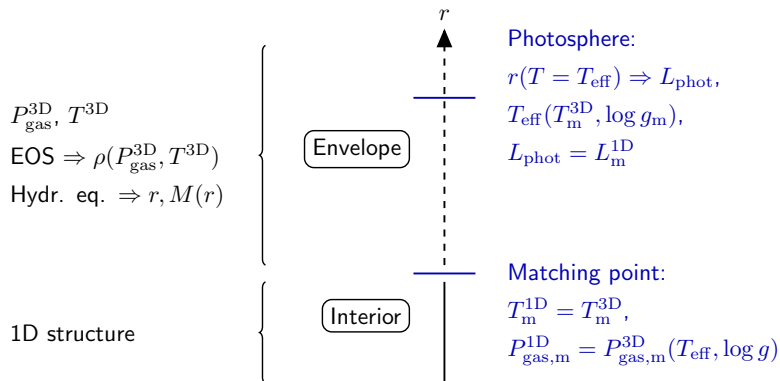


**Figure 7.1 | Schematic overview of the implementation.** How the  $\langle 3\text{D} \rangle$ -envelopes from the **STAGGER** grid are included in **GARSTEC**. The appended envelope is adopted from interpolated 3D simulations and yields the outer boundary conditions of the interior. The subscript ‘m’ refers to values at the **matching point**. Details in the text.

**GARSTEC** determines stellar structure models from the centre to the outer boundary by solving the stellar structure equations (section 1.2). Usually, the outer boundary is placed at the photosphere and the boundary conditions are obtained from Stefan-Boltzmann’s law and from an integration of an Eddington grey atmosphere (cf. section 1.6.1).

In our implementation we supply the two required outer boundary conditions by employing interpolated  $\langle 3\text{D} \rangle$ -envelopes. The method is sketched in fig. 7.1. As illustrated in this figure, we supply the boundary conditions of the interior model far below the photosphere at the so-called **matching point**. Outside of the **matching point**, the temperature as a function of gas pressure ( $T(P_{\text{gas}})$ ) is taken directly from interpolated  $\langle 3\text{D} \rangle$ -structures. We will use the superscripts ‘1D’ and ‘3D’ to indicate whether the value refers to the interior model or the  $\langle 3\text{D} \rangle$ -envelope, respectively.

As suggested by chapter 6, we interpolate  $P_{\text{gas}}^{3\text{D}}$  and  $T^{3\text{D}}$  in the  $(T_{\text{eff}}, \log g)$ -plane, scaling both quantities before the interpolation. To determine the scaling factor, we introduce the term “*density jump*” to denote the feature in the density profile near the surface, where a density inversion can take place in later evolutionary stages. This point is defined as the minimum in  $\partial \log \rho^{3\text{D}} / \partial \log P_{\text{gas}}^{3\text{D}}$ . The pressure at the density jump  $P_{\text{gas,jump}}^{3\text{D}}$  is set to be

the scaling factor. This scaling ensures that abrupt changes in all relevant quantities near the surface take place at the same scaled pressure, making the interpolation more reliable: as shown in fig. 6.2 on page 100, the scaled stratifications look rather similar for all simulations. Moreover, the scaling factors behave roughly linearly as a function of  $T_{\text{eff}}$  and  $\log g$  (cf. fig. 6.3). After the interpolation the scaling is reverted.

During an initial phase on the **PMS**, the **matching point** is slowly moved inwards starting near the photosphere. This is done for convergence purposes and implies that the scaled gas pressure at the **matching point** increases  $P_{\text{gas}}^{3\text{D}}/P_{\text{gas,jump}}^{3\text{D}}$ . When the desired value is reached, the quantity is kept fixed for the remaining evolution. For a given value of the scaled gas pressure, any combination of  $T_{\text{eff}}$  and  $\log g$  corresponds to a unique value of  $T^{3\text{D}}$  at the **matching point**:  $T_{\text{m}}^{3\text{D}}$ . Here, the subscript ‘m’ refers to the value at the **matching point** (cf. fig. 7.1).

In order to compute the gas pressure and the temperature of the  $\langle 3\text{D} \rangle$ -envelope at the **matching point**, we need to infer  $T_{\text{eff}}$ . We do this by enforcing a match in  $T$  at the **matching point**, i.e. by inverting the problem: we evaluate the effective temperature that corresponds to  $T_{\text{m}}^{3\text{D}} = T_{\text{m}}^{1\text{D}}$  and  $\log g_{\text{m}}$  by interpolation in the **STAGGER grid**.

Having established  $T_{\text{eff}}$ , we then compute the appropriate scaling factor for the gas pressure by interpolation. This gives us the pressure at the matching point of the interpolated  $\langle 3\text{D} \rangle$  structure  $P_{\text{gas,m}}^{3\text{D}}$ , which is to be compared with the gas pressure predicted by the interior model at the **matching point**  $P_{\text{gas,m}}^{1\text{D}}$ . This yields the first of our two boundary condition:  $P_{\text{gas,m}}^{1\text{D}}$  must match  $P_{\text{gas,m}}^{3\text{D}}$ . The Henyey scheme will iteratively adjust the interior structure to achieve this, which will lead to changes in  $P_{\text{gas,m}}^{1\text{D}}$ . For each Henyey iteration,  $T_{\text{eff}}$  and hence  $P_{\text{gas,m}}^{3\text{D}}$  are also re-evaluated until convergence.

Above the **matching point**,  $P_{\text{gas}}$  is determined based on the computed scaling factor and  $T$  as a function  $P_{\text{gas}}$  is derived by interpolation in the  $\langle 3\text{D} \rangle$ -envelope. Thus, we append  $P_{\text{gas}}$  and  $T$  from an interpolated  $\langle 3\text{D} \rangle$ -envelope in each iteration. The density at each mesh point in the appended envelope is then computed by the stellar evolution code from the **EOS**. We note that the **EOS** used in the stellar evolution code to obtain  $\rho$  is not identical to the **EOS** used in the 3D simulations. Nevertheless, as will be discussed in the next section,  $\rho$  is reproduced with high accuracy.

The radius  $r$  and contained mass  $M(r)$  are computed iteratively from hydrostatic equilibrium. In this work, we ignore the contribution from

the turbulent pressure. The remaining thermodynamic quantities in the envelope are determined from the **EOS**, including the first adiabatic index  $\Gamma_1$ . Since the surface layers are convective, the composition of the envelope is assumed to be the same as in the outermost point of the interior model. In this way, we end up with a pseudo- $\langle 3\text{D} \rangle$ -structure beyond the **matching point**.

Having established  $r$  of each mesh point, we determine  $r(T = T_{\text{eff}})$  by interpolation in order to locate the photosphere, where Stefan-Boltzmann's law (section 1.6.1) is assumed valid under the assumption that the energy generation in the appended envelope is negligible. The associated luminosity  $L_{\text{phot}}$  can then be compared to luminosity at the **matching point**  $L_{\text{m}}^{1\text{D}}$ . This is the second boundary condition for the Henyey scheme:  $L_{\text{phot}}$  must match  $L_{\text{m}}^{1\text{D}}$ .

### 7.3 A Solar Calibration

Having established the method, we performed a solar model calibration using interpolated  $\langle 3\text{D} \rangle$ -envelopes from the **STAGGER grid** on the fly as described above. We used a standard solar calibration (section 1.6.3), but changed the default target value of  $T_{\text{eff}}$  to that of the solar simulation in the **STAGGER grid**:  $T_{\text{eff}} = 5768.5$  K. The computation used **OPAL** opacities, the *Free-EOS*, and the **AGSS09** mixture (with a surface value of  $Z/X = 0.01828$ ). Due to microscopic diffusion, only the envelope of the final model of the present Sun has the same composition as the underlying  $3\text{D}$  simulation, because we do not interpolate in the composition of the  $3\text{D}$  simulations.

After an initial phase on the **PMS**, the logarithm of the scaled pressure at the **matching point** is fixed at

$$\log \frac{P_{\text{gas,m}}^{3\text{D}}}{P_{\text{gas,jump}}^{3\text{D}}} = 1.20 \quad (7.1)$$

throughout the entire subsequent evolution. For the associated model of the current Sun, the chosen scaled pressure corresponds to a temperature of  $T_{\text{m}} = 1.41 \times 10^4$  K and a depth of  $d_{\text{m}} = 0.94$  Mm below the photosphere. The **matching point** should be placed as deep within the  $1\text{D}$  model as possible, since the stratification becomes more adiabatic with increasing depth. The chosen scaled pressure at the **matching point** is a compromise between

**Table 7.1 | Resulting parameters from the solar calibrations.** Derived initial abundances as well as the helium surface abundance and the radius coordinate of the base of the convective envelope. Results shown for two solar calibrations: one with an Eddington atmosphere, and another using the **STAGGER grid**.

Bound. con.	$a_{\text{MLT}}$	$Y_{\text{i}}$	$Z_{\text{i}}$	$Y_{\text{s}}$	$r_{\text{cz}}/R_{\odot}$
Eddington	1.78	0.2653	0.0152	0.2343	0.7244
$\langle 3\text{D} \rangle$ -envelopes	3.30	0.2652	0.0152	0.2343	0.7243

this requisite and the limitations of the interpolation scheme imposed by the resolution of the **STAGGER grid** and by the depths of the simulations.

Our implementation of  $\langle 3\text{D} \rangle$ -envelopes in stellar models yields an  $a_{\text{MLT}}$  roughly a factor of two higher than the value obtained, when using an Eddington grey atmosphere. This reflects the fact that the mixing length is calibrated to reproduce  $R_{\odot}$ : When using the **STAGGER grid** as boundary conditions, the mixing length only directly affects the extent of a superadiabatic layer much thinner than the corresponding layer in an **SSM**, since the extent of the region beyond the **matching point** is dictated by the interpolated  $\langle 3\text{D} \rangle$ -envelope. Hence, the change in  $a_{\text{MLT}}$  partially reflects the fact that 3D atmospheres are more extended than their 1D counterparts, due to turbulent pressure and convective back-warming. A similar result was obtained by Schlattl, Weiss, and Ludwig (1997), who pointed out that a spatially variable mixing length must be introduced when appending more realistic outer layers in order to reproduce  $T(P_{\text{gas}})$ . Physically,  $a_{\text{MLT}}$  reproduces the mean temperature gradient between the top and bottom of the superadiabatic layer. With increasing matching depth, the average temperature gradient of the region modelled by **MLT** will be closer to being adiabatic; thus,  $a_{\text{MLT}}$  should increase accordingly.

As will be discussed in the companion paper by Mosumgaard et al. (2019) – included as chapter 8 – the obtained value of  $a_{\text{MLT}}$  is affected by the matching depth. However, this is shown to not shift the evolutionary track significantly if the **matching point** is placed sufficiently deep within the superadiabatic region.

The obtained  $a_{\text{MLT}}$  for the presented solar model is listed in table 7.1 alongside other quantities from the solar calibration.  $Y_{\text{s}}$  denotes the surface

helium abundance and can be compared to the helioseismic value obtained by Basu and Antia (2004) as  $Y_{s,\odot} = 0.2485 \pm 0.0035$ . Another quantity determined from **helioseismology** is radius coordinate of the base of the convection zone  $r_{cz}$ , inferred by Basu and Antia (1997) as  $r_{cz} = (0.713 \pm 0.001) R_{\odot}$ . The discrepancies can be attributed to the use of AGSS09 (Serenelli et al., 2009).

Table 7.1 also contains the corresponding values for a standard solar calibration with an Eddington grey atmosphere. As can be seen from table 7.1, our method, involving  $\langle 3D \rangle$ -envelopes, does not affect  $Y_s$  or  $r_{cz}$  significantly.

### 7.3.1 Structure of Outermost Layers

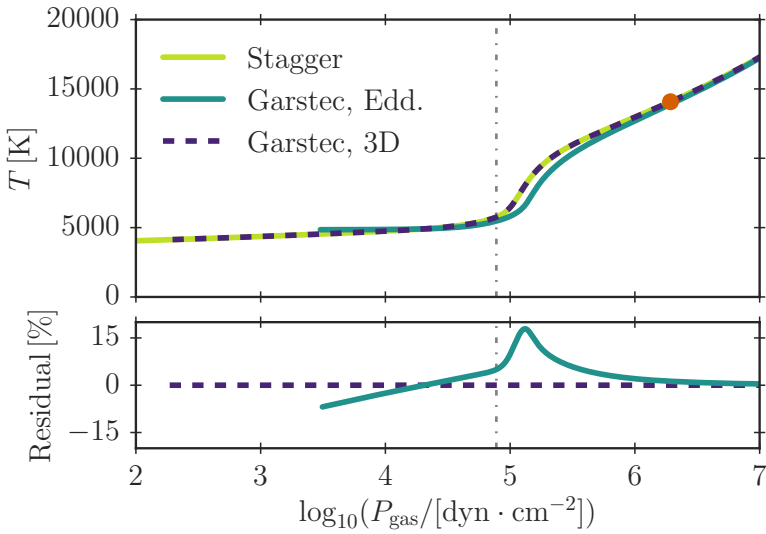
We now compare the structure obtained by **GARSTEC** with that of the specific 3D solar simulation in the **STAGGER grid**. The results are shown in figs. 7.2–7.4. The figures include both of the **GARSTEC** models from table 7.1 to have the Eddington case as reference.

Figure 7.2 shows  $T(P_{\text{gas}})$ , which by construction is reproduced correctly our new scheme. From fig. 7.3, we see that the **EOS** used by the 1D evolution code closely recovers  $\rho(P_{\text{gas}})$ , although the density is systematically 1 – 2 % too low. This may partly reflect differences in the **EOS** used by the 1D and 3D codes, and partially  $\rho$  being a non-linear function of  $P_{\text{gas}}$  and  $T$ . Specifically, the geometrical mean of the density in the **STAGGER grid** is not expected to correspond to the density derived from the average of  $P_{\text{gas}}$  and  $T$  (Trampedach et al., 2014a).

We note that  $\log g$  is assumed to be constant in the **STAGGER grid** envelope in contrast to the 1D simulation, which slightly skews the comparison in  $r$ . Having that in mind, fig. 7.4 shows that our method closely reproduces the depth of the underlying 3D envelope as a function of gas pressure, despite the neglect of turbulent pressure and the discrepancy in  $\rho$ . Thus, our new method reproduces the expected  $\langle 3D \rangle$ -structure from the **STAGGER grid** very well without the need for post-evolutionary patching. As expected, the Eddington grey atmosphere leads to much larger residuals.

### 7.3.2 Oscillation Frequencies

Having obtained a structure that closely resembles the mean stratification of 3D simulations, we computed stellar oscillation frequencies using **ADIPLS**.



**Figure 7.2 | Reproduction of the solar envelope using our new implementation.**

The vertical grey line indicates the position of the photosphere and the red dot denotes the location of the **matching point**. **Upper panel)** Temperature as function of gas pressure for the (3D) solar envelope in the **STAGGER grid** as well as the two solar calibrations listed in table 7.1. **Lower panel)** Relative residuals between the 3D solar envelope and each solar calibration.

Figure 7.5 on page 137 shows the frequency differences  $\delta\nu_{nl}$  (not to be confused with the small frequency separations) between the predicted model frequencies and observations from **BISON**.

For comparison, we have also included a solar patched model (**PM**) in fig. 7.5 constructed as described in chapter 6. The patching radius was determined based on  $T$ , resulting in a depth of 2.1 Mm below the surface, i.e. further down within the nearly adiabatic region than the **matching point** of our new implementation. The **PM** has been constructed such that it has the same interior as the final solar calibration model, whose outer layers are dictated by the **STAGGER grid**. As opposed to the models constructed with 3D on the fly, the **PM** includes turbulent pressure in the envelope. Note that turbulent pressure was neglected during the entire evolution and is not taken into account below the patched envelope.

In order to compute frequencies for the **PM**, one must account for the turbulent pressure in the oscillation equations. As elaborated upon by Houdek

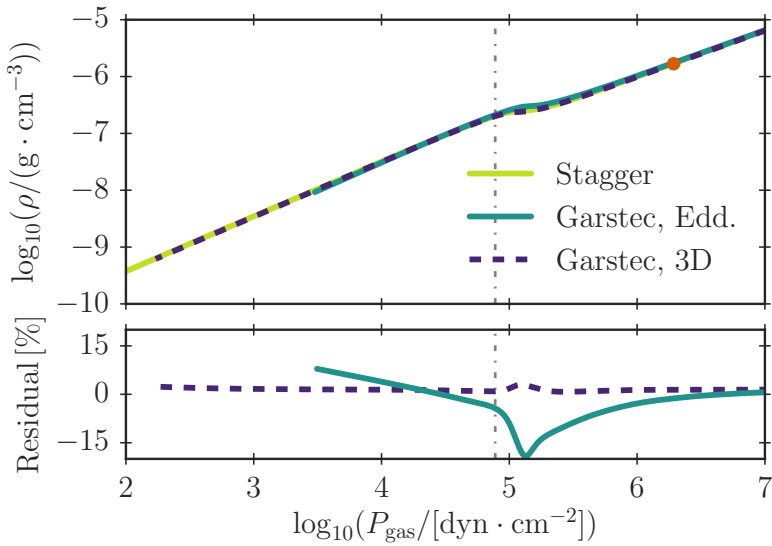


**Figure 7.3 | Reproduction of the solar envelope.** As fig. 7.2 but for the density as a function of gas pressure.

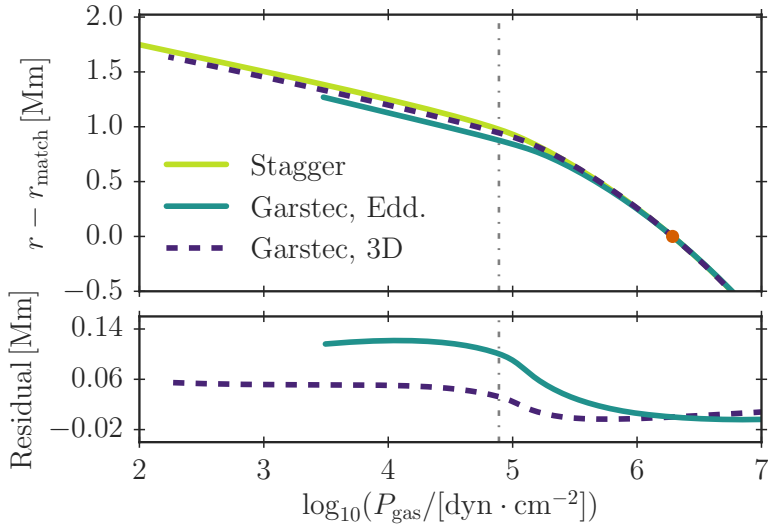


**Figure 7.4 | Reproduction of the solar envelope.** As fig. 7.2 but for the height above the matching point as a function of gas pressure. Here we show the absolute residuals.

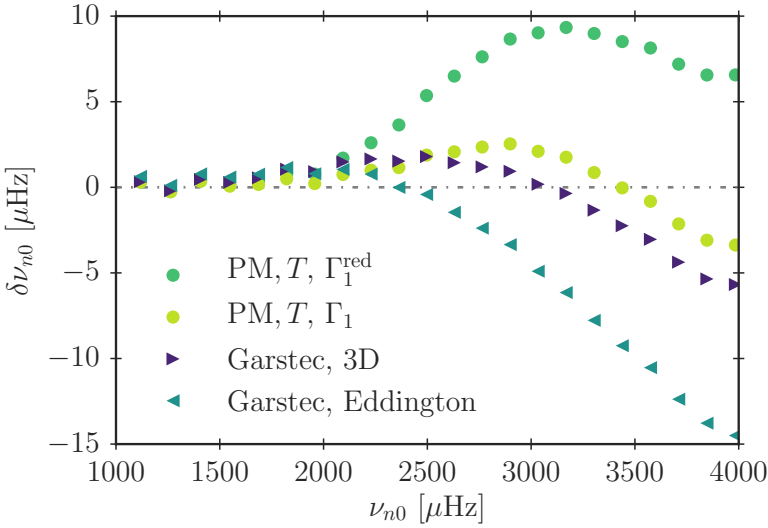


**Figure 7.5 | Reproduction of the solar oscillation frequencies.** Radial mode frequency difference between **BISON** observations and the solar models listed in table 7.1.

et al. (2017), this can be achieved by adjusting  $\Gamma_1$  by a factor of  $P_{\text{gas}}/P$  as

$$\Gamma_1^{\text{red}} = \frac{P_{\text{gas}}\Gamma_1^{\text{1D}}}{P}, \quad (7.2)$$

which is called “*reduced*  $\Gamma_1$ ” in the nomenclature of Rosenthal et al. (1999). The associated frequencies are included in fig. 7.5.

However, some authors (e.g. Ball et al., 2016; Magic and Weiss, 2016; Jørgensen et al., 2017) do not use  $\Gamma_1^{\text{red}}$  but compute frequencies of **PM**’s based on  $\Gamma_1$ . This amounts to the assumption that the turbulent pressure reacts in the same way as the gas pressure to density perturbations – the “*gas*  $\Gamma_1$ ” from Rosenthal et al. (1999). To facilitate an easy comparison with these authors, we have recomputed the frequencies under this approximation and included these in fig. 7.5.

As can be seen from the figure, our new method leads to model frequencies that are very similar to the frequencies obtained from **PM**’s when using  $\Gamma_1$  in the frequency calculations: at 4000  $\mu\text{Hz}$  the remaining frequency difference between our solar calibration and observations is only 6  $\mu\text{Hz}$ , while

the frequency difference is  $15 \mu\text{Hz}$  at the same frequency, when using an Eddington grey atmosphere. Thus, with our new method, we are able to significantly reduce the structural contribution to the **surface effect**.

The remaining frequency differences between the **PM's** and our solar calibration model with  $\langle 3\text{D} \rangle$ -envelopes as its boundary condition can partly be attributed to the neglect of turbulent pressure and the discrepancies in the density. Furthermore, this frequency differences will reflect the patching and matching depths, at least to some extent. However, as will be discussed in chapter 8, the frequencies are rather insensitive to the scaled pressure of the **matching point**, if the **matching point** is placed sufficiently deep within the superadiabatic region.

## 7.4 Conclusions

We have presented a novel method for including the mean pressure and temperature stratifications from 3D simulations directly in 1D stellar evolution codes and exploit this to adjust the structure at every time step. This has been achieved without the need of parametrizations or post-evolutionary patching. It is the first computation of a solar model, for which the structure from 3D simulations has been fully accounted for on the fly. The structure of the resulting 1D models is in very good agreement with the underlying 3D simulations, despite the neglect of turbulent pressure, and despite the fact that only a limited amount of information is taken from the 3D models.

We find that our new method is largely able to eliminate the structural **surface effect**, leading to very promising **p-mode** frequencies. Modal effects have not been accounted for. A direct comparison with post-evolutionarily patched models show only small frequency differences. We largely attribute the remaining differences to the neglect of turbulent pressure.

We address the impact of our new method on the evolutionary tracks in detail in chapter 8, where we will go beyond the present Sun. This includes the first asteroseismic analysis of stars in the *Kepler* field and an investigation of how well our method reproduces the correct structures of 3D-envelopes throughout  $(T_{\text{eff}}, \log g)$ -plane.

## Stellar Evolution with 3D Simulations On the Fly II

In the previous chapter, a novel method for using averaged 3D envelopes on the fly for stellar stellar evolution was presented. That work is continued and expanded in this chapter, where the analysis is performed for parameters across the HRD. Moreover, the procedure is verified to not specifically rely on the Trampedach grid by repeating the analysis with the Trampedach grid. The work was *originally published in*:

J. R. Mosumgaard, A. C. S. Jørgensen, A. Weiss, V. Silva Aguirre, and J. Christensen-Dalsgaard (2019). “Coupling 1D stellar evolution with 3D-hydrodynamical simulations on-the-fly II: Stellar Evolution and Asteroseismic Applications”. *Monthly Notices of the Royal Astronomical Society*, p. 2585

and is reproduced in this chapter. As was the case of the companion paper, the entire project was performed in close collaboration with Andreas C.S. Jørgensen. The additional reference models from the Trampedach grid in section 8.3.3 is taken directly from my work presented in chapter 5. I also conducted the investigation of RG stars in section 8.6 and the analysis leading to section 8.A. He sketched a rough draft of the content, but the final paper is mainly written by me.

The content has been re-typeset to match the thesis style. For this chapter, the presented text is very close to its original form with only minor alterations. Again, the introduction has been reduced with a chunk of it moved to the first two paragraphs of chapter 7 as the motivation. Parts of the conclusion have been moved to chapter 9.

## Summary of the Chapter

Models of stellar structure and evolution are an indispensable tool in astrophysics, yet they are known to incorrectly reproduce the outer convective layers of stars. In the first paper of this series, we presented a novel procedure to include the mean structure of 3D RHD simulations in stellar models on the fly and found it to significantly improve the outer stratification and oscillation frequencies of a SSM. In the present work, we extend the analysis of the method; specifically how the transition point between envelope and interior affects the models. We confirm the versatility of our method by successfully repeating the entire procedure for a different grid of 3D RHD-simulations. Furthermore, the applicability of the procedure was investigated across the HRD and an accuracy comparable to the solar case was found. Moreover, we explored the implications on stellar evolution and find that the RGB is shifted about 40 K to higher effective temperatures. Finally, we present for the first time an asteroseismic analysis based on stellar models fully utilising the stratification of 3D simulations on the fly. These new models significantly reduce the asteroseismic surface term for the two selected stars in the *Kepler* field. We extend the analysis to RG-stars and characterise the shape of the surface effect in this regime. Lastly, we stress that the interpolation required by our method would benefit from new 3D simulations, resulting in a finer sampling of the grid.

### 8.1 Introduction

As has been highlighted throughout this thesis, an essential part of stellar structure calculations is the description of convection. One of the most successful approaches from an astrophysical point of view is the MLT. The advantage of utilizing such parametrizations is that the nuclear reactions rather than the convection motion set the time scale for the evolution calculations. The MLT description of convection is known to be inadequate in the super-adiabatic regions and results in incorrectly modelled outer layers in low-mass stars with convective envelopes, giving rise to the (asteroseismic) surface effect.

In chapter 7, we presented our work to overcome the shortcomings of the traditional *static* and *dynamic* approach (chapter 4) of including information from 3D RHD simulations into stellar models. We used the proce-

cedure from chapter 6 to interpolate between 3D simulations in atmospheric parameters ( $T_{\text{eff}}$  and  $\log g$ ) to create a novel method for using averaged 3D-envelopes on the fly for stellar evolution. The  $\langle 3\text{D} \rangle$ -envelopes are both used as boundary conditions to determine the interior structure and are appended in each iteration of the calculation omitting any need for post-evolutionary patching. In the present work, we extend the investigation of using  $\langle 3\text{D} \rangle$ -envelope on the fly for stellar evolution. We elaborate upon aspects not treated in chapter 7 as well as extend the analysis to stars of different parameters.

The paper is organised as follows. In the next section, the method is briefly summarised, and in section 8.3 we investigate further aspects of the solar model. We apply our procedure to a different grid of 3D simulations in section 8.3.3. The impact on stellar evolution and structure models is examined in section 8.4. In section 8.5, we analyse the asteroseismic impact of our new models and extend the discussion to **RG**-stars in section 8.6.

## 8.2 Method

In this section we briefly summarize key aspects of our method from chapter 7 relevant for the later analyses. Our calculations are performed with **GARSTEC** combined with a grid of 3D **RHD** simulations of stellar surface convection at solar metallicity. In this chapter we rely on the **STAGGER** grid, except for in section 8.3.3 where the **Trampedach** grid is used.

We employ the interpolation from chapter 6 to determine an interpolated mean stratification from the current  $T_{\text{eff}}$  and  $\log g$  of the star. The fundamental quantity of the procedure is the gas pressure as a function of temperature  $P_{\text{gas}}(T)$  extracted from the full  $\langle 3\text{D} \rangle$  simulations. Note that the shallowest 3D simulation in the grid dictates the highest possible pressure in the interpolated envelope. When determining the interpolation range, it is important to exclude the un-physical border regions that strongly reflect the chosen lower boundary conditions.

The obtained  $\langle 3\text{D} \rangle$ -envelope is used to provide the outer boundary conditions for solving the stellar structure equations in the stellar model. In our implementation, the boundary conditions are established deep within the superadiabatic layer – we refer to the corresponding point in the model as the *matching point* (see next section). In other words, this **matching point**

is the outermost point in the interior part and the innermost point in the envelope.

As the photosphere is not a part of the interior model, the first step is to infer the current  $T_{\text{eff}}$  by other means. We do this by setting up another interpolation in the **STAGGER grid**, this time based on the **matching point** temperature  $T_m$ . By assuming the interior and envelope parts to have a common temperature at the **matching point**, the  $T_{\text{eff}}$  corresponding to this  $T_m$  can be evaluated from the interpolation. With  $T_{\text{eff}}$  established, we interpolate in the **STAGGER grid** to obtain the gas pressure as a function of temperature. Then the gas pressure at the bottom of the envelope is compared to the corresponding value predicted by the interior model for its outer mesh point – this is our boundary condition. Thus, in the converged model the gas pressure of the outermost point in the interior matches the value at the innermost point of the envelope; and by construction the temperature also matches.

Outside the **matching point** we directly adopt  $P_{\text{gas}}(T)$  from the interpolated  $\langle 3\text{D} \rangle$ -envelopes – we refer to this part of the combined model as the *appended envelope*. Here the density  $\rho$  and the first adiabatic index  $\Gamma_1$  are computed from the **EOS** used in the stellar evolution code. The radius  $r$  and mass  $M(r)$  at each mesh point in the envelope are calculated from hydrostatic equilibrium, and the photospheric radius of the star is determined based on  $T_{\text{eff}}$  and Stefan-Boltzmann’s law.

In all of our models we use the **OPAL** opacities extended with the low-temperature opacities from Ferguson et al. (2005), and the *Free-EOS*. To be consistent with the simulations in the **STAGGER grid** we use the Asplund et al. (2009, AGSS09) solar composition.

### 8.2.1 The Matching Point

An important feature in the stratification of the 3D simulations is the minimum in  $\partial \log \rho / \partial \log P_{\text{gas}}$ , which was called the *density jump* in the nomenclature of chapter 6 and chapter 7. Given the nature of this near-surface feature, the term *density inflection (point)* might be more accurate; however, to avoid the confusion of modifying the nomenclature, we keep the label *jump* in the following. The pressure and density at this point can be used to construct the *scaled pressure* and *scaled density*, which are the foundation

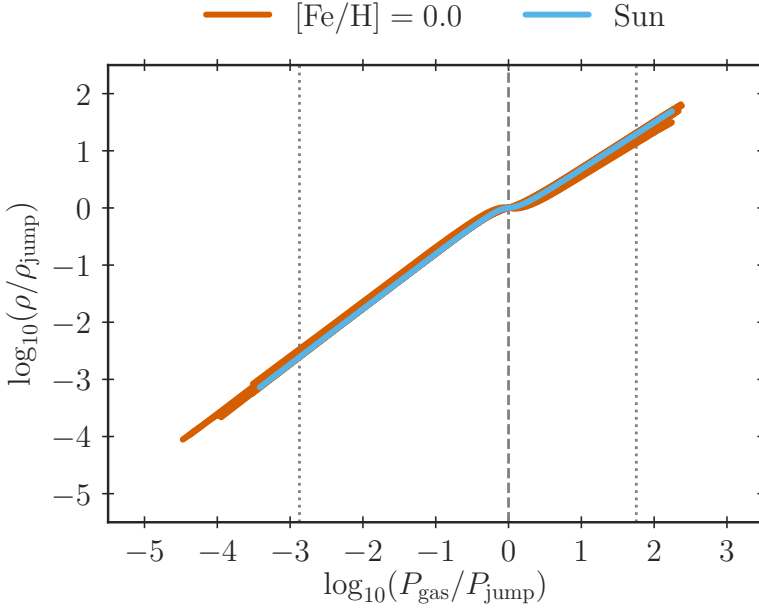


**Figure 8.1 | Scaled density stratification as a function of the scaled pressure.** Shown for all 28 **STAGGER** grid simulations at solar metallicity, with the stratification of the solar simulation highlighted. The dotted lines mark the interpolation range. The dashed line highlights the density inflection point, the so-called “density jump” (details in text). For the equivalent plot, including all 199 relaxed simulations from the **STAGGER** grid, we refer to fig. 6.2.

of our method. The logarithm of these quantities are shown for the simulations at solar metallicity from the **STAGGER** grid in fig. 8.1, where the density feature is also marked.

As introduced in section 7.2, the **matching point** between interior and appended  $\langle 3D \rangle$ -envelope is selected at a fixed scaled pressure. For convenience, we re-introduce the quantity from eq. (7.1) on page 132 with a slightly different notation as

$$K_m = \log \left( \frac{P_{\text{gas}}}{P_{\text{jump}}} \right)_{\text{matching point}} . \quad (8.1)$$

In other words, the value of the logarithm of the scaled pressure at the **matching point** is dubbed  $K_m$ . Our typical choice  $K_m = 1.20$  is near the

right dotted line in fig. 8.1, and implies that the pressure at the **matching point** is  $10^{1.20} \simeq 15.8$  times higher than the pressure at the density feature near the surface. The exact choice determines the depth and will influence the produced model, which we will explore in section 8.3.2.

## 8.3 Solar Models

In chapter 7 we performed a solar calibration with our new implementation to obtain a **SSM** with  $\langle 3D \rangle$ -envelopes appended on the fly in the evolution. In the following we will expand the discussion of the solar structure and evolution and address several aspects not treated in chapter 7.

### 8.3.1 The Equation of State

As mentioned above, temperature and pressure are taken directly from the interpolated  $\langle 3D \rangle$ -envelope in the appended part of the model, while we rely on the **EOS** from **GARSTEC** to supply the remaining quantities. Chapter 7 showed that the density is recovered to very high accuracy. Another important quantity is the first adiabatic index  $\Gamma_1$  which is not reproduced as accurately and thus might affect the asteroseismic result, and will be investigated in the following.

We utilize the same solar calibration as described in the previous chapter, targeting  $T_{\text{eff}} = 5769$  K of the **STAGGER grid** solar simulation. The  $\langle 3D \rangle$ -envelopes were used in the entire evolution, and the **matching point** placed at  $K_m = 1.20$ . From the calibration, a mixing-length parameter of  $a_{\text{MLT}} = 3.30$  was obtained, but note that a direct comparison between the mixing length used here and the standard mixing length used to characterize the superadiabatic region in normal **MLT** is not meaningful. In the present case, the role of the mixing-length parameter is to calibrate a tiny bit of superadiabaticity below the matching region, and hence it is very sensitive to the **matching point** and the details of the simulations. Thus, the actual numerical value of  $a_{\text{MLT}}$  are not important and in particular not relevant for any other model.

The predicted stellar oscillation frequencies  $\nu_{n1}$  are calculated with **ADIPLS**. As also discussed by chapter 7,  $\Gamma_1$  can be used directly in the frequency computation because we (currently) neglect turbulent pressure

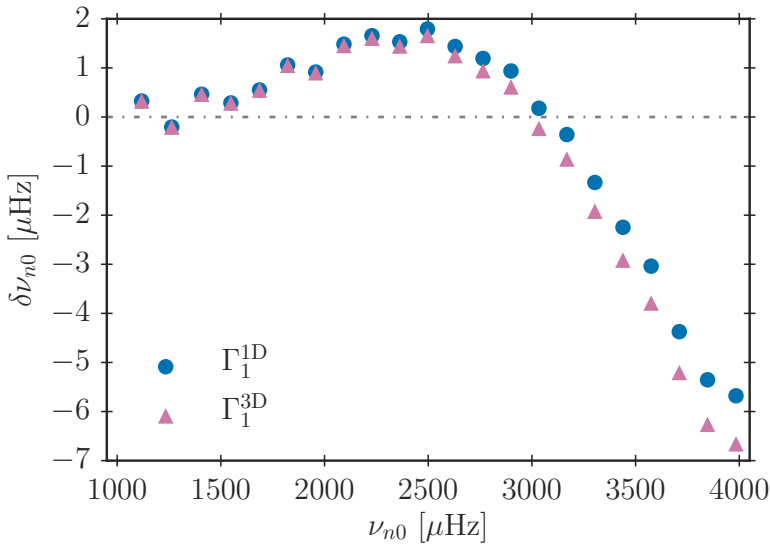


**Figure 8.2 | Frequency changes caused by EOS effects.** Frequency difference between radial modes from model predictions and **BISON** data. The predictions are from the the solar calibrated model from chapter 7 using either  $\Gamma_1$  from **GARSTEC**'s EOS ( $\Gamma_1^{1D}$ ) or directly from the interpolated  $\langle 3D \rangle$ -envelope ( $\Gamma_1^{3D}$ ).

in our models constructed on the fly (Rosenthal et al., 1999; Houdek et al., 2017). In order to assess the impact of using the adiabatic index from the EOS, we substitute the value computed by **GARSTEC**,  $\Gamma_1^{1D}$ , with the values taken directly from the interpolated  $\langle 3D \rangle$ -envelope,  $\Gamma_1^{3D}$ , in our calibrated solar model. We then recompute the oscillations using  $\Gamma_1$  directly again. As we are fully neglecting turbulent pressure, the different “ $\Gamma_1$  cases” from Rosenthal et al. (1999) are not relevant.

The comparison is shown in fig. 8.2, as frequency differences compared to observations from **BISON**. To keep the comparison simple and to not clutter the plot, only radial modes ( $l = 0$ ) are shown. As can be seen from the figure, the effect is very small; the impact on the frequencies is around 1  $\mu\text{Hz}$  at the highest frequencies, and even less at the **frequency of maximum power** ( $\nu_{\text{max}} \simeq 3100 \mu\text{Hz}$ ) and below.

### 8.3.2 The Matching Depth

The choice of **matching point** determines the depth of the appended envelope and affects the parameters of the solar calibration. In the following we perform ten different solar calibrations with different **matching points**, in order to investigate to which extent the **matching point** affects the obtained structure, evolution and helioseismic results. The different calibrations are computed to match a standard solar  $T_{\text{eff}} = 5779$  K instead of the `STAGGER` one and denominated by the  $K_m$  from eq. (8.1).

The selected **matching point** given by the scaled pressure is used in the entire solar calibration routine, i.e., for the full evolution and not just in the final solar model. This fixed scaled pressure of the **matching point** is by construction constant throughout the evolution; however, for any given model in the sequence, the radius coordinate  $r_m$  of the **matching point** can be reported as well but is valid only for that particular model. For the final resulting solar model this conversion can ease the discussion and especially in terms of physical matching depth below the surface  $d_m = R - r_m$ .

Firstly, we analyse the stellar oscillations for each of the ten solar models. Below a matching depth of  $d_m \simeq 0.6$  Mm – which roughly corresponds to the minimum in  $\Gamma_1$  near the surface – we find the computed model frequency differences to be virtually depth independent. Furthermore, when the **matching point** is placed close to the surface, the obtained frequencies are very similar to those obtained with a standard Eddington grey atmosphere. The difference between the predicted model frequency and `BISON` data for the radial oscillation mode ( $l = 0$ ) with an order of  $n = 28$  (at roughly 4000  $\mu\text{Hz}$ ) is shown in orange in fig. 8.3 as a function of matching depth for all of the different solar models.

Secondly, we investigate the mixing-length parameter  $\alpha_{\text{MLT}}$ , which is an output of the solar calibration. In order to correctly reproduce the solar surface properties, higher values of  $\alpha_{\text{MLT}}$  are required when matching deeper below the surface at a higher scaled pressure. The corresponding values for each matching depth are shown in blue in fig. 8.3, from which it is clear that  $\alpha_{\text{MLT}}$  is found to monotonically increase with increasing  $r_m$ . A similar result was obtained by Schlattl, Weiss, and Ludwig (1997), when appending mean structures of 2D envelope models. Also note that the calibration with the same matching depth as used in the previous section and chapter 7 ( $K_m = 1.20$ ) does not yield the same mixing-length parameter, due to the

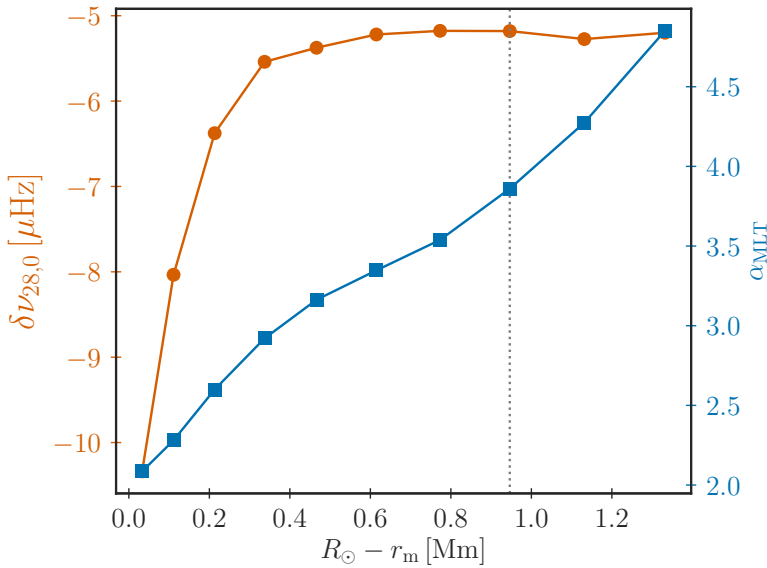


**Figure 8.3 | Solar calibrations with different matching depths.** The vertical dashed line marks the depth that correspond to the standard  $K_m = 1.20$ . The conversion to  $K_m$  for several depths is presented in fig. 8.4 and its caption. **Left ordinate, orange circles)** Difference between **BISON** data and model frequencies for the radial mode of order 28. **Right ordinate, blue squares)** The resulting calibrated mixing length parameter  $\alpha_{\text{MLT}}$ .

different target  $T_{\text{eff}}$ . The 10 K difference changes the value from  $\alpha_{\text{MLT}} = 3.30$  to  $\alpha_{\text{MLT}} = 3.86$ .

The influence of the **matching point** on the model’s evolution is worth investigating, especially since the matching depth significantly alters the calibrated value of  $\alpha_{\text{MLT}}$ . Therefore we calculated the evolution of the solar calibrated models continuing up the **RGB**. The resulting tracks for half of the cases (to not clutter the plot) are shown in fig. 8.4. In the plot, the tracks are denoted by their fixed  $K_m$  and shown alongside the simulations from the **STAGGER** grid used to obtain the interpolated  $\langle 3\text{D} \rangle$ -envelope appended on the fly.

From the figure it can be seen that the matching depth slightly alters the position of the **turn-off** as well as the temperature evolution on the **RGB**, but the effects are tiny. A more pronounced feature is the emerging

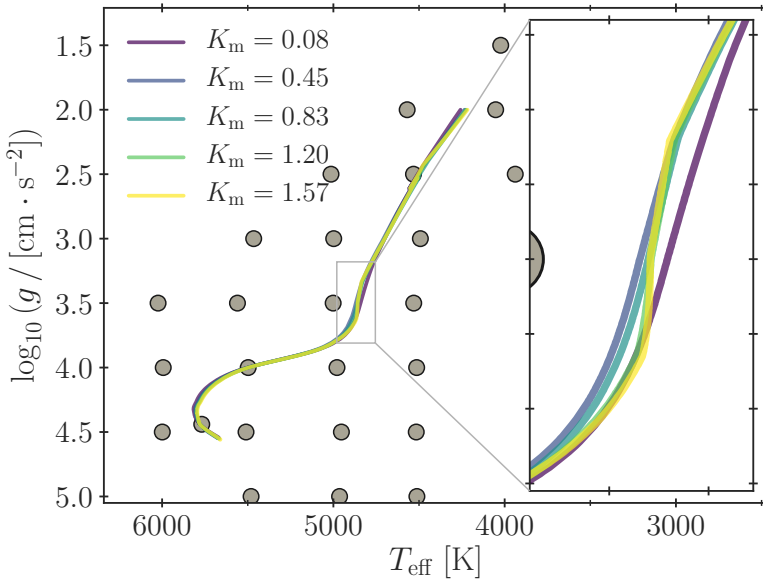


**Figure 8.4 | Evolution of the solar calibration models.** The ticks on the zoomed inset correspond to 100 K and 0.1 dex, respectively. The grey dots marks the **STAGGER grid** models at solar metallicity. The tracks are denoted by  $K_m$  and a larger value implies a larger matching depth. For the present Sun, the listed scaled pressures correspond to a depth of 0.11, 0.34, 0.61, 0.95, and 1.33 Mm, respectively (see fig. 8.3).

kink at the bottom of the **RGB**, which is clearly visible from the zoom-in in fig. 8.4 and suspected to be a result of the interpolation. As discussed briefly earlier, we compute the effective temperature  $T_{\text{eff}}$  of our models from interpolation in  $\log g$  and the temperature at the **matching point**  $T_m$  (in chapter 7 referred to as  $T_m^{3D}$ ). While the **STAGGER grid** is almost regular in the  $(T_{\text{eff}}, \log g)$ -plane, this is not the case in the  $(T_m, \log g)$ -plane due to the non-linear relationship between  $T_{\text{eff}}$  and  $T_m$ . This effect is shown in section 8.A for  $K_m = 1.20$ . Moreover, as the matching depth is changed, the simulation points move individually in this parameter space causing the separation between them to change.

The result is that the larger the matching depth gets, the lower the resolution in some regions of the  $(T_m, \log g)$ -plane is, which implies a higher risk for interpolation errors in the determined  $T_{\text{eff}}$ . As can be seen from

fig. 8.4, the evolutionary tracks show kinks on the **RGB** that become more pronounced with increasing matching depth. Based on this, our method would strongly benefit from a refinement of the **STAGGER grid**; specifically a few additional 3D simulations with  $\log g = 3.0 - 4.0$  and  $T_{\text{eff}} = 4500 - 5000$  K. We expand on the discussion of interpolation and grid resolution in section 8.4.1.

In order to fully take advantage of the 3D simulations, it is generally desirable to place the **matching point** as deep within the nearly adiabatic region as possible. As just mentioned, problems can however emerge in the post-**MS** evolution if the matching is performed near the bottom of the simulations. Thus, deciding on the matching depth is a compromise between these two considerations. Until further 3D simulations are calculated, an intermediate matching depth in the nearly adiabatic region is preferable – such as the depth used in section 8.3.1 and in the following sections corresponding to  $K_m = 1.20$ .

### 8.3.3 The Trapedach Grid

To investigate the versatility of our method, we have repeated the analysis of the solar model from chapter 7 with a different set of 3D simulations. Thus, in this section, the interpolated  $\langle 3D \rangle$ -envelopes are determined from the simulations in the *Trapedach grid*.

For consistency, we calculate our models with the same non-canonical solar mixture as this set of 3D simulations employs (Trapedach et al., 2013, table 1) – in which  $Z/X = 0.0245$  – as well as the specific atmospheric opacities from Trapedach et al. (2014a,b) provided by R. Trapedach (private communication). The low-temperature opacities are merged with interior opacities from the Opacity Project (OP, Badnell et al., 2005) for the same mixture.

The procedure for setting up the boundary conditions and appending the  $\langle 3D \rangle$ -envelopes on the fly is identical to what is described in section 8.2. In the nomenclature of earlier sections, the scaled pressure at the **matching point** is selected as  $K_m = 0.88$ . For the present Sun, the pressure at the **matching point** corresponds to a temperature of  $T_m = 1.29 \times 10^4$  K and a depth of  $d_m = 0.64$  Mm below the photosphere. The appended envelope is hence shallower than the envelope of the solar calibration model using the **STAGGER grid** presented in chapter 7.

**Table 8.1 | Results from the different solar calibrations.** Here the  $\langle 3D \rangle$ -envelopes is based on the **Trampedach grid**.  $\alpha_{\text{MLT}}$  denotes the mixing length,  $Y_i$  is the initial helium mass fraction,  $Z_i$  is the initial fraction of heavy elements,  $Y_s$  is the surface helium abundance, and  $r_{\text{cz}}/R_\odot$  is the radius of the base of the convective envelope.

Model	$\alpha_{\text{MLT}}$	$Y_i$	$Z_i$	$Y_s$	$r_{\text{cz}}/R_\odot$
Edd.	1.71	0.2680	0.0201	0.2388	0.7122
RT2014	1.82	0.2680	0.0201	0.2388	0.7122
$\langle 3D \rangle$ -envelopes	5.36	0.2678	0.0200	0.2387	0.7122

For comparison, we calculated a solar calibration with identical input physics, but using a standard Eddington grey atmosphere, which is labelled *Edd.* in the plots and table of this section. Moreover, the use of the grid from Trampedach et al. (2013) and compatible input physics allows us to compare our method to the work by Mosumgaard et al. (2018) – included in this thesis as chapter 5 – which is a different approach for using information from 3D simulation in stellar evolution models. This specific solar model utilising the 3D information from Trampedach et al. (2014a,b) is taken directly from Mosumgaard et al. (2018) and is denoted *RT2014* in the following.

The resulting parameters from the three different calibrations are shown in table 8.1. As found in chapter 7, our change in the outer boundary conditions does not affect the surface helium mass fraction  $Y_s$  nor the radius of the base of the convection zone  $r_{\text{cz}}$ . For comparison, the results from **helioseismology** are:  $Y_s = 0.2485 \pm 0.0035$  (Basu and Antia, 2004) and  $r_{\text{cz}} = (0.713 \pm 0.001) R_\odot$  (Basu and Antia, 1997). Regarding the mixing-length parameter, we find the same as before and refer to the earlier discussion: that a direct comparison of the two cases is not meaningful and that the actual values of  $\alpha_{\text{MLT}}$  are not important.

A comparison of the temperature structure of the resulting solar models and the 3D solar simulation in the **Trampedach grid** is shown in fig. 8.5. As can be seen from the figure, our new method appending  $\langle 3D \rangle$ -envelopes on the fly reproduces the stratification of the 3D simulation reliably throughout the envelope, which agrees with the **STAGGER grid** results in chapter 7. It is clear that the Eddington grey atmosphere is very different from the 3D **RHD**

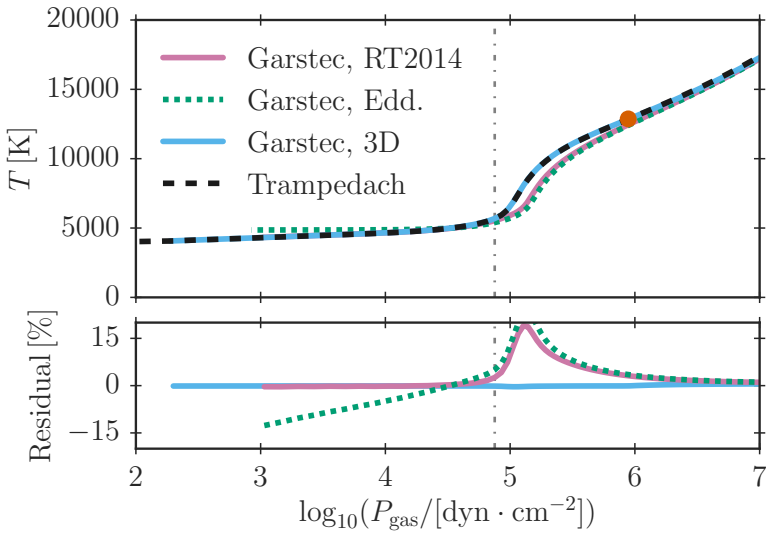


**Figure 8.5 | Reproduction of the 3D solar simulation.** Temperature as a function of gas pressure for the solar simulation in the **Trampedach grid** (*Trampedach*) and the different solar calibrations from **GARSTEC**: **3D** is appending  $\langle 3D \rangle$ -envelopes from the **Trampedach grid** on the fly, **RT2014** is using a calibrated  $\alpha_{\text{MLT}}$  and  $T(\tau)$  relation from the same grid, and **Edd.** is performed with a standard grey Eddington boundary and constant  $\alpha_{\text{MLT}}$ . The **matching point** of the  $\langle 3D \rangle$ -envelope-model is marked with a red dot. The residuals are with respect to the 3D solar simulation, in the sense “*Trampedach* – **GARSTEC**”. The dashed-dotted grey line indicates the position of the photosphere.

simulation. The **RT2014**-solar model using the 3D  $T(\tau)$  relations and  $\alpha_{\text{MLT}}$  mimics the correct structure above the photosphere, but deviates below – a similar result was found in chapter 5.

To assess the impact of using 3D information on the evolution, we continued the tracks from the solar calibrations up the **RGB**. As shown in chapter 5, the use of the 3D calibrated  $T(\tau)$  relation and  $\alpha_{\text{MLT}}$  shifts the **RGB** towards higher effective temperatures compared to the regular Eddington case. As expected, we find the same qualitative trend for our implementation of  $\langle 3D \rangle$ -envelopes on the fly, as can be seen in fig. 8.6, where the evolutionary tracks are shown alongside the 3D simulations from the **Trampedach grid**. In other words, models with a standard Eddington grey atmosphere have

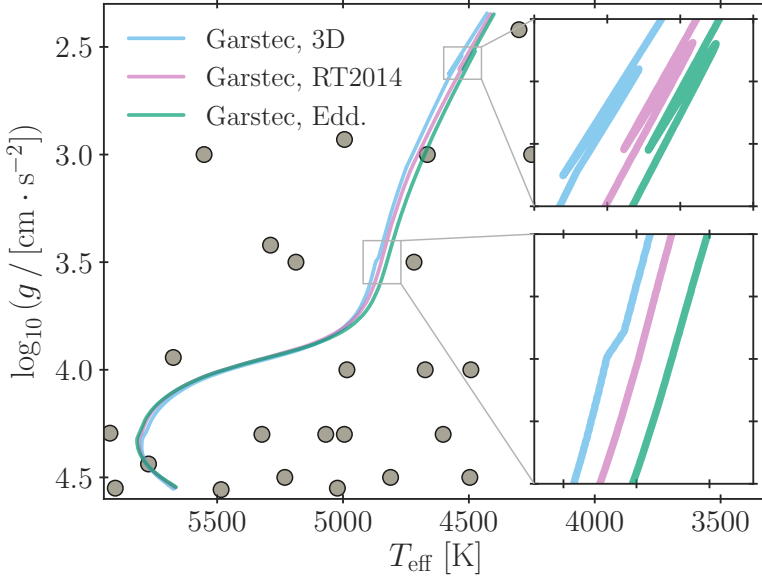


**Figure 8.6 | Evolutionary tracks of the solar models.** Colours and labels corresponds to fig. 8.5. The ticks on the zoomed insets correspond to 50 K and 0.05 dex, respectively. The grey dots show the location of a selection of the 3D simulations from the **Trampedach grid**.

systematically lower  $T_{\text{eff}}$  on the **RGB**. The difference between the track appending  $\langle 3D \rangle$ -envelopes on the fly and the Eddington reference is around  $\Delta T_{\text{eff}} \simeq 55$  K at the **RGB** luminosity bump. This difference is somewhere between the **RGB** temperature offset at solar metallicity predicted by Tayar et al. (2017) and Salaris et al. (2018); it is also around the same magnitude as the shift found by the latter when changing between common  $T(\tau)$  relation as boundary conditions for their models.

Moreover, fig. 8.6 suggest that our new method leads to a kink at the base of the **RGB**, which is similar to what was seen in the previous section. We attribute this again to interpolation errors due to the even lower resolution of the **Trampedach grid** in this region. The morphology of the kink is somewhat different being more like a sharp break, which likely stems from the irregular sampling of the **Trampedach grid** (compared to the almost uniform **STAGGER grid**). As pointed out in section 8.3.2, such kinks call for a refinement of the currently employed grids of 3D-envelopes – regardless

of the specific grid. In the following section we will investigate the effects of the grid resolution in more detail.

As a final note, we repeated the full matching-depth analysis from section 8.3.2 for the **Trapedach grid**. Bearing the slightly shallower 3D simulations from the **Trapedach grid** in mind, we observe the same qualitative behaviour for this grid as we did for the **STAGGER grid** (shown in fig. 8.3). Specifically,  $a_{\text{MLT}}$  increases with increasing matching depth, reaching  $a_{\text{MLT}} = 17$  for a scaled pressure corresponding to a matching depth of  $d_{\text{m}} = 0.95$  Mm for the present Sun. Regarding the frequencies as a function of matching depth, we observe the same trend as before: Below a certain depth – around  $d_{\text{m}} = 0.5 - 0.6$  Mm which is similar to what was seen for the **STAGGER grid** – the frequencies are virtually insensitive to the **matching point**. It should be noted that generally the agreement between the models frequencies and observations are worse in this case than for the **STAGGER grid**, as a result of the different opacities and chemical mixture.

In the remainder of this chapter, we will restrict ourselves to models that employ the **STAGGER grid** rather than the **Trapedach grid**, when appending (3D)-envelopes on the fly.

## 8.4 Stellar Evolution

To analyse the applicability of our procedure, we have produced a grid of stellar models appending **STAGGER grid** (3D)-envelopes on the fly along the entire evolution. The tracks are computed at solar metallicity with masses between  $0.7 M_{\odot}$  and  $1.3 M_{\odot}$ . In the calculations, the **matching point** is fixed to a scaled pressure factor of  $K_{\text{m}} = 1.20$  as usual. The tracks use a fixed  $a_{\text{MLT}} = 3.86$  from the solar calibration with the corresponding depth from section 8.3.2. A list of the input physics is provided in the final paragraph of section 8.2.

### 8.4.1 Evolutionary Tracks and Grid Resolution

A selected subset of the evolutionary tracks spanning the entire mass range of our grid is shown in fig. 8.7 up to  $\log g = 2.0$ . As can be seen from the figure, the evolutionary sequences are generally well behaved, but show different kinks (or changes in slope) – especially visible on the **RGB**, but not at the same location for the different tracks.

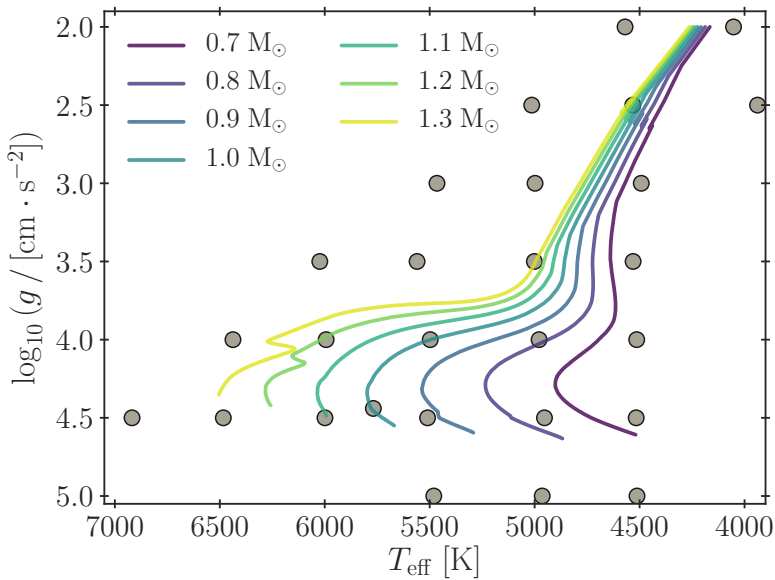


**Figure 8.7 | Evolutionary tracks of models with different stellar masses.** The grey dots show the location of the **STAGGER grid** models with solar metallicity.

The most prominent of these features are located between  $\log g = 3.5$  and  $\log g = 3.0$ , which is in the same region of the **Kiel diagram** where difficulties emerged for the solar model tracks in fig. 8.4 on page 148. Similar kinks can be seen for the majority of the tracks between  $\log g = 2.5$  and  $\log g = 2.0$ , and also in the **MS** for the  $0.8 M_{\odot}$  and  $0.9 M_{\odot}$  evolution. All of the cases are correlated with larger gaps in the **STAGGER grid**; and also with movement of the simulation footpoints in the  $(T_m, \log g)$ -plane (see section 8.A). Thus, the bends generally occur on the virtual line between two of the simulations, i.e., when the tracks move to a different zone in the triangulation-based interpolation scheme (in either one of the two parameter spaces). Specifically, it seems to be a problem with the sampling of the underlying grid of 3D simulations.

To investigate the influence of the grid sampling, we performed numerous tests of the triangulation and interpolation. We modified the grid used by our routines in **GARSTEC**; specifically we tried degrading the grid by strategically removing some of the **STAGGER** models. We also employed the code from chapter 6 to compute new interpolated envelopes in the gaps

(e.g. at  $T_{\text{eff}} = 4775$  K,  $\log g = 3.75$ ) to artificially refine the grid. All of the tests confirm the actual grid sampling to clearly affect the morphology of the **RGB**-kink: making the break smoother/sharper and more/less pronounced. The effect of the sampling in the different interpolation planes are discussed in section 8.A. To sum up, we need a denser grid of 3D **RHD** simulations in order to produce smoother evolutionary sequences.

Figure 8.7 illustrates the well-known effect that tracks are much closer to each other in temperature for the later evolutionary stages with lower surface gravities; at the **ZAMS** they span more than 2000 K, but this gets narrower moving up the **RGB** and the extent is less than 100 K at  $\log g = 2.0$ . In other words, during the **MS** the evolutionary tracks of different initial mass is spread across the entire grid, while the effective resolution is significantly reduced for **RG**-stars, with only a few simulations to cover the entire mass range. Another interesting observation is that the separation between the tracks decreases going up the **RGB**, whereas they are mostly parallel for standard evolution with an Eddington atmosphere. A potential future line of investigation would be to determine whether this is a true effect, or if it is due to a deficit in the low  $\log g$  simulations, or a result of the **RGB** grid resolution.

Looking at the figure, a final important thing to keep in mind is that the applicability of our method is strongly determined by the parameter space covered by the 3D **RHD** grid – both in terms of mass range and how far up the **RGB** the tracks can extend.

#### 8.4.2 Structure at Different Evolutionary Stages

Some of the evolutionary tracks contain models, where  $T_{\text{eff}}$  and  $\log g$  correspond to one of the existing **STAGGER grid** simulations; this is directly visible from fig. 8.7, where some of the selected tracks pass through a dot. This facilitates an easy comparison between the obtained structure from the appended  $\langle 3D \rangle$ -envelope in the stellar evolution model and the original 3D simulation. In other words, we want to verify that the direct output from our stellar structure model is consistent with the underlying full 3D simulations, including the quantities derived from the **EOS**.

We have performed several of such comparisons, which are listed in table 8.2 alongside the deviation in  $\log g$  (at the **matching point**) and  $T_{\text{eff}}$  between the model and corresponding 3D simulation. The matching is

**Table 8.2 | Comparison points with different stellar parameters.** Difference and relative deviation in  $T_{\text{eff}}$  at the photosphere and  $\log g$  at the **matching point**, between the 1D stellar model and corresponding 3D simulation (in the sense “1D – 3D”). The nomenclature specifies the surface parameters (details given in the text).

Sim.	$\delta T_{\text{eff}}$ [K]	$\delta T_{\text{eff}}/T_{\text{eff}}$	$\delta \log g$ [cgs]	$\delta \log g / \log g$
t45g25	-0.535	$-1.19 \times 10^{-4}$	$-5.10 \times 10^{-5}$	$-2.04 \times 10^{-5}$
t50g35	-0.248	$-4.96 \times 10^{-5}$	$7.79 \times 10^{-4}$	$2.23 \times 10^{-4}$
t55g40	0.600	$1.09 \times 10^{-4}$	$7.83 \times 10^{-4}$	$1.96 \times 10^{-4}$
t55g45	0.810	$1.47 \times 10^{-4}$	$1.56 \times 10^{-3}$	$3.47 \times 10^{-4}$
t60g40	-0.360	$-6.00 \times 10^{-5}$	$-9.93 \times 10^{-4}$	$-2.48 \times 10^{-4}$

within roughly 0.8 K and  $10^{-3}$  dex, resulting in relative deviations at the  $10^{-4}$  level or better. Especially the high precision in surface gravity at the **matching point** is important, as the interpolation is very sensitive to  $\log g$ . In the table, we have adopted the nomenclature from the **STAGGER grid** to label the models: as an example, the model named t50g35 has  $T_{\text{eff}} = 5000$  K and  $\log g = 3.5$ .

The resulting residuals in temperature and density as a function of gas pressure for five cases are shown in fig. 8.8 (using the same nomenclature), where the comparison of the Sun is added for reference. As can be seen from the top panel of the figure, our method reproduces the temperature stratification with high accuracy throughout the  $(T_{\text{eff}}, \log g)$ -plane, with residuals below 0.2 % above the **matching point**. The smallest residuals are seen for t45g25, which has the best match to the simulation surface parameters. But generally we find no clear trends in the residuals with the deviation in matching parameters from table 8.2.

Regarding the density – shown in the bottom panel of fig. 8.8 – the procedure works particularly well for the **MS** and **subgiant** stars in our sample, i.e., excluding the giant t45g25 (discussed separately below). The residuals are within a few percent, which is very similar to the levels seen for the solar model in chapter 7. As for the temperature, we see no correlation of the residuals with how well the models match. Because the interpolation is entering only through the temperature stratification, the density residuals are not directly reflecting (additional) interpolation errors. As was also argued

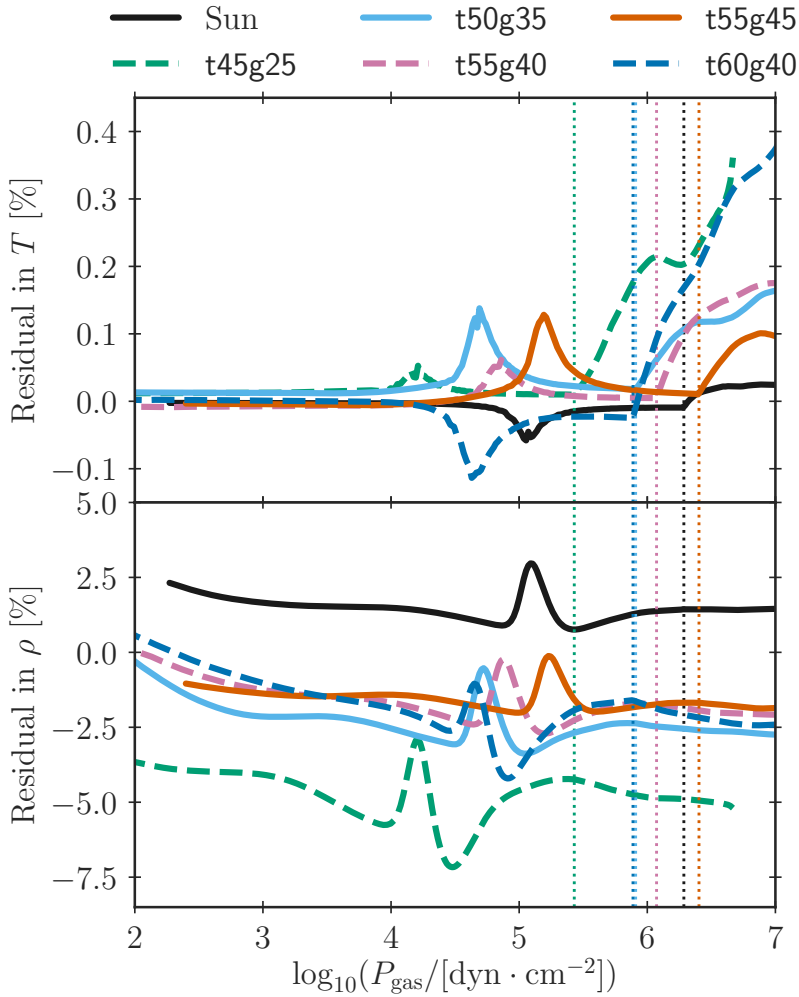


**Figure 8.8 | Structural residuals at the comparison points.** The points are listed in table 8.2 with identical nomenclature. For each set of surface parameters, a vertical dotted line with the corresponding colour indicates the location of the **matching point**. The residuals are calculated as “3D simulation – **CARSTEC**”. **Upper panel)** Comparison between the temperature stratification determined by **CARSTEC** and the corresponding **STAGGER grid** simulation at solar metallicity. **Lower panel)** As the upper panel but comparing the density stratification.

in chapter 7, the discrepancies partly reflect the difference in **EOS**, but also the non-linearity of the thermodynamic quantities. Specifically, we derive the density from the mean of  $P_{\text{gas}}$  and  $T$ , i.e.,  $\rho(\langle P_{\text{gas}} \rangle, \langle T \rangle)$ . Regardless of the **EOS**, this density is not expected to correspond exactly to the actual (geometrical) mean of the density  $\langle \rho(P_{\text{gas}}, T) \rangle$  in a 3D **RHD** simulation, because the density is a non-linear function of pressure and temperature (Trampedach et al., 2014a).

For the more evolved giant shown (t45g25), the residuals in density between the **STAGGER grid** simulation and outer parts of the stellar evolution model are somewhat larger – even though the level of the temperature residuals are not larger. The cause must be the above-mentioned difference in **EOS** and thermodynamic non-linearity, which clearly play a much larger role in the **RG**-regime. Another possible contribution is a composition effect; however, this is unlikely to constitute the full part, because compared to the initial model in the sequence the difference is less than 0.01 in [Fe/H] and around 0.02 in surface helium.

To sum up, the overall implementation is performing less well in the **RG** region of the parameter space. This is in line with the findings by chapter 6, namely that the residuals in the patching grows for the hottest and the most evolved stars. Thus, to fully utilize the potential of our method, more 3D simulations are required.

## 8.5 Asteroseismic Application

We want to investigate how our new procedure alters the results obtained from an asteroseismic analysis compared to a reference case. The selected stars must have an  $T_{\text{eff}}$  and  $\log g$  inside the **STAGGER grid**, and as we currently do not interpolate in metallicity, we are restricted to stars with a composition consistent with solar. Moreover, the method is expected to primarily perform well for cold **MS** stars, as discussed above. Based on these restrictions, we have selected two stars from the *Kepler* asteroseismic **LEGACY** sample with large frequency separations around  $\Delta\nu \sim 155 \mu\text{Hz}$ : KIC 9955598 ( $\Delta\nu = 153.3 \mu\text{Hz}$ ) and KIC 11772920 ( $\Delta\nu = 157.7 \mu\text{Hz}$ ). The stellar parameters resulting from the fit (described in the next section) are listed in table 8.3 on page 161.

For the grid-based modelling analysis, two sets of stellar models have been computed: One appending  $\langle 3\text{D} \rangle$ -envelopes from the **STAGGER grid**

on the fly and a reference grid with an Eddington grey atmosphere. The model grids contain the same microphysics as listed in section 8.2, but do not include microscopic diffusion. The grid appending  $\langle 3D \rangle$ -envelope on the fly uses  $\alpha_{\text{MLT}} = 3.86$  (the  $K_{\text{m}} = 1.20$  solar calibration from section 8.3.2), while the Eddington solar calibration yields  $\alpha_{\text{MLT}} = 1.80$ .

The grids have been calculated with **GARSTEC** and span the mass range  $M = 0.8 - 0.95 M_{\odot}$  in steps of  $0.001 M_{\odot}$ . For all models in the grids, **ADIPLS** has been utilised to calculate individual oscillation frequencies.

### 8.5.1 Determined Stellar Parameters

To compare the observations to the calculated stellar models we used **BASTA** (section 3.4.1), which utilises both classical observables and asteroseismic data. Based on the observed quantities, the likelihood of all models in the grid is determined and probability distributions and correlations constructed for the desired parameters. The reported values are the medians from these distributions with the 68.3 percentiles as corresponding uncertainties.

One way of using the asteroseismic data is to compare the observed individual oscillation frequencies  $\nu_{n,l}$  to those computed from the models applying a surface term correction (section 2.4). It should be noted that the exact shape of this correction is not known for our new stellar models appending  $\langle 3D \rangle$ -envelopes on the fly, where the **surface effect** has been partly eliminated. Another option is to instead use combinations of frequencies: the frequency separation ratios defined in section 3.3.2. These ratios have been shown to be less sensitive to the outer layers and primarily probe the interior of the star, and thus eliminate the need for a correction of the surface term.

To test the consistency of our new models, we used **BASTA** to estimate the stellar properties based on a fit to the spectroscopic temperature and the frequency ratios  $r_{010}$  and  $r_{02}$ . In the current context, the agreement between the two fits and not the actual parameter values is our primary concern. However, to guide the discussion, the inferred stellar parameters from both sets of models are listed in table 8.3 on page 161. It should be noted that the use of the  $r_{010}$  in combination with  $r_{02}$  was disputed by Roxburgh (2018), as also mentioned earlier. Due to the risk of overfitting the data, Roxburgh (2018) instead suggested using the single series  $r_{102}$  (or

$r_{012}$ ). However, fitting  $r_{012}$  in **BASTA**, we obtain parameters fully consistent with the ‘standard’ ratios fit.

In general, the resulting parameters from the grid of  $\langle 3D \rangle$ -envelope models and the grid of Eddington models show good agreement. The effective temperature is particularly interesting, as we know from an earlier section that the  $T_{\text{eff}}$  evolution can be different between the two sets of models. However, not much is predicted to change on **MS**; as expected, for KIC 9955598 the two values are within the uncertainties of each other, while for KIC 11772920 the quoted uncertainty bands in  $T_{\text{eff}}$  overlap. For both stars, for all of the remaining parameters – mass, radius, and age – the agreement between the two grids is even better and within half a standard deviation of each other.

After verifying the consistency with the non-surface dependent separation ratios, we repeated the procedure using instead the individual oscillation frequencies. We assume the two-term surface correction from Ball and Gizon (2014) and fit the stars using the same two sets of models. The inferred parameters from this analysis are not shown; however, they are similar to the presented results from the fit to the  $r_{010}$  and  $r_{02}$  ratios. The determined parameters from the Eddington and the  $\langle 3D \rangle$ -envelope grid show the same level of agreement as above, i.e., less than half a standard deviation for all of the parameters except  $T_{\text{eff}}$ . Moreover, all of the fits to the same star using the different sets of asteroseismic observables are internally consistent, too.

### 8.5.2 The Surface Effect

Besides estimating the stellar parameters, we want to investigate the impact on the important asteroseismic **surface effect**. In order to isolate the surface term, we add an additional assumption to our fitting: The model must match the observed lowest order  $l = 0$  mode within  $3\sigma$ . From **BASTA** we can get the full stellar model corresponding to the point with the highest assigned likelihood – given our extra assumption – also known as the **BFM**. By comparing the **BFM** from each grid, we can investigate if our new models alters the individual oscillation frequencies.

In fig. 8.9, the **BFM**-comparison of KIC 11772920 is shown in the form of frequency difference with respect to the observations. Looking at the figure, it is clear that the frequencies of our new model appending  $\langle 3D \rangle$ -envelopes

**Table 8.3 | Resulting parameters of the modelled *Kepler* stars.** The fits using models either appending  $\langle 3D \rangle$ -envelope on the fly (*Stag.*), or using Eddington grey atmospheres (*Edd.*) as boundary conditions. Inferred using **BASTA** (details in the text). The listed values correspond to the median of the obtained probability distributions from **BASTA** and the uncertainties denote 68.3 % bayesian credibility intervals.

KIC	Model	$T_{\text{eff}}$ [K]	$\log g$ [cgs]	Mass [ $M_{\odot}$ ]	$R_{\text{phot}}$ [ $R_{\odot}$ ]	Age [Myr]
9955598	<i>Edd.</i>	$5572_{-13}^{+13}$	$4.4983_{-0.0012}^{+0.0011}$	$0.897_{-0.005}^{+0.005}$	$0.8839_{-0.0019}^{+0.0021}$	$6997_{-349}^{+360}$
9955598	<i>Stag.</i>	$5584_{-10}^{+10}$	$4.4989_{-0.0012}^{+0.0011}$	$0.899_{-0.005}^{+0.004}$	$0.8840_{-0.0019}^{+0.0019}$	$6944_{-322}^{+352}$
11772920	<i>Edd.</i>	$5423_{-15}^{+15}$	$4.5061_{-0.0013}^{+0.0013}$	$0.849_{-0.006}^{+0.005}$	$0.8520_{-0.0023}^{+0.0023}$	$9874_{-499}^{+528}$
11772920	<i>Stag.</i>	$5449_{-16}^{+16}$	$4.5069_{-0.0013}^{+0.0013}$	$0.852_{-0.006}^{+0.006}$	$0.8529_{-0.0022}^{+0.0023}$	$9752_{-506}^{+510}$

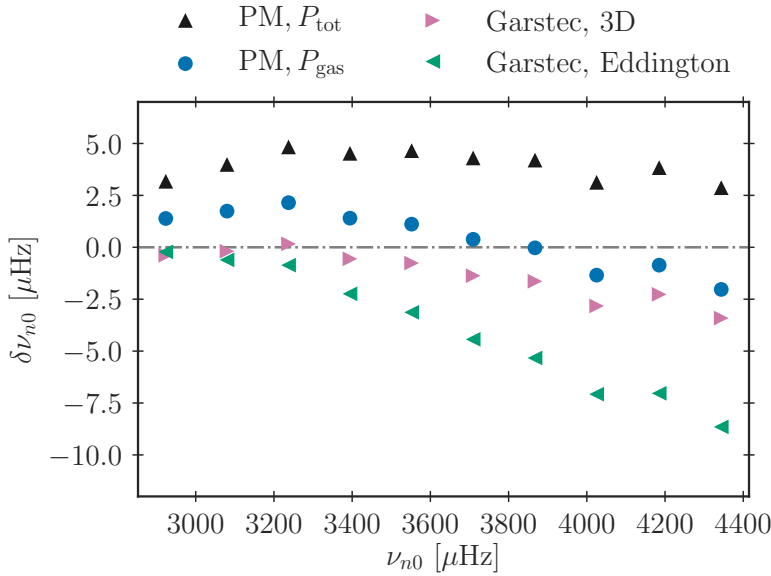


**Figure 8.9 | Frequency differences between model predictions and observations for  $\kappa$  IC 11772920.** The plot includes the **BFM** with an Eddington grey atmosphere and with **STAGGER grid** ( $\langle 3\text{D} \rangle$ )-envelopes on the fly. Based on the latter, we have constructed two **PM**'s: one where the *total* pressure enters the computation of the depth scale; and one where only the gas *pressure* does.

on the fly deviates less from the observations without the need of a surface correction.

The figure likewise contains two patched models (**PM**) constructed following the procedure described by chapter 7 and chapter 6. The base model for the present patching exercise is the **GARSTEC** model employing our new implementation. In each case we have substituted the outer layers of this model with the full ( $\langle 3\text{D} \rangle$ )-structure of an interpolated **STAGGER grid** envelope with the same  $T_{\text{eff}}$  and  $\log g$ . The first case – denoted as “**PM**,  $P_{\text{tot}}$ ” in the figure – is taken as it is, i.e., it includes turbulent pressure in the patched layers. In the second case, which is dubbed “**PM**,  $P_{\text{tot}}$ ”, the depth scale of the patched ( $\langle 3\text{D} \rangle$ )-envelope is recalculated solely based on the gas pressure.

Since our **GARSTEC** implementation neglects turbulent pressure and infers  $\rho$  and  $\Gamma_1$  from the **EOS**, especially the first case substitution is expected

to alter the structure and affect the model frequencies. To facilitate a meaningful comparison with the frequencies from stellar evolution models, we do not include the contribution from turbulent pressure in the oscillation equations for this **PM** (the “gas  $\Gamma_1$  approximation”, see section 7.3.2).

From fig. 8.9 we see that including the turbulent pressure in the patched exterior give rise to model frequencies which are 4 – 7  $\mu\text{Hz}$  lower than the frequencies of the underlying **GARSTEC** model. Note that the so-called *modal effects* are not included in the current treatment, but would still play a significant role for the remaining discrepancy (Houdek et al., 2017).

When recomputing the depth scale of the patched (3D)-envelope purely based on the gas pressure, this mismatch in the oscillations is reduced to less than approximately 2  $\mu\text{Hz}$ . This illustrates the importance of taking turbulent pressure properly into account. The remaining discrepancy between the **PM** and the model that has been obtained, using our new implementation, may partly be attributed to a mismatch in the stratification of  $\rho$  or  $\Gamma_1$  — that is, frequency differences may be attributed to the **EOS** or assumptions made by the **EOS**. Furthermore, this discrepancy may partly reflect interpolation errors.

Moving on to the other case, KIC 9955598, we return to the **surface effect** and the stellar evolution models. The frequencies of the two **BFM**’s – obtained from the grid-based fit with an additional constraint on the lowest  $l = 0$  mode – and the observations of KIC 9955598 can be seen in fig. 8.10. The comparison is shown in the form of an échelle diagram separated into two – one for each degree ( $l = 0$  and  $l = 1$ ) – to make the visualisation clearer. From the figure it is very clear that the model appending (3D)-envelopes on the fly has frequencies deviating significantly less from the observed values for both orders. All in all, compared to canonical stellar evolution models, the oscillation frequencies from our new models are much closer to the observations, without the use of any sort of correction of the asteroseismic surface term.

## 8.6 Red-Giant Branch Models

In line with the previous section, we investigate further the asteroseismic implications of our new method, focusing here on the solar-like acoustic oscillations in stars on the **RGB** and how the **surface effect** changes. **RG** stars

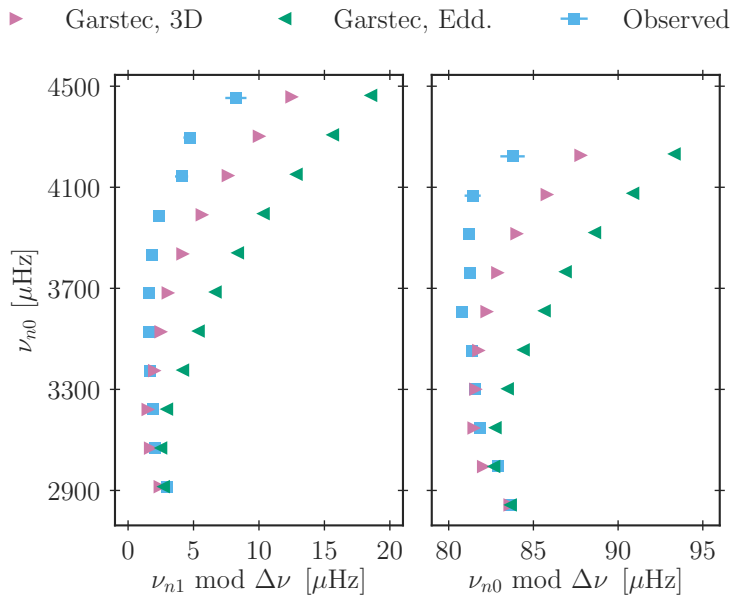


**Figure 8.10 | Échelle diagram of KIC 9955598 separated in degrees.** Model frequencies from the **BFM** obtained with **BASTA**, using one of two different grids of stellar models with either Eddington atmospheres or  $\langle 3D \rangle$ -envelopes.

are very important for many astrophysical fields, e.g. for probing distant regions in the Galaxy or studying star clusters. The analysis of such stars has matured rapidly in the era of space-based photometry and **asteroseismology** with **COROT** and *Kepler*, but the modelling deficiencies in the near surface layers are still not well understood.

In order to perform a detailed differential frequency analysis of two stellar models, the two must be very similar seismically. It is natural to compare models of identical mean density, which is correlated with the asteroseismic **large frequency separation**  $\Delta\nu$ . To ensure this, we adopted the convergence criterion devised for the *Aarhus Red Giants Challenge* – a series of workshops dedicated to modelling of **RG**-stars and especially to detailed comparisons of many different stellar evolution codes (Silva Aguirre et al., accepted; Christensen-Dalsgaard et al., submitted). For a given model (*mod*) the minimum acceptable convergence at *a* solar masses

and  $b$  solar radii is defined as

$$\Delta_{\text{convergence}} = \left| 1 - \frac{G_{\text{mod}} M_{\text{mod}} / R_{\text{mod}}^3}{G(a \times M_{\odot}) / (b \times R_{\odot})^3} \right| \leq 2 \times 10^{-4} , \quad (8.2)$$

where  $G$  is the gravitational constant. The choice of  $2 \times 10^{-4}$  is a compromise between the uncertainties in the asteroseismic frequencies and the ease of finding the required model as discussed by Silva Aguirre et al. (accepted).

For models calculated with the same stellar evolution code,  $G$  is of course invariant and the convergence is solely determined by the mass and radius. For the model to match a reference model with the desired radius  $R_{\text{ref}}$ , the criterion can be rewritten and reduced to

$$\Delta_{\text{convergence}} = \left| 1 - \frac{M_{\text{mod}} R_{\text{ref}}^3}{M_{\text{ref}} R_{\text{mod}}^3} \right| \leq 2 \times 10^{-4} , \quad (8.3)$$

where  $M_{\text{ref}}$  is the mass of the reference model at radius  $R_{\text{ref}}$ .

For this analysis we use the same settings in the computations as in sections 8.4 and 8.5 and two initial masses:  $1.00$  and  $1.30 M_{\odot}$ . Like in the previous section, two different sets of models were calculated: One appending STAGGER (3D)-envelopes on the fly and another using a standard Eddington  $T(\tau)$  relation. The models with STAGGER (3D)-envelopes are taken as the reference model in eq. (8.3) and the Eddington model is carefully calculated to match within the convergence limit. For the comparison we selected RGB models at different surface gravity positions of  $\log g = 3.0$ ,  $\log g = 2.5$ , and  $\log g = 2.0$ ; and an overview can be seen in table 8.4 (alongside the results described below).

For a set of matching models, the oscillation frequencies are computed with ADIPLS and compared. An example of the frequency difference comparison for models with  $M = 1.00 M_{\odot}$  at  $R = 9.32 R_{\odot}$  is shown in fig. 8.11. For the other comparison points, the shape of the differences looks almost identical, albeit with lower frequencies and fewer modes the lower  $\log g$  gets.

To quantify this, and to compare the actual shape of the deviation between the different comparison points we need to scale the quantities. Thus, we calculate the frequency of maximum power  $\nu_{\text{max}}$ , using the scaling relation from eq. (3.6) on page 53 assuming  $\nu_{\text{max},\odot} = 3090 \mu\text{Hz}$ . For a given set of converged models,  $\nu_{\text{max}}$  is calculated using the quantities of the (3D)-envelope model – due to the convergence defined by eq. (8.3),  $\nu_{\text{max}}$  of the

**Table 8.4 | Comparison points for RGB models.** The convergence in radius is according to eq. (8.3) with STAGGER  $\langle 3D \rangle$ -envelopes on the fly as the reference, and Eddington computed to match. The frequency of maximum power  $\nu_{\max}$  is determined from the STAGGER models using eq. (3.6). The frequency difference is “ $3D - \text{Eddington}$ ” and determined as a 3-point average around  $\nu_{\max}$  (see the text for details).

$M [M_{\odot}]$	$\log g$	$R [R_{\odot}]$	$\nu_{\max} [\mu\text{Hz}]$	$\delta\nu_{\nu_{\max}} [\mu\text{Hz}]$	$\delta\nu_{\nu_{\max}}/\nu_{\max}$
1.00	3.0	5.24	124.49	-0.510	$-4.10 \times 10^{-3}$
1.00	2.5	9.32	40.34	-0.309	$-7.67 \times 10^{-3}$
1.00	2.0	16.47	13.31	-0.097	$-7.31 \times 10^{-3}$
1.30	3.0	5.97	123.75	-0.564	$-4.56 \times 10^{-3}$
1.30	2.5	10.63	40.10	-0.228	$-5.70 \times 10^{-3}$
1.30	2.0	18.89	13.11	-0.104	$-7.95 \times 10^{-3}$

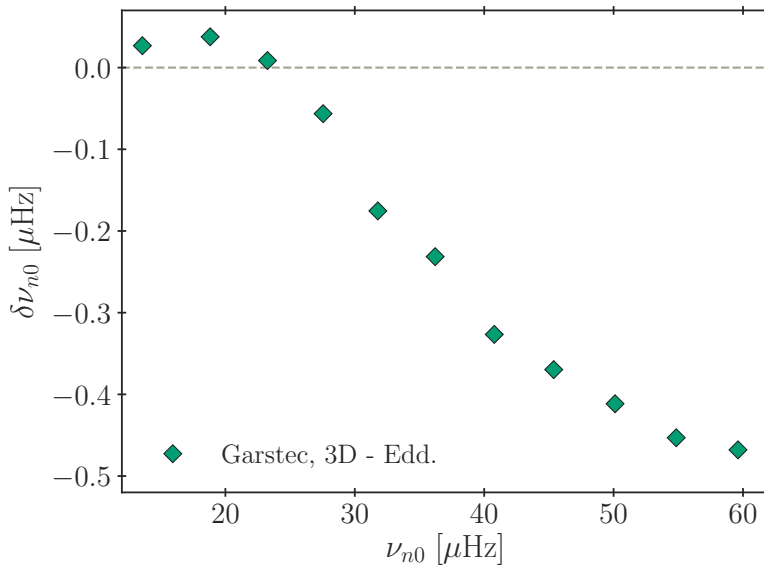


**Figure 8.11 | Frequency comparison at the RGB.** Difference in radial modes of the model with  $\langle 3D \rangle$ -envelopes appended on the fly and standard Eddington model with initial masses of  $1.00 M_{\odot}$  as a function of  $\langle 3D \rangle$ -envelope frequencies. The comparison point is chosen near  $\log g = 2.5$  at  $R = 9.32 R_{\odot}$ .

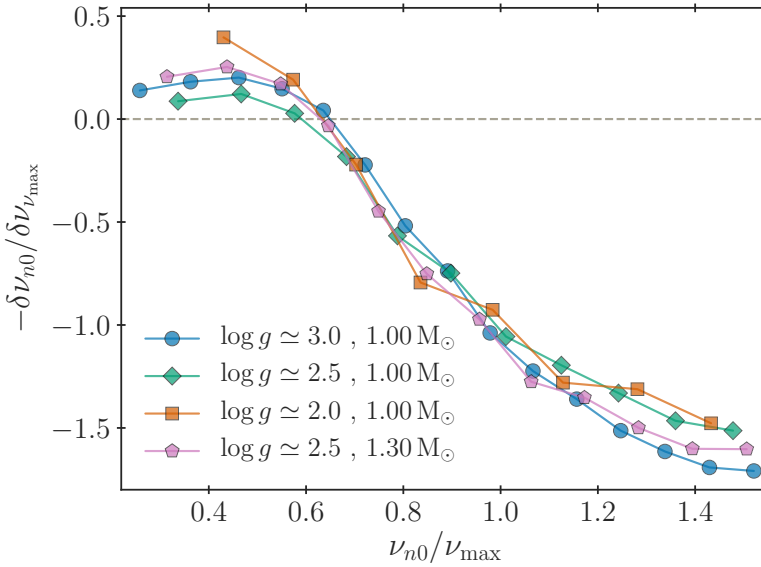


**Figure 8.12 | Scaled frequency comparison for RGB models.** Differences are “3D – Eddington”. For a given comparison, the model frequencies and frequency differences are scaled by respectively  $\nu_{\max}$ , and the difference at this point  $\delta\nu_{\nu_{\max}}$  (details in the text). The green diamonds are identical to those in fig. 8.11 except for the applied scaling. All quantities and comparison points are listed in table 8.4

two models in a pair are almost identical, with the variation caused by the differences in  $T_{\text{eff}}$  (on the order of 40 K). Then we select the oscillation mode closest to  $\nu_{\max}$  and the two adjacent modes – one on either side – and calculate the average frequency deviation of these three modes, which we denote  $\delta\nu_{\nu_{\max}}$ . Now, the frequencies are scaled by  $\nu_{\max}$  and the frequency differences by  $\delta\nu_{\nu_{\max}}$ .

All of the quantities are listed in table 8.4, and in all cases the relative difference at the frequency of **frequency of maximum power** is below 1%. Additionally, four of the resulting curves are shown in fig. 8.12, and they turn out to be remarkably similar. From this figure, it is clear that the shape of the deviation is independent of position on the RGB, and equally important independent of mass as well.

As also mentioned in the introduction, the application of atmospheric 3D RHD simulations to study the **surface effect** of solar-like oscillators has

been the focus of different studies in the recent years. Several groups have utilized the patched model technique to perform investigations across the **HRD** or **Kiel diagram**. One to highlight in the current context is the work by Sonoi et al. (2015), because two of their comparison points are denoted as **RG**-stars: Their model *I* ( $T_{\text{eff}} = 5885$  K,  $\log g = 3.5$ ) and model *J* ( $T_{\text{eff}} = 4969$  K,  $\log g = 2.5$ ). Even though it is somewhat hotter, the latter is especially interesting for our comparison being furthest up the **RGB**. Note, however, that the performed patch for *J* is using a  $M = 3.76 M_{\odot}$  model, which is very different from our cases.) They derive corrections both in the form of the classical Kjeldsen, Bedding, and Christensen-Dalsgaard (2008) power law and their own “modified Lorentzian formulation”, where one of the quantities in both fits can be directly translated to  $\delta v/v_{\text{max}}$  at  $v = v_{\text{max}}$  (denoted  $\delta v_{v_{\text{max}}}/v_{\text{max}}$  above). We predict the same sign of the deviation and, taking the quite different approaches into account, our results are roughly of the same magnitude. Furthermore, their equation 10 provides the fitting factors as a function of  $\log g$  and  $T_{\text{eff}}$ ; we do not see a clear surface gravity trend as they predict, but the magnitude of the estimates from this is also in line with our findings.

However, as very recently shown by Jørgensen et al., 2019 based on an analysis of 315 patched models, the coefficients in the Lorentzian formulation by Sonoi et al. (2015) strongly depend on the underlying sample. Consequently, there exists no set of coefficient values that is universally applicable throughout the parameter space. The authors note that the formulation derived by Sonoi et al. (2015) suffers from a selection bias, as it is predominantly based on models, for which  $T_{\text{eff}} > 6000$  K and  $\log g \geq 4.0$ . It follows that their fit cannot be directly applied to stars on the **RGB**. Our current results are in line with this conclusion.

Finally, we note that neither the Lorentzian formulation by Sonoi et al. (2015) nor the frequency difference we present in fig. 8.12 can be directly translated into a surface correction relation, since modal effects and turbulent pressure have been neglected.

## 8.7 Conclusions

We have presented an extensive analysis of stellar models that append (3D)-envelopes on the fly from the **STAGGER grid** at each time step following the

procedure introduced by chapter 7. These models provide a more physically accurate description of the outermost layers in low-mass stars.

When calculating the appended  $\langle 3\text{D} \rangle$ -envelopes, we use the **EOS** from the stellar evolution code. In chapter 7, we verified that the density and temperature obtained from the **EOS** showed good agreement with the 3D solar simulation. Here we verified that the resulting first adiabatic index  $\Gamma_1$  does not significantly shift the obtained oscillation frequencies compared to using  $\Gamma_1$  directly from the 3D simulation.

By performing different solar calibrations, we investigated the effect of the so-called **matching point**, i.e., the depth above which the  $\langle 3\text{D} \rangle$ -envelopes are appended to the stellar model. We find the mixing length to increase monotonically with increasing matching depth, which is in qualitative agreement with Schlattl, Weiss, and Ludwig (1997). This being said, the evolutionary tracks are relatively insensitive to the **matching point**, provided that it is placed sufficiently deep within the superadiabatic outer layers. Moreover, we find that the oscillation frequencies are equally independent of the matching depth for sufficiently high values.

We have performed a solar model analysis using the **Trapedach grid** of 3D simulations, and find consistency with the **STAGGER grid** results (shown in chapter 7). Moreover, the computed evolutionary tracks are shifted towards higher effective temperatures on the **RGB** compared to reference Eddington-grey models. As shown in chapter 5, the same qualitative effect was found by Mosumgaard et al. (2018) utilising parametrised information from the same 3D grid extracted by Trapedach et al. (2014a,b).

Moving on from the Sun, we have computed evolutionary tracks for stars of different mass to further test our procedure for including  $\langle 3\text{D} \rangle$ -envelope on the fly. The tracks show prominent kinks at the boundaries of the grid of 3D simulations, as well as in regions where the sampling is sparse – especially problematic on the **RGB** and in the **PMS**. This calls for a refinement of the 3D grids to make the interpolation more reliable. Furthermore, more simulations at higher temperatures will extend the usefulness of our method by widening the allowed mass range.

Moreover, we took advantage of the different models across the **Kiel diagram** to further investigate the applicability of our method and specifically the equation **EOS**. By comparing to full 3D simulations, we can conclude that the density is reproduced accurately for **MS** stars and **subgiants**; however the residuals are slightly larger for more evolved giants. This is partially a

resolution effect due to the very few simulations along the **RGB**, where the tracks are close to each other. For the first time, an asteroseismic analysis using stellar models including  $\langle 3D \rangle$ -envelope on the fly is presented. Using a grid-based approach and **BASTA**, we determined the stellar parameters of two stars from the *Kepler LEGACY* sample. We find that the obtained parameters are consistent – in the sense that they agree within the uncertainties – between the grid with our new method and the reference Eddington case. This consistency also holds between fits to individual frequencies and frequency separation ratios. Furthermore, comparing the best-fitting models from both grids to the observations, we see that the asteroseismic **surface effect** is strongly reduced by using  $\langle 3D \rangle$ -envelopes on the fly. In other words, our new models are able to predict frequencies much closer to observations without using any additional corrections, and are able to do so consistently across stellar parameters.

Finally, we extended the asteroseismic investigation to **RG**-stars. We carefully matched standard Eddington models with  $\langle 3D \rangle$ -envelopes appended on the fly to look at the detailed differences in their oscillation frequencies. We see a relative difference below 1 % at the **frequency of maximum power**, and no trend in shape or relative deviation with either mass or surface gravity.

Although the differences between the new models and the patched ones are rather minor, we have demonstrated the robustness of the method with regard to details of the application of the  $\langle 3D \rangle$ -envelopes, both for **MS** and **RG** stars. We expect larger effects for lower metallicity **RG**-stars, which we treat in a future work. As a last remark, we want to once again stress the need for a denser grid of 3D atmospheres/envelopes, and the requirement to compute new **RHD** simulations to achieve this. This will enable the use of  $\langle 3D \rangle$ -envelopes on the fly for stellar evolution to reach its full potential resulting in more realistic models.

## 8.A Grid Morphology

The **STAGGER grid** is designed with spectroscopy in mind and is therefore regular in the **Kiel diagram**, i.e., in the  $(T_{\text{eff}}, \log g)$ -plane. However, as described above, we also need to set up a triangulation in the  $(T_m, \log g)$ -space, where  $T_m$  is the temperature at the **matching point** given the choice of  $K_m$ . This is required by our implementation in order to infer  $T_{\text{eff}}$  by interpolation.

In section 8.3.2 and section 8.4.1, it was discussed that the effective resolution of **STAGGER grid** in the  $(T_m, \log g)$ -plane is different from the almost-regular  $(T_{\text{eff}}, \log g)$ -space. This is an effect of the given simulation points moving as a function of  $K_m$ .

In the top panel of fig. 8.13, the **STAGGER grid** at solar metallicity is shown in the traditional **Kiel diagram**. To ease the discussion, the individual simulation is annotated with a number: 1 for the lowest  $T_{\text{eff}}$  and 28 for the highest. In the bottom panel of the figure, the grid is shown in the form of  $T_m$  and  $\log g$  for our usual choice of  $K_m = 1.20$ . The simulation points in this figure have the same labels as in the first one. In both figures, a  $1.00 M_{\odot}$  track using our new implementation with  $K_m = 1.20$  is shown for reference.

From the plots, it is clear that the morphology of the grid changes. It is also evident that the “movement” of the points depends on the surface parameters of the simulation. This has the profound effect that some of the simulation points switch places in the temperature ordering. As an example, simulation 2 is colder than 3 looking at  $T_{\text{eff}}$ , but hotter in  $T_m$ ; the opposite is the case for 8 and 6, where the former has the highest  $T_{\text{eff}}$ , but the latter highest  $T_m$ . Another trend is the tendency for the cold simulations to “clump”, which is very evident looking at [5, 12, 18] or [7, 11]. On the other hand, simulations like [3, 10] or [9, 16] instead move away from each other.

These changes in the temperature ordering can affect the triangulation, thus altering the interpolation results; thus, this is directly linked to the observed kinks in the evolutionary tracks in the **Kiel diagram**.

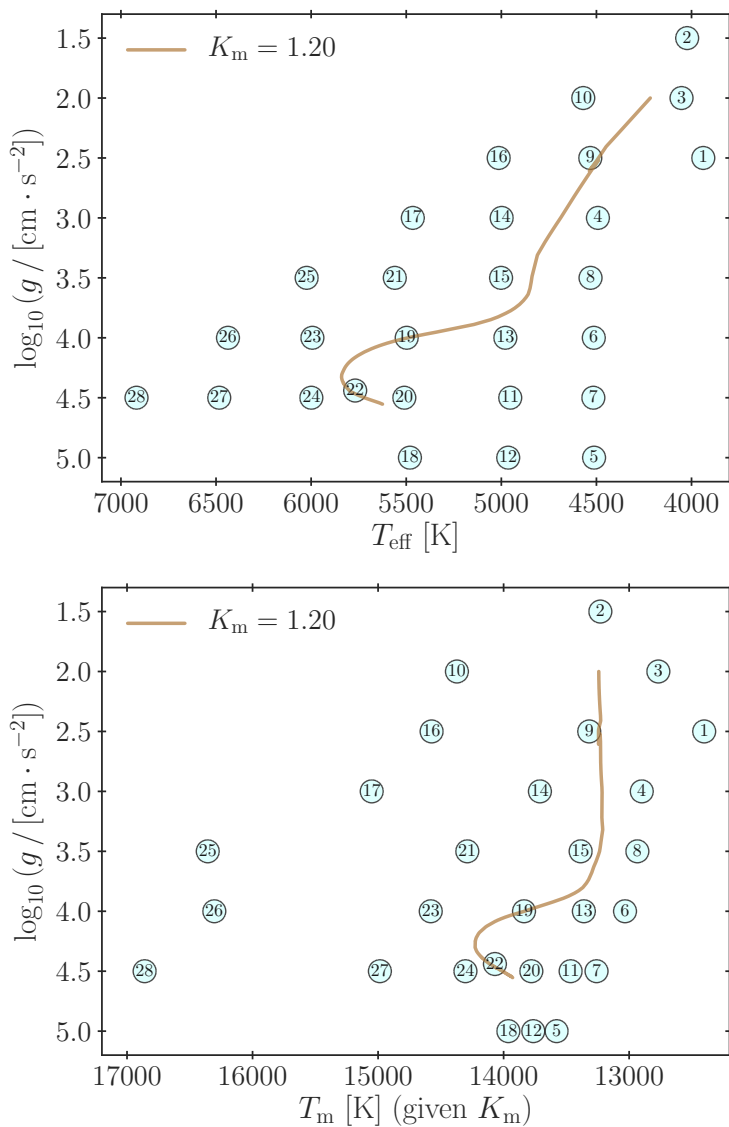


**Figure 8.13 | The STAGGER grid at solar metallicity.** The simulation points are numbered according to  $T_{\text{eff}}$ . The evolutionary track is for a  $1.00 M_{\odot}$  star using  $\langle 3\text{D} \rangle$ -envelope on the fly. *Top panel:* Kiel diagram with the STAGGER grid at solar metallicity. *Bottom panel:* Temperature at the matching point,  $T_m$ , for  $K_m = 1.20$ .

## Conclusions and Outlook

In this thesis, I have presented the work carried out during my PhD studies concerning the sparkly dots we call stars. The focus of my research has been to improve the physical description of the outer convective layers in traditional stellar models. Specifically, I have pursued several different methods for including the insights gained from 3D *radiation-coupled hydrodynamics* (RHD) simulations of atmospheres in stellar evolution codes.

The first part of the thesis established the required theoretical framework for understanding the research. In chapters 1 and 2 the fundamental principles of stellar evolution theory and *asteroseismology* are reviewed. A key conclusion from these is that current stellar models incorrectly model the convection in stars with a simplified theory, which results in a shift in the observed frequencies known as the *asteroseismic surface effect*. Chapter 3 introduced tools with which fundamental stellar properties are determined from observations, which is relied on in later chapters. A fundamentally different approach to convection was concisely reviewed in chapter 4: numerical 3D RHD simulations of stellar atmospheres. The chapter outlined the three different methods to be presented in the second part of the thesis, as well as introduced the two grids of 3D models to be used.

In the second part, my research results were presented. Firstly, chapter 5 dealt with the use of *condensed 3D simulations*, also dubbed the *dynamic approach*. In the work presented, we consistently implemented results extracted from 3D RHD simulations of stellar convection in the stellar evolution codes: the *Garching stellar evolution code* (GARSTEC) and *Modules for Experiments in Stellar Astrophysics* (MESA). The new implementation consists of two parts: a temperature stratification in the form of  $T(\tau)$  relations and corresponding corrected temperature gradients; and a calibrated,

variable mixing-length parameter  $a_{\text{MLT}}(T_{\text{eff}}, \log g)$ . The evolutionary tracks are shifted, but the asteroseismic and structural impacts are minor. This work is an advancement over the earlier efforts by Salaris and Cassisi (2015), as our implementation is seemingly more consistent and our analysis is more extensive (including e.g. asteroseismology and a comparison of the structure).

Secondly, the *static* approach was presented by chapter 6. This deals with the construction of the so-called *patched models*, where the outer layers of a stellar structure model is peeled off and replaced by an averaged structure from a 3D model. Such methods have significant impact on the structural part of the *surface effect*, but cannot influence the evolution as the patching is performed as an independent, final step. More importantly, a new interpolation method was devised enabling the construction of patched models with any atmospheric parameters (inside the grid of 3D simulations). This work presents a significant improvement over earlier efforts, which have been restricted to building patched models exactly matching the parameters of an underlying 3D simulation.

Neither of the two approaches proved fully satisfactory, as the *static* one left the evolution unaltered, and the *dynamic* one only had a small structural impact. This led to the third approach, which is dubbed “3D on the fly”, and described in chapters 7 and 8. The work presented is a novel approach that relies on using the mean structure from interpolated 3D envelopes as boundary conditions for the stellar evolution code, while also appending the structure at every timestep. As is shown, the result is a structural impact equivalent to patched models, but consistently taken into account throughout the evolution. We demonstrated the robustness of the method with regard to details of the application of the  $\langle 3D \rangle$ -envelopes, both for main-sequence and red giant stars. We also extended the asteroseismic analysis to characterise the behaviour of the *surface effect* in the red-giant regime. The work presented in those chapters is a substantial advancement compared to earlier works, as a similar implementation has not been successfully attempted before. Additionally because we are able to predict frequencies much closer to observations without using any additional corrections, and are able to do so consistently across stellar parameters.

A general conclusion from the presented research works is how the interpolation methods would benefit from more 3D simulations. The scheme is verified to work, but is also clearly limited by the range and sampling rate

of the currently available collections of 3D models. The need for a denser grid of 3D atmospheres/envelopes and the requirement to compute new RHD simulations to achieve this must be stressed. This will enable the use of  $\langle 3D \rangle$ -envelopes on the fly for stellar evolution to reach its full potential resulting in more realistic models.



In the future, two lines of work seems particularly alluring. First of all, the kinks in the tracks must be eliminated in order to fully trust the evolutionary results from 3D on the fly. Essentially, the work presented in section 8.A is already making progress in this direction and has provided clues to the origin of the problem.

Secondly, the text natural step for extending the method is to tackle interpolation in metallicity. In the same framework as presented in chapter 6, Jørgensen et al. (2019) explored the interpolation across metallicities in the STAGGER grid proving the basic principle. However, the details of the on-the-fly-implementation in GARSTEC are in some sense fundamentally different and rely on another triangulation making it non-trivial to transfer. Moreover, the resulting kinks in the methods should be dealt with first, and preferably the resolution in metallicity of the grid should be improved. Nonetheless, it will significantly extend the applicability of the method, and it is a clear requirement for the future use of our procedure.

Having physically accurate stellar models are important for many different branches of astrophysics and astronomy. An example is the future PLATO mission (Rauer et al., 2014) currently set to be launched in 2026, with the objective of characterising the population of rocky exoplanets orbiting solar-like stars. The coming data will also provide an invaluable contribution to the field of galactic archaeology (Miglio et al., 2017). An integral part of the mission is determining precise and accurate fundamental stellar parameters. To successfully perform this task, the best possible methods and more importantly the most advanced stellar models are required – our new models using  $\langle 3D \rangle$ -envelopes on-the-fly seem like a strong candidate.

The work presented in this thesis constitutes a major step forward in the research field of stellar evolution theory, and is pushing the frontier in the quest for better stellar models.



# Glossary

- Aarhus adiabatic pulsation code (ADIPLS)** Sometimes *Aarhus adiabatic oscillation package*. A code to calculate adiabatic oscillation frequencies from stellar models developed by Prof. Jørgen Chistensen-Dalsgaard. The pulsation code used in this thesis work; [xix](#), [42](#), [59](#), [86](#), [105](#), [113](#), [114](#), [134](#), [144](#), [159](#), [165](#)
- Aarhus stellar evolution code (ASTEC)** A stellar evolution code developed by Prof. Jørgen Chistensen-Dalsgaard used to produce the reference solar model *Model S*; [xix](#), [96](#)
- acoustical cut-off frequency** Characteristic frequency for the outer/upper turning point of pressure-modes. Sometimes just the *acoustic* cut-off; [34](#), [35](#), [39](#), [45](#), [54](#)
- asteroseismology** Also *asteroseismic*. The study of oscillations in stars to characterise their interior; [2](#), [3](#), [31](#), [32](#), [36](#), [37](#), [39](#), [40](#), [43–45](#), [47–52](#), [54–57](#), [59](#), [63](#), [67](#), [72](#), [74](#), [86](#), [87](#), [90](#), [94–96](#), [108](#), [110](#), [112](#), [113](#), [115](#), [117](#), [124](#), [125](#), [129](#), [138](#), [140](#), [141](#), [144](#), [158–160](#), [163–165](#), [170](#), [173](#), [174](#)
- Bag of Stellar Tracks and Isochrones (BASTI)** Formally *BaSTI*. Extensive library of isochrones suitable for stellar population studies; [xix](#), [88](#)
- BAyesian STellar Algorithm (BASTA)** Flexible grid-based modelling pipeline based on Bayesian statistics and asteroseismic inference; [xix](#), [58](#), [59](#), [93](#), [115](#), [116](#), [122](#), [159–161](#), [164](#), [170](#)

- best-fitting model (BFM)** Models with highest assigned likelihood in a grid-based analysis; [xix, 115, 160, 162–164](#)
- Birmingham Solar-Oscillations Network (BISON)** Formally *BiSON*. Global network dedicated to observing low degree p-modes in the Sun; [xix, 37, 38, 40, 41, 43, 44, 86, 87, 105, 107, 135, 137, 145–147](#)
- Brunt–Väisälä frequency** Characteristic frequency for gravity-modes. Also known as the buoyancy frequency; [34, 35, 105](#)
- COncvection ROtation and planetary Transits (COROT)** Formally *CoRoT*. Photometric satellite mission launched in December 2006.; [xix, 164](#)
- core-hydrogen exhaustion (CHE)** The end of the main sequence. Also known as the *turn-off* point; [xix, 83, 90](#)
- equation of state (EOS)** Relation between thermodynamic quantities (pressure, density, temperature). One of the constitutive equations in stellar structure theory; [xix, 12, 44, 81, 106, 107, 113, 122, 131, 132, 134, 142, 144, 145, 155, 158, 162, 163, 169](#)
- frequency of maximum power** Centre of the envelope traced by the oscillations in a power spectrum. Denoted by  $\nu_{\max}$ ; [37, 52, 145, 165–167, 170](#)
- full-spectrum theory (FST)** A theory of stellar convection. An alternative to *mixing-length theory*; [xix, 107](#)
- g-mode** Gravity-mode. Oscillation mode where the restoring force is buoyancy; [34, 35, 56](#)
- Gaia** Astrometric space mission launched in December 2013.; [53](#)
- Garching stellar evolution code (GARSTEC)** A stellar evolution code mainly developed by Prof. Dr. Achim Weiss. The primary stellar evolution code used in this thesis work; [xix, 27, 28, 44, 59, 67, 71, 75–82, 84, 86, 88–92, 97, 104, 106, 113, 114, 128–130, 134, 141, 144, 145, 151, 154, 157, 159, 162, 163, 175](#)

**Hayashi track** Limit of hydrostatic equilibrium in the Hertzsprung-Russel diagram. Followed by fully convective (pre-main sequence) stars; 14

**helioseismology** Also *helioseismic*. The study of oscillations in the Sun to characterise its interior; 3, 29, 31, 32, 42–45, 51, 62, 66, 86, 90, 105, 106, 110, 111, 124, 128, 134, 146, 150

**Hertzsprung-Russel diagram (HRD)** Diagram of stellar surface luminosity against  $T_{\text{eff}}$ ; xx, 13, 15, 74, 111, 114, 124, 139, 140, 168

**InfraRed Flux Method (IRFM)** A method to determine stellar effective temperatures from photometry; xx, 117

**KAGES sample** A sample of 33–35 exoplanet-candidate host stars *Kepler* showing solar-like oscillations with high data quality; 50, 113, 117

**Kepler** Space telescope launched in March 2009 to perform photometric time-series measurements.; 49, 50, 65, 73, 94, 95, 97, 111, 113, 115, 116, 124, 138, 140, 158, 164, 170

**Kiel diagram** Diagram of  $T_{\text{eff}}$  against  $\log g$ . Also known as a “spectroscopic Hertzsprung-Russel diagram”; 13–15, 74, 75, 154, 168, 169, 171, 172

**Lamb frequency** Characteristic frequency for pressure-modes. Linked to the inner turning/reflection point. Also known as the characteristic acoustic frequency; 34

**large frequency separation** Asymptotic separation in frequency between modes of consecutive orders. Denoted by  $\Delta\nu$ ; 36, 39–41, 52, 113, 158, 164

**LEGACY sample** A sample of the 66 “best” main-sequence stars from *Kepler* showing solar-like oscillations.; 50, 113, 117, 158, 170

**main sequence (MS)** Evolutionary phase with hydrogen fusion in the stellar core; xx, 15, 16, 22, 32, 35, 36, 50, 55, 82, 89, 99, 103, 124, 149, 154–156, 158, 160, 169, 170

- matching point** The transition point between interior model and appended mean 3D envelope in the “on the fly” implementation; 130–133, 135, 136, 138, 141–144, 146–149, 151, 153, 155–157, 169, 171, 172
- mixing-length theory (MLT)** A theory of stellar convection. The most commonly used in stellar evolution calculations; xx, 22–24, 27, 61, 63–66, 73, 79, 80, 88, 107, 133, 140, 144
- Modules for Experiments in Stellar Astrophysics (MESA)** An open-source stellar evolution code; xx, 72–74, 76, 77, 79–81, 83, 84, 86–92, 211–213
- p-mode** Pressure-mode. Oscillation mode where the restoring force is the pressure gradient; 34–37, 56, 105, 122, 128, 129, 138
- patched model (PM)** The resulting model after replacement of the outer layers by a stratification from a hydrodynamical simulation; xx, 97, 105, 106, 110, 112, 116, 123, 135, 162, 163
- PLANetary Transits and Oscillation of stars (PLATO)** Formally PLATO 2.0. Future photometric satellite mission to be launched in 2026.; xx
- pre-main sequence (PMS)** Evolutionary phase prior to the ignition of hydrogen fusion; xx, 28, 72, 75, 82–84, 90, 131, 132, 169
- probability density function (PDF)** Sometimes *probability distribution function*. Distribution of a random variable. Used to describe inferred parameters in a Bayesian framework; xx, 59, 115
- radiation-coupled hydrodynamics (RHD)** Numerical simulations where the equations of hydrodynamics is solved alongside a full computations of radiative transfer; xx, 62–66, 73, 77, 89, 90, 95, 96, 99, 105, 124, 125, 127, 129, 140, 141, 150, 155, 158, 167, 170, 173, 175
- red giant (RG)** A star on the *red-giant branch*; xx, 42, 50, 56, 73, 99, 139–141, 155, 158, 163, 164, 168, 170

- red-giant branch (RGB)** Evolutionary phase with a dense helium core, hydrogen fusion in a shell and extended convective envelope; **xx**, 32, 36, 72, 73, 82–84, 90, 140, 147–149, 151–153, 155, 163, 165, 167–170
- STAGGER grid** A grid of stellar atmosphere simulations (to model surface convection) calculated using 3D radiation-coupled hydrodynamics.; 63–65, 67, 90, 96, 98, 100–110, 112, 115–119, 129–135, 141–144, 147–150, 152–158, 162, 168, 169, 171, 172, 175, 184
- standard solar model (SSM)** A model of the Sun, which reproduces the solar surface parameters at the solar age. Sometimes just *solar model*; **xx**, 28, 43, 51, 64, 72, 81, 84, 89, 90, 96, 105, 122, 123, 129, 133, 140, 144
- subgiant** Evolutionary phase with inert helium core and hydrogen fusion in a shell. Rapid evolution roughly following the Kelvin-Helmholtz timescale; 14, 15, 32, 42, 56, 114, 156, 169
- surface effect** Discrepancy between observed and calculated oscillation frequencies as a result of deficiencies in stellar models; 3, 43, 44, 54, 63, 64, 87, 90, 95, 108, 113, 119, 120, 124, 129, 138, 140, 159, 160, 163, 167, 170, 173, 174
- Trampedach grid** A grid of stellar atmosphere simulations (to model surface convection) calculated using 3D radiation-coupled hydrodynamics.; 63, 65, 66, 74, 75, 96, 100, 103–106, 108, 110, 112–116, 118, 122, 123, 139, 141, 149–153, 169, 183
- Transiting Exoplanet Survey Satellite (TESS)** Photometric satellite mission launched in April 2018.; **xx**
- turn-off** The termination of main-sequence evolution. Equivalent to core-hydrogen exhaustion; 15, 82, 83, 147
- Two Micron All Sky Survey (2MASS)** Survey comprised of infrared photometry of the entire celestial sphere; **xix**

**un-patched model (UPM)** The base model in a patching procedure before the patching has been performed; **xx**, 94–97, 105–107, 109–112, 115–119, 121–124

**zero-age main sequence (ZAMS)** The onset of hydrogen fusion; **xx**, 36, 114, 155

# List of Figures

1.1	Evolution of a 1 solar mass star in a Kiel diagram . . . . .	14
1.2	Drawing of the typical occurrences of stellar convection zones	22
2.1	Frequency spectrum of the Sun as-a-star . . . . .	38
2.2	Échelle diagram of the observed low-degree frequencies in the Sun . . . . .	41
2.3	Asteroseismic surface effect in the Sun . . . . .	44
5.1	A Kiel diagram showing the <i>Trampedach</i> grid of 3D simulations	75
5.2	The implemented changes to a stellar structure model . . . . .	80
5.3	Stellar evolutionary tracks from <i>GARSTEC</i> . . . . .	82
5.4	Stellar evolutionary tracks from <i>MESA</i> . . . . .	83
5.5	Temperature as a function of optical depth in the outermost parts of the solar models . . . . .	85
5.6	Temperature as a function of radius . . . . .	86
5.7	Difference between observed and calculated oscillation frequencies of the Sun . . . . .	87
5.8	Stellar evolution with <i>SC15</i> settings . . . . .	92
5.9	Magnitude of the gradient correction term . . . . .	92
6.1	Pressure stratification of a <i>PM</i> and an <i>UPM</i> . . . . .	98
6.2	Shifting the stratification by the position of the density jump .	100
6.3	Behaviour of the pressure at the density jump . . . . .	101
6.4	Reproduction of the solar simulation using interpolation . . .	102
6.5	Residuals from interpolation when excluding simulations . .	103
6.6	Residuals from interpolation when excluding simulations . .	104

6.7	Comparing different patched solar models . . . . .	106
6.8	Comparison of convection theories using patched models . .	107
6.9	Comparison of different patching quantities . . . . .	109
6.10	The effect of deviation in atmospheric parameters . . . . .	112
6.11	Patched model analysis of KIC 9025370 . . . . .	118
6.12	Patched model analysis of KIC 9955598 . . . . .	119
6.13	Patched model analysis of KIC 11133306 . . . . .	120
6.14	Patched model analysis of KIC 11772920 . . . . .	121
6.15	Comparison of patching quantities in a solar model . . . . .	123
7.1	Schematic overview of the implementation . . . . .	130
7.2	Reproduction of the solar envelope using our new implemen- tation . . . . .	135
7.3	Reproduction of the solar envelope . . . . .	136
7.4	Reproduction of the solar envelope . . . . .	136
7.5	Reproduction of the solar oscillation frequencies . . . . .	137
8.1	Scaled density stratification as a function of the scaled pressure	143
8.2	Frequency changes caused by EOS effects . . . . .	145
8.3	Solar calibrations with different matching depths . . . . .	147
8.4	Evolution of the solar calibration models . . . . .	148
8.5	Reproduction of the 3D solar simulation . . . . .	151
8.6	Evolutionary tracks of the solar models . . . . .	152
8.7	Evolutionary tracks of models with different stellar masses . .	154
8.8	Structural residuals at the comparison points . . . . .	157
8.9	Frequency differences between model predictions and obser- vations for KIC 11772920 . . . . .	162
8.10	Échelle diagram of KIC 9955598 separated in degrees . . . . .	164
8.11	Frequency comparison at the RGB . . . . .	166
8.12	Scaled frequency comparison for RGB models . . . . .	167
8.13	The STAGGER grid at solar metallicity . . . . .	172

# List of Tables

6.1	Parameters of the analysed <i>Kepler</i> stars . . . . .	116
7.1	Resulting parameters from the solar calibrations . . . . .	133
8.1	Results from the different solar calibrations . . . . .	150
8.2	Comparison points with different stellar parameters . . . . .	156
8.3	Resulting parameters of the modelled <i>Kepler</i> stars . . . . .	161
8.4	Comparison points for RGB models . . . . .	166



# Bibliography

- Adelberger, E. G.; García, A.; Robertson, R. G. H.; Snover, K. A.; Balantekin, A. B.; Heeger, K.; Ramsey-Musolf, M. J.; Bemmerer, D.; Junghans, A.; Bertulani, C. A.; Chen, J.-W.; Costantini, H.; Prati, P.; Couder, M.; Uberseder, E., et al. (2011). “Solar fusion cross sections. II. The pp chain and CNO cycles”. *Reviews of Modern Physics* 83.1, pp. 195–246.
- Adelberger, E. G.; Austin, S. M.; Bahcall, J. N.; Balantekin, A. B.; Bogaert, G.; Brown, L. S.; Buchmann, L.; Cecil, F. E.; Champagne, A. E.; de Braekeleer, L.; Duba, C. A.; Elliott, S. R.; Freedman, S. J.; Gai, M.; Goldring, G., et al. (1998). “Solar fusion cross sections”. *Reviews of Modern Physics* 70.4, pp. 1265–1291.
- Aerts, C.; Christensen-Dalsgaard, J., and Kurtz, D. W. (2010). *Asteroseismology*. Astronomy and Astrophysics Library. Springer Science+Business Media.
- Akima, H. (1970). “A New Method of Interpolation and Smooth Curve Fitting Based on Local Procedures”. *Journal of the ACM* 17.4, p. 589.
- Akima, H. (1991). “A method of univariate interpolation that has the accuracy of a third-degree polynomial”. *ACM Transactions on Mathematical Software* 17.3, p. 341.
- Alexander, D. R. and Ferguson, J. W. (1994). “Low-Temperature Rosseland Opacities”. *Astrophysical Journal* 437, p. 879.
- Anders, E. and Grevesse, N. (1989). “Abundances of the elements: Meteoritic and solar”. *Geochimica et Cosmochimica Acta* 53.1, pp. 197–214.

- Angulo, C.; Arnould, M.; Rayet, M.; Descouvemont, P.; Baye, D.; Leclercq-Willain, C.; Coc, A.; Barhoumi, S.; Aguer, P.; Rolfs, C.; Kunz, R.; Hammer, J. W.; Mayer, A.; Paradellis, T.; Kossionides, S., et al. (1999). "A compilation of charged-particle induced thermonuclear reaction rates". *Nuclear Physics A* 656.1, pp. 3–183.
- Asplund, M.; Grevesse, N., and Sauval, A. J. (2005). "The Solar Chemical Composition". In: *Cosmic Abundances as Records of Stellar Evolution and Nucleosynthesis in honor of David L. Lambert, ASP Conference Series, Vol. 336, Proceedings of a symposium held 17-19 June, 2004 in Austin, Texas. Edited by Thomas G. Barnes III and Frank N. Bash. San Francisco: Astronomical Society of the Pacific, 2005., p.25.* Ed. by I. Barnes Thomas G. and F. N. Bash. Vol. 336. ASP Conference Series. Astronomical Society of the Pacific, p. 25.
- Asplund, M.; Grevesse, N.; Sauval, A. J., and Scott, P. (2009). "The Chemical Composition of the Sun". *Annual Review of Astronomy & Astrophysics* 47.1, pp. 481–522.
- Badnell, N. R.; Bautista, M. A.; Butler, K.; Delahaye, F.; Mendoza, C.; Palmeri, P.; Zeippen, C. J., and Seaton, M. J. (2005). "Updated opacities from the Opacity Project". *Monthly Notices of the Royal Astronomical Society* 360.2, pp. 458–464.
- Baglin, A.; Auvergne, M.; Barge, P.; Deleuil, M.; Catala, C.; Michel, E.; Weiss, W., and COROT Team (2006). "Scientific Objectives for a Minisat: CoRoT". In: *The CoRoT Mission Pre-Launch Status - Stellar Seismology and Planet Finding.* Ed. by M. Fridlund; A. Baglin; J. Lochard, and L. Conroy. Vol. 1306. ESA Special Publication, p. 33.
- Bahcall, J. N.; Basu, S.; Pinsonneault, M., and Serenelli, A. M. (2005). "Helioseismological Implications of Recent Solar Abundance Determinations". *Astrophysical Journal* 618.2, pp. 1049–1056.
- Ball, W. H.; Beeck, B.; Cameron, R. H., and Gizon, L. (2016). "MESA meets MURaM. Surface effects in main-sequence solar-like oscillators computed using three-dimensional radiation hydrodynamics simulations". *Astronomy and Astrophysics* 592, A159.
- Ball, W. H. and Gizon, L. (2014). "A new correction of stellar oscillation frequencies for near-surface effects". *Astronomy and Astrophysics* 568, A123.

- Basu, S. and Antia, H. M. (1997). "Seismic measurement of the depth of the solar convection zone". *Monthly Notices of the Royal Astronomical Society* 287.1, pp. 189–198.
- Basu, S. and Antia, H. M. (2004). "Constraining Solar Abundances Using Helioseismology". *The Astrophysical Journal Letters* 606.1, pp. L85–L88.
- Basu, S. and Antia, H. M. (2008). "Helioseismology and solar abundances". *Physics Reports* 457.5-6, pp. 217–283.
- Bedding, T. R. (2014). "Solar-like oscillations: An observational perspective". In: *Asteroseismology, 22nd Canary Islands Winter School of Astrophysics*. Edited by Pere L. Pallé and Cesar Esteban, Cambridge, UK: Cambridge University Press, 2014, p.60. Ed. by P. L. Pallé and C. Esteban, p. 60.
- Bedding, T. R.; Mosser, B.; Huber, D.; Montalbán, J.; Beck, P.; Christensen-Dalsgaard, J.; Elsworth, Y. P.; García, R. A.; Miglio, A.; Stello, D.; White, T. R.; De Ridder, J.; Hekker, S.; Aerts, C.; Barban, C., et al. (2011). "Gravity modes as a way to distinguish between hydrogen- and helium-burning red giant stars". *Nature* 471.7340, pp. 608–611.
- Beeck, B.; Cameron, R. H.; Reiners, A., and Schüssler, M. (2013). "Three-dimensional simulations of near-surface convection in main-sequence stars. I. Overall structure". *Astronomy and Astrophysics* 558, A48.
- Bergemann, M.; Ruchti, G. R.; Serenelli, A.; Feltzing, S.; Alves-Brito, A.; Asplund, M.; Bensby, T.; Gruyters, P.; Heiter, U.; Hourihane, A.; Korn, A.; Lind, K.; Marino, A.; Jofre, P.; Nordlander, T., et al. (2014). "The Gaia-ESO Survey: radial metallicity gradients and age-metallicity relation of stars in the Milky Way disk". *Astronomy and Astrophysics* 565, A89.
- Biermann, L. (1932). "Untersuchungen über den inneren Aufbau der Sterne. IV. Konvektionszonen im Innern der Sterne. (Veröffentlichungen der Universitäts-Sternwarte Göttingen, Nr. 27. ) Mit 5 Abbildungen." *Zeitschrift für Astrophysik* 5, p. 117.
- Böhm-Vitense, E. (1958). "Über die Wasserstoffkonvektionszone in Sternen verschiedener Effektivtemperaturen und Leuchtkräfte. Mit 5 Textabbildungen". *Zeitschrift für Astrophysik* 46, p. 108.

- Borucki, W. J.; Koch, D.; Basri, G.; Batalha, N.; Brown, T.; Caldwell, D.; Caldwell, J.; Christensen-Dalsgaard, J.; Cochran, W. D.; DeVore, E.; Dunham, E. W.; Dupree, A. K.; Gautier, T. N.; Geary, J. C.; Gilliland, R., et al. (2010). “Kepler Planet-Detection Mission: Introduction and First Results”. *Science* 327.5968, p. 977.
- Broomhall, A.-M.; Chaplin, W. J.; Davies, G. R.; Elsworth, Y.; Fletcher, S. T.; Hale, S. J.; Miller, B., and New, R. (2009). “Definitive Sun-as-a-star p-mode frequencies: 23 years of BiSON observations”. *Monthly Notices of the Royal Astronomical Society* 396.1, pp. L100–L104.
- Brown, T. M. (1984). “Solar p-Mode Eigenfrequencies are Decreased by Turbulent Convection”. *Science* 226.4675, pp. 687–689.
- Brown, T. M.; Gilliland, R. L.; Noyes, R. W., and Ramsey, L. W. (1991). “Detection of Possible p-Mode Oscillations on Procyon”. *Astrophysical Journal* 368, p. 599.
- Buldgen, G.; Reese, D. R.; Dupret, M. A., and Samadi, R. (2015). “Stellar acoustic radii, mean densities, and ages from seismic inversion techniques”. *Astronomy and Astrophysics* 574, A42.
- Caffau, E.; Ludwig, H.-G.; Steffen, M.; Freytag, B., and Bonifacio, P. (2011). “Solar Chemical Abundances Determined with a CO<sub>5</sub>BOLD 3D Model Atmosphere”. *Solar Physics* 268.2, pp. 255–269.
- Canuto, V. M.; Goldman, I., and Mazzitelli, I. (1996). “Stellar Turbulent Convection: A Self-consistent Model”. *Astrophysical Journal* 473, p. 550.
- Canuto, V. M. and Mazzitelli, I. (1991). “Stellar Turbulent Convection: A New Model and Applications”. *Astrophysical Journal* 370, p. 295.
- Canuto, V. M. and Mazzitelli, I. (1992). “Further Improvements of a New Model for Turbulent Convection in Stars”. *Astrophysical Journal* 389, p. 724.
- Casagrande, L.; Ramírez, I.; Meléndez, J.; Bessell, M., and Asplund, M. (2010). “An absolutely calibrated  $T_{\text{eff}}$  scale from the infrared flux method. Dwarfs and subgiants”. *Astronomy and Astrophysics* 512, A54.
- Casagrande, L.; Schönrich, R.; Asplund, M.; Cassisi, S.; Ramírez, I.; Meléndez, J.; Bensby, T., and Feltzing, S. (2011). “New constraints on the chemical evolution of the solar neighbourhood and Galactic disc(s).

- Improved astrophysical parameters for the Geneva-Copenhagen Survey". *Astronomy and Astrophysics* 530, A138.
- Casagrande, L.; Silva Aguirre, V.; Stello, D.; Huber, D.; Serenelli, A. M.; Cassisi, S.; Dotter, A.; Milone, A. P.; Hodgkin, S.; Marino, A. F.; Lund, M. N.; Pietrinferni, A.; Asplund, M.; Feltzing, S.; Flynn, C., et al. (2014). "Strömgren Survey for Asteroseismology and Galactic Archaeology: Let the SAGA Begin". *Astrophysical Journal* 787.2, 110.
- Cassisi, S.; Potekhin, A. Y.; Pietrinferni, A.; Catelan, M., and Salaris, M. (2007). "Updated Electron-Conduction Opacities: The Impact on Low-Mass Stellar Models". *Astrophysical Journal* 661.2, pp. 1094–1104.
- Cassisi, S.; Salaris, M., and Irwin, A. W. (2003). "The Initial Helium Content of Galactic Globular Cluster Stars from the R-Parameter: Comparison with the Cosmic Microwave Background Constraint". *Astrophysical Journal* 588.2, pp. 862–870.
- Chaplin, W. J.; Lund, M. N.; Handberg, R.; Basu, S.; Buchhave, L. A.; Campante, T. L.; Davies, G. R.; Huber, D.; Latham, D. W.; Latham, C. A.; Serenelli, A.; Antia, H. M.; Appourchaux, T.; Ball, W. H.; Benomar, O., et al. (2015). "Asteroseismology of Solar-Type Stars with K2: Detection of Oscillations in C<sub>1</sub> Data". *Publications of the Astronomical Society of the Pacific* 127.956, p. 1038.
- Chaplin, W. J.; Elsworth, Y.; Howe, R.; Isaak, G. R.; McLeod, C. P.; Miller, B. A.; van der Raay, H. B.; Wheeler, S. J., and New, R. (1996). "BiSON Performance". *Solar Physics* 168.1, pp. 1–18.
- Chaplin, W. J. and Miglio, A. (2013). "Asteroseismology of Solar-Type and Red-Giant Stars". *Annual Review of Astronomy & Astrophysics* 51.1, pp. 353–392.
- Christensen-Dalsgaard, J. (2002). "Helioseismology". *Reviews of Modern Physics* 74.4, pp. 1073–1129.
- Christensen-Dalsgaard, J. (2008a). "ADIPLS — the Aarhus adiabatic oscillation package". *Astrophysics and Space Science* 316.1-4, pp. 113–120.
- Christensen-Dalsgaard, J. (2008b). "ASTECS — the Aarhus Stellar Evolution Code". *Astrophysics and Space Science* 316.1-4, pp. 13–24.

- Christensen-Dalsgaard, J. (2008c). *Lecture Notes on Stellar Structure and Evolution*. Sixth Edition. Institut for Fysik og Astronomi, Aarhus Universitet.
- Christensen-Dalsgaard, J. (2012). “Stellar model fits and inversions”. *Astronomische Nachrichten* 333.10, p. 914.
- Christensen-Dalsgaard, J.; Dappen, W.; Ajukov, S. V.; Anderson, E. R.; Antia, H. M.; Basu, S.; Baturin, V. A.; Berthomieu, G.; Chaboyer, B.; Chitre, S. M.; Cox, A. N.; Demarque, P.; Donatowicz, J.; Dziembowski, W. A.; Gabriel, M., et al. (1996). “The Current State of Solar Modeling”. *Science* 272.5266, pp. 1286–1292.
- Christensen-Dalsgaard, J.; Dappen, W., and Lebreton, Y. (1988). “Solar oscillation frequencies and the equation of state”. *Nature* 336.6200, pp. 634–638.
- Christensen-Dalsgaard, J. and Gough, D. (1984). “Implications of observed frequencies of solar p modes.” In: *Solar Seismology from Space*. Ed. by R. K. Ulrich; J. Harvey; J. Rhodes E. J., and J. Toomre. JPL, NASA, United States, pp. 199–204.
- Christensen-Dalsgaard, J.; Proffitt, C. R., and Thompson, M. J. (1993). “Effects of Diffusion on Solar Models and Their Oscillation Frequencies”. *The Astrophysical Journal Letters* 403, p. L75.
- Cline, A. K. and Renka, R. L. (1984). “A storage-efficient method for construction of a Thiessen triangulation”. *Rocky Mountain Journal of Mathematics* 14.1, pp. 119–140.
- Cox, J. P. and Giuli, R. T. (1968). *Principles of stellar structure*. New York: Gordon and Breach.
- Creevey, O. L.; Monteiro, M. J. P. F. G.; Metcalfe, T. S.; Brown, T. M.; Jiménez-Reyes, S. J., and Belmonte, J. A. (2007). “The Complementary Roles of Interferometry and Asteroseismology in Determining the Mass of Solar-Type Stars”. *Astrophysical Journal* 659.1, pp. 616–625.
- da Silva, L.; Girardi, L.; Pasquini, L.; Setiawan, J.; von der Lühe, O.; de Medeiros, J. R.; Hatzes, A.; Döllinger, M. P., and Weiss, A. (2006). “Basic physical parameters of a selected sample of evolved stars”. *Astronomy and Astrophysics* 458.2, pp. 609–623.

- Däppen, W.; Mihalas, D.; Hummer, D. G., and Mihalas, B. W. (1988). “The Equation of State for Stellar Envelopes. III. Thermodynamic Quantities”. *Astrophysical Journal* 332, p. 261.
- Davies, G. R.; Broomhall, A.-M.; Chaplin, W. J.; Elsworth, Y., and Hale, S. J. (2014). “Low-frequency, low-degree solar p-mode properties from 22 years of Birmingham Solar Oscillations Network data”. *Monthly Notices of the Royal Astronomical Society* 439.2, pp. 2025–2032.
- Davies, G. R.; Silva Aguirre, V.; Bedding, T. R.; Handberg, R.; Lund, M. N.; Chaplin, W. J.; Huber, D.; White, T. R.; Benomar, O.; Hekker, S.; Basu, S.; Campante, T. L.; Christensen-Dalsgaard, J.; Elsworth, Y.; Karoff, C., et al. (2016). “Oscillation frequencies for 35 Kepler solar-type planet-hosting stars using Bayesian techniques and machine learning”. *Monthly Notices of the Royal Astronomical Society* 456.2, pp. 2183–2195.
- Eddington, A. S. (1926). *The Internal Constitution of the Stars*.
- Ferguson, J. W.; Alexander, D. R.; Allard, F.; Barman, T.; Bodnarik, J. G.; Hauschildt, P. H.; Heffner-Wong, A., and Tamanai, A. (2005). “Low-Temperature Opacities”. *Astrophysical Journal* 623.1, pp. 585–596.
- Gaia Collaboration; Brown, A. G. A.; Vallenari, A.; Prusti, T.; de Bruijne, J. H. J.; Babusiaux, C.; Bailer-Jones, C. A. L.; Biermann, M.; Evans, D. W.; Eyer, L.; Jansen, F.; Jordi, C.; Klioner, S. A.; Lammers, U.; Lindegren, L., et al. (2018). “Gaia Data Release 2. Summary of the contents and survey properties”. *Astronomy and Astrophysics* 616, A1.
- Gaia Collaboration; Prusti, T.; de Bruijne, J. H. J.; Brown, A. G. A.; Vallenari, A.; Babusiaux, C.; Bailer-Jones, C. A. L.; Bastian, U.; Biermann, M.; Evans, D. W.; Eyer, L.; Jansen, F.; Jordi, C.; Klioner, S. A.; Lammers, U., et al. (2016). “The Gaia mission”. *Astronomy and Astrophysics* 595, A1.
- Gilliland, R. L.; Brown, T. M.; Christensen-Dalsgaard, J.; Kjeldsen, H.; Aerts, C.; Appourchaux, T.; Basu, S.; Bedding, T. R.; Chaplin, W. J.; Cunha, M. S.; De Cat, P.; De Ridder, J.; Guzik, J. A.; Handler, G.; Kawaler, S., et al. (2010). “Kepler Asteroseismology Program: Introduction and First Results”. *Publications of the Astronomical Society of the Pacific* 122.888, p. 131.

- Gough, D. O. (1977a). "Mixing-length theory for pulsating stars." *Astrophysical Journal* 214, pp. 196–213.
- Gough, D. O. (1977b). "The current state of stellar mixing-length theory". In: *In: Problems of stellar convection; Proceedings of the Thirty-eighth Colloquium, Nice, France, August 16-20, 1976. (A78-28526 11-90)* Berlin and New York, Springer-Verlag, 1977, p. 15-56. Ed. by E. A. Spiegel and J. P. Zahn. Vol. 71, pp. 15–56.
- Gough, D. O. (1990). "Comments on Helioseismic Inference". In: *Progress of Seismology of the Sun and Stars, Proceedings of the Oji International Seminar Held at Hakone, Japan, 11-14 December 1989. Lecture Notes in Physics, Vol. 367, edited by Y. Osaki and H. Shibahashi.* Springer-Verlag, Berlin Heidelberg New York, 1990, p.283. Ed. by Y. Osaki and H. Shibahashi. Vol. 367, p. 283.
- Gough, D. O. and Weiss, N. O. (1976). "The calibration of stellar convection theories." *Monthly Notices of the Royal Astronomical Society* 176, pp. 589–607.
- Grevesse, N. and Noels, A. (1993). "Cosmic abundances of the elements." In: *Origin and Evolution of the Elements.* Ed. by N. Prantzos; E. Vangioni-Flam, and M. Casse, pp. 15–25.
- Grevesse, N. and Sauval, A. J. (1998). "Standard Solar Composition". *Space Science Reviews* 85, pp. 161–174.
- Handberg, R. and Campante, T. L. (2011). "Bayesian peak-bagging of solar-like oscillators using MCMC: a comprehensive guide". *Astronomy and Astrophysics* 527, A56.
- Heney, L. G.; Forbes, J. E., and Gould, N. L. (1964). "A New Method of Automatic Computation of Stellar Evolution." *Astrophysical Journal* 139, p. 306.
- Heney, L.; Vardya, M. S., and Bodenheimer, P. (1965). "Studies in Stellar Evolution. III. The Calculation of Model Envelopes." *Astrophysical Journal* 142, p. 841.
- Hidalgo, S. L.; Pietrinferni, A.; Cassisi, S.; Salaris, M.; Mucciarelli, A.; Savino, A.; Aparicio, A.; Silva Aguirre, V., and Verma, K. (2018). "The Updated BaSTI Stellar Evolution Models and Isochrones. I. Solar-scaled Calculations". *Astrophysical Journal* 856.2, 125.

- Hjørringgaard, J. G.; Silva Aguirre, V.; White, T. R.; Huber, D.; Pope, B. J. S.; Casagrande, L.; Justesen, A. B., and Christensen-Dalsgaard, J. (2017). “Testing stellar evolution models with the retired A star HD 185351”. *Monthly Notices of the Royal Astronomical Society* 464.3, pp. 3713–3719.
- Houdek, G.; Trampedach, R.; Aarslev, M. J., and Christensen-Dalsgaard, J. (2017). “On the surface physics affecting solar oscillation frequencies”. *Monthly Notices of the Royal Astronomical Society* 464.1, pp. L124–L128.
- Huber, D.; Chaplin, W. J.; Chontos, A.; Kjeldsen, H.; Christensen-Dalsgaard, J.; Bedding, T. R.; Ball, W.; Brahm, R.; Espinoza, N.; Henning, T.; Jordán, A.; Sarkis, P.; Knudstrup, E.; Albrecht, S.; Grundahl, F., et al. (2019). “A Hot Saturn Orbiting an Oscillating Late Subgiant Discovered by TESS”. *Astronomical Journal* 157.6, 245.
- Hummer, D. G. and Mihalas, D. (1988). “The Equation of State for Stellar Envelopes. I. an Occupation Probability Formalism for the Truncation of Internal Partition Functions”. *Astrophysical Journal* 331, p. 794.
- Huynh, H. T. (1993). “Accurate monotone cubic interpolation”. *SIAM Journal on Numerical Analysis* 30.1, pp. 57–100.
- Iglesias, C. A. and Rogers, F. J. (1996). “Updated Opal Opacities”. *Astrophysical Journal* 464, p. 943.
- Itoh, N.; Mitake, S.; Iyetomi, H., and Ichimaru, S. (1983). “Electrical and thermal conductivities of dense matter in the liquid metal phase. I - High-temperature results”. *Astrophysical Journal* 273, pp. 774–782.
- Jørgensen, A. C. S.; Mosumgaard, J. R.; Weiss, A.; Silva Aguirre, V., and Christensen-Dalsgaard, J. (2018). “Coupling 1D stellar evolution with 3D-hydrodynamical simulations on the fly - I. A new standard solar model”. *Monthly Notices of the Royal Astronomical Society* 481, pp. L35–L39.
- Jørgensen, A. C. S.; Weiss, A.; Angelou, G., and Silva Aguirre, V. (2019). “Mending the structural surface effect of 1D stellar structure models with non-solar metallicities based on interpolated 3D envelopes”. *Monthly Notices of the Royal Astronomical Society* 484.4, pp. 5551–5567.

- Jørgensen, A. C. S.; Weiss, A.; Mosumgaard, J. R.; Silva Aguirre, V., and Sahlholdt, C. L. (2017). "Theoretical oscillation frequencies for solar-type dwarfs from stellar models with (3D)-atmospheres". *Monthly Notices of the Royal Astronomical Society* 472.3, pp. 3264–3276.
- Jørgensen, B. R. and Lindegren, L. (2005). "Determination of stellar ages from isochrones: Bayesian estimation versus isochrone fitting". *Astronomy and Astrophysics* 436.1, pp. 127–143.
- Kippenhahn, R.; Weigert, A., and Weiss, A. (2012). *Stellar Structure and Evolution*. 2nd ed. Springer-Verlag Berlin Heidelberg.
- Kjeldsen, H. and Bedding, T. R. (1995). "Amplitudes of stellar oscillations: the implications for asteroseismology." *Astronomy and Astrophysics* 293, pp. 87–106.
- Kjeldsen, H.; Bedding, T. R., and Christensen-Dalsgaard, J. (2008). "Correcting Stellar Oscillation Frequencies for Near-Surface Effects". *The Astrophysical Journal Letters* 683.2, p. L175.
- Koch, D. G.; Borucki, W. J.; Basri, G.; Batalha, N. M.; Brown, T. M.; Caldwell, D.; Christensen-Dalsgaard, J.; Cochran, W. D.; DeVore, E.; Dunham, E. W.; Gautier Thomas N., I.; Geary, J. C.; Gilliland, R. L.; Gould, A.; Jenkins, J., et al. (2010). "Kepler Mission Design, Realized Photometric Performance, and Early Science". *The Astrophysical Journal Letters* 713.2, pp. L79–L86.
- Krishna Swamy, K. S. (1966). "Profiles of Strong Lines in K-Dwarfs". *Astrophysical Journal* 145, p. 174.
- Kupka, F. and Muthsam, H. J. (2017). "Modelling of stellar convection". *Living Reviews in Computational Astrophysics* 3.1, 1.
- Li, T.; Bedding, T. R.; Huber, D.; Ball, W. H.; Stello, D.; Murphy, S. J., and Bland-Hawthorn, J. (2018). "Modelling Kepler red giants in eclipsing binaries: calibrating the mixing-length parameter with asteroseismology". *Monthly Notices of the Royal Astronomical Society* 475.1, pp. 981–998.
- Ludwig, H.-G.; Freytag, B., and Steffen, M. (1999). "A calibration of the mixing-length for solar-type stars based on hydrodynamical simulations. I. Methodical aspects and results for solar metallicity". *Astronomy and Astrophysics* 346, pp. 111–124.

- Lund, M. N.; Basu, S.; Silva Aguirre, V.; Chaplin, W. J.; Serenelli, A. M.; García, R. A.; Latham, D. W.; Casagrande, L.; Bieryla, A.; Davies, G. R.; Viani, L. S.; Buchhave, L. A.; Miglio, A.; Soderblom, D. R.; Valenti, J. A., et al. (2016a). “Asteroseismology of the Hyades with K2: first detection of main-sequence solar-like oscillations in an open cluster”. *Monthly Notices of the Royal Astronomical Society* 463.3, pp. 2600–2611.
- Lund, M. N.; Chaplin, W. J.; Casagrande, L.; Silva Aguirre, V.; Basu, S.; Bieryla, A.; Christensen-Dalsgaard, J.; Latham, D. W.; White, T. R.; Davies, G. R.; Huber, D.; Buchhave, L. A., and Handberg, R. (2016b). “Asteroseismic Properties of Solar-type Stars Observed with the NASA K2 Mission: Results from Campaigns 1-3 and Prospects for Future Observations”. *Publications of the Astronomical Society of the Pacific* 128.970, p. 124204.
- Lund, M. N.; Silva Aguirre, V.; Davies, G. R.; Chaplin, W. J.; Christensen-Dalsgaard, J.; Houdek, G.; White, T. R.; Bedding, T. R.; Ball, W. H.; Huber, D.; Antia, H. M.; Lebreton, Y.; Latham, D. W.; Handberg, R.; Verma, K., et al. (2017). “Standing on the Shoulders of Dwarfs: the Kepler Asteroseismic LEGACY Sample. I. Oscillation Mode Parameters”. *Astrophysical Journal* 835.2, 172.
- Magic, Z.; Chiavassa, A.; Collet, R., and Asplund, M. (2015). “The Stagger-grid: A grid of 3D stellar atmosphere models. IV. Limb darkening coefficients”. *Astronomy and Astrophysics* 573, A90.
- Magic, Z.; Collet, R.; Asplund, M.; Trampedach, R.; Hayek, W.; Chiavassa, A.; Stein, R. F., and Nordlund, Å. (2013a). “The Stagger-grid: A grid of 3D stellar atmosphere models. I. Methods and general properties”. *Astronomy and Astrophysics* 557, A26.
- Magic, Z.; Collet, R.; Hayek, W., and Asplund, M. (2013b). “The Stagger-grid: A grid of 3D stellar atmosphere models. II. Horizontal and temporal averaging and spectral line formation”. *Astronomy and Astrophysics* 560, A8.
- Magic, Z. and Weiss, A. (2016). “Surface-effect corrections for the solar model”. *Astronomy and Astrophysics* 592, A24.
- Magic, Z.; Weiss, A., and Asplund, M. (2015). “The Stagger-grid: A grid of 3D stellar atmosphere models. III. The relation to mixing length convection theory”. *Astronomy and Astrophysics* 573, A89.

- Majewski, S. R.; Schiavon, R. P.; Frinchaboy, P. M.; Allende Prieto, C.; Barkhouser, R.; Bizyaev, D.; Blank, B.; Brunner, S.; Burton, A.; Carrera, R.; Chojnowski, S. D.; Cunha, K.; Epstein, C.; Fitzgerald, G.; García Pérez, A. E., et al. (2017). “The Apache Point Observatory Galactic Evolution Experiment (APOGEE)”. *Astronomical Journal* 154.3, 94.
- Michel, E.; Baglin, A.; Auvergne, M.; Catala, C.; Samadi, R.; Baudin, F.; Appourchaux, T.; Barban, C.; Weiss, W. W.; Berthomieu, G.; Boumier, P.; Dupret, M.-A.; García, R. A.; Fridlund, M.; Garrido, R., et al. (2008). “CoRoT Measures Solar-Like Oscillations and Granulation in Stars Hotter Than the Sun”. *Science* 322.5901, p. 558.
- Miglio, A.; Chiappini, C.; Morel, T.; Barbieri, M.; Chaplin, W. J.; Girardi, L.; Montalbán, J.; Valentini, M.; Mosser, B.; Baudin, F.; Casagrande, L.; Fossati, L.; Silva Aguirre, V., and Baglin, A. (2013). “Galactic archaeology: mapping and dating stellar populations with asteroseismology of red-giant stars”. *Monthly Notices of the Royal Astronomical Society* 429.1, pp. 423–428.
- Miglio, A.; Chiappini, C.; Mosser, B.; Davies, G. R.; Freeman, K.; Girardi, L.; Jofré, P.; Kawata, D.; Rendle, B. M.; Valentini, M.; Casagrande, L.; Chaplin, W. J.; Gilmore, G.; Hawkins, K.; Holl, B., et al. (2017). “PLATO as it is : A legacy mission for Galactic archaeology”. *Astronomische Nachrichten* 338.6, pp. 644–661.
- Mihalas, D.; Däppen, W., and Hummer, D. G. (1988). “The Equation of State for Stellar Envelopes. II. Algorithm and Selected Results”. *Astrophysical Journal* 331, p. 815.
- Mihalas, D.; Hummer, D. G.; Mihalas, B. W., and Däppen, W. (1990). “The Equation of State for Stellar Envelopes. IV. Thermodynamic Quantities and Selected Ionization Fractions for Six Elemental Mixes”. *Astrophysical Journal* 350, p. 300.
- Morel, P.; van’t Veer, C.; Provost, J.; Berthomieu, G.; Castelli, F.; Cayrel, R.; Goupil, M. J., and Lebreton, Y. (1994). “Incorporating the atmosphere in stellar structure models: the solar case”. *Astronomy and Astrophysics* 286, pp. 91–102.

- Mosumgaard, J. R.; Ball, W. H.; Silva Aguirre, V.; Weiss, A., and Christensen-Dalsgaard, J. (2018). “Stellar models with calibrated convection and temperature stratification from 3D hydrodynamics simulations”. *Monthly Notices of the Royal Astronomical Society* 478, pp. 5650–5659.
- Mosumgaard, J. R.; Jørgensen, A. C. S.; Weiss, A.; Silva Aguirre, V., and Christensen-Dalsgaard, J. (2019). “Coupling 1D stellar evolution with 3D-hydrodynamical simulations on-the-fly II: Stellar Evolution and Asteroseismic Applications”. *Monthly Notices of the Royal Astronomical Society*, p. 2585.
- Mosumgaard, J. R.; Silva Aguirre, V.; Weiss, A.; Christensen-Dalsgaard, J., and Trampedach, R. (2017). “Improving 1D Stellar Models with 3D Atmospheres”. In: *European Physical Journal Web of Conferences*. Vol. 160. European Physical Journal Web of Conferences.
- Ness, M.; Hogg, D. W.; Rix, H.-W.; Ho, A. Y. Q., and Zasowski, G. (2015). “The Cannon: A data-driven approach to Stellar Label Determination”. *Astrophysical Journal* 808.1, 16.
- Nordlund, Å. (1982). “Numerical simulations of the solar granulation. I. Basic equations and methods.” *Astronomy and Astrophysics* 107, pp. 1–10.
- Nordlund, Å. and Dravins, D. (1990). “Stellar granulation. III. Hydrodynamic model atmospheres.” *Astronomy and Astrophysics* 228, pp. 155–183.
- Nordlund, Å. and Stein, R. F. (1990). “3-D simulations of solar and stellar convection and magnetoconvection”. *Computer Physics Communications* 59.1, pp. 119–125.
- Nordlund, Å.; Stein, R. F., and Asplund, M. (2009). “Solar Surface Convection”. *Living Reviews in Solar Physics* 6.1, 2.
- Nordström, B.; Mayor, M.; Andersen, J.; Holmberg, J.; Pont, F.; Jørgensen, B. R.; Olsen, E. H.; Udry, S., and Mowlavi, N. (2004). “The Geneva-Copenhagen survey of the Solar neighbourhood. Ages, metallicities, and kinematic properties of  $\sim 14\,000$  F and G dwarfs”. *Astronomy and Astrophysics* 418, pp. 989–1019.

- Oti Floranes, H.; Christensen-Dalsgaard, J., and Thompson, M. J. (2005). "The use of frequency-separation ratios for asteroseismology". *Monthly Notices of the Royal Astronomical Society* 356.2, pp. 671–679.
- Paxton, B.; Bildsten, L.; Dotter, A.; Herwig, F.; Lesaffre, P., and Timmes, F. (2011). "Modules for Experiments in Stellar Astrophysics (MESA)". *The Astrophysical Journal Supplement Series* 192.1, 3.
- Paxton, B.; Cantiello, M.; Arras, P.; Bildsten, L.; Brown, E. F.; Dotter, A.; Mankovich, C.; Montgomery, M. H.; Stello, D.; Timmes, F. X., and Townsend, R. (2013). "Modules for Experiments in Stellar Astrophysics (MESA): Planets, Oscillations, Rotation, and Massive Stars". *The Astrophysical Journal Supplement Series* 208.1, 4.
- Paxton, B.; Marchant, P.; Schwab, J.; Bauer, E. B.; Bildsten, L.; Cantiello, M.; Dessart, L.; Farmer, R.; Hu, H.; Langer, N.; Townsend, R. H. D.; Townsley, D. M., and Timmes, F. X. (2015). "Modules for Experiments in Stellar Astrophysics (MESA): Binaries, Pulsations, and Explosions". *The Astrophysical Journal Supplement Series* 220.1, 15.
- Paxton, B.; Schwab, J.; Bauer, E. B.; Bildsten, L.; Blinnikov, S.; Duffell, P.; Farmer, R.; Goldberg, J. A.; Marchant, P.; Sorokina, E.; Thoul, A.; Townsend, R. H. D., and Timmes, F. X. (2018). "Modules for Experiments in Stellar Astrophysics (MESA): Convective Boundaries, Element Diffusion, and Massive Star Explosions". *The Astrophysical Journal Supplement Series* 234.2, 34.
- Paxton, B.; Smolec, R.; Schwab, J.; Gaultschi, A.; Bildsten, L.; Cantiello, M.; Dotter, A.; Farmer, R.; Goldberg, J. A.; Jermyn, A. S.; Kanbur, S. M.; Marchant, P.; Thoul, A.; Townsend, R. H. D.; Wolf, W. M., et al. (2019). "Modules for Experiments in Stellar Astrophysics (MESA): Pulsating Variable Stars, Rotation, Convective Boundaries, and Energy Conservation". *The Astrophysical Journal Supplement Series* 243.1, 10.
- Pedersen, B. B.; Vandenberg, D. A., and Irwin, A. W. (1990). "The Prediction of Stellar Effective Temperatures from the Mixing-Length Theory of Convection". *Astrophysical Journal* 352, p. 279.
- Piau, L.; Collet, R.; Stein, R. F.; Trampedach, R.; Morel, P., and Turck-Chièze, S. (2014). "Models of solar surface dynamics: impact on eigenfrequencies and radius". *Monthly Notices of the Royal Astronomical Society* 437.1, pp. 164–175.

- Pietrinferni, A.; Cassisi, S.; Salaris, M., and Castelli, F. (2004). “A Large Stellar Evolution Database for Population Synthesis Studies. I. Scaled Solar Models and Isochrones”. *Astrophysical Journal* 612.1, pp. 168–190.
- Pinsonneault, M. H.; Elsworth, Y.; Epstein, C.; Hekker, S.; Mészáros, S.; Chaplin, W. J.; Johnson, J. A.; García, R. A.; Holtzman, J.; Mathur, S.; García Pérez, A.; Silva Aguirre, V.; Girardi, L.; Basu, S.; Shetrone, M., et al. (2014). “The APOKASC Catalog: An Asteroseismic and Spectroscopic Joint Survey of Targets in the Kepler Fields”. *The Astrophysical Journal Supplement Series* 215.2, 19.
- Pont, F. and Eyer, L. (2004). “Isochrone ages for field dwarfs: method and application to the age-metallicity relation”. *Monthly Notices of the Royal Astronomical Society* 351.2, pp. 487–504.
- Rauer, H.; Catala, C.; Aerts, C.; Appourchaux, T.; Benz, W.; Brandeker, A.; Christensen-Dalsgaard, J.; Deleuil, M.; Gizon, L.; Goupil, M.-J.; Güdel, M.; Janot-Pacheco, E.; Mas-Hesse, M.; Pagano, I.; Piotto, G., et al. (2014). “The PLATO 2.0 mission”. *Experimental Astronomy* 38.1-2, pp. 249–330.
- Ricker, G. R.; Winn, J. N.; Vanderspek, R.; Latham, D. W.; Bakos, G. Á.; Bean, J. L.; Berta-Thompson, Z. K.; Brown, T. M.; Buchhave, L.; Butler, N. R.; Butler, R. P.; Chaplin, W. J.; Charbonneau, D.; Christensen-Dalsgaard, J.; Clampin, M., et al. (2014). “Transiting Exoplanet Survey Satellite (TESS)”. In: *Proceedings of the SPIE, Volume 9143, id. 914320 15 pp.* (2014). Vol. 9143. SPIE Conference Series. Society of Photo-Optical Instrumentation Engineers.
- Rogers, F. J. and Iglesias, C. A. (1992). “Radiative Atomic Rosseland Mean Opacity Tables”. *The Astrophysical Journal Supplement Series* 79, p. 507.
- Rogers, F. J. and Nayfonov, A. (2002). “Updated and Expanded OPAL Equation-of-State Tables: Implications for Helioseismology”. *Astrophysical Journal* 576.2, pp. 1064–1074.
- Rogers, F. J.; Swenson, F. J., and Iglesias, C. A. (1996). “OPAL Equation-of-State Tables for Astrophysical Applications”. *Astrophysical Journal* 456, p. 902.

- Rosenthal, C. S.; Christensen-Dalsgaard, J.; Nordlund, Å.; Stein, R. F., and Trampedach, R. (1999). "Convective contributions to the frequencies of solar oscillations". *Astronomy and Astrophysics* 351, pp. 689–700.
- Roxburgh, I. W. (2005). "The ratio of small to large separations of stellar p-modes". *Astronomy and Astrophysics* 434.2, pp. 665–669.
- Roxburgh, I. W. and Vorontsov, S. V. (2003). "The ratio of small to large separations of acoustic oscillations as a diagnostic of the interior of solar-like stars". *Astronomy and Astrophysics* 411, pp. 215–220.
- Roxburgh, I. W. (2018). "Overfitting and correlations in model fitting with separation ratios". *arXiv e-prints*, arXiv:1808.07556.
- Sahlholdt, C. L.; Silva Aguirre, V.; Casagrande, L.; Mosumgaard, J. R., and Bojsen-Hansen, M. (2018). "Testing asteroseismic radii of dwarfs and subgiants with Kepler and Gaia". *Monthly Notices of the Royal Astronomical Society* 476.2, pp. 1931–1941.
- Sahlholdt, C. L. and Silva Aguirre, V. (2018). "Asteroseismic radii of dwarfs: new accuracy constraints from Gaia DR2 parallaxes". *Monthly Notices of the Royal Astronomical Society* 481.1, pp. L125–L129.
- Salaris, M. and Cassisi, S. (2008). "Stellar models with the ML2 theory of convection". *Astronomy and Astrophysics* 487.3, pp. 1075–1080.
- Salaris, M. and Cassisi, S. (2015). "Stellar models with mixing length and  $T(\tau)$  relations calibrated on 3D convection simulations". *Astronomy and Astrophysics* 577, A60.
- Salaris, M.; Cassisi, S.; Schiavon, R. P., and Pietrinferni, A. (2018). "Effective temperatures of red giants in the APOKASC catalogue and the mixing length calibration in stellar models". *Astronomy and Astrophysics* 612, A68.
- Salaris, M. and Weiss, A. (2002). "Homogeneous age dating of 55 Galactic globular clusters. Clues to the Galaxy formation mechanisms". *Astronomy and Astrophysics* 388, pp. 492–503.
- Schlattl, H.; Weiss, A., and Ludwig, H.-G. (1997). "A solar model with improved subatmospheric stratification." *Astronomy and Astrophysics* 322, pp. 646–652.

- Schuster, W. J. and Nissen, P. E. (1988). "Four-color UVBY and H $\beta$  photometry of high-velocity and metal-poor stars. I. The catalogue of observations." *Astronomy and Astrophysics Supplement Series* 73, pp. 225–241.
- Schuster, W. J. and Nissen, P. E. (1989). "Uvby-beta photometry of high-velocity and metal-poor stars. II. Intrinsic color and metallicity calibrations." *Astronomy and Astrophysics* 221, pp. 65–77.
- Schwarzschild, M. (1975). "On the scale of photospheric convection in red giants and supergiants." *Astrophysical Journal* 195, pp. 137–144.
- Serenelli, A. M. (2010). "New results on standard solar models." *Astrophysics and Space Science* 328.1-2, pp. 13–21.
- Serenelli, A. M. (2016). "Alive and well: A short review about standard solar models." *European Physical Journal A* 52.4, 78.
- Serenelli, A. M.; Basu, S.; Ferguson, J. W., and Asplund, M. (2009). "New Solar Composition: The Problem with Solar Models Revisited." *The Astrophysical Journal Letters* 705.2, pp. L123–L127.
- Serenelli, A. M.; Bergemann, M.; Ruchti, G., and Casagrande, L. (2013). "Bayesian analysis of ages, masses and distances to cool stars with non-LTE spectroscopic parameters." *Monthly Notices of the Royal Astronomical Society* 429.4, pp. 3645–3657.
- Serenelli, A.; Johnson, J.; Huber, D.; Pinsonneault, M.; Ball, W. H.; Tayar, J.; Silva Aguirre, V.; Basu, S.; Troup, N.; Hekker, S.; Kallinger, T.; Stello, D.; Davies, G. R.; Lund, M. N.; Mathur, S., et al. (2017). "The First APOKASC Catalog of Kepler Dwarf and Subgiant Stars." *The Astrophysical Journal Supplement Series* 233.2, 23.
- Silva Aguirre, V. (2018). "Stellar Evolution and Modelling Stars". In: *Asteroseismology and Exoplanets: Listening to the Stars and Searching for New Worlds*. Ed. by T. Campante; N. Santos, and M. J. P. F. G. Monteiro. Springer International Publishing, pp. 3–25.
- Silva Aguirre, V.; Ballot, J.; Serenelli, A. M., and Weiss, A. (2011). "Constraining mixing processes in stellar cores using asteroseismology. Impact of semiconvection in low-mass stars." *Astronomy and Astrophysics* 529, A63.

- Silva Aguirre, V.; Bojsen-Hansen, M.; Slumstrup, D.; Casagrande, L.; Kawata, D.; Ciuc, I.; Handberg, R.; Lund, M. N.; Mosumgaard, J. R.; Huber, D.; Johnson, J. A.; Pinsonneault, M. H.; Serenelli, A. M.; Stello, D.; Tayar, J., et al. (2018). "Confirming chemical clocks: asteroseismic age dissection of the Milky Way disc(s)". *Monthly Notices of the Royal Astronomical Society* 475.4, pp. 5487–5500.
- Silva Aguirre, V.; Davies, G. R.; Basu, S.; Christensen-Dalsgaard, J.; Creevey, O.; Metcalfe, T. S.; Bedding, T. R.; Casagrande, L.; Handberg, R.; Lund, M. N.; Nissen, P. E.; Chaplin, W. J.; Huber, D.; Serenelli, A. M.; Stello, D., et al. (2015). "Ages and fundamental properties of Kepler exoplanet host stars from asteroseismology". *Monthly Notices of the Royal Astronomical Society* 452.2, pp. 2127–2148.
- Silva Aguirre, V.; Lund, M. N.; Antia, H. M.; Ball, W. H.; Basu, S.; Christensen-Dalsgaard, J.; Lebreton, Y.; Reese, D. R.; Verma, K.; Casagrande, L.; Justesen, A. B.; Mosumgaard, J. R.; Chaplin, W. J.; Bedding, T. R.; Davies, G. R., et al. (2017). "Standing on the Shoulders of Dwarfs: the Kepler Asteroseismic LEGACY Sample. II. Radii, Masses, and Ages". *Astrophysical Journal* 835.2, 173.
- Skrutskie, M. F.; Cutri, R. M.; Stiening, R.; Weinberg, M. D.; Schneider, S.; Carpenter, J. M.; Beichman, C.; Capps, R.; Chester, T.; Elias, J.; Huchra, J.; Liebert, J.; Lonsdale, C.; Monet, D. G.; Price, S., et al. (2006). "The Two Micron All Sky Survey (2MASS)". *Astronomical Journal* 131.2, pp. 1163–1183.
- Sonoi, T.; Belkacem, K.; Dupret, M.-A.; Samadi, R.; Ludwig, H.-G.; Caffau, E., and Mosser, B. (2017). "Computation of eigenfrequencies for equilibrium models including turbulent pressure". *Astronomy and Astrophysics* 600, A31.
- Sonoi, T.; Samadi, R.; Belkacem, K.; Ludwig, H.-G.; Caffau, E., and Mosser, B. (2015). "Surface-effect corrections for solar-like oscillations using 3D hydrodynamical simulations. I. Adiabatic oscillations". *Astronomy and Astrophysics* 583, A112.
- Stein, R. F. and Nordlund, Å. (1989). "Topology of Convection beneath the Solar Surface". *The Astrophysical Journal Letters* 342, p. L95.
- Stein, R. F. and Nordlund, Å. (1998). "Simulations of Solar Granulation. I. General Properties". *Astrophysical Journal* 499.2, pp. 914–933.

- Stein, R. F. and Nordlund, Å. (2000). “Realistic Solar Convection Simulations”. *Solar Physics* 192, pp. 91–108.
- Stokholm, A.; Nissen, P. E.; Silva Aguirre, V.; White, T. R.; Lund, M. N.; Mosumgaard, J. R.; Huber, D., and Jessen-Hansen, J. (2019). “The subgiant HR 7322 as an asteroseismic benchmark star”. *Monthly Notices of the Royal Astronomical Society* 489.1, pp. 928–940.
- Strömberg, B. (1966). “Spectral Classification Through Photoelectric Narrow-Band Photometry”. *Annual Review of Astronomy & Astrophysics* 4, p. 433.
- Suresh, A. and Huynh, H. T. (1997). “Accurate Monotonicity-Preserving Schemes with Runge Kutta Time Stepping”. *Journal of Computational Physics* 136, pp. 83–99.
- Tanner, J. D.; Basu, S., and Demarque, P. (2014). “The Effect of Metallicity-dependent  $T$ - $\tau$  Relations on Calibrated Stellar Models”. *The Astrophysical Journal Letters* 785.1, L13.
- Tayar, J.; Somers, G.; Pinsonneault, M. H.; Stello, D.; Mints, A.; Johnson, J. A.; Zamora, O.; García-Hernández, D. A.; Maraston, C., and Serenelli, A. (2017). “The Correlation between Mixing Length and Metallicity on the Giant Branch: Implications for Ages in the Gaia Era”. *Astrophysical Journal* 840.1, 17.
- Thoul, A. A.; Bahcall, J. N., and Loeb, A. (1994). “Element Diffusion in the Solar Interior”. *Astrophysical Journal* 421, p. 828.
- Torres, G.; Andersen, J., and Giménez, A. (2010). “Accurate masses and radii of normal stars: modern results and applications”. *The Astronomy and Astrophysics Review* 18.1-2, pp. 67–126.
- Townsend, R. H. D.; Goldstein, J., and Zweibel, E. G. (2018). “Angular momentum transport by heat-driven g-modes in slowly pulsating B stars”. *Monthly Notices of the Royal Astronomical Society* 475.1, pp. 879–893.
- Townsend, R. H. D. and Teitler, S. A. (2013). “GYRE: an open-source stellar oscillation code based on a new Magnus Multiple Shooting scheme”. *Monthly Notices of the Royal Astronomical Society* 435.4, pp. 3406–3418.

- Trampedach, R.; Aarslev, M. J.; Houdek, G.; Collet, R.; Christensen-Dalsgaard, J.; Stein, R. F., and Asplund, M. (2017). “The asteroseismic surface effect from a grid of 3D convection simulations - I. Frequency shifts from convective expansion of stellar atmospheres”. *Monthly Notices of the Royal Astronomical Society* 466.1, pp. L43–L47.
- Trampedach, R.; Asplund, M.; Collet, R.; Nordlund, Å., and Stein, R. F. (2013). “A Grid of Three-dimensional Stellar Atmosphere Models of Solar Metallicity. I. General Properties, Granulation, and Atmospheric Expansion”. *Astrophysical Journal* 769.1, 18.
- Trampedach, R.; Däppen, W., and Baturin, V. A. (2006). “A Synoptic Comparison of the Mihalas-Hummer-Däppen and OPAL Equations of State”. *Astrophysical Journal* 646.1, pp. 560–578.
- Trampedach, R.; Stein, R. F.; Christensen-Dalsgaard, J.; Nordlund, Å., and Asplund, M. (2014a). “Improvements to stellar structure models, based on a grid of 3D convection simulations - I.  $T(\tau)$  relations”. *Monthly Notices of the Royal Astronomical Society* 442.1, pp. 805–820.
- Trampedach, R.; Stein, R. F.; Christensen-Dalsgaard, J.; Nordlund, Å., and Asplund, M. (2014b). “Improvements to stellar structure models, based on a grid of 3D convection simulations - II. Calibrating the mixing-length formulation”. *Monthly Notices of the Royal Astronomical Society* 445.4, pp. 4366–4384.
- Ulrich, R. K. (1986). “Determination of Stellar Ages from Asteroseismology”. *Astrophysical Journal* 306, p. L37.
- VandenBerg, D. A.; Brogaard, K.; Leaman, R., and Casagrande, L. (2013). “The Ages of 55 Globular Clusters as Determined Using an Improved  $\Delta V_{TO}^{HB}$  Method along with Color-Magnitude Diagram Constraints, and Their Implications for Broader Issues”. *Astrophysical Journal* 775.2, 134.
- Vernazza, J. E.; Avrett, E. H., and Loeser, R. (1981). “Structure of the solar chromosphere. III. Models of the EUV brightness components of the quiet sun.” *The Astrophysical Journal Supplement Series* 45, pp. 635–725.
- Viani, L. S.; Basu, S.; Chaplin, W. J.; Davies, G. R., and Elsworth, Y. (2017). “Changing the  $v_{max}$  Scaling Relation: The Need for a Mean Molecular Weight Term”. *Astrophysical Journal* 843.1, 11.

- Vitense, E. (1953). “Die Wasserstoffkonvektionszone der Sonne. Mit 11 Textabbildungen”. *Zeitschrift für Astrophysik* 32, p. 135.
- Vögler, A. and Schüssler, M. (2003). “Studying magneto-convection by numerical simulation”. *Astronomische Nachrichten* 324.4, pp. 399–404.
- Vögler, A.; Shelyag, S.; Schüssler, M.; Cattaneo, F.; Emonet, T., and Linde, T. (2005). “Simulations of magneto-convection in the solar photosphere. Equations, methods, and results of the MURaM code”. *Astronomy and Astrophysics* 429, pp. 335–351.
- Weiss, A. and Schlattl, H. (2008). “GARSTEC — the Garching Stellar Evolution Code. The direct descendant of the legendary Kippenhahn code”. *Astrophysics and Space Science* 316.1-4, pp. 99–106.
- White, T. R.; Benomar, O.; Silva Aguirre, V.; Ball, W. H.; Bedding, T. R.; Chaplin, W. J.; Christensen-Dalsgaard, J.; Garcia, R. A.; Gizon, L.; Stello, D.; Aigrain, S.; Antia, H. M.; Appourchaux, T.; Bazot, M.; Campante, T. L., et al. (2017). “Kepler observations of the asteroseismic binary HD 176465”. *Astronomy and Astrophysics* 601, A82.
- White, T. R.; Huber, D.; Maestro, V.; Bedding, T. R.; Ireland, M. J.; Baron, F.; Boyajian, T. S.; Che, X.; Monnier, J. D.; Pope, B. J. S.; Roettenbacher, R. M.; Stello, D.; Tuthill, P. G.; Farrington, C. D.; Goldfinger, P. J., et al. (2013). “Interferometric radii of bright Kepler stars with the CHARA Array:  $\theta$  Cygni and 16 Cygni A and B”. *Monthly Notices of the Royal Astronomical Society* 433.2, pp. 1262–1270.
- White, T. R.; Bedding, T. R.; Stello, D.; Christensen-Dalsgaard, J.; Huber, D., and Kjeldsen, H. (2011). “Calculating Asteroseismic Diagrams for Solar-like Oscillations”. *Astrophysical Journal* 743.2, 161.



# *Appendices*



# A

## The Dynamic Approach in MESA

The following is originally *Appendix A* from Mosumgaard et al. (2018) originally titled “Technical details of the MESA implementation”. Being very technical, it has been moved here from chapter 5 to not break the flow of the main text. The details were published in the paper, because we made our implementation into openly available MESA-module.



The opacity tables,  $T(\tau)$  relation and mixing-length parameters  $a_{\text{MLT}}$  of the simulations by Trampedach et al. (2013, 2014a,b) are available from the MESA marketplace<sup>1</sup> as an archive that should be extracted over an existing installation of MESA revision 9575. Code to use the  $T(\tau)$  relation in MESA runs is provided in a new folder `hydro_Ttau_examples` in two examples: `calibrate_hydro_Ttau` and `evolve_hydro_Ttau`. The archive includes code for the equivalent “reference” runs with an Eddington grey atmosphere as well. These are in the folders `calibrate_edd` and `evolve_edd`.

The first example, `calibrate_hydro_Ttau`, provides an example case that was used to calibrate the scaling factor presented in section 5.4.1. It implements a solar calibration using the `astero` module, with a small *Python* script that optimizes the model parameters. This example can be adapted by users wishing to use the 3D  $T(\tau)$  relation alongside the `astero` module. The second example, `evolve_hydro_Ttau`, provides an example used to compute the evolutionary track presented in section 5.4.2, and can be adapted for normal evolutionary calculations. In both examples, the code that interpolates the 3D  $T(\tau)$  relations and *mixing-length theory (MLT)* parameters

1: [http://cococubed.asu.edu/mesa\\_market/](http://cococubed.asu.edu/mesa_market/)

$a_{\text{MLT}}$  and modifies the boundary conditions and radiative gradient is included in the files `run_star_extras.f` and `624.dek`. The code for these two examples is also now part of the main MESA codebase and will appear in the test suite of MESA next public release (after revision 10398). Because of small changes elsewhere in MESA, the results of those test cases are not identical to the results presented here.

## A.1 Modification of radiative gradient

Since revision 9575, MESA has included a “porosity” factor  $\phi$  that reduces the opacity. By default, when  $\phi > 1$ , the opacity  $\kappa$  is replaced by  $\kappa/\phi$  when computing the radiative gradient, so the radiative gradient  $\nabla_{\text{rad}}$  is replaced by  $\nabla_{\text{rad}}/\phi$ . To modify the radiative gradient as in eq. (5.4) on page 78, we therefore assign

$$\phi = \frac{1}{1 + q'(\tau)} , \quad (\text{A.1})$$

where  $q(\tau)$  has been extracted as described in section 5.3. It is important to note that the changes to the porosity factor do *not* currently affect the optical depth  $\tau$ . If this should change in subsequent versions of MESA, the current implementation will no longer be valid.

In the main codebase for MESA revision 9575, the porosity factor is hard-coded to have a minimum value of unity. In the  $q(\tau)$  given by Trampedach et al. (2014a), this would limit us to  $q'(\tau) < 0$ , so our archive includes modified versions of core source files (`hydro_eqns.f90` and `mlt_info.f90` in `star/private`) that lift this restriction on the porosity factor. The restriction is also lifted in public releases after revision 10398 by the creation of a user control for the porosity limit.

## A.2 Boundary conditions

With the outermost meshpoint located above the photosphere, MESA needs new outer boundary conditions. We choose these to correspond to an Eddington grey atmosphere evaluated at the optical depth of the outermost

meshpoint. For the gas pressure  $P_g$ , we therefore have

$$\begin{aligned}
 P_g &= \left( \frac{g}{\kappa} - \frac{F}{c} \right) \tau \\
 &= \left( \frac{g}{\kappa} - \frac{L}{4\pi R^2 c} \right) \tau \\
 &= \left( \frac{g}{\kappa} - \frac{Lg}{4\pi GMc} \right) \tau , \tag{A.2}
 \end{aligned}$$

where  $g$  is the gravity,  $\kappa$  the Rosseland mean opacity,  $F$  the radiative flux,  $c$  the speed of light,  $\tau$  the optical depth,  $R$  the radius at the outermost point,  $G$  the gravitational constant and  $M$  the total mass of the star.

For the radiation pressure  $P_r$ , we have

$$\begin{aligned}
 P_r &= \frac{1}{3} a T^4 \\
 &= \frac{4\sigma}{3c} \cdot \frac{3}{4} T_{\text{eff}}^4 (\tau + q(\tau)) \\
 &= \frac{L}{4\pi R^2 c} (\tau + q(\tau)) \\
 &= \frac{Lg}{4\pi GMc} (\tau + q(\tau)) , \tag{A.3}
 \end{aligned}$$

where  $a$  is the radiation constant,  $T$  the temperature,  $\sigma$  the Stefan-Boltzmann constant,  $T_{\text{eff}}$  the effective temperature and  $q$  the Hopf function defined in eq. (1.37).

The total pressure  $P$  at the outermost meshpoint is therefore

$$\begin{aligned}
 P(\tau) &= P_g(\tau) + P_r(\tau) = \frac{g}{\kappa} \tau + \frac{Lg}{4\pi GMc} q(\tau) \\
 &= \frac{g}{\kappa} \tau \left[ 1 + \frac{\kappa}{\tau} \frac{L}{4\pi GMc} q(\tau) \right] . \tag{A.4}
 \end{aligned}$$

These are, in effect, equivalent to the initial conditions that **MESA** uses when integrating an atmosphere from small optical depths down to the photosphere to obtain photospheric boundary conditions.